The Dissertation Committee for Adam Boretsky Certifies that this is the approved version of the following dissertation:

Image-Based Biomarkers in Retinal Disease: Applications in Macular Degeneration

Committee:

Massoud Motamedi, Ph.D

Erik van Kuijk, M.D., Ph.D.

Bernard F. Godley, M.D., Ph.D., M.B.A., FACS

Ronald G. Tilton, Ph.D.

Gracie Vargas, Ph.D.

Dean, Graduate School

Image-Based Biomarkers in Retinal Disease: Applications in Macular Degeneration

by

Adam Raymond Boretsky, B.S.

Dissertation

Presented to the Faculty of the Graduate School of

The University of Texas Medical Branch

in Partial Fulfillment

of the Requirements

for the Degree of

Doctor of Philosophy

The University of Texas Medical Branch

August 2014

Dedication

To my family and friends who have been incredibly supportive throughout this journey.

Acknowledgements

This dissertation represents the culmination of nearly 6 years of exciting research in the Center for Biomedical Engineering under the direction of Dr. Massoud Motamedi. He gave me my first job as a biomedical engineer and later encouraged me to apply that knowledge in the pursuit of my doctorate. Above all, I learned that creativity and the willingness to take chances to pursue crazy ideas often yields the most rewarding, and sometimes unexpected, results that keep science fun. I will forever be grateful for the opportunities and experiences that he facilitated over the years in his lab. Likewise, I would not be where I am today without the guidance of my co-mentor Dr. Erik van Kuijk. He was instrumental in helping me understand and fully appreciate the clinical and translational aspects of my research while also being an advocate in my professional life and personal life.

Above all, I would like to sincerely thank my parents, Bruce and Debbie, and my brother, Andy, for providing their unconditional love and support. From an early age, you encouraged my curiosity and inquisitive nature even when my constant stream of questions likely pushed them beyond the normal human limits of patience. I love you guys.

Brent Bell and Dr. Alexander Kholodnykh were instrumental in my early career development in the CBME. The knowledge and skills I learned from you provided the foundation for my education in optical systems and in a broader sense, scientific research. Similarly, Dr. Jeffery Oliver and Dr. Ginger Pocock were friends and collaborators at the

Air Force Research Lab who contributed a great deal to my education and career development. There were also a number of graduate students, medical students, post-docs, and residents who made significant contributions to the research projects highlighted in this dissertation. I am truly grateful for all of your help. It was a pleasure working with you all.

To Shelley and Robert, I doubt I will ever be able to fully express my gratitude for all that you have done for me over the past decade. From the moment I moved to Texas, you supported me and welcomed me into your family. I could not have accomplished this without you. And last but certainly not least, to Elysse. Through it all, your love, encouragement and friendship were immeasurable sources of comfort on this crazy adventure. I will treasure all of the wonderful times together and I wish you all the happiness in the world.

Image-Based Biomarkers in Retinal Disease: Applications in Macular Degeneration

Publication No._____

Adam Boretsky, Ph.D.

The University of Texas Medical Branch, 2014

Supervisor: Massoud Motamedi

The purpose of this research was to investigate and objectively quantify image-based biomarkers of ocular injury and disease using a combination of non-invasive high resolution imaging techniques. High resolution imaging and sensing provides the basis for the diagnosis of most retinal diseases so effective characterization of endogenous molecular and morphological biomarkers may provide greater insight into the underlying biological processes responsible for tissue damage and visual dysfunction. Moreover, the non-invasive nature of the data acquisition provides an opportunity to investigate dynamic effects and establish a more complete spatial and temporal profile of disease processes within the retina.

The intrinsic optical properties of the eye allow us to quantify differences in depth resolved scattering and fluorescence signatures directly related to retinal pathology. The research presented in this dissertation consists of multiple studies aimed at utilizing high resolution imaging tools to identify and objectively analyze image-based biomarkers of retinal degeneration. A combination of imaging and enhancement techniques that

included confocal scanning laser ophthalmoscopy, white light fundoscopy, optical coherence tomography and adaptive optics were used for the *in vivo* data collection.

To achieve these goals we investigated small animal models of retinal disease, small animal models of inducible retinal injury and human subjects exhibiting retinal pathology. Collectively, these studies demonstrate the utility of multimodal retinal imaging in the detection and monitoring of perturbations within the retina discrete layers of the retina. The complementary visualization techniques provided multiple metrics which may be used validate the utility of small animal models and establish new clinical criteria for the assessment of ocular diseases at a cellular or even molecular level.

TABLE OF CONTENTS

List of Tables

List of Figures

List of Abbreviations

AFOSR	Air Force Office of Scientific Research
AO	Adaptive Optics
AMD	Age-related Macular Degeneration
APD	Avalanche Photodiode
AREDS	Age Related Eye Disease Study
ARVO	The Association for Research in Vision and Ophthalmology
ASLMS	The American Society for Laser Medicine and Surgery
BM	Bruch's Membrane
BRVO	Branch Retinal Vein Occlusion
CCD	Charge-coupled Device
CNV	Choroidal Neovascularization
cSLO	Confocal Scanning Laser Ophthalmoscope/Ophthalmoscopy
CSR	Central Serous Retinopathy
DHA	Docosahexaenoic acid
DIC	Differential Interference Contrast
eGFP	Enhanced Green Fluorescent Protein
ELM	External Limiting Membrane
ERG	Electroretinography
FA	Fluorescein Angiography
FAF	Fundus Autofluorescence
FOV	Field of View
GA	Geographic Atrophy
GCL	Ganglion Cell Layer
GWAS	Genome Wide Association Study
HS-WS	Hartman-Shack Wavefront Sensor
ICG	Indocyanine Green
ILM	Inner Limiting Membrane
INL	Inner Nuclear Layer
IP	Intraperitoneal
IPL	Inner Plexiform Layer
IS/OS	Inner Segment/Outer Segment Junction
LCA	Longitudinal Chromatic Aberration
MEMS	Microelectro-Mechanical Systems
MPOD	Macular Pigment Optical Density
MVL	Minimal Visible Lesion
NFL	Nerve Fiber Layer
NIR	Near-Infrared
OCT	Optical Coherence Tomography
OD	Oculus Dexter (Right Eye)
OPL	Outer Plexiform Layer
OS	Oculus Sinister (Left Eye)
PBS	Phosphate Buffered Saline

PDR	Proliferative Diabetic Retinopathy
POS	Photoreceptor Outer Segments
PUFA	Polyunsaturated Fatty Acid
RGC	Retinal Ganglion Cell
RNFL	Retinal Nerve Fiber Layer
ROS	Reactive Oxygen Species
RPE	Retinal Pigment Epithelium
ROI	Region of Interest
SD-OCT	Spectral Domain Optical Coherence Tomography
SLD	Superluminescent Diode
SLO	Scanning Laser Ophthalmoscope/Ophthalmoscopy
SNP	Single Nucleotide Polymorphism
VEGF	Vascular Endothelial Growth Factor

Chapter 1: Introduction

Over the past three decades, diagnostic imaging in the field of ophthalmology has undergone a renaissance which has led to an unprecedented view of the eye and a greater understanding of ocular pathology. Prior to the 1980s, most ophthalmic instruments used to visualize the retina were based on the designs originally developed by Hermann von Helmholtz in 1851(2). Today, we have the ability to visualize complex vascular networks, depth-resolved morphological features at a cellular level, biochemical indicators and cellular function *in vivo*. Collectively, these techniques can provide a detailed assessment of the structure, function and molecular activity within the living eye.

This dissertation encompasses over five years of research using advanced imaging techniques to non-invasively investigate injury and disease in the retina. High-resolution multimodal imaging provided the basis for the investigation of image-based biomarkers in the living eye using both animal models and human volunteers. A summary of the experimental models used for imaging and analysis are presented in Table 1-1.

Table 1-1. Summary of Imaging Modalities and Analysis for Each Experimental Model

	Model/Disease	***In vivo* Imaging Methods**	***In vivo* Imaging Analysis**	***Ex vivo* Analysis**
Mouse	Light-induced retinal degeneration	Fluorescence SLO, NIR-SLO, SD-OCT, WL Fundoscopy	CTCF (Fluorescence), Lesion characterization	IHC, Histology, Microscopy
Rat	Light-induced retinal degeneration	SLO, NIR-SLO, SD-OCT, WL Fundoscopy	Dual-λ FAF, Fundoscopy, NIR-SLO	IHC, Histology
Human	AMD/ Outer Retinal Pathology	FAF, NIR0-SLO, SD-OCT, WL Fundoscopy, AO-SLO	Retinal Thickness, PR Density, PR Spacing	Density*, Spacing* (Comparison based on previous reports)

A series of experiments was performed using focused light sources to induce retinal injury to the retinal pigment epithelium (RPE) and photoreceptor cells in rat and mouse models. This experimental system was used to help investigate inflammation and morphological perturbations which have implications in age-related macular degeneration (AMD). A series of clinical studies was performed in parallel with the small animal research to demonstrate the applicability of our experimental models and highlight the translational implications of our findings. For the clinical study, 25 patients spanning the entire clinical spectrum of AMD volunteered to participate in the non-invasive imaging examination. Imaging data was collected using clinical diagnostic tools and a custom-built instrument capable of visualizing individual cells, particularly cone photoreceptor cells, in the living human retina. The ultimate goal of each study was to determine image-based biomarkers of injury and disease within the living eye to better understand the development and progression of AMD.

Chapter 2 provides an overview of common diagnostic imaging and sensing tools used in the field of ophthalmology with particular emphasis on the imaging modalities used to visualize the retina in our experimental systems. Each modality is addressed independently and representative images accompany each section to demonstrate orientation of the imaging plane and typical anatomical features. Methods of retinal image enhancement through the use of adaptive optics (AO) are also covered to provide insight into the next generation of ophthalmic diagnostic imaging which is currently being studied at UTMB. Multimodal retinal imaging, simultaneously acquiring data with multiple techniques to provide complimentary views of the posterior segment of the eye, is also discussed.

Chapter 3 highlights the prevalence of AMD and many of the prevailing theories regarding the pathogenesis of the disease. The epidemiology of the disease and the multitude of factors which can potentiate the progression of AMD are also covered to emphasize the complexity of the interactions between innate genetic factors and environmental mediators. Although the specific cause of AMD is still unknown, a brief summary of the proposed mechanisms for pathogenesis are presented. These mechanisms generally converge on the deleterious effects of age-related morphological changes in the outer retina, inflammation, oxidative stress, and dysfunctional regulation of lipid metabolism.

Chapter 4 introduces the emerging field of small animal retinal imaging which is a fast, efficient method of evaluating spatial and temporal changes in retinal structure, function and molecular activity in numerous disease models. This chapter also addresses the anatomical similarities in retinal structure as well as the differences in ocular anatomy which need to be considered in experimental design. Despite the abundance of animal models used to study diseases such as AMD, non-invasive imaging may be applied to quickly screen animals and examine the extent to which these models mimic pathology in humans.

Chapter 5 chronicles a non-invasive imaging study in a model of laser induced retinal injury using aged brown Norway rats. This study was supported by the Air Force Office of Scientific Research (AFOSR) to develop sensitive methods to detect sub-threshold laser injury in ocular tissue. The endogenous fundus autofluorescence (FAF) signal generated by the aggregate fluorescence pigment lipofuscin provided the basis of the non-invasive detection of laser induced degeneration in the outer retina. The role of

lipofuscin autofluorescence and outer retinal degeneration established a link between the laser injury study and clinical indications of AMD. This work was published in 2011 in the peer-reviewed journal *Investigative Ophthalmology and Visual Sciences* under the title: "Quantitative Evaluation of Retinal Response to Laser Photocoagulation Using Dual-Wavelength Fundus Autofluorescence Imaging in a Small Animal Model."

Chapter 6 expands upon the low dose laser-induced retinal injury model by incorporating additional morphological and molecular imaging modalities to assess tissue remodeling and inflammation in the retina. A transgenic mouse strain (*cis*-NF-κβ^{eGFP}) with an enhanced green fluorescent protein (eGFP) reporter was used to provide a signal suitable for non-invasive molecular imaging in the posterior segment of the mouse eye. This study was the first to demonstrate the use of this model in the context of retinal inflammation. The findings from this study yielded two conference proceedings papers based on multimodal imaging of laser-induced retinal degeneration:

(1) Laser Injury And *In Vivo* Multimodal Imaging Using A Mouse Model (2011)
(2) NF-kB activation as a biomarker of light injury using a transgenic mouse model (2012)

Chapter 7 transitions to the translational applications of high-resolution imaging of the retina using multimodal clinical imaging systems and a custom built adaptive optics scanning laser ophthalmoscope (AO-SLO) capable of visualizing individual cells within the living human eye. This investigational imaging system was designed and optimized in collaboration with engineers at Physical Sciences Inc. (Andover, MA). The acquisition parameters were developed and refined using a model eye system and healthy volunteers. The custom image processing algorithms and analytical parameters were also developed to establish quantitative metrics associated with image-based biomarkers in the retina.

Chapter 8 applied the AO-SLO imaging and analysis methodology to investigate patients with AMD. The pilot study consisting of one patient representing each of the four clinical stages of AMD was the first demonstration of AO enhanced imaging across the entire spectrum of AMD. This study was published in 2012 in the peer reviewed journal *Lasers in Surgery and Medicine* under the title: "In Vivo Imaging of Photoreceptor Disruption Associated With Age-Related Macular Degeneration: A Pilot Study(1)." The patient population was then expanded to include 20 volunteers to further investigate the impact of AMD on macular cone photoreceptor cells in the living human eye. The analytical methods were used to investigate signs of pathology by assessing local perturbations in the cone photoreceptor mosaic within patients and examining patterns among groups of patients.

Chapter 9 offers some insight into the future directions of high resolution retinal imaging for research applications as well as clinical diagnostics. Many of the recent developments like AO are still relatively rare but as the technology continues to mature, investigations of pathology are expected to increase significantly. Similarly, other imaging techniques are being adapted for ophthalmic instruments. Non-linear optical imaging and super resolution microscopy methods have already been applied to visualize ocular tissue. All of these new imaging tools provide an opportunity to not only improve diagnostics but also help evaluate new therapeutic intervention to determine efficacy.

Chapter 2: Non-Invasive Retinal Imaging and Sensing

2.1 Introduction

Historically, non-invasive imaging techniques have been used to visualize retinal pathology based on gross morphological changes. Many of these alterations in retinal structure are accompanied by reductions in visual acuity. In recent years, diagnostic imaging in ophthalmology has shifted the focus to microscopic features at the cellular or even molecular level. The extraordinary amount of detail within these images may be used to study physiology in a dynamic system and identify biomarkers of disease. Ideally, early indicators of pathology may be identified prior to visual decline enabling preventative therapeutic intervention. Moreover, the application of automated algorithms to quantify image-based biomarkers provides an objective diagnostic assessment which may be standardized.

Regardless of the imaging modality used to visualize the retina, it is important to consider that the objective lens will always be the eye of the subject being imaged. Minor imperfections in the ocular tissue or opacity of the ocular media can have a profound impact on overall quality of the data. Therefore, it is important to consider these limitations in the design of diagnostic imaging tools to maximize the quality and fidelity of the data. The following sections provide a brief overview of many common diagnostic imaging and sensing techniques currently used in the field of ophthalmology.

2.2 Confocal Scanning Laser Ophthalmoscopy (cSLO)

The scanning laser ophthalmoscope (SLO), originally dubbed the flying spot TV ophthalmoscope, was a novel instrument for collecting images of the fundus presented by

Webb, Hughes, and Pomerantzeff in 1980(3). The system employed a laser to illuminate a single spot on the retina while oscillating mirrors were synchronized to quickly raster scan the fundus. Notably, this configuration enabled images of the retina to be collected at video rate while using light exposures approximately two orders of magnitude less than standard clinical instrumentation at the time(4). The fast acquisition was particularly helpful in minimizing the effects of eye motion which can induce a blur artifact in traditional fundus photography. The addition of a confocal pinhole to the scanning laser ophthalmoscope was demonstrated in 1987 by Webb, Hughes, and Delori(5) and marked a significant improvement in image contrast and provided some axial sectioning capabilities as well. Similar to applications in conventional microscopy, the confocal pinhole was place in front of the detection element to reject light reflected or backscattered from outside the desired retinal plane. The same basic design and techniques are currently used in clinical confocal scanning laser ophthalmoscopes (cSLOs) today. Modifications to the standard cSLO configuration also permit additional features to be visualized non-invasively. In the following sections, I will describe a few of the common cSLO image acquisition modes that were used in our studies.

2.2.1 Reflectance

Monochromatic light is generally used in cSLO applications to highlight specific features within the eye. Near infrared (NIR) light sources are typically used for reflectance imaging which generates an *en face* view of the fundus to reveal topographic features in the posterior segment such as the optic disc, vessel arcades, and the nerve

fiber layer. The NIR wavelengths provide enhanced penetration depth in tissue and are much less susceptible to scattering caused by ocular opacities like cataracts.

Wavelengths in the visible spectrum may also be used for reflectance imaging. Red-free reflectance is another type of cSLO imaging technique which uses an argon laser (~488 nm) as an illumination source. This provides additional contrast around the blood vessels, the retinal nerve fiber layer and the epiretinal membrane. Figure 2-1 demonstrates a variety of fundus imaging techniques which each highlight different aspects of the posterior segment of the eye.

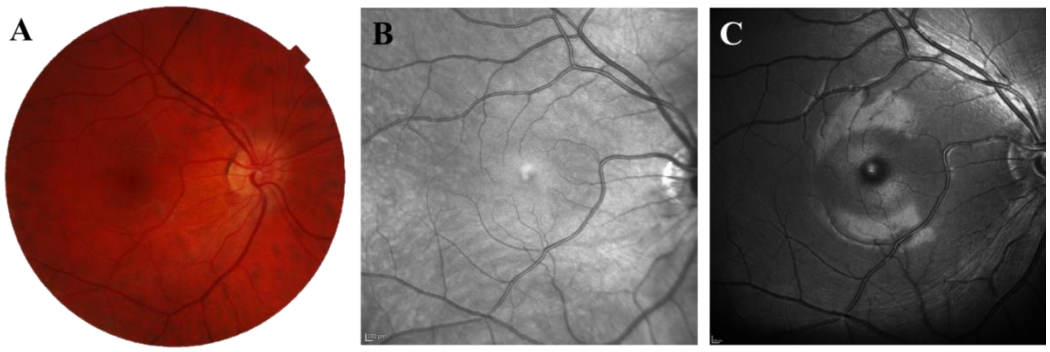

Figure 2-1. Fundus imaging in a healthy emmetrope using (A) white light fundus photography with a 45° FOV (B) NIR reflectance cSLO with a 30° FOV and (C) Red-free reflectance cSLO with a 30° FOV.

2.2.2 Angiography

Fluorescent dyes are also used to provide sufficient contrast for studying hemodynamics in the eye. Angiography is used clinically to detect a variety of complications such as occluded vessels, neovascularization, microaneurysms, and breakdown of the blood-retina barrier. Features including hyper- or hypo-fluorescence, temporal angiographic phase, and location within the eye may be used to assess vascular

complications and morphological perturbations in the retina and choroid. Two commonly used contrast agents are fluorescein and indocyanine green (ICG) which may be administered systemically to visualize vasculature in the retina and choroid. For fluorescein angiography (FA), blue-green light is used to excite the dye while a barrier filter allows only the emitted yellow-green fluorescent light to pass to the detector. ICG is a near-infrared fluorophore which is particularly adept at revealing details of the choroidal vessels since the longer excitation and emission (Ex: ~785 nm, Em: ~830 nm) wavelengths are not absorbed by the melanin in the retinal pigment epithelium (RPE). Fluorescein angiograms in three different species (human, rabbit, and rat) are shown in Figure 2-2 to highlight the orientation of the vasculature.

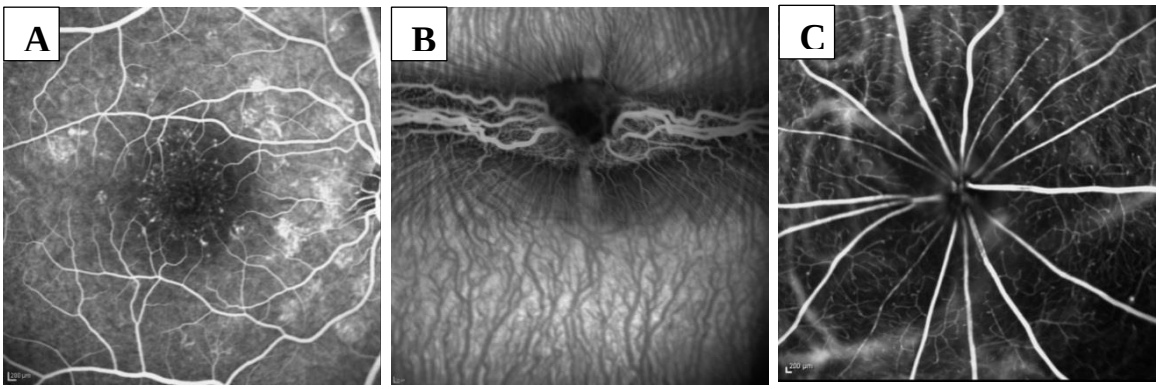

Figure 2-2. Fluorescein angiography in (A) a human patient with multiple evanescent white dot syndrome (B) an albino rabbit and (C) an albino Sprague-dawley rat.

2.2.3 Autofluorescence

Fundus autofluorescence (FAF) images are routinely used to evaluate changes in the retina associated with aging or pathology. The FAF signal is predominantly generated by autofluorescent lipofuscin granules in the RPE(6). Lipofuscin accumulates in post-mitotic cells throughout the body and originates in the RPE as a byproduct of the

lysosomal degradation of photoreceptor outer segments(7). Lipofuscin granules are comprised of multiple fluorescent components which yield a broadband emission spectrum when excited with UV or short wavelength visible light. Apart from the normal low levels of FAF and the age-related accumulation of lipofuscin, aberrant accumulation of fluorescent pigments may be indicative of pathology such as AMD and fundus flavimaculatus (Stargardt's Disease). (*Additional information on lipofuscin and its role in pathology may be found in Chapter 5)*

Traditionally, the same commercial argon lasers (~488 nm) which are used to excite fluorescein dye for angiography are also used for FAF excitation. A barrier filter is used to block the short wavelength light used for excitation while the emitted fluorescent light (> 500 nm) is collected with a sensitive photodetector. FAF patterns are highly variable and may be influenced by numerous factors but can be used as an additional tool to detect underlying pathology, particularly in the RPE. Finally, near infrared light sources have also demonstrated unique features within the fundus when used in fluorescence imaging modes but the clinical applications of this technique are still being investigated. Multiple studies have suggested melanin may be responsible for the near infrared fundus autofluorescence (NIR-FAF) which may have diagnostic implications for diseases such as AMD which have a profound impact on the RPE(8, 9). A comparison of visible features from FAF and NIR-FAF images of a patient with multiple evanescent white dot syndrome is shown in Figure 2-3.

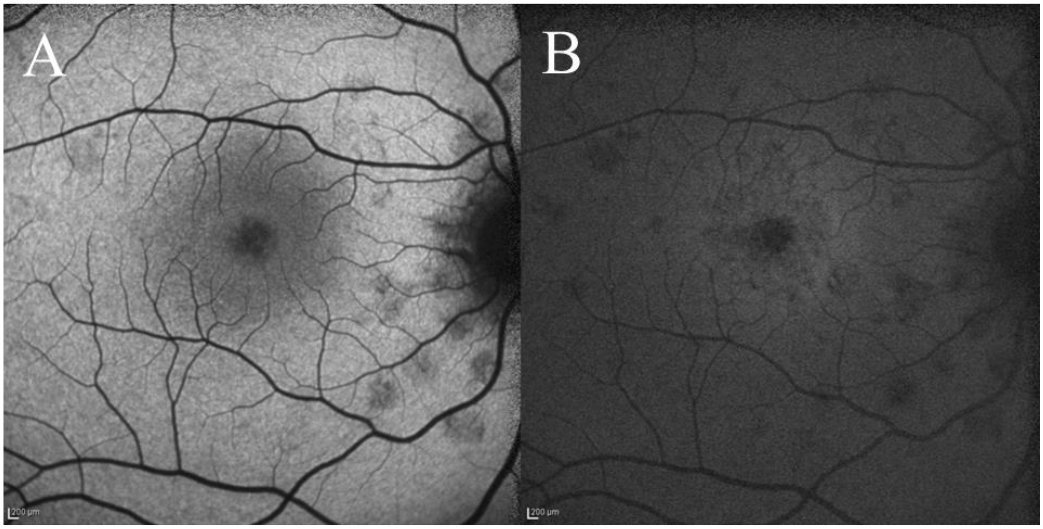

Figure 2-3. Fundus autofluorescence (FAF) imaging of outer retinal pathology in a 26 year old female patient with multiple evanescent white dot syndrome (MEWDS). (A) Traditional FAF with blue light excitation (488 nm) highlighting perifoveal lesions along the primary vessel arcades. (B) Near infrared fundus autofluorescence (NIR-FAF) revealed enhanced detail of the

2.3 Optical Coherence Tomography (OCT)

Optical coherence tomography (OCT) is an imaging modality which can generate high-resolution, cross-sectional views of tissue non-invasively by interpreting signals from backscattered light to generate an optical biopsy. The first cross-sectional OCT imaging in tissue was demonstrated by Huang *et al.* in 1991(10) and soon followed by *in vivo* imaging of the human retina two years later(11, 12). OCT signals are generated by dividing the incident light source into two paths known as the sample arm and the reference arm. When light is reflected from both paths and reaches a photodetector simultaneously, an interference signal is produced. The contrast in OCT images is created by measuring the time delay and magnitude of the interference signal of the light backscattered from the tissue. Spatial variations in structure, index of refraction and

partial absorption enable features to be easily differentiated. This technique is analogous to the detection of echoes used in ultrasound imaging.

Conventionally, OCT data is characterized based on the orientation of the scan in one of 3 ways (1) an A-scan is a single in-depth profile of the backscattered light depicted on an intensity scale (2) a B-scan is a single slice view of the tissue cross-section and (3) a C-scan, also known as *en face,* which provides a tomographic view of the tissue in the direction of light propagation. For retinal imaging applications, the *en face* view is equivalent to the fundus images generated with SLO but with improved axial resolution and reduced transverse resolution. Cross-sectional views of the tissue are generated by rapidly scanning the light source and mapping the intensity profile of adjacent A-scans which produces the B-scan view. By minimizing the spacing between B-scans, a high resolution optical biopsy of the tissue may be used to inspect depth resolved morphological features. Volumetric imaging of the human macula is shown in Figure 2-4.

A near infrared (NIR) light source, typically a superluminescent diode (SLD) or swept source laser, is used to direct photons into the tissue. The axial resolution of OCT imaging systems corresponds to the coherence length of the source and is inversely proportional to the bandwidth. Therefore, broadband sources (~60-300 nm bandwidth) with a short coherence length are often used to achieve the highest possible axial resolution and discern fine structural detail. The theoretical maximum axial resolution can be calculated using the following formula(13):

$$\Delta z = (2 \ln 2/\pi)\left(\frac{\lambda^2}{\Delta\lambda}\right)$$

where λ and $\Delta\lambda$ correspond to the wavelength of the source and the bandwidth, respectively.

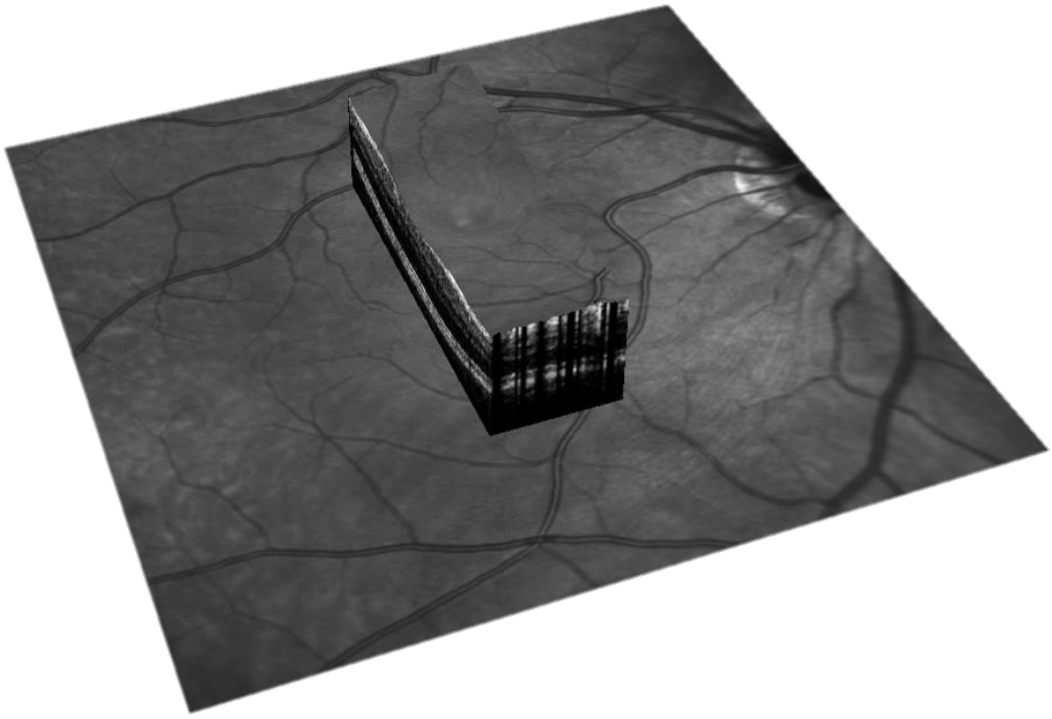

Figure 2-4. Volumetric SD-OCT imaging data (15° x 5°) scanning along the Superior-Inferior meridian depicting the macula of a healthy 29 year old volunteer in relation to a wide field fundus reflectance image. Images acquired with the Heidelberg Spectralis™ HRA+OCT in high resolution mode at a scan rate of 20kHz with an average of 20 B-scans for each position and a distance of 30µm between each B-scan.

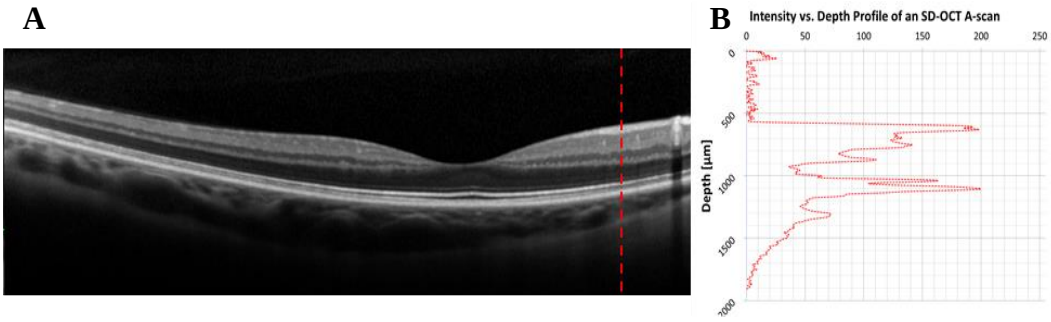

Figure 2-5. Intensity v. depth profile of SD-OCT data **(A)** SD-OCT B-scan through the fovea of a healthy volunteer. **(B)** The intensity vs. depth plot on the right represents the A-scan indicated by the dashed red line. The intensity profile may be used to differentiate retinal layers or signs of pathology.

Most modern OCT systems are knows as Fourier or frequency domain, as opposed to the original time domain OCT systems. In Fourier domain systems, the entire optical echo of each A-scan is interpreted simultaneously using an optical grating and spectrometer which improves the acquisition speed by approximately 50 times(14). This reduces motion induced artifacts and permits 3-dimensional data acquisition.

OCT has seen considerable development in the field of ophthalmology due largely to the amenable optical properties of the eye and the inaccessibility of the retina for evaluation using conventional techniques such as tissue biopsies. As shown in Figure 2-5, the retina is a stratified tissue with distinct cellular layers that are relatively easy to identify. An enhanced view of the SD-OCT b-scan is with each visible layer labeled [(NFL) Nerve fiber layer (GCL) Ganglion cell layer (IPL) Inner plexiform layer (INL) Innner nuclear layer (OPL) Outer plexiform layer (ONL) Outer nuclear layer (ELM) External limiting membrane (IS/OS) Inner segment/outer segment junction (RPE) Retinal pigment epithelium] shown in Figure 2-6. The depth resolved morphological data is used to diagnose and monitor disease and injury in the posterior segment which may not be visible when viewed using superficial fundus imaging techniques. Current clinical instruments are capable of achieving an axial resolution of 3-7 μm and a transverse resolution of approximately 15 μm(14).

The advent of new high speed scanning hardware and improved sensing elements has also led to the development of specialized OCT systems designed to measure blood flow, tissue oxygenation, and contrast-free mapping of vasculature throughout the body. Doppler OCT(15) and polarization-sensitive OCT(16) are two techniques which have demonstrated potential clinical utility with respect to retinal blood flow and

birefringence, respectively. The advancement of OCT technology remains an active area of biomedical research which includes both hardware and software based solutions for identifying characteristic features of normal morphology and pathology throughout the body.

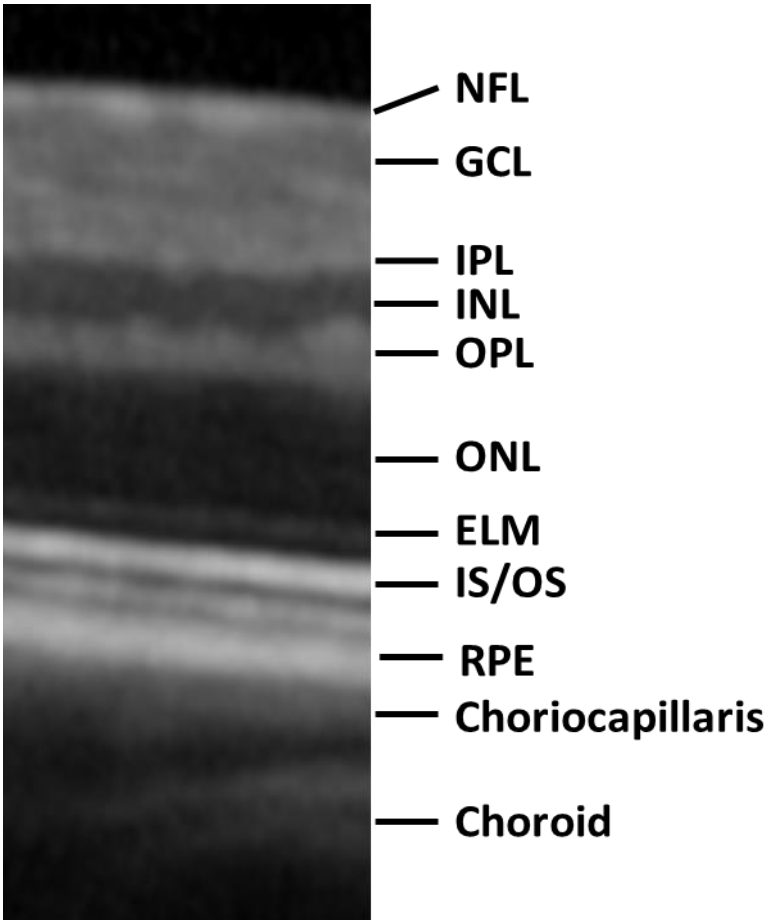

Figure 2-6. Enlarged view of an SD-OCT cross-section of the retina. (NFL) Nerve fiber layer (GCL) Ganglion cell layer (IPL) Inner plexiform layer (INL) Innner nuclear layer (OPL) Outer plexiform layer (ONL) Outer nuclear layer (ELM) External limiting membrane (IS/OS) Inner segment/outer segment junction (RPE) Retinal pigment epithelium.

2.4 Adaptive Optics (AO)

Adaptive Optics (AO) is a technique originally developed for applications in astronomy to compensate for optical aberrations in the atmosphere but has found multiple applications in biotechnology in recent years. This technology was first adapted for ocular imaging by Liang, Miller and Williams in 1997(17) to compensate for optical aberrations from the ocular tissue, primarily the cornea an lens, and observe individual photoreceptors cells in the living eye. In 2002, Roorda et al.(18) demonstrated the first AO enhanced SLO instrument. Generally, the AO component of an imaging system consists of three primary elements (1) a deformable element, typically a MicroElectroMechanical Systems (MEMS) deformable mirror (2) a wavefront sensor and (3) feedback control system to actively communicate between the sensor and the mirror. A cartoon depiction of the AO components and operation is shown in Figure 2-7. Together, these components can measure and compensate for distortions in the wavefront in real time. By correcting the aberrations caused by imperfections in the ocular tissue, it is possible to achieve resolution approaching the diffraction limit *in vivo*. It is important to note that AO alone does not actually produce an image, but may be incorporated into traditional imaging modalities such as SLO, OCT or flood illuminated fundus cameras to enhance the resolution within the eye.

Wavefront sensing provides the basis for AO correction necessary to achieve resolution approaching the diffraction limit in a living eye. The most common technique for measuring optical aberrations in the eye is through the use of a Shack-Hartmann wavefront sensor. For this type of sensor, a lenslet array is used to effectively divide the wavefront into small points to sample the wavefront across the pupil. The magnitude and

direction of the local shift in the wavefront from each lenslet position can be represented mathematically as(19):

$$\frac{\partial W(x,y)}{\partial x} = \frac{\Delta x}{f} \text{ and } \frac{\partial W(x,y)}{\partial y} = \frac{\Delta y}{f}$$

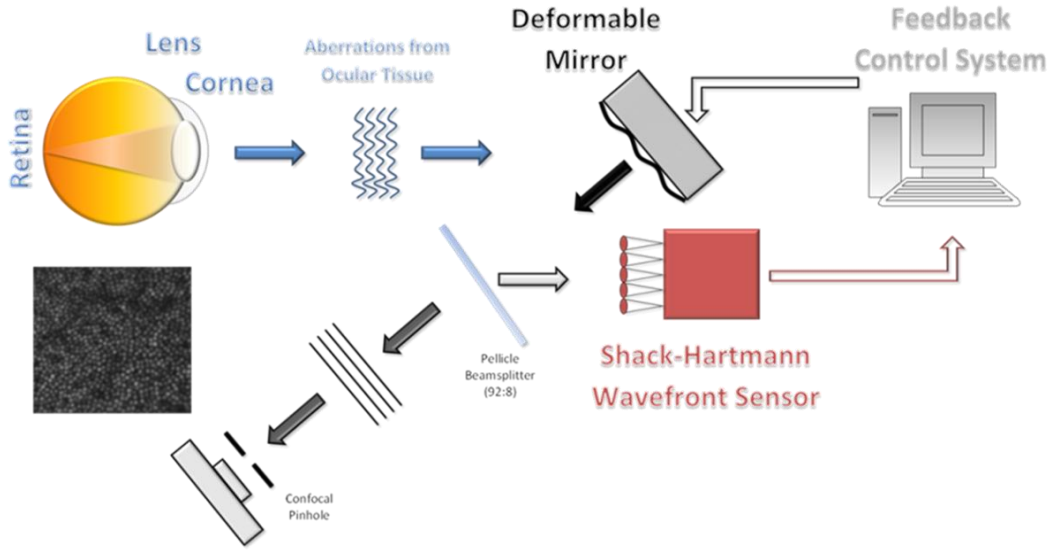

Figure 2-7. Cartoon depiction of the principal components of an adaptive optics system used to correct optical aberrations from ocular tissue. The aberrations from the wavefront ware reflected back through the optical path where a small portion of the light (8% for the UTMB system) is diverted to the Shack-Hartmann wavefront sensor. The magnitude and direction of the distortion for each point sampled across the pupil are then relayed to the deformable mirror via a computer controlled feedback system. The distortions in wavefront error are corrected by controlling an array of independent actuators to alter the surface of the mirror thereby creating a plane wavefront.

where the wavefront error, *W(x,y)* can be reconstructed based on the lateral shifts (*Δx* and *Δy*) of each focused point from the lenslet array onto the charge-coupled device (CCD) camera. By compensating for these changes in magnitude and direction, one can reconstruct an ideal plane wavefront with a specialized optical surface such as a MEMS

deformable mirror. A dynamic surface is necessary since each eye has a unique set of aberrations and patient motion can alter the orientation of the incident light with respect to the pupil. AO-SLO images from healthy volunteers are shown in Figure 2-8.

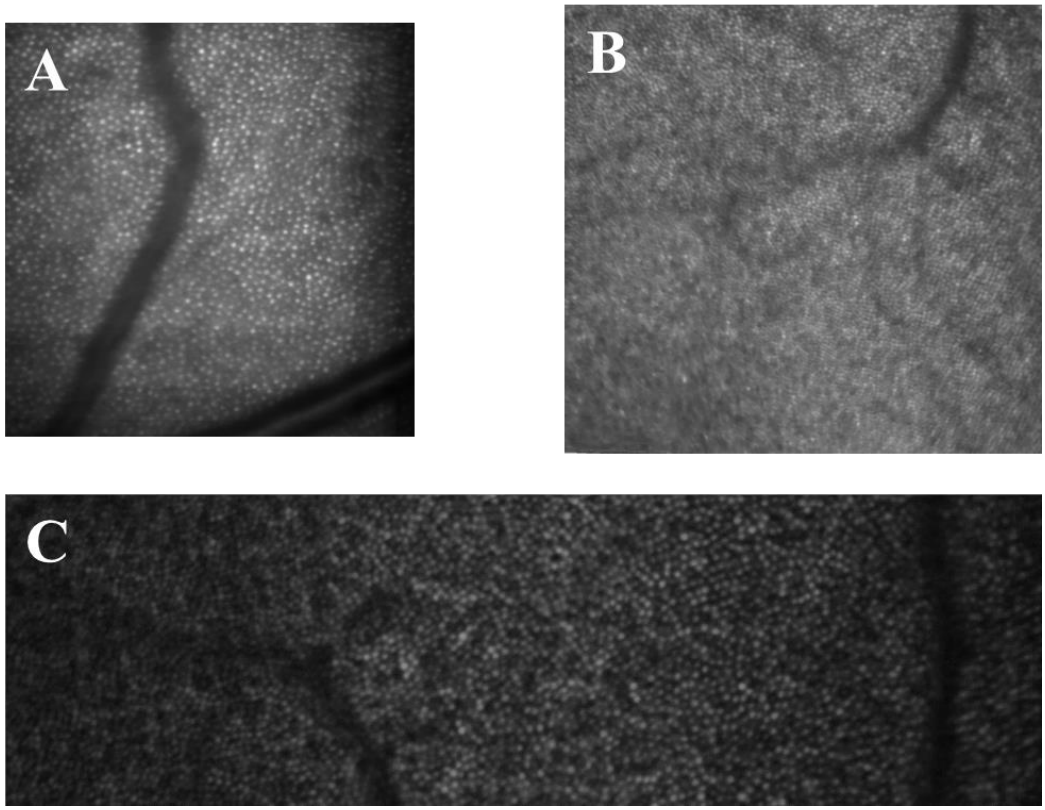

Figure 2-8. AO-SLO images from healthy volunteers demonstrating a continuous cone photoreceptor mosaic at different retinal eccentricities.

Imaging modalities enhanced with AO are now able to provide clinicians and researchers with the ability to visualize individual cells within the living retina. The development and refinement of processing algorithms for AO retinal imaging systems is an active area of research due to the wealth of information available and relative novelty of the technique for biomedical applications. Recent studies have also demonstrated applications of AO which go beyond imaging highly reflective features like the

photoreceptors. Vascular mapping without contrast agents(20-23), fluorescence imaging of the RPE(24-27) and detailed analysis of the lamina cribrosa morphology(28, 29) are among the most promising clinical prospects in ophthalmology.

2.5 Functional Imaging and Sensing

Data obtained with the previously described imaging modalities rely predominantly on the morphological observations to evaluate the health of the retina. Visual psychophysical tests and functional sensing (visual acuity, perimetry, color vision, contrast sensitivity, etc.) encompass a variety of techniques designed to quantify sensory function and visual perception based on external stimuli. Functional measurements in the retina may be obtained using a variety of methods such as perimetry and electroretinography (ERG). Perimetry is a method used to systematically detect and quantify visual deficits in the peripheral regions of the retina. Microperimetry is similar diagnostic technique which determines the sensitivity threshold in the central visual field (i.e. the macula). The preferred location of fixation and stability of fixation may also be monitored to evaluate progressive deterioration. Microperimetry provides enhanced detail regarding functional deficits associated with diseases such as AMD when compared to traditional visual acuity measurements.

ERG is used to measure the electrical responses from a variety of cells within the full field of the retina including the photoreceptors, ganglion, amacrine and bipolar cells. The amplitude of these signals and time course of the response may be used to identify regions of the retina with reduced functionality associated with underlying pathology. Multifocal ERG (mfERG) simultaneously measures the response from multiple locations

to map the function across the central 40-50° of the central visual field(30). An example of the topographic mapping of the retinal function in a patient with central visual deficits is shown in Figure 2-9.

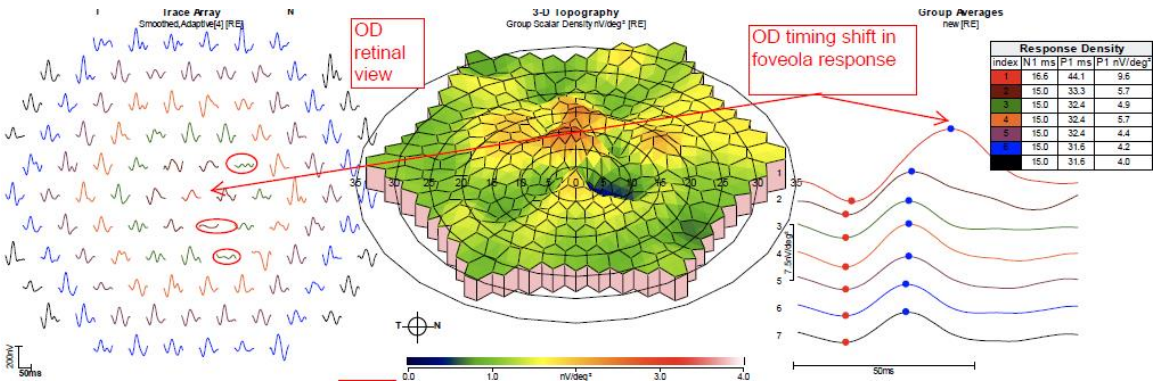

Figure 2-9. mfERG recording from a patient demonstrating focal reductions in signal amplitude in the central visual field as noted in the trace array (Left) The 3-D topography (Center) depicting the hexagonal regions of the stimulus delivery. (Right) Plot of response timing.

2.6 Multimodal Retinal Imaging

Each of the imaging and sensing methods described in the previous sections have numerous strengths and weaknesses that are dictated by the methods in which the data are generated. Many of the weaknesses can be mitigated by combining two or more imaging modalities to visualize complimentary features. For example, combining SLO and OCT enables detailed fundus imaging of structural details with high transverse resolution from the SLO channel coupled with depth-resolved morphological information from the OCT channel (Figure 2-10). Together, co-registered images utilizing these techniques can provide a more accurate assessment of retinal health than either method alone. Similarly, functional assessments may be improved by utilizing the high transverse resolution of

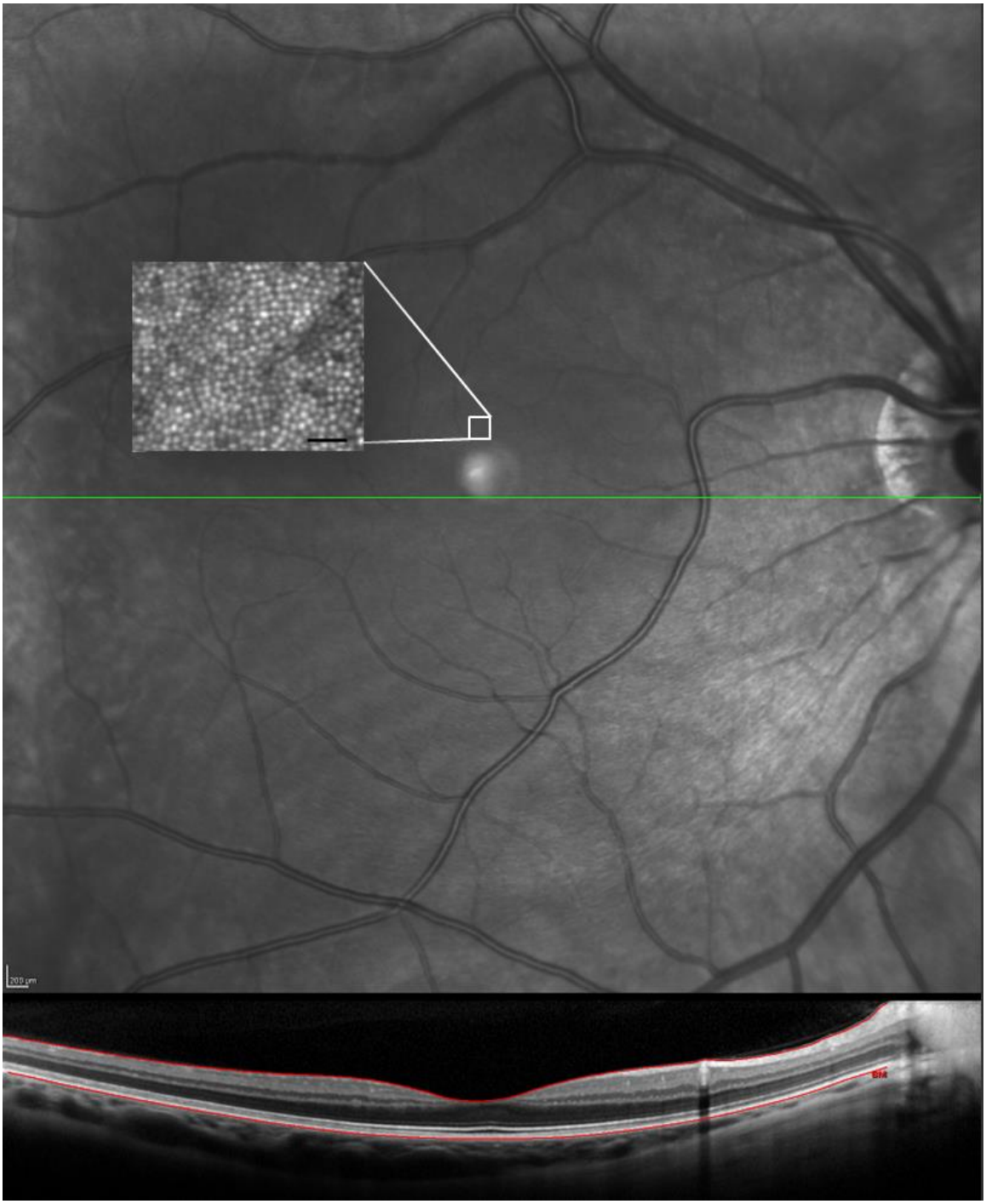

Figure 2-10. Multimodal clinical imaging in a healthy patient incorporating (A) Wide field NIR-cSLO (B) SD-OCT cross-sectional view of the retina indicated by the green line in the wide field SLO image. Inset demonstrates the scale of the images acquired with the investigational AO-cSLO at UTMB.

fundus imaging techniques such as SLO to guide stimulus delivery and test to a specific

area of interest. New imaging systems using SLO guided microperimetry offer such advantages. Moreover, the ability to monitor structure and function within a specified location over the course of time may provide valuable information regarding the progression of a disease or even the benefits of therapeutic intervention.

The incorporation of AO into multimodal imaging systems represents the next stage in the development of high-resolution diagnostics. Multiple groups have successfully demonstrated the integration of AO into systems with SD-OCT and SLO(31-34). The fidelity of functional test may also be improved with AO by utilizing the small field of view and cellular detail. Recently, AO-SLO guided microperimetry was successfully applied to measure the sensitivity of individual photoreceptor cells *in vivo*(35). The identification of clinically relevant parameters for diagnostic applications with these new techniques will undoubtedly improve our understanding of ocular pathology.

Chapter 3: Age-Related Macular Degeneration

3.1 Introduction

Age-related macular degeneration (AMD) is the leading cause of irreversible vision loss in industrialized countries and the third leading cause worldwide(36, 37). In the United States alone, approximately 8 million people over the age of 40 currently exhibit signs of AMD, and nearly 2 million have advanced AMD(38). Based on current projections, the number of AMD patients is expected to increase by 50% within the next 10 years(37). This disease targets the specialized and highly sensitive area in the central region of the retina known as the macula. Although the macula represents a relatively small fraction of the entire retinal area, it is home to the vast majority of the cone photoreceptor cells which enable humans to distinguish color and visualize fine detail.

AMD is subdivided into two major classes (1) exudative (*wet)* or (2) non-exudative *(dry).* The wet form of AMD is generally considered a more severe manifestation of the disease due to the rapid vision loss associated with aberrant growth of blood vessels and vascular leakage within the macula. Over the past decade, the use of anti-vascular endothelial growth factor (VEGF) antibodies aptamers has become the standard of care for patients with wet AMD. Although this treatment does not treat the underlying cause of the disease, anti-VEGF therapy can help preserve visual function and quality of life. However, the wet form of AMD comprises only 10-15 % of all AMD patients. The dry form of the disease represents the remaining 85-90% of the patient population and is characterized by pigment abnormalities in the retina and the presence of extracellular deposits called drusen, which form along the basal surface of the retinal

pigment epithelium (RPE). To date, there are no approved treatment options available to reverse vision loss in dry AMD but certain vitamin supplements have been shown to help delay the progression of the disease(39, 40).

As a global health epidemic, AMD also presents a major financial burden in terms of health care costs. According to AMD Alliance International, the global cost of visual impairment associated with AMD is approximately $343 billion (USD) with roughly two thirds attributed to direct healthcare costs(41). The prevalence of AMD combined with increasing life expectancy and lack of effective treatment options for the non-exudative form of the disease underscore the need for additional research.

3.2 Epidemiology

The etiology of AMD is complex with many intrinsic and extrinsic factors contributing to onset and progression of pathological degeneration in the retina. Numerous population-based studies have been conducted throughout the world to estimate the prevalence of AMD among a wide range of racial and ethnic backgrounds(37, 42-46). Additional studies have also described risk factors such as age, cigarette smoking, diet, sunlight exposure, and hypertension. Meta-analysis performed by Friedman et al.(37) demonstrated the prevalence of AMD increases exponentially after the age of 55 in the Caucasian population. This effect is somewhat reduced in other ethnicities, but there is still a significant increase associated with age across ethnicities.

Smoking is the most prominent modifiable risk factor for developing AMD. In most studies, smoking increases the risk for developing advanced AMD by a factor of 2.5 to 4.5 in current smokers. Although the exact reason is not known, it has been suggested

that smoking promotes the progression of AMD through a variety of mechanisms including increasing oxidative stress, reducing choroidal blood flow, and hypoxia. Smoking habits vary considerably, but most studies suggest that smoking cessation for an extended period of time can actually decrease AMD risk when compared to active smokers.

Nutritional factors also play an important role in the development of AMD. Most epidemiological studies have focused on effects of three types of nutritional components: antioxidants (zinc, β-carotene, vitamin C, and vitamin E), carotenoids (lutein and zeaxanthin), and omega-3 polyunsaturated fatty acids. A randomized, placebo-controlled clinical trial demonstrated that a combination of these antioxidants can reduce the risk of progression from intermediate to advanced AMD by 25%(39). The antioxidants likely mitigate the detrimental effects of reactive oxygen species (ROS) generated as a byproduct of the high metabolic activity in the retina and light exposure. The carotenoids, collectively known as macular pigment, accumulate within the macular region of the retina where they act as free radical scavengers to reduce the overall oxidative stress burden. Additionally, macular pigment has an absorption peak at 460 nm which enables it to filter high-energy blue light that has been shown to induce phototoxic effects in the retina(47, 48). Since macular pigment is not synthesized *de novo* it must be acquired through dietary intake in foods like green leafy vegetables. Multiple studies demonstrated a reduced risk for AMD in patients with high plasma concentrations of carotenoids(49-51). Omega-3 polyunsaturated fatty acids (PUFA) are another nutritional component which may reduce the risk of AMD via anti-inflammatory and anti-apoptotic functions. The long-chain omega-3 fatty acid derivative docosahexaenoic acid (DHA) is also a

primary component of photoreceptor cells and thereby provides a structural function as well(52, 53).

Although the associations across studies are occasionally inconsistent, there has been agreement in most large-scale comparative studies with regards to the detrimental effects of smoking and a protective role of antioxidants, carotenoids, and PUFAs. Likewise, familial history has been one of the most consistent indications of disease risk replicated in multiple studies signifying a strong genetic component in the development of AMD. Determining the underlying genetic risk factors remains an active area of research, but a wide variety of genes associated with AMD have already been characterized.

3.3 Genetics of AMD

Although there are a multitude of environmental risk factors which can potentiate the development of AMD, recent work to determine genetic risk factors has revealed an even greater level of complexity. A number of genomic regions have been implicated in AMD susceptibility based on meta-analysis of genome wide association studies (GWAS). These AMD-associated loci include genes which function in integral biological pathways such as the complement pathway, oxidative stress, angiogenesis, extracellular matrix, and lipid metabolism. Early detection of genetic risk factors may allow early therapeutic intervention and lifestyle changes to minimize the influence of modifiable risk factors such as smoking and diet to slow the progression of the disease.

Identification of at risk patients may be established through genetic screening, and although it is not common practice yet, screening may soon provide ophthalmologists

with another tool to devise effective treatment strategies before the onset of debilitating central vision loss. Recent studies have begun to investigate the response of antioxidant supplements(54) and pharmaceutical intervention(55, 56) in patients with known genetic risk factors.

The identification of complement pathway genes associated with increased risk for developing AMD, particularly genes coding for complement factor H (CFH), was first published in a series of papers in 2005(57-60). CFH provides negative inhibition of the alternative pathway of the complement system(61). Common single nucleotide polymorphisms (SNPs) can alter the function of CFH resulting in the over-activation of the immune response leading to persistent inflammation in the retina and damage to healthy tissue. These findings provided a genetic basis to support the belief that local pro-inflammatory events contribute to the development of AMD. Additional elements in the complement cascade (CFB(62), CFI(63), C2(64), and C3(65)) have also been identified as risk factors, although they seem to have a minor influence relative to CFH.

The age-related maculopathy susceptibility 2 gene (ARMS2) has also been identified as a contributing factor to the development of AMD(66, 67), however, the precise role of this locus has not been determined. Recent studies have identified the ARMS2 protein in the outer mitochondrial membrane of photoreceptor cells, and reduced mitochondrial populations in the RPE cells of AMD donor eyes(68, 69). Multiple research groups have suggested a prominent role of mitochondrial dysfunction in the pathogenesis of AMD through increased oxidative stress and apoptosis(70-73) which may be facilitated by certain ARMS2 variants.

It has been estimated that approximately 55-60 % of the heritability of advanced AMD may be attributed to genetic loci that have already been discovered(74). It should be noted that although these insights offer clues into the underlying mechanisms, a multitude of extrinsic factors can substantially impact the development and progression of AMD. Moreover, these modifiable risk factors can further complicate the analysis and interpretation of longitudinal studies investigating potential therapies.

3.4 Pathogenesis of AMD

Each of the following topics have already been reviewed in great detail in the literature, however, I would like to provide a brief overview of the potential mechanisms responsible for AMD pathogenesis while noting how advanced imaging techniques continue to further our understanding of the disease in a clinical setting and in experimental models.

It is generally accepted that the outer retinal complex, consisting of the photoreceptor cells, RPE, Bruch's Membrane and the choriocapillaris, is the site of AMD pathogenesis but the specific events that trigger pathology as opposed to normal aging are still unknown. Many of the proposed mechanisms of AMD pathogenesis converge on the deleterious effects of morphological changes in the outer retina, inflammation, oxidative stress on the RPE, and dysfunctional regulation of lipid metabolism.

Age-related changes in the choroid have been noted in multiple studies which may have implications in the development of AMD. For instance, Ramrattan *et al.*(75) used morphometric analysis to demonstrate a progressive thinning of the choroid whereby patients in their ninth and tenth decades exhibited a 60% decrease in total

choroidal thickness compared to young patients. Likewise, scanning laser Doppler flowmetry (SLDF) imaging demonstrated a reduction in submacular choroidal blood flow and volume associated with age(76) and further reductions in patients with AMD(77). These alterations in the choroid seen with age and AMD may contribute to the pathogenesis of AMD by compromising the exchange of nutrients and waste products with the neurosensory retina.

Bruch's membrane (BM) is the thin, multilayered extracellular matrix which acts at the interface between the retina and the choroid. Numerous age-related changes occur within BM which may contribute to the pathogenesis of AMD. Most notably, BM increases in thickness from 2 μm to approximately 4μm due to the accumulation of cellular debris and extracellular matrix proteins which become trapped in the inner collagenous layers(78, 79). This effect is more pronounced within the macular region which may explain the predisposition for morphological and functional perturbations in the central retina seen in AMD patients. Additional changes in the structural properties of BM caused by calcification and crosslinking of advanced glycation end products (AGEs) effectively impede the transport between the choroid and neural retina(80, 81).

SD-OCT is particularly useful in determining the age-related morphological changes in the outer retina since these subsurface features cannot be seen with standard fundus imaging techniques. The decrease in choroidal thickness may be measured non-invasively with techniques such as enhanced depth imaging OCT (EDI-OCT) to assess the correlation between submacular vascular alterations and changes in the neurosensory retina. Although the gradual thickening of BM is close to the current axial resolution

limits of the most advanced OCT systems, alterations in the composition of the tissue and the accumulation of extracellular deposits may be observed.

The preceding alterations in outer retinal morphology associated with age likely contribute to the development of AMD through a complex process which includes the oxidative stress, inflammation, mitochondrial dysfunction, and lipid metabolism. The retinal pigment epithelium (RPE) is a post-mitotic monolayer of cells that supports the overlying photoreceptors by maintaining the blood-retinal barrier, phagocytosis of the photoreceptor outer segments (POS), immune regulation, secretion of cytokines, and regulating metabolic activity within the retina. RPE senescence is thought to contribute to the progression of AMD since the exposure to high levels of oxidative stress is cumulative within these cells. A byproduct of POS phagocytosis is the accumulation of the autofluorescent pigment lipofuscin which has been shown to negatively impact lysosome function and cholesterol metabolism(82). Inflammation associated with morphological changes in the tissue and the presence of extracellular debris also contributes to the progression of AMD. Inflammatory mediators and immune cells responsible for pro-inflammatory signaling have been identified at the site of characteristic AMD lesions(83). The two primary inflammatory pathways implicated AMD are the complement cascade and microglial activation. The cumulative effects of stressors in the outer retina are believed to elicit a low level of inflammation, dubbed para-inflammation. Persistent para-inflammation in response to stress from exogenous factors is thought to have a significant contribution to the development of AMD(84, 85).

Fundus autofluorescence imaging (FAF) can reveal details regarding lipid metabolism and the lysosomal degradation of photoreceptor outer segments in the retina

based on the degree of lipofuscin autofluorescence within the RPE. Each patient exhibits a unique FAF pattern and the appearance of hypoautofluorescence or hyperautofluorescence may be used to identify regions of pathology (Figure 3-1). Similarly, angiography may be used to help identify changes such as voids in the RPE indicative of atrophy or thinning of the RPE associated with subretinal deposits.

3.5 Drusen

Vision loss associated with early and intermediate stages of dry AMD is typically minimal and attributed to the disruptive influence of extracellular deposits, known as drusen, which form along the basal surface of the RPE. Drusen represent one of the earliest visible biomarkers of AMD. The appearance of drusen in fundus photography (i.e. size, shape, location) is used as the basis for clinical diagnosis of early and intermediate stages of the disease. Additional imaging techniques such as SLO, FAF and SD-OCT may also be used to refine the characterization of drusen phenotypes. A summary of the AMD categories according to the Age-Related Eye Disease Study (AREDS) may be found in Table 3-1. Although it is widely accepted that drusen are risk factors associated with progression of AMD, little is known about the cause-effect relationships among the morphological disruption, functional loss and local inflammatory response as a function of disease progression.

The presence of a few small drusen (< 63 μm) distributed sparingly throughout the macula is thought to be a natural byproduct of the aging process. However, the

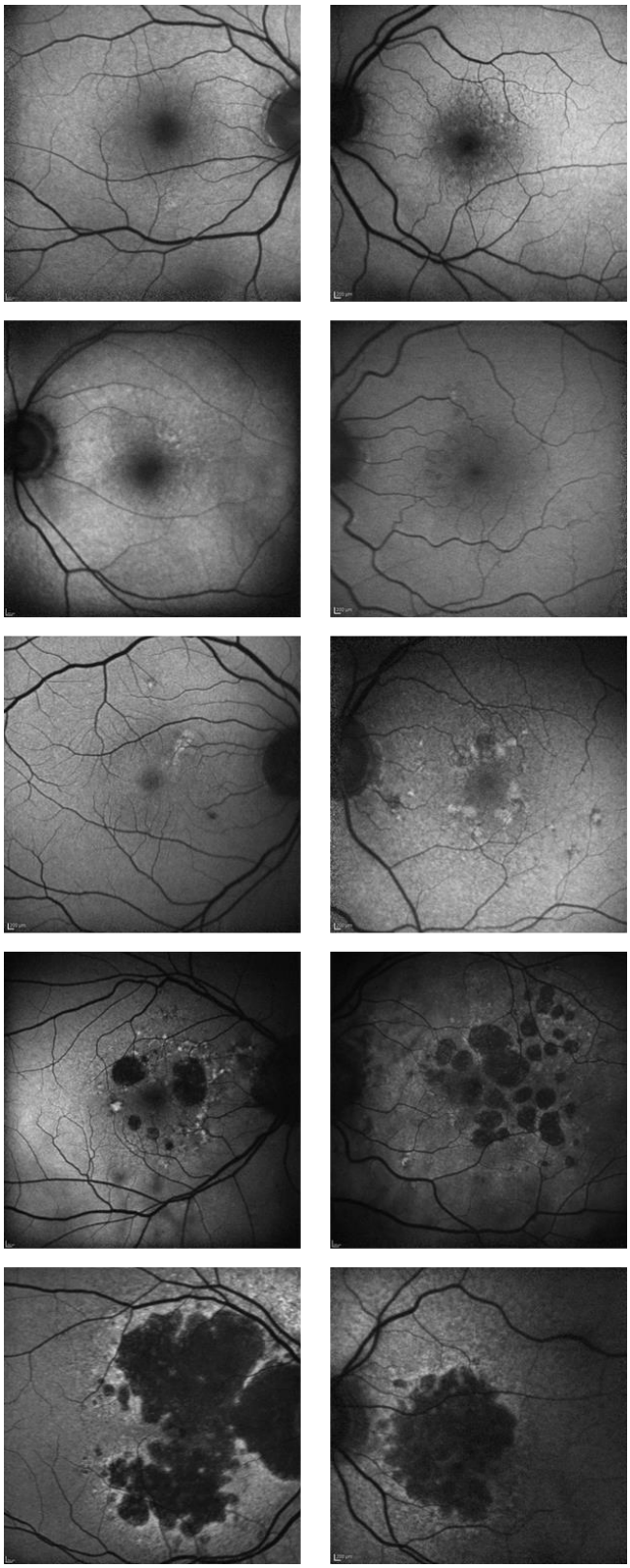

Figure 3-1. Variable appearance of AMD phenotypes encompassing each clinical stage of disease progression visualized with FAF imaging.

presence of numerous drusen in the sub-RPE space has been shown to elicit a low level inflammatory response which may develop into a persistent state of parainflammation within the microenvironment surrounding drusen(86-92). It has been hypothesized that this chronic inflammation may trigger the progression of AMD(84, 85, 87). As AMD progresses, drusen often coalesce into larger deposits which disrupt the outer retinal morphology and impede the nutrient-waste exchange functions of the RPE and choroid. Pervasive drusen may ultimately lead to the advanced form of dry AMD, known as geographic atrophy (GA), in which the death of the RPE and photoreceptor cells in the macula causes severe, irreversible vision loss. A cartoon depiction of AMD progression in a cross-sectional view of the outer retina is shown in Figure 3-2.

Table 3-1. Characterization of AMD based on the appearance of drusen using standard fundus photography methods.

Age-Related Eye Disease Study (AREDS) Stages of AMD(93)	
Category I	No or few small drusen (<63 μm)
Category II	Intermediate drusen (<125 μm)
Category III	Extensive intermediate or large drusen (>125 μm)
Category IV	Neovascular AMD or Central Geographic Atrophy

The lexicon of drusen characterization can often be confusing based on the periodic changes in nomenclature, but advancements in diagnostic imaging techniques have revealed some degree of clarity with respect to drusen phenotypes. Scanning laser ophthalmoscopy (SLO) and optical coherence tomography (OCT) have been particularly adept at discerning irregularities in the outer retina associated with AMD. Hard drusen

are common in aged individuals and generally seen as benign, but widespread hard drusen (> 8) may be associated with an increased risk of developing intermediate or advanced AMD(94). Soft drusen are larger aggregates (> 63 μm) of extracellular debris associated with a higher risk of progression to late stage AMD. Basal linear deposits (diffuse drusen) consist of membranous material such as extracellular matrix protein fragments and form between the basal membrane of the RPE cells and the inner collagenous layers of BM(95). Basal laminar drusen (cuticular drusen) typically occur in middle age, are relatively benign, and exhibit a characteristic "stars-in-the-sky" pattern during angiography. Reticular pseudodrusen (subretinal drusenoid deposits) are located between the RPE and inner segment/outer segment junction (IS/OS) of the photoreceptors(96). Reticular pseudodrusen are easy to discriminate on SD-OCT scans based on the location within the retina and were recently associated with a significant risk of developing late AMD(97).

Multiple classification systems have been developed over the past 30 years(98-100), but the Age-Related Eye Disease Study (AREDS) criteria are most commonly used clinically due to the broad applicability and simplicity of the grading scale(93). Generally, the severity scales use a combination of innate features that can be easily detected during a routine clinical examination. A concerted effort to standardize diagnostic criteria and reporting of AMD patients based on well-defined metrics was one of the primary objectives of the AREDS. The AREDS classification system relies on extensive clinical data which was used to develop a predictive model for the development of advanced AMD, either neovascular or geographic atrophy, based on observed risk factors. It remains to be seen whether specific genotypes actually correspond with distinct

phenotypes but high resolution imaging systems and large catalogues of imaging data from AMD patients would certainly facilitate such investigations.

The composition of drusen has revealed a multitude of constituents including trace elements (Ca, Fe, Zn)(101), nearly 150 proteins(102), and lipids(91, 103). The majority of these components are synthesized by the RPE, neural retinal cells, and choroidal cells. The largest component of drusen is lipid, primarily in the forms of esterified cholesterol, unesterified cholesterol and phosphatidylcholine(104). Prominent proteins include vitronectin, crystallins, apolipoprotein B, apolipoprotein E, clusterin, amyloid P, and multiple components of the complement complex(105). Many of the genes already identified as risk factors play a significant part in the regulation of inflammatory and metabolic pathways associated with the aforementioned proteins found in drusen.

3.6 Geographic Atrophy (GA)

The most advanced form of non-exudative AMD is geographic atrophy (GA) in which the loss RPE and photoreceptor cells results in extensive central visual deficits. GA accounts for approximately 20% of the legal blindness associated with AMD patients(106, 107). Abnormal RPE cells are the hallmark of GA and manifest as a variety of morphological alterations in the outer retinal complex such as atrophy, hypertrophy, hyperpigmentation, hypopigmentation, and cell migration(108) (Figure 3-3). Atrophic regions continue to enlarge over time but rates of progression vary greatly from patient to patient(109-112). GA has a distinct appearance on FAF which may be used to monitor the progression of atrophy. Regions within GA appear dark on FAF due to the lack

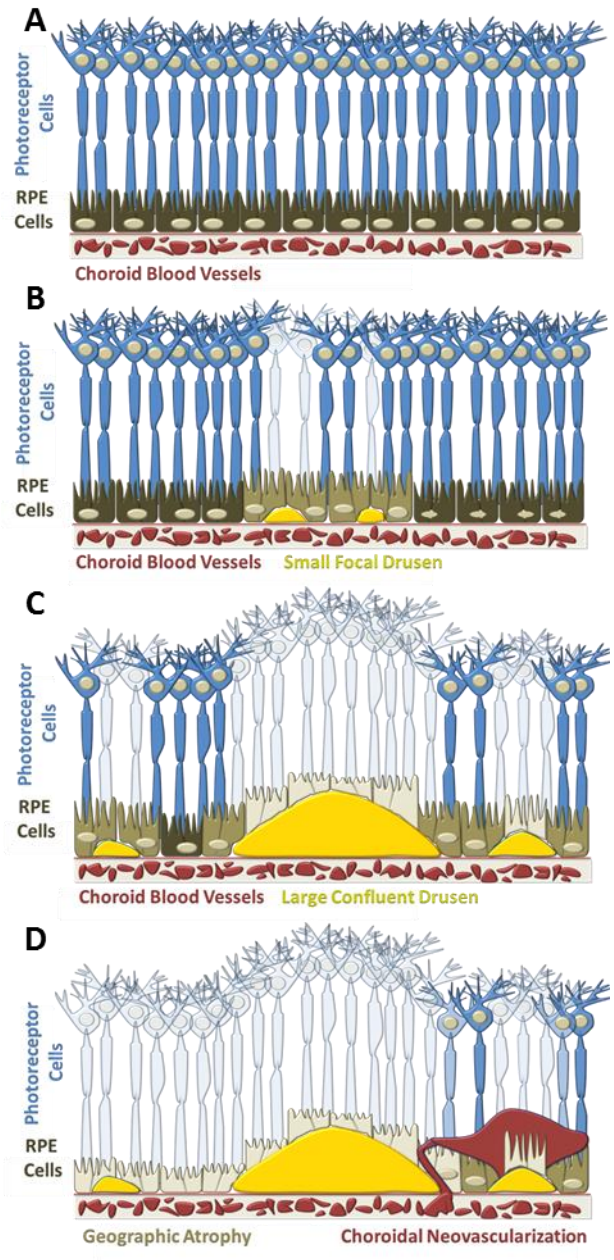

Figure 3-2. Cartoon depiction of the outer retinal cross-section at each stage of AMD progression (A) Healthy retina exhibiting a uniform photoreceptor mosaic (B) Early signs of AMD represented by small focal drusen in the sub-RPE space causing minimal disruption of the overlying photoreceptor cells. (C) Intermediate AMD with larger confluent drusen and more extensive loss of photoreceptor cells. (D) Advanced AMD exhibiting extensive central geographic atrophy of the RPE cells and choroidal neovascularization. *(Modified from Boretsky et al. 2012)*

of viable RPE cells and lipofuscin; however, the marginal zones of GA appear hyper-

autofluorescent from the release of lipofuscin granules during phagocytosis and possibly RPE hypertrophy(90, 113-115). A regression of drusen may also be observed since the presumed origins of the extracellular debris, the RPE and photoreceptor cells, have little or no metabolic activity at this stage of the disease.

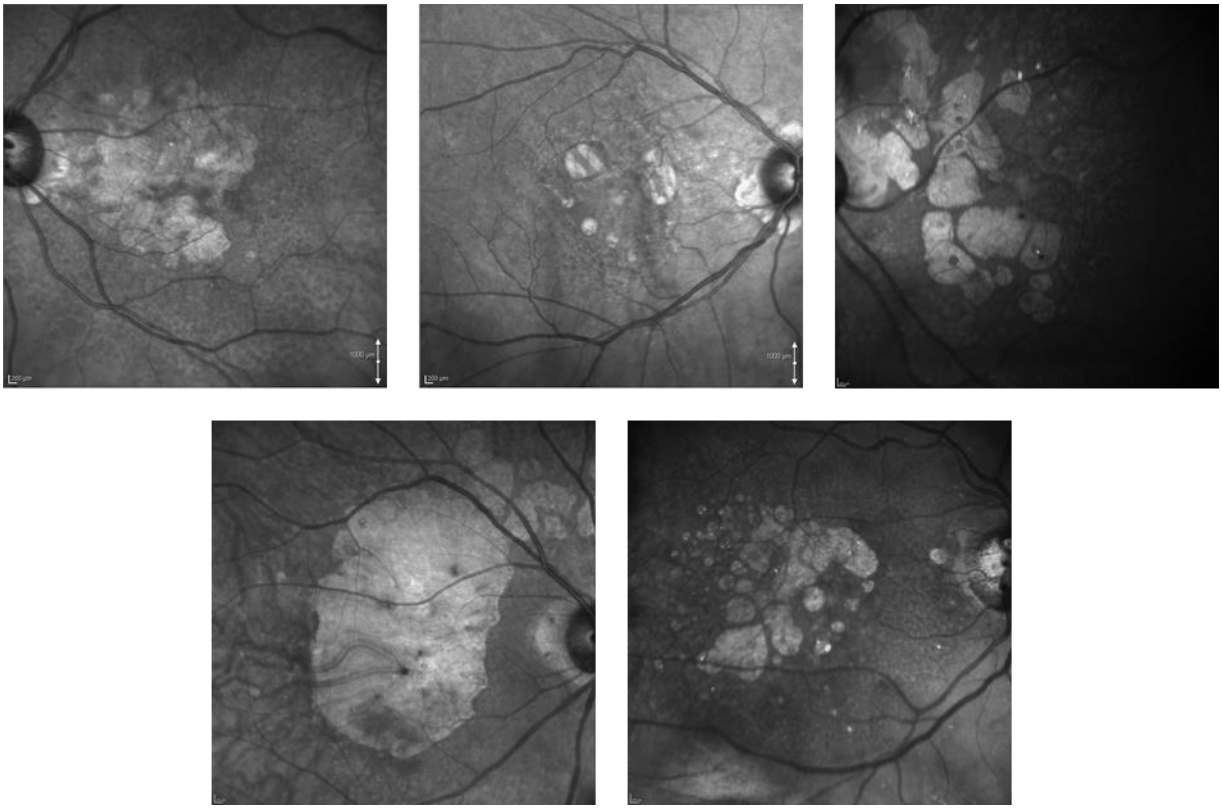

Figure 3-3. Variable patterns of geographic atrophy in 5 patients with advanced AMD viewed using NIR-reflectance cSLO.

The appearance of GA on SD-OCT cross-sections provides additional information and insight into the morphology of advanced AMD. The absence of melanin from the RPE reduces absorption and scattering of the incident light resulting in increased penetration depth in the ocular tissue. This effect can been useful in determining the boundaries of atrophic lesions. Similarly, the regression of drusen, degeneration of

photoreceptor outer segments, Bruch's membrane thickening and choroidal thinning may also be measured. Multimodal imaging of a patient exhibiting GA is shown in Figure 3-4.

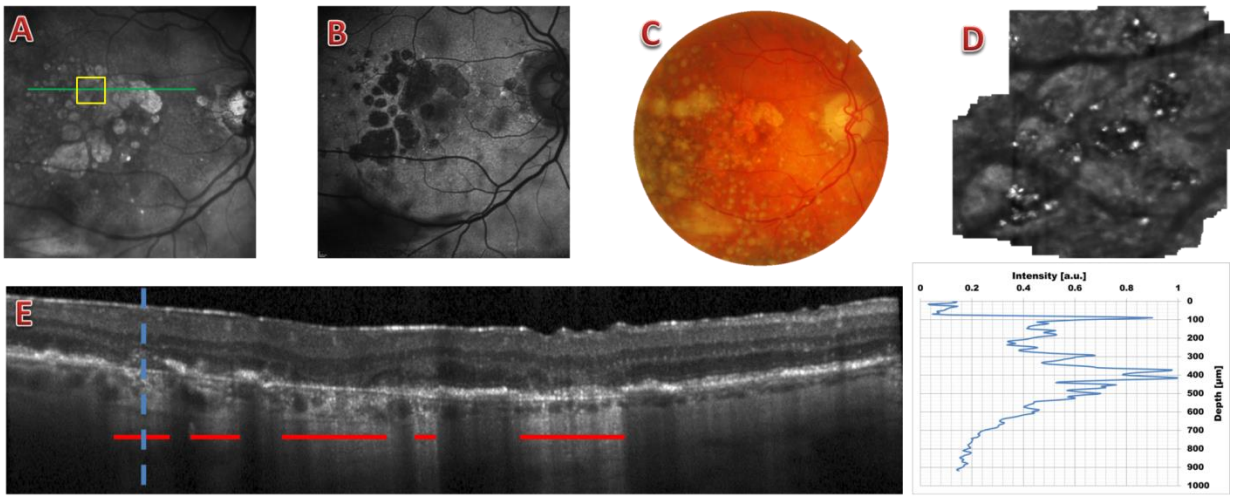

Figure 3-4. Multimodal imaging of a patient with extensive geographic atrophy throughout the macula. (A) NIR-reflectance image of the fundus (B) FAF image (C) White light fundus photograph (D) high resolution AO-SLO mosaic of the atrophic lesions representing the yellow box from panel A (E) SD-OCT cross-section indicated by the green line in panel A. Horizontal red lines denote enhanced light penetration into the choroid due to the absence of scattering and absorption from melanin in the RPE. Corresponding intensity profile in depth indicated by the dashed blue line in the SD-OCT scan.

3.7 Choroidal Neovascularization (CNV)

The aberrant growth of blood vessels from the choroid into the retinal space is the alternative form of advanced AMD known as choroidal neovascularization (CNV). The vascular leakage, bleeding and scarring within the macula often lead to visual field defects, visual distortion, and decreased visual acuity. Fluorescein angiography (FA) may be used to visualize retinal circulation and reveal anatomical changes associated with the growth of new vessels. A breakdown of the blood ocular barrier results in leakage of fluorescent dye into the retinal space. In some cases, CNV can also result in subretinal

hemorrhaging, macular edema or pigment epithelial detachment which may be observed in SD-OCT cross-sectional images.

In contrast to GA, a greater understanding of pathogenesis associated with CNV has led to the development of multiple therapies targeting the leaky vascular growth. The most commonly used agents are anti- vascular endothelial growth factor (VEGF) drugs which are administered via intravitreal injections. Although this approach does not treat the underlying cause of the disease, anti-VEGF therapies have been very effective in preserving visual function when administered regularly.

3.8 Treatment Strategies and Therapeutic Targets

Various therapeutic targets have been identified based on proposed mechanisms of pathogenesis associated with the development of non-exudative AMD. There are numerous clinical trials underway to test candidate molecules and intervention strategies(116). Disparate approaches including RPE stem cell transplants(117), anti-amyloid therapy(118), anti-complement therapy(119), and rheopheresis(120) have all been proposed. The variability in the design of appropriate treatment strategies has a great deal to do with the complexity of the disease and our limited understanding of the pathogenesis of AMD. Currently, vitamin supplementation is the only proven treatment option to delay the progression of dry AMD. Many of these trials have already demonstrated some degree of success. However, all of these approaches would benefit from a highly sensitive, objective, non-invasive and reproducible method to assess long-term patient outcomes and identify the most suitable treatment regimen.

Chapter 4: Small Animal Retinal Imaging of Injury and Disease

4.1 Introduction

The use of modified clinical instrumentation has become an increasingly popular method of studying the influence of progressive diseases in small animal models. The truncated timetable in which disease and injury may be evaluated enables investigators to quickly ascertain key elements in pathological development. The development of transgenic animals also provides an opportunity to investigate specific molecules and genes thought to play a role in human disease.

Non-invasive imaging of the rodent eye provides the opportunity to investigate many of the spatial and temporal changes in retinal morphology associated with pathology. Moreover, modern imaging systems have demonstrated capabilities which yield comparable data to traditional techniques such as histology(121-123). A recent comparison of high-resolution spectral domain optical coherence tomography (SD-OCT) data with histology in multiple murine models of retinal degeneration demonstrated a strong correlation ($r^2 = 0.897$) between the central retinal thickness measurements using both methods(124). Similarly, changes in retinal morphology have been documented using non-invasive imaging techniques in a variety of disease models such as diabetic retinopathy(125-129), glaucoma(130-132), and AMD(133-139).

As discussed in the previous chapter, AMD is a multifaceted disease with multiple environmental and genetic risk factors. The investigation of numerous animal models has greatly enhanced our understating of fundamental processes involved in the pathogenesis of AMD. However, no single model has been able to encompass the breadth

of AMD phenotypes and account for myriad causative factors which potentiate the disease. As a result, dozens of transgenic mouse models have been created to study changes in retinal ultrastructure and molecules involved in key inflammatory pathways and regulatory processes(135, 138, 140-142). Additionally, inducible models of AMD-like pathology have been used to reproduce specific characteristics of the disease. This chapter is not intended to be a review of every model of AMD, but designed to provide a brief introduction to many of the common themes in the design of these experimental models and provide a comparison between the murine retina and the primate retina.

4.2 - Anatomy of the Rodent Eye vs. Primate Eye

Despite the similarities between the rodent retina and human retina, there are notable differences in ocular anatomy which must be taken into consideration. A comparison of ocular anatomy among humans, rats and mice is summarized in Table 4-1. First, the rodent lacks a true macula which makes investigating the molecular mechanisms and innate features of AMD particularly problematic. This region of the retina is heavily populated with cone photoreceptors in primates which enables sharp central visual perception. The rodent eye lacks this cone-dense region and consequently has a much lower cone-to-rod ratio of photoreceptors when compared to primates. The mean cone density in the rodent retina is similar to the primate retina at approximately 3-4 mm eccentricity from the fovea(138). Therefore, any analysis of photoreceptor topography would need to account for these differences. Figure 4-1 provides a comparison of fundus images acquired using near infrared confocal scanning laser

ophthalmoscopy (SLO) and color fundus photography in a healthy human volunteer and a wild type C57BL/6 mouse.

The anterior segment of the rodent eye is considerably different than the primate. The crystalline lens of the rodent eye occupies a much larger percentage of the total ocular volume and the radius of the corneal curvature is considerably less. As a result, the optical power of the rodent eye is much greater than that of the human eye. Mouse, rat, and human eyes have optical powers of 560 diopters(143), 300 diopters(144) and 60 diopters(145), respectively. These differences in the optical properties result in a higher numerical aperture (NA) in the rodent eye. The mouse has a NA of approximately 0.49 with a 2 mm pupil diameter versus a NA of approximately 0.18 for a 6 mm pupil diameter in humans(146). Theoretically, the resolving power should be greater in the rodent eye yielding a diffraction-limited transverse resolution of 0.7 μm versus 1.4 μm in the human eye(147).

Table 4-1. Comparison of Ocular Anatomy

	Axial Length [mm]	Subtense [μm/degree]	Retinal Area [mm^2]	Retinal Arc [mm]	Cone:Rod Ratio	Aqueous Volume [μL]	Vitreous Volume [mL]
Human	24	290	1024	51	1:18	260	5.2
Mouse	3.37	31	15.6	4.9	1:36	4.4	0.005
Rat	6.3	59	52	10.6	-	13.6	0.05

Although there are anatomical differences, mice remain the most commonly used experimental models of AMD for numerous reasons. First and foremost, the presumed origin of AMD pathogenesis is the basal surface of the retinal pigment epithelium (RPE)

where the retina is separated from the choroidal circulation by Bruch's membrane (BM). The interface between the RPE and BM is evolutionarily conserved in mammals and serves the same role in supporting retinal homeostasis through nutrient and waste exchange to support the visual cycle. Figure 4-2 depicts fundus reflectance images and

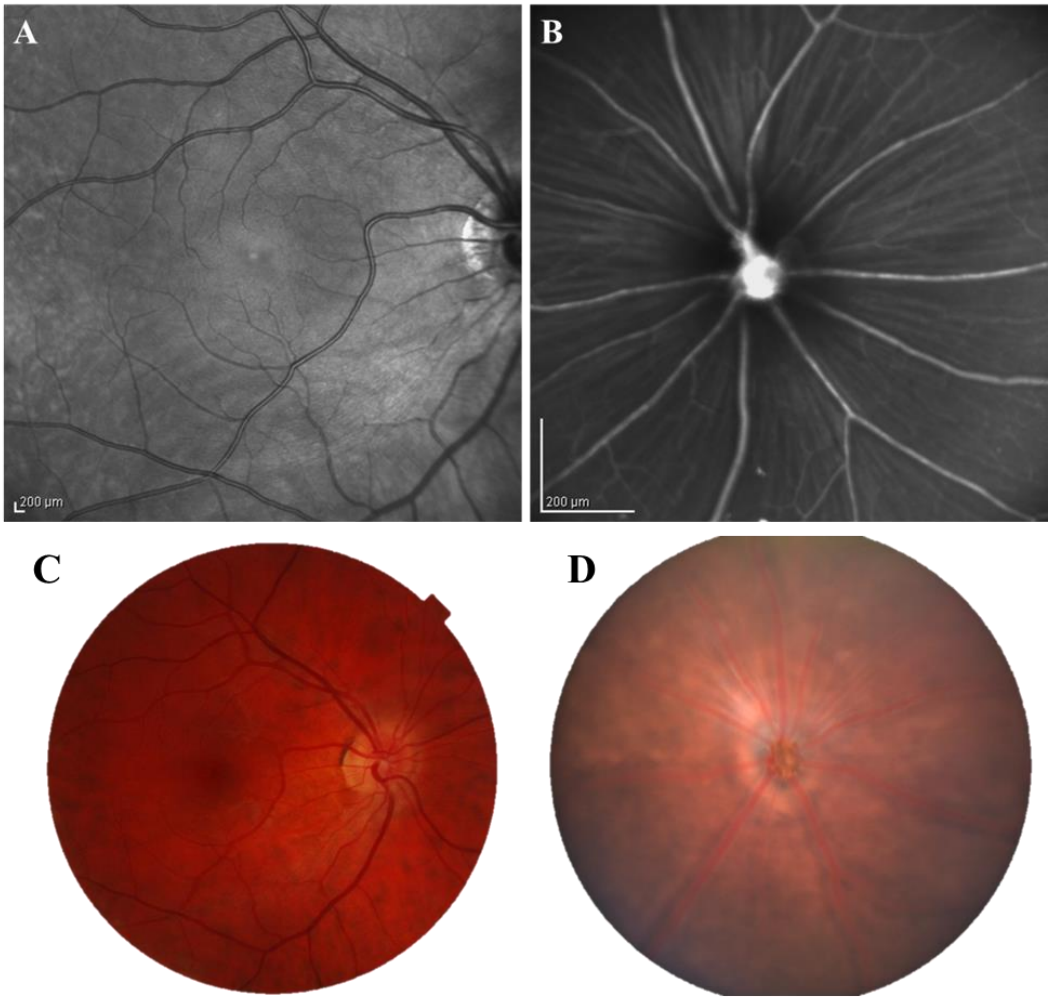

Figure 4-1. Comparison of the **(A)** Human fundus and **(B)** Mouse fundus images acquired using the Spectralis HRA. Both cSLO reflectance images represent a 30° field of view in the respective species. (C, D) White light fundus photography of a healthy human and a wild type C57BL/6 pigmented mouse. Scale bars = 200 µm.

spectral domain optical coherence tomography (SD-OCT) cross-sectional views of the human and mouse eye. It is important to note that the layered organization of the retinal

cells and total thickness of the retina is similar in both species despite the difference in total size of the eye.

The genetic factors described in the previous chapter, which contribute to the development and progression of AMD, are difficult to replicate in rodent models. This is often due to the single nucleotide polymorphisms (SNPs) associated with human disease. SNPs generally influence the functionality of a gene but do not necessarily ablate the function altogether. Therefore, knockout animal models may not accurately mimic the entire disease progression. Likewise, the impact of environmental factors on genetically

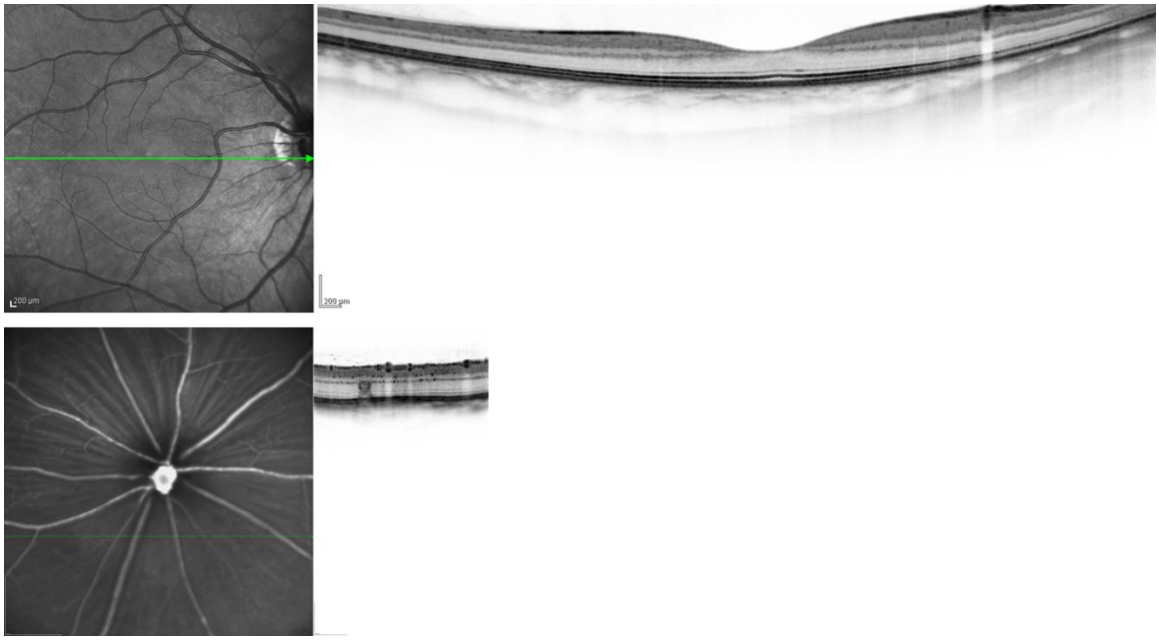

Figure 4-2. Multimodal imaging through the human macula and central retina of a C57Bl/6 mouse. Simultaneous near infrared reflectance scanning laser ophthalmoscopy (SLO) and spectral domain optical coherence tomography (SD-OCT) in a ***(Top)*** Healthy volunteer and ***(Bottom)*** C57BL/6 mouse. Both images represent a 30° field of view and a single cross-sectionals scan through the retina.

modified mice is often difficult to interpret. Many research groups are now trying to characterize the influence of factors such as diet(139), light exposure(134), and

smoking(148) in small animal models. The investigation of extrinsic factors on specific molecules implicated in AMD may provide additional insight into the role of modifiable risks associated with pathogenesis.

4.3 - Common Models of Dry AMD

A multitude of rodent models have been developed which mimic symptomatic features of AMD which include heightened accumulation of autofluorescence, reduced visual function, focal retinal lesions, formation of outer retinal deposits, and photoreceptor degeneration(135). Transgenic animals with alterations in the physiology of the RPE and photoreceptors have been shown to develop many of the morphological changes observed clinically in AMD patients. The *Abcr-/-* (149), *ELOVL4*(150), and $Ctsd^{mcd/mcd}$ (137) transgenic mice all exhibit accelerated accumulation of A2E and lipofuscin in the RPE and extracellular deposits due to impaired phagocytosis of photoreceptor outer segments. The presence of these features is not only an indication of pathology but is also suspected in promoting the progression of AMD to advanced stages where patients may experience permanent debilitating vision loss.

The suspected role of inflammation in AMD is largely based on the presence of inflammatory mediators in drusen, particularly components related to oxidative stress and the complement system(105, 151). Therefore, many research groups have targeted specific components of these inflammatory pathways. One popular model demonstrating both wet and dry AMD phenotypes was reported by Ambati et al. using senescent mice deficient in either Ccl-2 or Ccr-2(152). This model suggests a possible role of

macrophage dysfunction and damage induced by host inflammatory cells. However, a link between either Ccl-2 or Ccr-2 has not been established as a causative factor in patients with AMD. Similarly, Malek et al. developed a dry AMD mouse model with an isoform of apolipoprotein E which is a genetic risk factor for AMD. Interestingly, the mice only developed the AMD phenotype using a combination of the genetic variant, advanced age and a high fat diet(153). This model highlights the complexity and multifaceted nature of AMD.

Oxidative damage is another key component in AMD which has prompted the development of small animal models. Deficiency in Cu,Zn-superoxide dismutase (*Sod1*) in mice led to the accumulation of drusen-like deposits and neovascularization(154) and modifications to *Sod2* in mice produced progressive degeneration of the RPE, photoreceptors and thickening of Bruch's membrane(136). Once again, many of the hallmarks of AMD were demonstrated in a mouse model but the genes modified in these mice have not been associated with AMD in patients. Similarly, a recently characterized transgenic mouse deficient of nuclear factor erythroid 2-related factor 2 (*Nrf2-/-*) exhibited retinal pathology such as drusen-like deposits, accelerated lipofuscin accumulation, spontaneous choroidal neovascularization, and inflammatory proteins in the sub-RPE space(133). The NRF2 transcription factor is integral in retinal antioxidant response and autophagy. This model provided evidence of a link between autophagy and oxidative stress in the pathogenesis of AMD.

Inducible models of retinal degeneration are alternative methods used to examine features of AMD, particularly the loss of photoreceptor cells and atrophy of the RPE. Laser injury is commonly used to induce choroidal neovascularization (CNV) as a model of wet AMD

in small animals. Additional light-induced retinal degeneration models have also been used to investigate the loss of photoreceptor cells and atrophy of the RPE. This may be achieved through the use of low dose broadband exposures to cause widespread photochemical damage(155, 156) or targeted low dose photothermal laser exposures which cause outer retinal damage without eliciting new vessel growth(157-161). These light-induced retinal degeneration models share some of the morphological alterations observed in AMD but the mechanisms of damage and time course are substantially different (Figure 4-3). Similarly, chemically induced methods of retinal degeneration, such as systemic administration of sodium iodate ($NaIO_3$)(162, 163), have demonstrated AMD-like characteristics in the RPE and neurosensory retina.

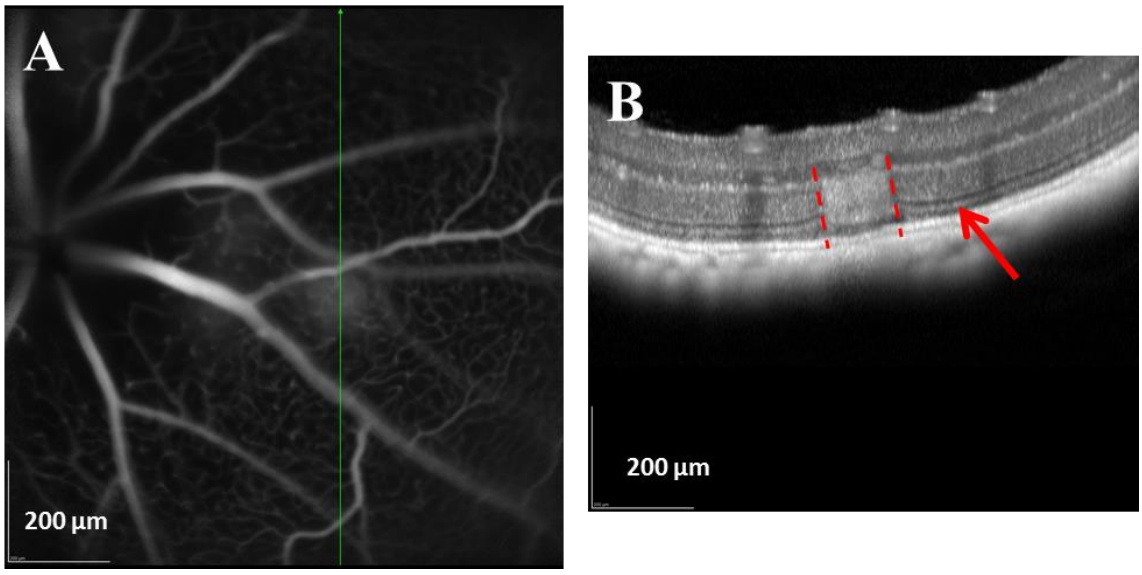

Figure 4-3. Laser induced retinal degeneration in a wild type C57BL/6 mouse. **(A)** Fluorescein angiography of the mouse retinal vasculature with amorphous fluorescence indicating regions of compromised RPE continuity from focal photothermal laser exposure. The green line indicates the SD-OCT scan **(B)** SD-OCT cross section through the center of the laser lesion. The dashed lines indicate the lesion boundaries while the arrow shows an adjacent area exhibiting intact retinal structure including continuity of the RPE and inner segment/ outer segment junction (IS/OS).

In addition to manipulating gene function in mice, the incorporation of fluorescent reporter molecules such as enhanced green fluorescent protein (eGFP) may be used to label molecules or cells of interest. These endogenous probes can be encoded in the rodent genome at a specified locus to act as a biomarker for molecular activation or upregulation. A number of imaging techniques may be used to visualize the spatial and temporal distribution of fluorescently labeled molecules to determine the influence on pathology. Advanced imaging systems now permit *in vivo* molecular imaging via endogenous fluorescent reporters in transgenic animals(161, 164-166) or functionalized molecular probes such as quantum dots(167, 168).

Larger animals have also been used to study AMD. Obviously, non-human primates provide the closest approximation of the human eye since they are similar in size and have a macula, but the high cost of maintaining an aged colony is prohibitive in most cases. Likewise, pigs and rabbits have been used due to the similarity in the size of the eye but significant differences in the rabbit vasculature and slow disease development in pigs limit the research and development applications. The cost associated with housing and caring for these animals typically precludes large scale studies. The study of experimental models of AMD has greatly improved our knowledge of basic pathophysiology and led to many new developments and breakthroughs. However, the abundance of animal models and experimental systems underscores complexity of AMD and the difficulty encompassing all of the contributing factors.

In conclusion, the use of retinal imaging techniques has broad implications for investigations of small animal models of injury and disease. The large number of small animal models currently being studied as well as novel models yet to be developed would

greatly benefit from non-invasive methods of evaluating complex and dynamic processes within the living eye. Current instrumentation has already demonstrated exceptional capabilities in visualizing microscopic features within the rodent eye after minor modifications to compensate for differences in ocular optics.

Chapter 5: Quantitative Fundus Autofluorescence Imaging in a Rodent Model of Retinal Injury

Fundus autofluorescence (FAF) is a non-invasive technique that is able to generate contrast in retinal images based on the properties of endogenous fluorescent pigments within the eye. These fluorophores can be sensitive indicators of injury and disease within specific cellular layers of the retina. As a result, FAF has become a fixture in clinical examinations to help diagnose a wide range of pathological conditions. The distribution of endogenous fluorophores provides insight into the development of diseases such as age-related macular degeneration and may be used to monitor rates of progression. The majority of the autofluorescence signal in the retina originates within the retinal pigment epithelium (RPE) through the excitation of the fluorophore lipofuscin. Excitation of retinal lipofuscin with visible light often reveals features which cannot be observed using fundus photography or near-infrared reflectance (NIR) imaging techniques. In the present study, we used a novel dual-wavelength (λ) FAF technique to assess retinal tissue following light-induced injury to the RPE and photoreceptors in a brown Norway rat model. The implications for this study are varied but include the demonstration of a sensitive diagnostic imaging application, furthering our understating of light-induced damage in the retina, and introducing an aged rodent model to study characteristics of AMD.

The majority of the data presented in this chapter was published in the peer-reviewed journal *Investigational Ophthalmology and Visual Science:*

Boretsky A, Motamedi M, Bell B, van Kuijk F. Quantitative Evaluation of Retinal Response to Laser Photocoagulation Using Dual-Wavelength Fundus Autofluorescence Imaging in a Small Animal Model. *Invest Ophthalmol Vis Sci.* 2011 Aug 9; 52(9):6300-7.

5.1 Introduction

The widespread use of lasers in both therapeutic and diagnostic applications in the field of ophthalmology has prompted substantial interest in characterizing damage mechanisms and identifying biomarkers of injury and disease in the eye. A variety of light sources may be used to identify characteristic features within the retina. Many of these techniques were reviewed briefly in Chapter 2 of this dissertation. However, certain wavelengths and intensities can induce phototoxic effects. Light-induced injury is divided into three regimes (1) photothermal, (2) photochemical, and (3) photomechanical(169). The distinctions are made based on the exposure parameters which include wavelength, exposure area, power, and duration. Certain ocular diseases such as age-related macular degeneration (AMD) and diabetic retinopathy can benefit from photocoagulation (photothermal exposures) to prevent vascular leakage or reduce excessive oxidative stress. Similarly, photodynamic therapy (PDT) may be used to prevent vascular leakage by targeting the affected area with the use of light activated chemicals which are administered systemically. The frequency, and often necessity, of the use of lasers and intense light sources in eye warrants a thorough evaluation of phototoxicity.

A number of studies have investigated light-induced retinal injury in small animal models using techniques such as fluorescein angiography (FA), near infrared reflectance (NIR), and white light fundoscopy(170-175). Histology(158, 176-181) and electroretinography (ERG) (159, 182) have also been used to assess the structural and functional impact of light-induced retinal damage. Visible perturbations in retinal morphology associated with photothermal injury are often viewed using white light fundoscopy. The gross morphological changes observed are the result of a local increase

in the temperature of the RPE by at least 10°C which causes protein denaturation(183). Thermal diffusion of the laser energy can also lead to the death of neighboring cells in the RPE and the neural retina. Higher powered laser exposures are even capable of rupturing Bruch's membrane (BM) which may lead to choroidal neovascularization (CNV).

The dual-wavelength FAF technique used to investigate retinal damage in the present study was originally developed to quantify macular pigment optical density (MPOD)(184). This technique may also be used to visualize native contrast generated by the accumulation autofluorescent pigment lipofuscin within the RPE cells. Similar studies have already demonstrated applications of FAF with a single excitation wavelength to measure the effects of photochemical damage in the retina(24, 25). The heightened sensitivity and quantifiable parameters of the customized dual-wavelength FAF imaging system are uniquely capable of monitoring subtle changes in the rodent retina following photothermal injury.

5.1.1 Lipofuscin

Lipofuscin is an aggregate of cellular debris which accumulates in metabolically active, post-mitotic cells throughout the body(185, 186). Within the retina, lipofuscin is generated primarily through the continual breakdown and regeneration of photoreceptor outer segments (POS). With age, this process of recycling POS via lysosomal degradation becomes increasingly inefficient(82). As a result, lipofuscin granules accumulate within the lysosomal compartments of the RPE cells. This accumulation of lipofuscin within the RPE cells can be observed as an increase in FAF in the living eye(6, 7, 114, 187). Lipofuscin granules are approximately 1 μm in diameter and localize near the basal surface of the RPE cells(7, 188). According to one study, progressive lipofuscin

accumulation can account for approximately 20% of the total cytoplasmic volume of RPE cells by age 80(186).

Although numerous groups have investigated characteristics of lipofuscin, there are many unanswered questions regarding its role in ocular pathology(189, 190). This can be partially attributed to the multitude of components, difficulty in extraction of pure lipofuscin and oxidative modifications of extracted proteins(191). However, recent proteomic analysis of purified lipofuscin granules found minimal protein indicating that the phototoxic substances in lipofuscin are the bisretinoids and lipids(192).

Multiple fluorophores have been identified in RPE lipofuscin. The most prominent lipofuscin fluorophore implicated in retinal damage and degeneration is the bis-retinoid N-retinylidene-N-retinylethanolamine (A2E). A2E is present in the POS and in the RPE as a by-product of the retinoid cycle which is used to regenerate the pigments necessary for transduction of visual signals. The central region of the eye seems particularly susceptible to deleterious effects of A2E due to the high density of photoreceptor cells and exposure to short wavelength visible light. Blue light has been shown to photoactivate A2E resulting in the production of singlet oxygen molecules which can stimulate apoptosis in the RPE(193-196). Additional *in vitro* studies demonstrated complement activation in the presence of A2E(197, 198) and perturbations in cholesterol metabolism even in the absence of photoactivation(199). This evidence implicates lipofuscin in the progression of AMD and suggests that lipofuscin levels may be used as a biomarker for the disease.

Lipofuscin emits a characteristic broadband autofluorescence signature from 500 to 800 nm with peak excitation of the fluorophores occurring between 480 and 520

nm(200). Numerous diseases exhibit detectable changes in FAF patterns or intensity as a function of progression. Among the most common are AMD(109, 113-115, 189, 201-203), fundus flavamaculatus (Stargardt's disease)(204, 205), and vitelliform macular dystrophy (Best disease)(206). The development of reliable and sensitive means of assessing FAF quantitatively would likely benefit patients with the aforementioned diseases. In this study, we demonstrated the value of quantitative dual-wavelength fundus autofluorescence imaging in the detection and monitoring of photothermal retinal injury.

5.2 Methods

All experimental procedures were approved by the Institutional Animal Care and Use Committee at the University of Texas Medical Branch and complied with the ARVO Statement for the Use of Animals in Ophthalmic and Vision Research.

5.2.1 Animal Model:

Brown Norway rats (Charles River Laboratories) at least 9 months of age were used in this study. Aged rats were necessary because they exhibited sufficient autofluorescence signal from the accumulation of lipofuscin in the RPE. Likewise, pigmented animals were necessary to limit the amount of backscattered light from the choroid and provide sufficient contrast for imaging the FAF. Animals exhibiting visible retinal defects or opacity of the lens and cornea were excluded from the study. All animals were housed under standard conditions with a 12-hour light/ 12-hour dark cycle. Prior to imaging, animals were anesthetized with isofluorane (1 - 2 %) and pupils were dilated with tropicamide (1%). Corneal hydration was maintained during image acquisition by regularly applying 0.5% hypromellose lubricating eye drops (Alcon

Laboratories) every 2-3 minutes. An adjustable, heated platform was used to position the animals for imaging and photocoagulation.

5.2.2 Photothermal Laser Exposure and White Light Fundoscopy:

An argon laser (Ultima 2000, 514 nm; Coherent, Santa Clara, CA) was integrated into a slit lamp (Zeiss 30 SL-M) to deliver laser radiation at specified locations within the retina. Pre-exposure images were acquired to perform a before and after evaluation of the fundus and establish the minimal visible lesion (MVL) threshold criteria for our experimental model. A MVL was defined as the lowest exposure inducing a visible blanching of the retinal tissue under white light fundoscopy. Funduscopic evaluations were performed within 30 minutes of laser exposure. White light fundoscopy was performed via digital photography by mounting a digital-SLR camera (Nikon D70s, Nikon Inc., Melville, NY) onto the slit lamp. A fixed exposure time (0.1 seconds), spot size (0.1 mm), and wavelength (514 nm) were used in all experiments.

A specialized 5.4 mm fundus laser lens (Ocular Instruments; Bellevue, WA**)** was used for all exposures to accommodate for the corneal curvature and higher optical power of the rat eye. A 2.5 % hypromellose gel (Gonak™, Akorn, Inc., Lake Forest, IL) was applied prior to placing the lens to provide better optical coupling and prevent dehydration of the cornea. An aiming beam was used to specify the retinal location for photothermal lesion placement. Particular care was taken to avoid damage to the large blood vessels radiating from the optic disc. Likewise, we did not exceed 50% of the energy required to induce CNV in the rat as demonstrated by Dobi et al. (207) and Frank et al. (208) to avoid unintentionally promoting new vessel growth from the choroid.

A total of 21 aged brown Norway rats were used to investigate changes in retinal autofluorescence associated with photothermal laser exposure for up to 6 months. The animals were divided into 4 groups. Group 1 (n = 6, 12 eyes) was used for dosimetry to determine the minimal visible lesion (MVL) criteria and establish subthreshold, threshold and suprathreshold conditions for the laser exposures. Group 2 (n = 3) received multiple exposures at 8, 13.5, 16, and 22 mW to encompass the subthreshold, threshold and suprathreshold categories. Group 3 (n = 6) received multiple exposures at 16 and 22 mW to investigate threshold and suprathreshold response in each rat. Finally, Group 4 (n = 6) received multiple exposures at 20 and 22 mW to determine the difference in response between two suprathreshold exposures and assess the sensitivity of the dual wavelength FAF ratio analysis. The experimental setup (Figure 5-1) allowed color fundus photography and FAF images to be acquired in rapid succession to minimize temporal effects.

5.2.3 Dosimetry:

A range of exposure powers from 5 mW to 22 mW were used to determine threshold limits of MVLs in our rat model. This range was selected to compare threshold values in our rat model with previously published data in additional rodent strains(158, 159, 171, 177, 209, 210), non-human primates(170, 176, 211), and cell culture models (178, 183, 212-214). Six rats (12 eyes) were used to perform the dosimetry experiments. Multiple lesions at each exposure power were evaluated in at least 3 rats to assess inter-subject variability and intra-subject variability due to spatial irregularities in pigment density and absorption of the laser energy.

5.2.4 Dual Wavelength FAF Imaging

A modified confocal scanning laser ophthalmoscope (cSLO) was used to acquire FAF images of the brown Norway rat. Two independent argon lasers were used as excitation sources at 488 nm and 514 nm. A barrier filter at 520 nm was used to block the excitation wavelengths and allow only the emitted autofluorescence (~520 – 800 nm) to reach the detector. The emitted autofluorescence can be represented mathematically using the following equation:

$$F(\Lambda) = \int_{\lambda=520}^{800} R(\lambda) \cdot F^{*}(\Lambda, \lambda) \cdot 10^{-D(\Lambda)-D(\lambda)} \cdot I(\Lambda) \cdot d\lambda$$

F(Λ) denotes the emitted fluorescence that reaches the detector , $I(\Lambda)$ is the intensity of the excitation source at a particular wavelength *Λ*. The terms $10^{-D(\Lambda)}$ and $10^{-D(\lambda)}$ denote the absorption of the excitation wavelength Λ and emitted autofluorescence wavelengths λ, respectively.

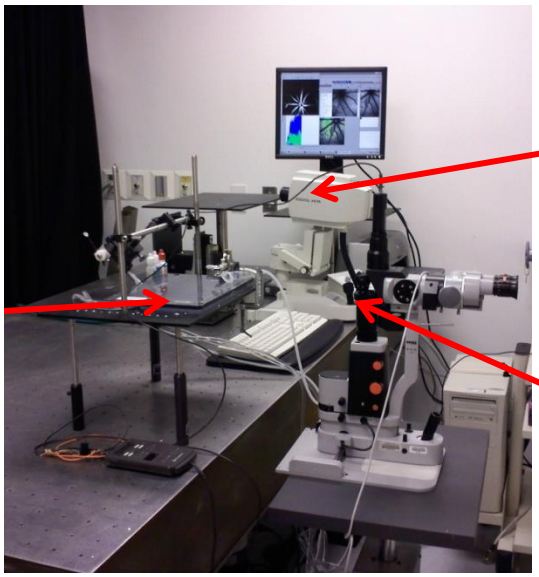

Figure 5-1. Laboratory setup for dual wavelength fundus autofluorescence imaging, white light fundus photography and photothermal laser delivery.

5.2.5 Image Acquisition Procedure:

Dual wavelength FAF images were collected using a modified Heidelberg Retinal Angiogram (Heidelberg Engineering, Heidelberg, Germany) confocal scanning laser ophthalmoscope (cSLO). Endogenous retinal fluorophores were excited using independent argon lasers operating at 488 nm and 514 nm. A 30° x 30° field of view (FOV) was used for sequential image acquisition. All images were acquired in the high-resolution mode (512 x 512 pixels) and the detector sensitivity was maintained at a fixed value. A sequential imaging protocol was used to collect 16 frames at each wavelength in less than 3 seconds to minimize the impact of involuntary eye movement in the anesthetized rats. Individual, non-normalized frames were registered based on morphometric features and averaged to improve overall signal to noise ratio. The hardware configuration and analytical software package was originally developed by Heidelberg Engineering to measure MPOD. However, rodents lack the equivalent of a primate macula so the instrument was used to investigate the distribution of lipofuscin autofluorescence and monitor localized changes in FAF following photothermal injury. An example of dual-λ FAF imaging in the rat retina following photothermal laser exposure is shown in Figure 5-2.

Radiant exposure values were calculated for each imaging modality using typical image acquisition parameters. A retinal subtense value of 59 micrometers per degree, based on the Hughes schematic eye for the rat(144), was used to determine the scaling for radiant exposure calculations over the 30° x 30° field of view. A summary of the light exposure parameters used during image acquisition may be found in Table 5-1.

5.2.6 Dual-Wavelength FAF Measurements

Lipofuscin autofluorescence was calculated by measuring the difference in optical density for each excitation wavelength (488 nm and 514 nm). Fixed extinction coefficients were used for each source based on the original configuration and calibration performed by Heidelberg Engineering. The difference in the emission profiles of the lipofuscin in the RPE based on the excitation source provided the foundation of the ratiometric measurements. The ratios of the optical densities within each region of

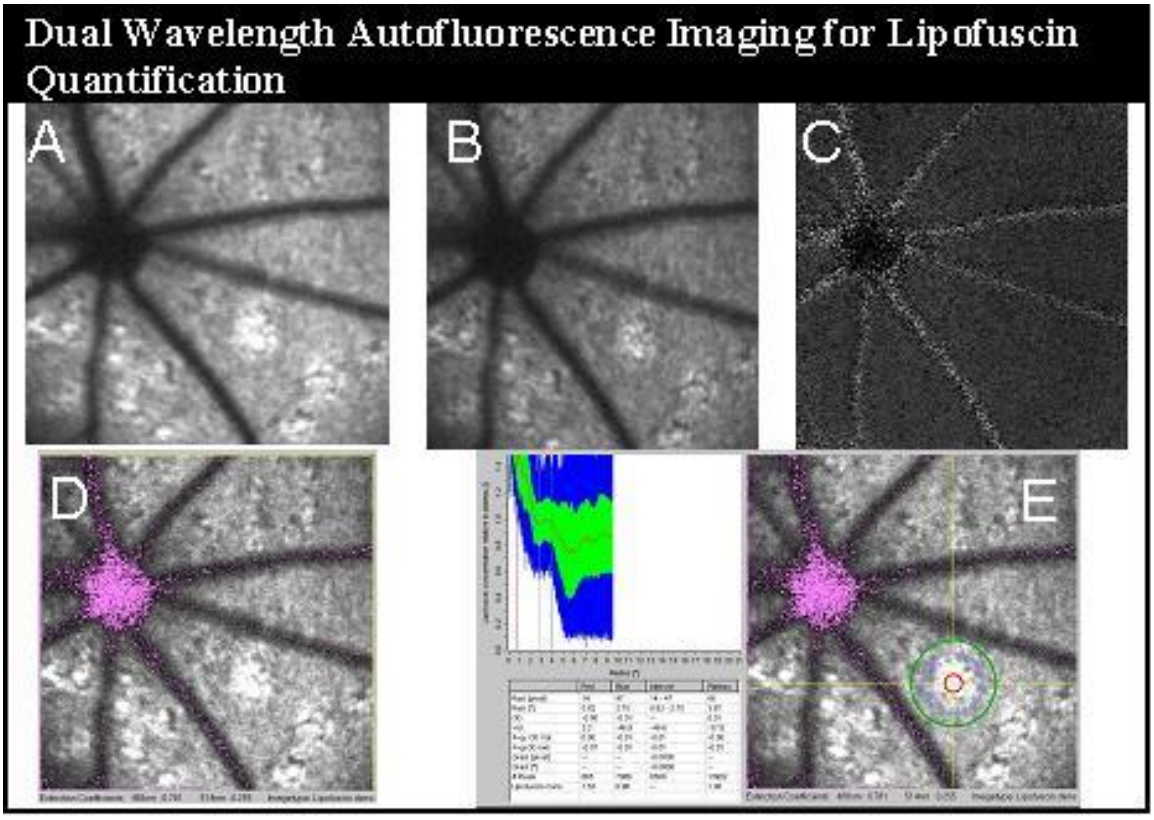

Figure 5-2. Image acquisition for lipofuscin density measurements based on ratiometric analysis of dual wavelength fluorescence excitation. (A) 30° FOV autofluorescence image of the rat retina using a 488 nm source for excitation (B) 30° FOV autofluorescence image of the rat retina using a 514 nm source for excitation (C) Optical density map of the retina (D) Lipofuscin density map based on ratiometric analysis of the FAF images acquired at each wavelength. (E) Analysis of the lipofuscin distribution using the custom software developed by Heidelberg Engineering.

interest (ROI) were normalized to the baseline dual-wavelength autofluorescence ratio measured prior to exposure. This enabled multiple rats to be grouped and observe trends in the FAF profile with respect to time. Variability in retinal illumination due to pupil size and orientation of the optical axis were negated by using the ratiometric measurements. Therefore, only the changes in the FAF pattern associated with laser-induced damage to the retina were measured.

Table 5-1. Light Exposure Parameters Used During Image Acquisition

Light Source	***Wavelength (nm)***	***Output Power (μW)***	***Radiant Exposure* (J/cm^2)***
Diode Laser	830	60	0.11
Argon Laser	514	290	0.03
Argon Laser	488	300	0.03

*An exposure duration of 60 seconds (typical) was assumed in the calculation of the radiant exposure for NIR-reflectance and 3 seconds for each argon laser source.

5.2.7 Fluorescein Angiography

Fluorescein angiography (FA) was performed following the FAF imaging procedure in the group of animals used in the dosimetry experiments. A 1% solution of fluorescein sodium (Akorn, Inc., Lake Forest, IL) was administered via intraperitoneal (IP) injection following laser exposure, at 24 hours, 1 week and 2 weeks.

5.3 Results

5.3.1 Dosimetry

Laser dosimetry was performed to establish the minimal visible lesion (MVL) threshold criteria in the aged brown Norway rat model. Figure 5-3 depicts a range of

powers used grade laser damage based on white light fundus photography and FAF in a single eye. The dosimetry group (n=6, 12 eyes) was used to determine the inter-subject and intra-subject variability in response to retinal photocoagulation.

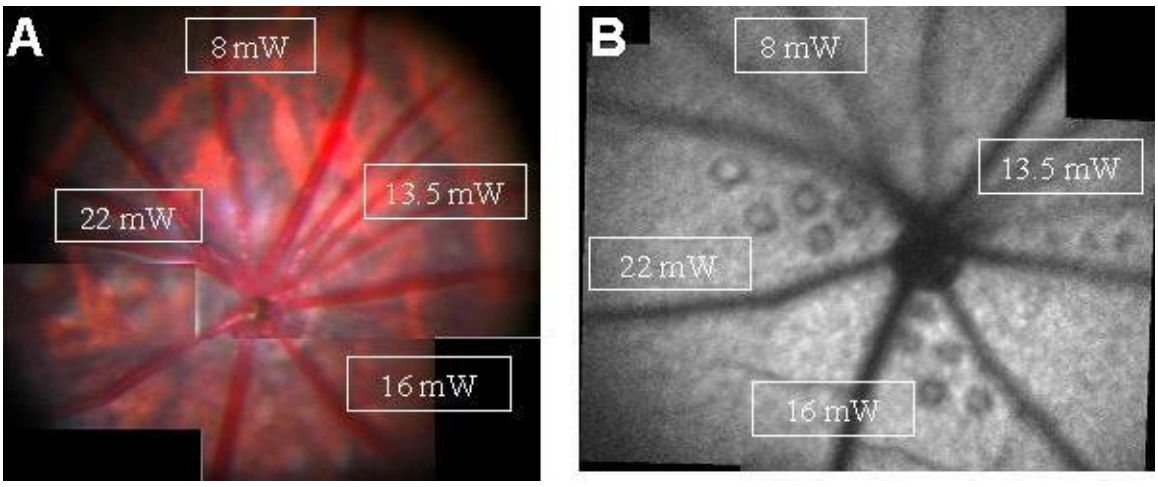

Figure 5-3. Dosimetry to establish the clinically defined MVL threshold using our laser exposure configuration and the parameters already described. (**A**) Composite white light image exhibiting the characteristic blanching immediately after laser exposure at powers of at least 16 mW. (**B**) autofluorescence images (488-nm excitation shown) exhibit a higher degree of definition and disruption of the retina as a result of the photothermal insult. **Modified from Boretsky et al. 2011*

A comprehensive slit lamp evaluation was conducted within 30 minutes of photothermal exposure. For each rat in the dosimetry group, characteristic circular gray lesions were visible at exposure powers of 16 mW and 22 mW in fundus photographs (Figure 5-3A), whereas lower powered laser exposures did not reveal any evidence of damage. Thus, the threshold for a MVL was set at 16 mW with the fixed 0.1 mm spot size, 514 nm λ, and 0.1 second exposure duration. Laser powers greater than 22 mW were classified as suprathreshold and therefore not used to investigate the lower limits of our autofluorescence detection threshold. The corresponding FAF images were acquired

immediately after laser exposure and revealed heightened contrast and definition of lesion boundaries. Subthreshold exposures at 13.5 mW were also visible with FAF; however, the 8 mW exposures did not produce any detectable changes with either fundus imaging technique.

5.3.2 Acute Changes in FAF Immediately After Photocoagulation

We were able to measure baseline FAF intensity in our aged brown Norway rat model due to the heightened accumulation of lipofuscin in the RPE. Subsequent measurements were normalized to the baseline level to account for innate variability among rats. We tested the sensitivity of our imaging technique using the 4 exposure powers described in the dosimetry experiment (8, 13.5, 16, and 22 mW) and included an additional suprathreshold exposure power of 20 mW. Immediately after photocoagulation, we observed a dose-dependent decrease in the FAF which is shown in Figure 5-4. The number of lesions evaluated for each exposure power is presented in Table 5-2 along with the radiant exposure and mean dual-wavelength FAF ratio. Laser powers greater than 8 mW yielded a significant reduction in the dual-wavelength FAF ratio as a function of exposure power (ANOVA, $p < 0.001$; observed power = 1).

Table 5-2. Immediate Reduction in Autofluorescence

Power [mW]	***# of Lesions Evaluated***	***Radiant Exposure [J/cm^2]***	***Dual λ FAF Ratio (mean)*** †	***Standard Error***
8	5	10.2	1.003	± 0.008
13.5	5	17.2	0.889	± 0.013
16	17	20.4	0.752	± 0.029
20	9	25.8	0.717	± 0.039
22	17	28.0	0.641	± 0.015

† The laser powers greater than 8 mW resulted in a significant decrease in the autofluorescence ratio relative to the magnitude of the laser power (ANOVA, P < 0.001). No significant changes in autofluorescence were detectable at 8 mW

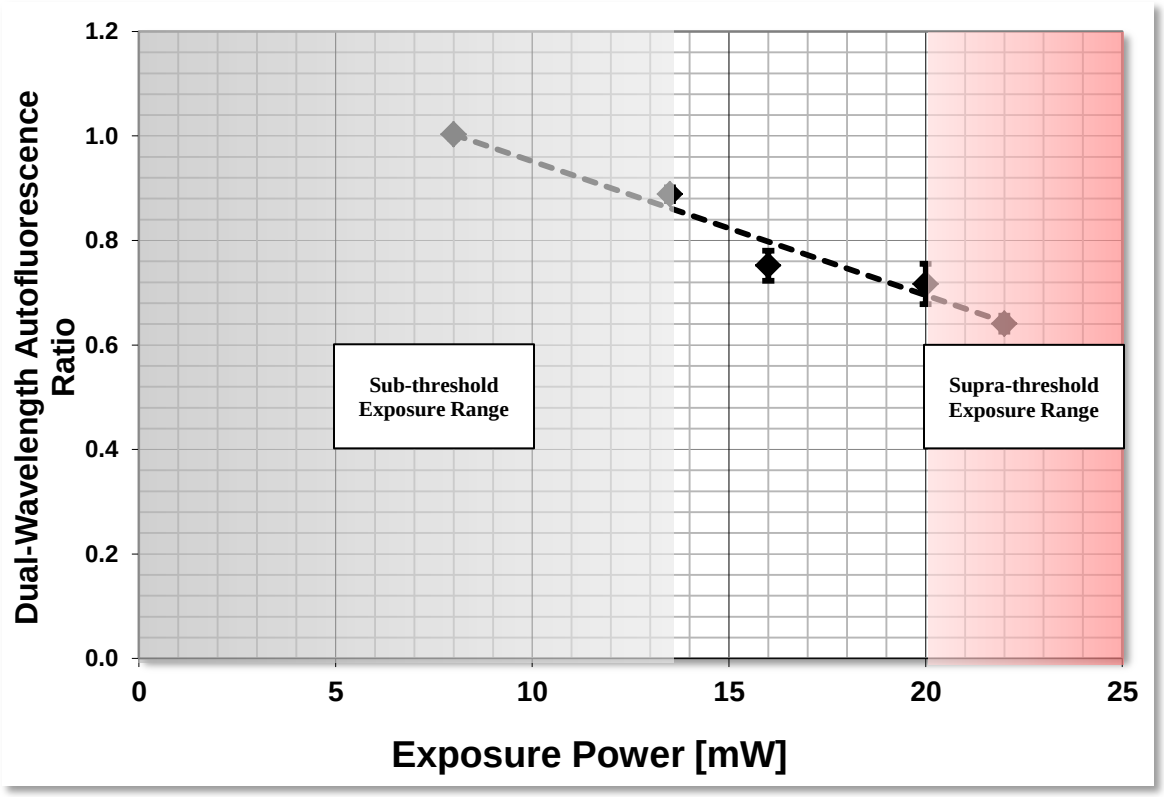

Figure 5-4. Dose-dependent changes in the dual wavelength autofluorescence ratio measured immediately after laser exposure. The ratio of the intensity values from each excitation wavelength (488 nm and 514 nm) were normalized to the baseline FAF for each rat. The linear regression profile of the dose-dependent response for this exposure regime is represented by the dashed line (R^2 = 0.9605). The subthreshold, threshold, and suprathreshold exposures were determined based on the MVL criteria outlined in the methods section and assessed by white light fundus photography. **Modified from Boretsky et al. 2011*

Color fundus photographs and FAF images were also acquired within the first week after laser exposure to examine the sensitivity of each technique in identifying the damaged regions of the retina. The MVLs at 16 and 22 mW appeared as distinct gray spots with white light fundoscopy immediately after exposure but the lesions appeared to fade at the 24 and 48 hour time points. At 72 hours post-exposure, the lesion sites were no longer distinguishable. Likewise, no evidence of the laser exposure was noted at any time beyond 3 days. The laser lesions in the FAF images appeared hypoautofluorescent

immediately after laser exposure relative to the background autofluorescence of the undamaged RPE. At 24 hours, the threshold and suprathreshold lesions had become hyperautofluorescent. At 48 hours, the threshold lesions (16 mW) were amorphous hyperautofluorescent regions and a confluence of multiple lesions was observed. The suprathreshold exposures (22 mW) also exhibited increased hyperautofluorescence but the circular shape was still discernable. At one week, the FAF images of the threshold and suprathreshold lesions still exhibited heightened autofluorescence (Figure 5-5).

5.3.3 Dynamics of FAF Following Laser Exposure

We monitored the rats for up to 6 months to assess longitudinal changes in the FAF profile as a function of both time and exposure power. Two-way ANOVA was performed on the dual-wavelength AF ratio data to establish statistical significance of the observed changes based on time after exposure ($p = 0.002$, observed power = 0.931) and laser power ($p = 0.04$, observed power = 0.496).

A return to baseline FAF levels was observed for the subthreshold (13.5 mW) and threshold (16 mW) lesions at 3 weeks and 4 months, respectively. Paired t-tests were used to compare pre-exposure FAF levels with the time points in which recovery was noted (13.5 mW lesions, *paired t-test P* = 0.601; 16 mW lesions, *paired t-test P* = 0.937) (Figure 5-6). Half of the rats from group 3 ($n = 3$) were evaluated again at 6 months and still demonstrated hyperautofluorescence associated with the photothermal laser exposure. A summary of the FAF recovery times is presented in Table 5-3.

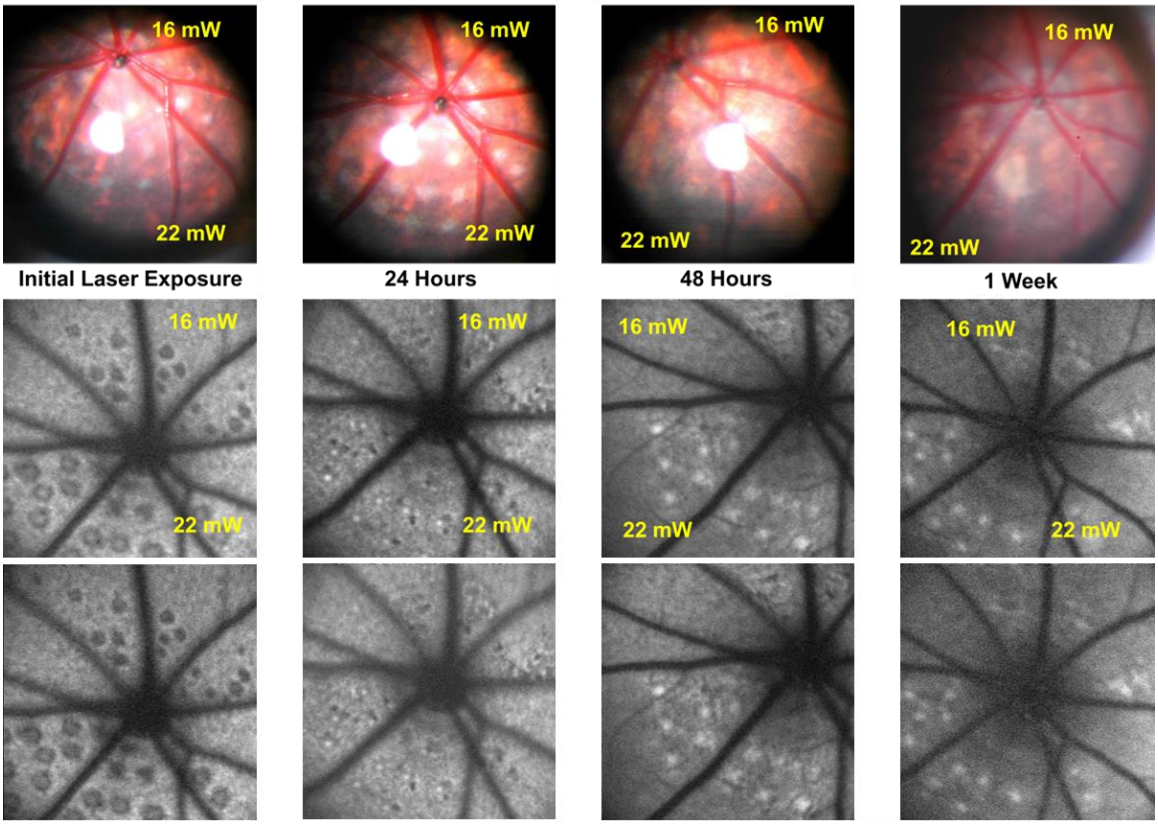

Figure 5-5. Longitudinal evaluation of threshold and suprathreshold laser lesions using white light fundus photography and Dual λ FAF imaging. (**A**–**D**) White light funduscopy of near-threshold and suprathreshold laser lesions in a Brown Norway rat (**A**–**C**; *bright white spots* are back reflections from the slit lamp). Both 16-mW and 22-mW lesions appear as distinct *gray spots* that fade entirely after 48 hours. (**E**–**H**) Corresponding autofluorescence imaging of a Brown Norway rat using 488-nm excitation. (**E**) AF image immediately after near-threshold and supra-threshold laser exposure (16 and 22 mW). (**F**) AF image at 24 hours shows the healing process occurring in the 16-mW lesions and the periphery of the 22-mW lesions. (**G**) AF images at 48 hours exhibit the reappearance of the higher powered lesions as hyperfluorescent spots. (**H**) In contrast to the white light funduscopy image, AF imaging 1 week still shows the clearly defined hyperfluorescent spots from 22-mW lesions and amorphous areas corresponding to the 16-mW laser exposure. (**I**–**L**) Corresponding autofluorescence imaging using 514-nm excitation. **Modified from Boretsky et al. 2011*

5.3.4 Fluorescein Angiography

Fluorescein angiography was performed within the first hour following laser exposure to verify location of the laser lesions and confirm a disruption in the continuity

of the RPE. We observed the characteristic halos around the lesions immediately after exposure, however these features were no longer present during follow up imaging at 1 and 2 weeks post exposure. Furthermore, no other indications of CNV were observed throughout the course of the *in vivo* imaging.

Table 5-3. Long-Term Fundus Autofluorescence Recovery

Power [mW]	***# of Lesions Evaluated***	***Recovery of Autofluorescence***
8	5	N/A†
13.5	4	3 weeks post exposure
16	5	4 months post exposure
20	9	Retinal damage still evident at 6 months
22	9	Retinal damage still evident at 6 months

† - No significant change in autofluorescence signal detectable after laser exposure

5.3.5 Histology

A histological assessment was performed in a limited number of rat eyes. At the conclusion of the study, one eye from each group of animals was extracted. The entire globe was flash frozen in liquid nitrogen. The tissue was then sent to a contract laboratory (Brown & Associates Medical Laboratories, Houston, TX) for further processing which included sectioning and staining of the samples with hematoxylin and eosin. Histological evaluation of the eyes did not reveal any indication of new vessel growth using standard H&E staining techniques (Figure 5-7).

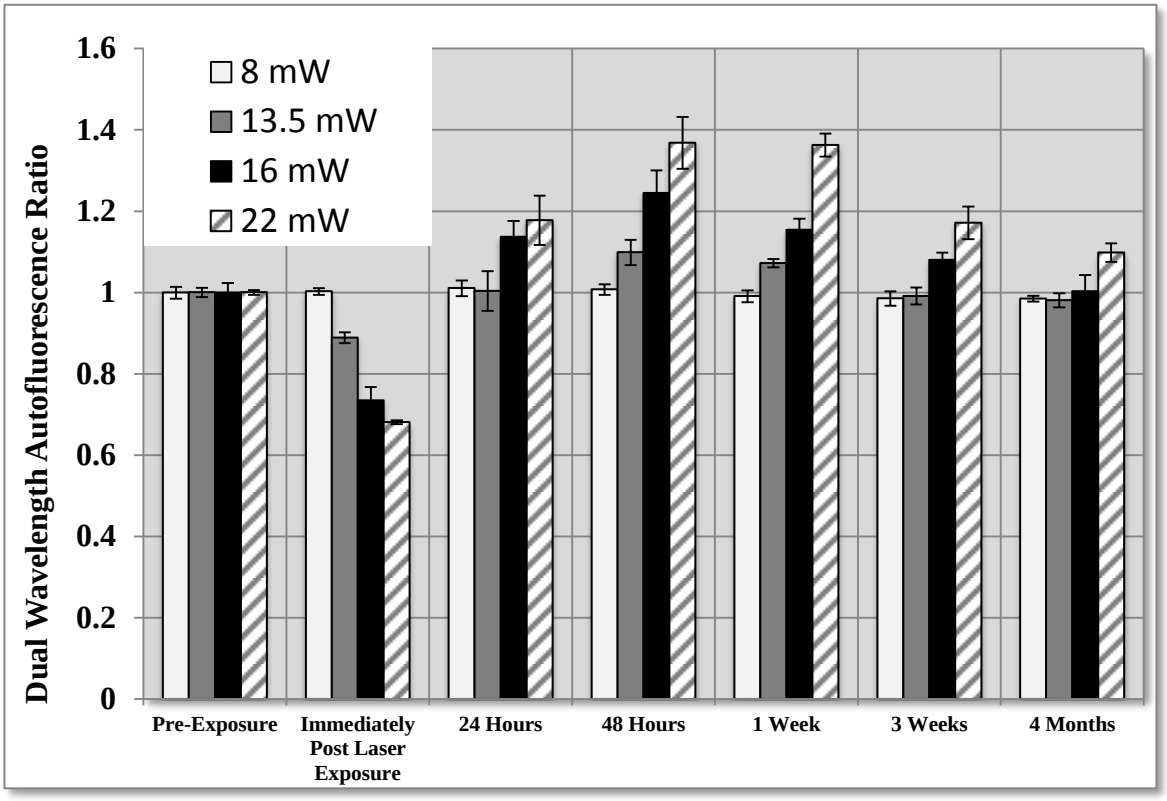

Figure 5-6. Laser dosimetry evaluation to establish long-term threshold limits for retinal damage based on autofluorescence imaging: 8 mW (white), 13.5 mW (gray), 16 mW (black), 22 mW (hatched). Complete recovery of baseline autofluorescence was still not present 6 months after exposure for 22-mW exposures. The dual-wavelength autofluorescence ratio represents the ratio of FAF intensities from each excitation light source (488 and 514 nm) normalized to the baseline FAF for each subject. **Modified from Boretsky et al. 2011*

5.3.6 Comparison Between Rat and Human Response

A sample data set of longitudinal FAF imaging in a patient receiving subthreshold laser therapy for drusen was used to examine the similarity between the human response to photocoagulation and rodent response to comparable exposure parameters (Figure 5-8). In both cases, the lesions exhibited hypoautofluorescence immediately after laser exposure. Similarly, a transition to hyperautofluorescence was observed during follow up examinations. The time course of this transition was substantially different between species; however, the overall dynamic response appeared to follow a consistent pattern.

5.4 Discussion

The goal of this study was to demonstrate a novel application of *in vivo* fluorescence cSLO imaging to measure changes in the outer retina, particularly the RPE, following photothermal damage. Heightened definition of the retinal lesions was observed using FAF when compared to NIR-reflectance cSLO and white light fundoscopy in our aged brown Norway rat model. The increase in contrast provided by the lipofuscin autofluorescence allowed for dynamic monitoring of the RPE following photothermal exposure. Moreover, we demonstrated measurable changes in the FAF signal caused by exposures below the MVL threshold established using white light fundoscopy. Although we did not explore other regimes of light-induced injury, it is likely that photochemical and photomechanical exposures would also yield detectable perturbations in the FAF signal from the outer retina.

The dynamics of the FAF pattern offer some insight into the biochemical and morphological alterations in the acute phase of injury and wound healing in the retina. The immediate decrease in the FAF signal intensity at the lesion sites is not clear, but it may be attributed to increased attenuation of the excitation light source by denatured proteins affected by the thermal diffusion through the tissue. This is one possible explanation for the relatively rapid transition from hypoautofluorescence to hyperautofluorescence observed within the first 48 hours after laser exposure. Similar observations were reported in clinical studies based on traditional FAF imaging(202, 211, 215, 216). Alternatively, changes in the FAF profile could be influenced by photobleaching or decreased absorption of melanin in the RPE. Time-dependent photobleaching of melanosomes has been demonstrated in response to intense visible

light sources(217, 218) and may possibly contribute to the hypoautofluorescence. Photooxidation of melanin can also compromise the ability of RPE cells to perform antioxidant functions(218). This could potentially impede the wound healing process in the aged rats and contribute to the extended periods of hyperautofluorescence we noted with the suprathreshold laser exposures.

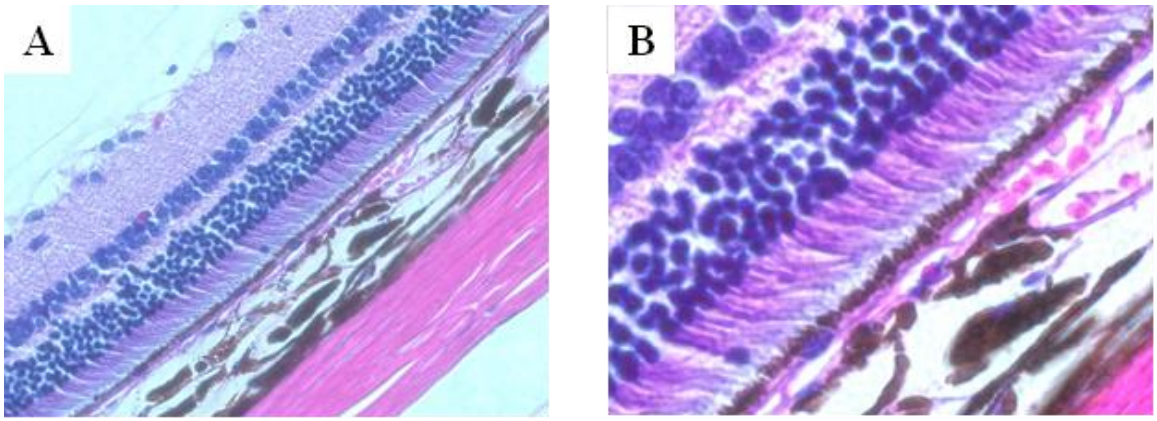

Figure 5-7. Hematoxylin and eosin (H & E) staining of a brown Norway rat retinal cross-section at (A) 20 x magnification and (B) 40 x magnification. Serial sectioning did not reveal any visible defects in the outer retina following subthreshold lesions of 13.5 mW at the experimental endpoint of 4 months.

In addition to detecting acute changes in the retina associated with laser exposure, we were able to monitor the dynamics of the FAF signal for up to 6 months. The longitudinal studies revealed even more detail regarding the FAF patterns and dose-dependent nature of fluorescence recovery. A complete recovery of baseline FAF was observed for the subthreshold (13.5 mW) and threshold (16 mW) lesions at 3 weeks and 4 months, respectively. In the absence of ultrastructural analysis or functional assessments, we cannot state with complete certainty that there were no latent effects from the laser exposure but the recovery of baseline FAF levels likely indicated viable RPE cells were

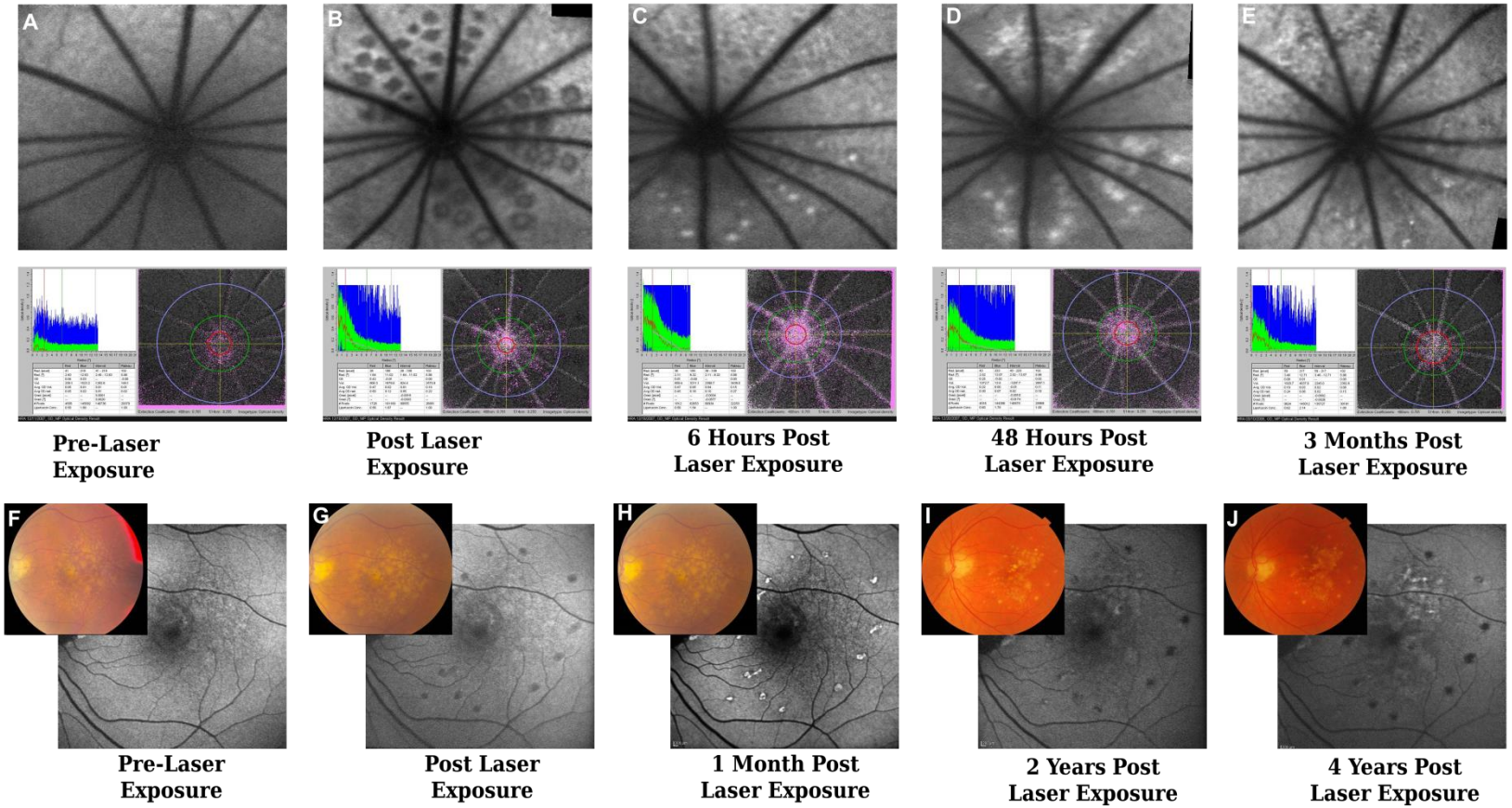

Figure 5-8. (A-E) Time-course autofluorescence imaging of the aged Brown Norway rat before and after argon laser exposure with corresponding retinal pigment optical density surrounding the optic disc. Near-threshold lesions and supra-threshold lesions were created using powers of 16 mW & 22 mW measured at the cornea. The retinal pigment optical density was evaluated by measuring the differences in optical densities for the blue and green light (extinction coefficient values are expressed below each image). (F-J) Time-course autofluorescence imaging of a patient treated with sub-threshold focal laser therapy and associated white light fundoscopy. Many of the dynamic changes observed in clinical autofluorescence imaging after laser exposure are apparent in the small animal model but occur over a shorter period.

still present. Moreover, the accumulation of lipofuscin autofluorescence suggests that the

overlying photoreceptors were still actively shedding the outer segments to produce the necessary metabolic byproducts. This supports the use of lipofuscin as a biomarker for retinal damage to compliment traditional imaging modalities such as fundus photography and NIR reflectance SLO. Likewise, we observed a trend towards recovery of baseline levels of FAF with suprathreshold exposures at 20 mW and 22 mW. Multiple reports of photoreceptor migration to fill in damaged areas of the retina have been documented following UV light exposure(159, 219, 220). This may account for the reduction in lesion size observed during the longitudinal FAF imaging experiments. Similar studies used histology to demonstrate a decrease in laser lesion diameter 3 weeks after the initial exposure in an apparent remodeling phase in the retina(158). Electroretinography (ERG) studies in rats have also shown either partial or full recovery of function at 60 days with comparable exposure parameters to our study(159).

The observed changes in the fluorescence signal were particularly useful in the longitudinal analysis of the RPE since the color fundus images and NIR-reflectance SLO did not reveal any perturbations in the tissue. The improved sensitivity of this technique may also be coupled with additional imaging modalities such as spectral domain optical coherence tomography (SD-OCT) to correlate structural changes in the outer retina with alterations in the FAF profile (Figure 5-9).

There are a few important considerations that need to be taken into account when quantifying FAF images. Traditional FAF and dual-wavelength FAF both assume that fluorophores in the RPE are the only contributing fluorescent components. Similarly, there is an assumption that only one fluorophore (lipofuscin) is present. Despite the fact that multiple fluorescent components are present within lipofuscin, it is still considered a

single fluorophore with a broadband emission spectrum. The dual-wavelength method does offer some distinct advantages over traditional single-wavelength FAF (1) the concentration of the fluorophore does not have to be constant throughout the retina (2) non-uniform illumination effects will be equivalent at both wavelengths so only the difference is noted and (3) location dependent effects will only be influenced if they are highly wavelength specific. Since both excitation wavelengths are only separated by 26 nm this is unlikely.

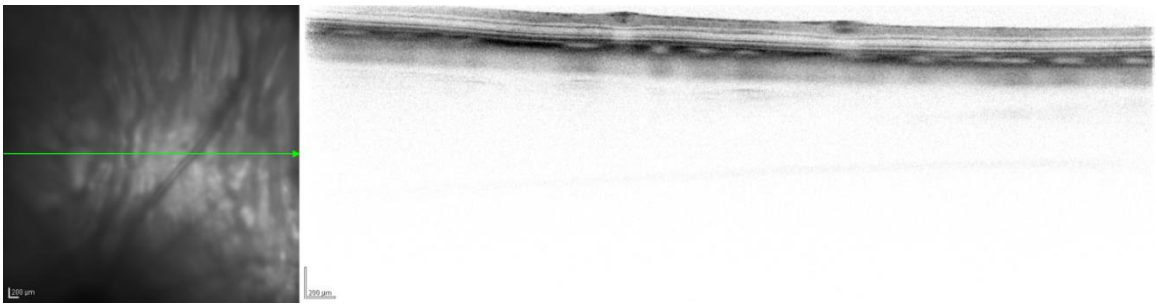

Figure 5-9. Multimodal imaging of the brown Norway rat retina. (Left) NIR reflectance SLO image of the rat retina in the superior quadrant (Right) SD-OCT cross section demonstrating the layered structure of the rat retina.

FAF imaging may be used to supplement traditional imaging techniques such as white light fundoscopy and NIR reflectance SLO. Generally, these latter methods are used to guide the placement of light-based therapies but this study demonstrated the contrast provided by lipofuscin revealed greater detail of the lesion morphology. The dual wavelength FAF technique also offers distinct advantages over traditional FAF imaging, particularly when performing quantitative analysis. Many factors can confound fluorescence intensity measurements when acquiring images with a single wavelength. Extensive calibration procedures are often necessary to ensure reproducibility of imaging

data(221, 222). By using two wavelengths for excitation, we were able to compensate for variables such as non-uniform illumination, pupil diameter, and heterogeneous pigment distribution.

The widefield view (30° x 30°) of the fundus described in this study is well suited for lipofuscin density measurements; however, it does not provide sufficient transverse resolution to visualize individual RPE cells. Recent studies incorporating high resolution adaptive optics fluorescence scanning laser ophthalmoscopy were able to provide that degree of detail at the cellular level in non-human primate models(24, 25, 223). Interestingly, the light sources used for fluorescence excitation in these studies resulted in photochemical damage to the tissue at levels below the current American National Standards Institute (ANSI) guidelines(224). Presumably, the small field of view, high energy visible light sources, and relatively long exposure durations were sufficient to produce transient, and in some cases permanent, changes in the FAF signal. It should be noted that despite the difference in the mechanism of damage (photothermal vs. photochemical) the total radiant exposures used in our study and the fluorescence AO-SLO imaging study were similar. Subsequent AO imaging studies with fluorescence have implemented designs which significantly improve yield without the risk of phototoxicity to the retina by limiting exposures to less than 2.44 J/cm^2 (27). Similarly, multiphoton microscopy has been used to provide a high degree of detail of spatial detail with respect to retinal fluorophores in animal models both *in vivo(225)* and *ex vivo(226-228).*

This study has numerous implications for diagnostic and therapeutic applications in a wide variety of retinal diseases, including AMD. The brown Norway rat model may be used to characterize regions of divergent autofluorescence associated with injury and

induced disease states. Recent reports have proposed classification methods for various dry AMD phenotypes based on the observed FAF characteristics(229, 230). The use of targeted laser exposures to ablate the RPE and photoreceptors could be used to model morphological changes in the fundus similar to the patterns in patients with geographic atrophy (GA). Additionally, this methodology could be used to study the kinetics of laser tissue interaction in the retina in therapeutic applications. Photocoagulation may be used to treat a variety of retinal conditions such as proliferative diabetic retinopathy (PDR), neovascular AMD, branch retinal vein occlusion (BRVO), and central serous retinopathy (CSR). Although the use of low-dose radiant exposures is not a novel concept(231, 232), recent advanced in diagnostic imaging capabilities provides an opportunity to refine current standards to reduce the risk of collateral damage in the retina.

Chapter 6: Morphological and Molecular Imaging of Induced Retinal Degeneration in a Transgenic Mouse Model

Endogenous fluorophores are prevalent throughout the body and may be used to monitor changes in biochemical activity or perturbations associated with injury and disease as demonstrated in the previous chapter. However, this native autofluorescence does have limitations due to the broadband emission spectrum and inability to provide direct information on molecular activity. The development of transgenic animals with fluorescent reporter genes provides the opportunity to investigate the activation or upregulation of specific molecules of interest in models of pathology. This approach enables researchers to actively monitor molecular activity in a living animal which provides a dynamic model to study pathology, potential interventions, and helps to reduce the number of animals needed in biomedical research. The use of fluorescently labeled molecules is particularly appealing for retinal research due to the uniquely accessible nature of the tissue when using optical imaging techniques. In the second phase of our small animal studies, a transgenic mouse model was selected to non-invasively study morphological perturbations and molecular dynamics of the transcription factor nuclear factor kappa beta (NF-κβ) in response to low-dose retinal photocoagulation.

6.1 Introduction

As an immune privileged site in the CNS, the retina must maintain tight regulation over the activation of inflammatory pathways. Neuroinflammation in the retina is primarily stimulated by activated microglial cells which lead to the release of cytotoxic mediators and reactive oxygen species (ROS)(233). Many common signs of pathologic

neuroinflammation have been observed in progressive diseases like AMD(84, 85, 234) which leads to decreased visual acuity through the loss of photoreceptors, retinal pigment epithelial (RPE) cells and in some cases, neovascularization. Dysfunctional regulation of inflammatory pathways has also been implicated in a variety of other common ocular diseases, including glaucoma(130, 235) and diabetic retinopathy(128, 236-239). Non-invasive imaging techniques are the primary means of diagnosing and monitoring these conditions. Therefore, it is essential to identify image-based biomarkers that capture the spatial and temporal characteristics of neuroinflammation within the eye. This knowledge will lead to a better understanding of pathological mechanisms and targeted treatment strategies.

The family of transcription factors known collectively as nuclear factor-kappa B (NF-kB) plays a critical role in the regulation of inflammation and cellular stress response pathways(240-243). Significant increase in the activity of NF-kB has been shown in neurons and microglia throughout the CNS, particularly in brain tissue, in patients with neurodegenerative diseases such as Parkinson's and Alzheimer's(244-247). An increase in NF-kB activity has also been shown in the retina in response to a variety of stimuli including oxidative stress(248-250), ischemia(251), glutamate(183) and intense light exposure(155, 156, 160, 165, 219, 252). The dynamics of this cellular stress response are difficult to determine using conventional techniques due to the conditional signaling events and localization of specific cell types within the eye. Conventional techniques such as immunohistochemistry, histology and western blots have been used to evaluate tissue post mortem but were not able to investigate the temporal response within an individual subject.

In the present study, a laser-induced retinal injury model was used to investigate molecular activity of NF- κβ in relation to morphological perturbation. Fluorescence confocal scanning laser ophthalmoscopy (cSLO) was used to investigate the spatial and temporal upregulation of NF-κβ (p65) *in vivo.* Likewise, dynamics of the retinal structure were investigated using spectral domain optical coherence tomography (SD-OCT) to correlate the morphological perturbations with molecular activity. The *in vivo* findings were then compared with *ex vivo* analysis of the tissue using immunohistochemistry and multiple microscopy methods.

6.2 Methods

All experimental procedures were approved by the Institutional Animal Care and Use Committee at the University of Texas Medical Branch and complied with the ARVO Statement for the Use of Animals in Ophthalmic and Vision Research.

6.2.1 Animal Model

The *cis*-NF-κβ^{eGFP} reporter mouse was created at the University of North Carolina and designed to investigate the spatial and temporal upregulation of NF-κβ induced transcription in response to injury and disease. A gene-targeting approach was used to incorporate a single copy of the NF-κβ reporter. This approach minimized transgene expression due to basal NF-κβ activity and insured only a single copy of the transgene at a well-characterized locus, 5' of the mouse hypoxanthine phosphoribosyltransferase (HPRT) gene(166).

A breeding trio was obtained from the University of North Carolina (Chapel Hill, NC) to establish a colony of the *cis*-NF-κβ^{eGFP} mice at the University of Texas Medical Branch. The first three generations of mice, including the original breeding trio, were genotyped (Transnetyx, Cordova, TN) based on tissue collected from a tail snip to verify incorporation of the transgene. Subsequent generations were phenotyped using fluorescence microscopy techniques to detect the presence of the eGFP reporter.

Prior to imaging and laser exposure, mice were anesthetized with isofluorane (1 – 2%) and placed on an adjustable, heated platform positioned orthogonal to the imaging system. A topical ocular anesthetic (0.5% Proparacaine hydrochloride, Bausch & Lomb, Tampa, FL) was first applied, and then the pupils were dilated with 1% Tropicamide (Bausch & Lomb, Tampa, FL). Corneal hydration was maintained throughout the imaging session by periodically administering 0.5% hypromellose lubricating eye drops.

6.2.2 Laser Induced Retinal Injury

The laser injury and color fundus imaging protocols for this study were detailed in the previous chapter. Dosimetry tests were performed in 14 mice to ensure that the damage thresholds remained unchanged between the rat and transgenic mouse model (Table 6-1). The only difference in the experimental set up was the use of 3.2 mm fundus laser lens (Ocular Instruments Inc., Bellevue, WA) to account for the smaller corneal curvature of the mouse eye. For a subset of the animals, a newly acquired Micron III fundus imaging system (Phoenix Research Labs, Pleasanton, CA) was used to collect color fundus images and videos.

Table 6-1. Laser Dosimetry Parameters[†]

Power (mW)	# Exposures	Radiant Exposure (J/cm2)	Grade
8.4	15 (n = 3)	10.7	Sub-threshold
14.6	30 (n = 5)	18.6	Threshold
28.9	45 (n = 6)	36.8	Supra-threshold

[†]Exposure duration: 0.1 s, Exposure λ: 514 nm, Exposure Spot Size: 0.1 mm were fixed

6.2.3 *In vivo* Imaging

A modified clinical imaging system (Spectralis HRA+OCT, Heidelberg Engineering, Heidelberg, Germany) was used to collect multimodal imaging data from the fundus and retinal cross-sections. A +25 diopter achromatic lens was mounted on the front of the imaging system to compensate for the optics of the mouse eye. The confocal scanning laser ophthalmoscope (cSLO) utilized multiple light sources to highlight specific features of the fundus. An argon laser (488 nm) and two diode lasers (790/820 nm) were used for eGFP fluorescence imaging, fundus autofluorescence (FAF), fluorescein angiography (FA), red free reflectance (RF) and near infrared reflectance (NIR) imaging modes. The cSLO featured a scan rate of 15 frames/sec and multiple frames were averaged to improve the overall signal to noise ratio (SNR) using the TruTrack™ active eye tracking system. The TruTrack™ system created a reference scan and actively compensated for eye motion enabling multiple images to be registered and averaged in near real-time. All fundus images were acquired in the high-resolution mode over a 30° x 30° (1536 x 1536 pixels) or 20° x 20° (1024 x 1024 pixels) field of view (FOV).

High resolution cross-sectional views of the retina were generated using the SD-OCT channel of the modified clinical imaging system. To compensate for the difference

in the axial length of the mouse eye, the reference arm offset was decreased in the hardware initialization file for the Spectralis. The addition of a line of code in the HRA2.ini file was used to reduce the geometric pathlength of the reference arm by the empirically determined value of 6 mm in air. The HRA2.ini file is stored in C:\\heyex\plugins. Additional line of code in the OCT section of the initialization file:

[OCT]
ReferenceArmOffest = -6000

Likewise, a corneal curvature value of 0.67 was used to provide the appropriate scaling factor for the fundus images of the mouse(122). A broadband superluminescent diode (SLD, λ = 870 nm) was used to generate the SD-OCT images at a rate of 20,000 or 40,000 A-scans per second for high resolution or high speed acquisition, respectively. The high resolution mode was used to observe heightened detail of the retinal layers based on multiple averaged frames (> 30 frames). The high speed mode was used to acquire dense volumetric scans where each B-scan was separated by only 3.8 μm. For volumetric scanning, only 3-10 frames were averaged to reduce motion artifacts and overall scan time. This enabled volumetric analysis of the retinal morphology and regions of laser-induced injury, particularly when viewed in the *en face* plane.

6.2.4 *Ex Vivo* Tissue Preparation

At the conclusion of the *in vivo* imaging studies, the eyes of each subject were enucleated and preserved for further analysis. Retinal flatmounts were prepared by fixing the tissue in 4% paraformaldehyde (PFA) for 24 hours. Next, the eye was dissected by making an incision at the interface of the cornea and sclera to remove the anterior segment, lens, and vitreous. A small spatula was used to peel the neural retina from the

remainder of the eye cup. Four small incisions were made along the edge of the tissue enabling it to be flattened and mounted on a slide. Whole eyes were also prepared for cryosectioning. Each eye was enucleated, placed in Tissue-Tek® optimum cutting temperature (O.C.T.) (Sakura Finetek, Torrance, CA), flash frozen in liquid nitrogen and stored at -80°C. Eight to sixteen micrometer cryosections were made along the transverse plane through the entire globe for each sample and thaw-mounted on Fisherbrand™ Superfrost™ Plus glass slides (Fisher Scientific, Pittsburgh, PA) in preparation for staining.

6.2.5 Immunohistochemistry and Histology

Immunohistochemistry was performed with multiple fluorescently labeled antibodies: ionizing calcium-binding adaptor molecule 1 (Iba-1), glial fibrillary acidic protein (GFAP), NeuN, isolectin B4 and p65. Texas red (Molecular Probes) was the fluorescent label in each case to identify microglia and macrophages (Iba-1), glial cells (GFAP), vasculature (Isolectin B4), and the p65 subunit of NF-κβ (p65). Briefly, the tissue was washed in PBS, permeabilized in 1% Triton and blocked in 10% normal goat serum (NGS) for 30 minutes at room temperature. Tissues were incubated overnight at 4°C in the primary antibody, rinsed in PBS (x3) and incubated in the secondary antibody for 4 hours at 4°C. The tissue was then mounted on a slide with VECTASHIED® mounting media (Vector Laboratories, Burlingame, CA) with DAPI to stain cell nuclei. This method enabled multi-channel fluorescence microscopy with the eGFP transgene occupying the green channel, the labeled cells, proteins or vasculature occupying the red channel and cell nuclei stained with DAPI on the blue channel. The stained flatmount

preparations provided a complimentary view to the *in vivo* fundus imaging with cSLO while the stained cryosections provided a complimentary view to the *in vivo* SD-OCT imaging data to compare alterations in retinal morphology.

6.2.6 Microscopy

Multiple microscopy techniques were used to visualize the excised retinal tissue to investigate alterations in morphology and fluorescence expression. Flatmount preparations were used to provide comparable views to the *in vivo* SLO fundus images. Two-photon microscopy (Ultima IV, Prairie Technologies, Middleton, WI) was used to visualize the spatial distribution of the eGFP fluorescence associated with the upregulation of NF-κβ in 3-dimesnions (Ex 2PE: 900-1000 nm; Em: 510 nm). Similarly, confocal laser scanning microscopy (LSM 510 META, Zeiss, Thornwood, NY) was performed in the retinal flatmounts to investigate the eGFP fluorescence (Ex: 488 nm; EM: 510 nm). Differential interference contrast (DIC) microscopy (Eclipse 800, Nikon Instruments Inc., Melville, NY) was performed to visualize the orientation of the photoreceptors cells and investigate the morphology of the neural retina following laser injury.

6.2.7 Image Analysis

Single images were exported from the Heidelberg Eye Explorer software (Heidelberg Engineering, Heidelberg, Germany) as .tiff files in the native resolution to prevent data loss due to compression. The SD-OCT data sets, either volumetric or single B-scans, were exported as raw data files in the .vol format. Raw data sets were imported

into ImageJ (Wayne Rasband, National Institute of Health, Bethesda, MD) using the Open Heyex Raw Files plugin developed by Kris Sheets (http://rsb.info.nih.gov/ij/plugins/heyex/index.html)(122).

The dynamics of the retinal lesions were evaluated in the volumetric SD-OCT data sets by measuring changes in the lesion diameter as a function of time. The *en face* spatial resolution in the axial direction. Each lesion was manually delineated based on the appearance of distorted boundaries along the RPE and IS/OS junction. Each lesion was assumed to have a circular shape at any given depth based on Gaussian profile of the argon laser used for photocoagulation and the thermal diffusion throughout the tissue.

The changes in eGFP fluorescence were measured using the corrected total cell fluorescence (CTCF) technique(253) which is based on the integrated density measurement for regions of interest and background sampling to compensate for illumination effects and background autofluorescence:

CTCF = Integrated Density – (Area of ROI x mean background fluorescence)

where the integrated density is the product of the mean intensity and the ROI area. This method was used to measure localized increases in eGFP while accounting for the background eGFP fluorescence associated with the basal expression of NF-κβ.

6.3 Results

6.3.1 Characterization of Baseline Fluorescence *In Vivo*

The baseline fluorescence signal originating from the endogenous eGFP was unique for each mouse in the study. Figure 6-1 demonstrates the variability of the basal

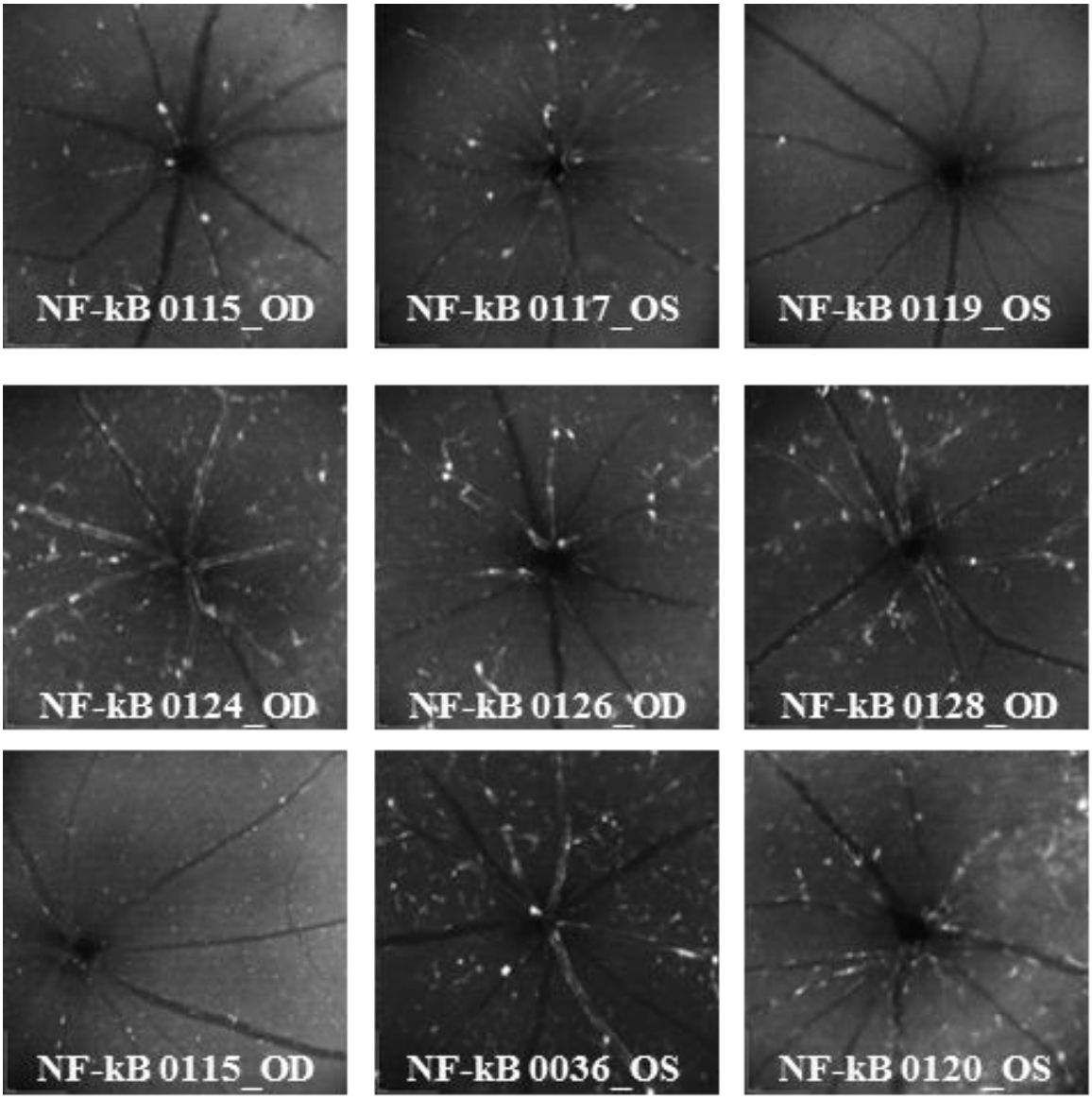

Figure 6-1. Variability in native eGFP expression in naïve *cis*-NF-κβ^{eGFP} transgenic mice using fluorescence cSLO imaging in the neural retina of naïve mice.

expression from a sub set of animals. The degree of eGFP fluorescence also appeared to be bilateral regardless of expression levels. The eGFP signal in the naïve transgenic mice was predominantly located within the neurosensory retina and around branch points of

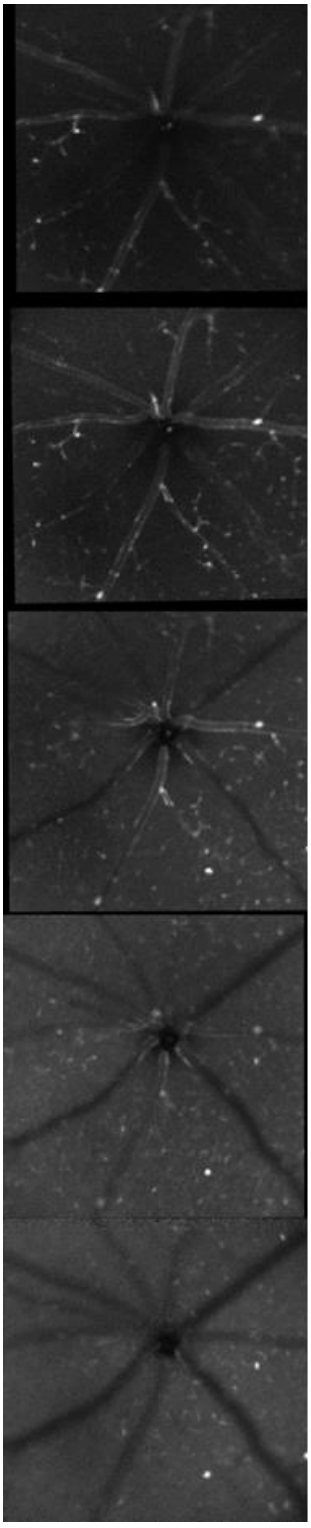

Figure 6-2. Differential fluorescence expression profiles based on focal depth of the cSLO. The inner retinal focus at the nerve fiber layer (+10 diopters) revealed increased fluorescence along the major blood vessels and punctate hyperfluorescent regions near vessel branch points. The outer retinal focus at the RPE (-10 diopters) demonstrated fewer eGFP fluorescent regions but heightened background autofluorescence from lipofuscin.

the vasculature. As the focal plane of the cSLO was moved to the outer retina, the background FAF signal attributed to lipofuscin in the RPE became visible but the eGFP signal was minimal (Figure 6-2). The baseline fluorescence intensity at different focal

depths was calculated and presented in arbitrary units (Figure 6-3). The variability in fluorescence intensity based on focal depth necessitated the selection of the same focal plane when analyzing CTCF across multiple mice and at multiple time points. In contrast to the transgenic mice, wild type C57BL/6 mice only exhibited background fluorescence from lipofuscin in the RPE (Figure 6-4).

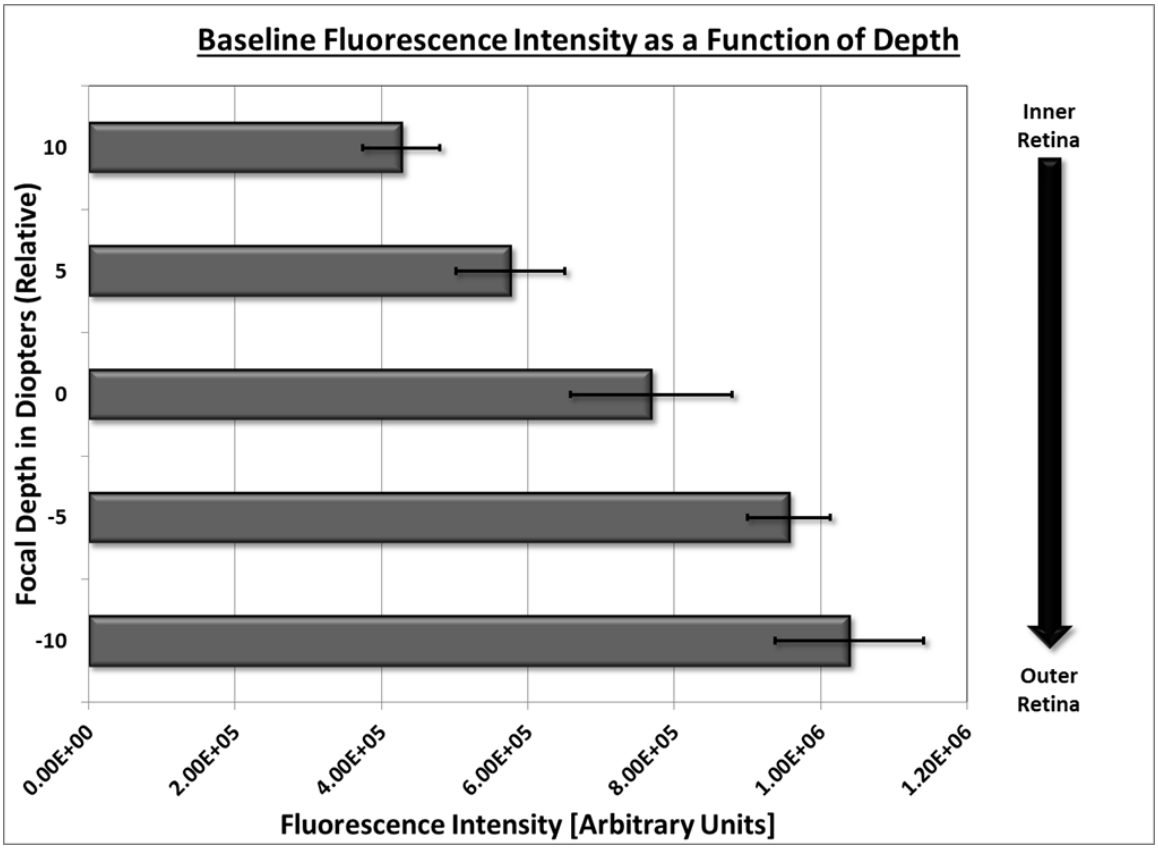

Figure 6-3. Baseline fluorescence signal as a function of focal depth in naïve *cis*-NF-κβ^{eGFP} reporter mice (n=6). Fluorescence values are presented in arbitrary units.

6.3.2 Fundus Imaging Following Photothermal Injury

Threshold and suprathreshold laser exposures resulted in injury which was immediately visible using fundus photography, NIR reflectance cSLO, red free cSLO,

and SD-OCT. The upregulation in NF-κβ indicated by a localized increase in eGFP was not visible until approximately 4-8 hours after exposure. Presumably, this lag is due to

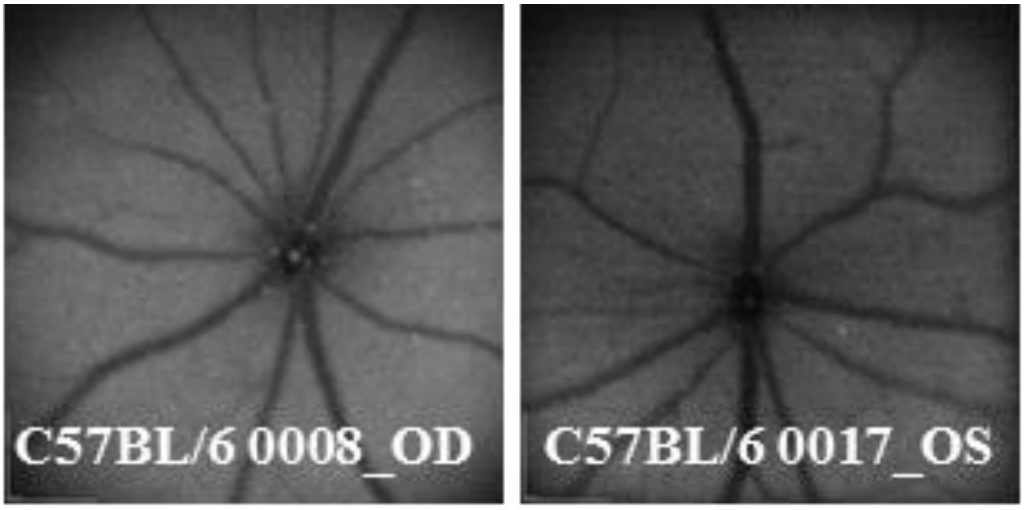

Figure 6-4. Wild type C57BL/6 FAF pattern in naïve mice.

the time required for eGFP accumulation to reach sufficient levels for the avalanche photodiode. Fluorescence intensity continued to increase for up to 48 hours and appeared as clusters of heightened eGFP expression. From the 24 hour time point to the 48 hour time point, CTCF measurements increased nearly 20% indicating continued upregulation of NF-κβ. After reaching maximum expression levels around 48 hours, the CTCF values gradually declined over subsequent weeks (Figure 6-5). At the conclusion of the four week study, the eGFP fluorescence was 56% lower than peak levels observed at 48 hours (Figure 6-6).

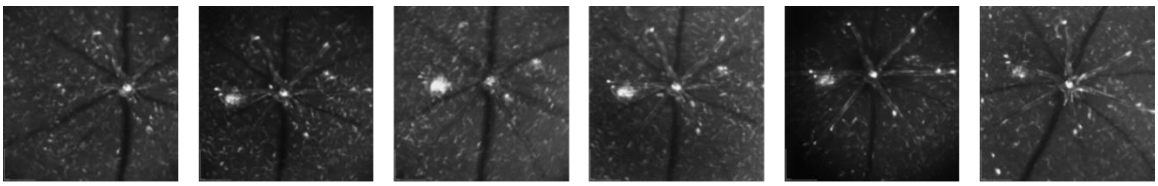

Figure 6-5. Longitudinal imaging of a single suprathreshold photothermal lesion over a one month period demonstrating the local upregulation in eGFP in response to the injury.

Comparable exposures were also tested in wild type C57BL/6 mice to ascertain any differences in response. The multimodal fundus images obtained with the cSLO are shown in Figure 6-7. The NIR and RF images clearly show the characteristic circular lesions, FA was used to demonstrate discontinuity of the RPE associated with the laser exposure and the FAF images revealed small perturbations in the lipofuscin autofluorescence similar to the previous experiments with the brown Norway rats. As expected, the appearance of the retinal injury was similar to the transgenic mice with the exception of the eGFP signal on the fluorescence channel.

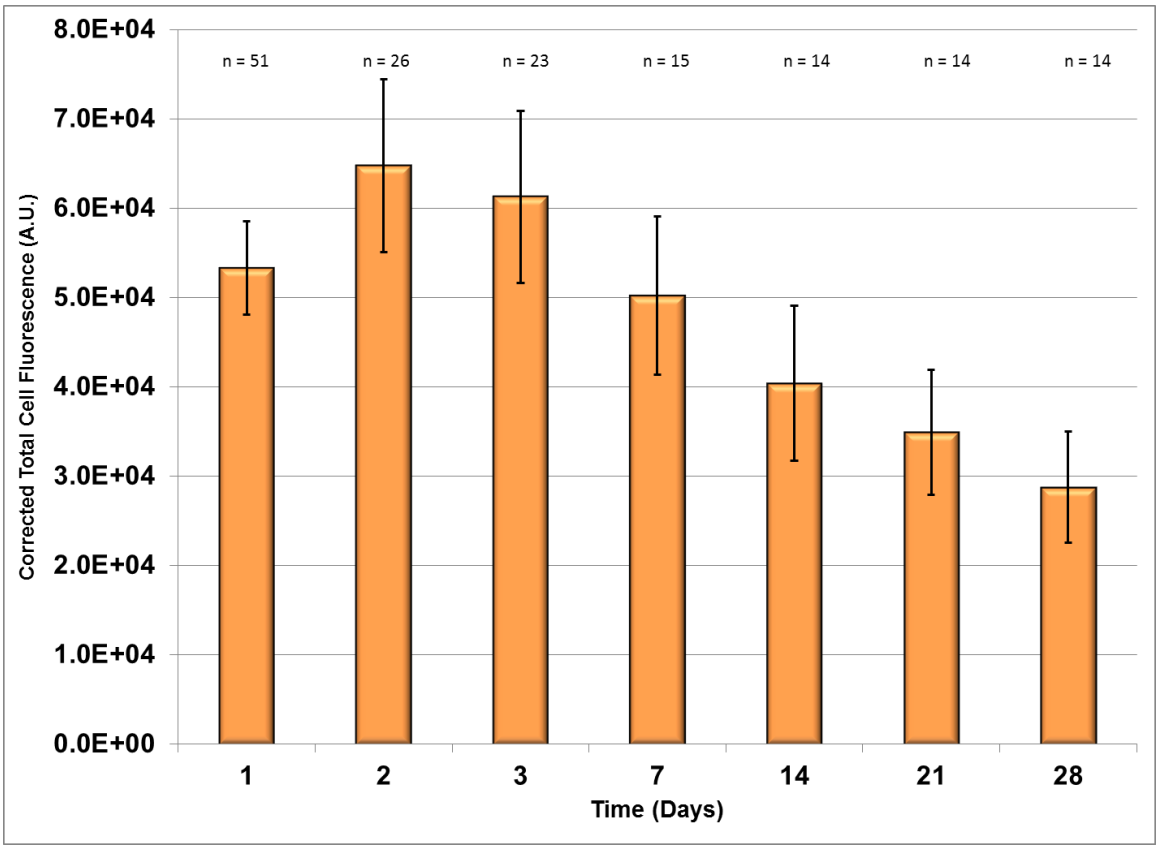

Figure 6-6. Longitudinal CTCF measurements of suprathreshold photothermal exposures in *cis*-NF-κβ^{eGFP} mice (n=15) based on fluorescence cSLO imaging. The number of lesions included in each measurement is noted above the respective bar.

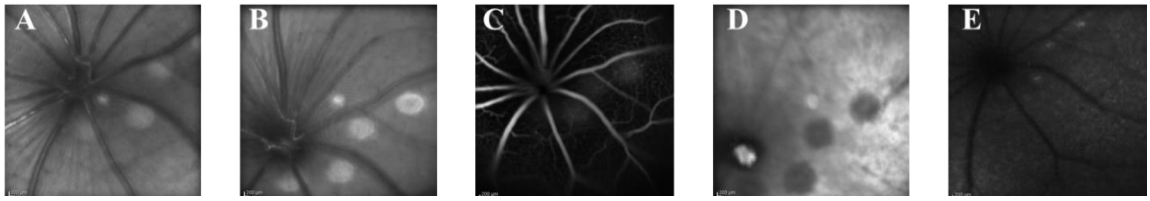

Figure 6-7. Multimodal cSLO fundus imaging used to evaluate laser damage in a wild type C57BL/6 mouse (A) Red-free (RF) reflectance immediately after exposure (B) RF-reflectance at 24 hours post exposure (C) Fluorescein angiography at 24 hours (D) NIR-reflectance focused at the RPE at 24 hours (E) FAF at 8 days post exposure.

6.3.3 SD-OCT Imaging Following Photothermal Injury

Imaging of the retinal structure with SD-OCT was used to complement the molecular imaging with the eGFP reporter gene. Volumetric data sets were acquired over the same period of time to investigate changes in structure relative to the upregulation of NF-κβ. In contrast to the fluorescence signal, the SD-OCT images revealed immediate changes in the optical characteristics of the retinal following photocoagulation. These effects were visualized within the neural retina and the RPE. The nerve fiber layer (RNFL), ganglion cell layer (GCL), and inner plexiform layer (IPL) did not exhibit signs of altered morphology over the course of 28 days (Figure 6-8). The majority of the laser energy was absorbed by the melanin in the RPE which caused localized disruption in the outer retina. The early stages of photothermal injury were easily identified by the altered backscattering profile within the outer nuclear layer (ONL), inner segment/ outer segment junction (IS/OS), and the RPE.

Volumetric imaging of the photothermal lesions was also performed to investigate lesion morphology based on appearance in the *en face* plane (Figure 6-9). Heightened detail of the lesion boundaries was observed and the depth sectioning capabilities permitted

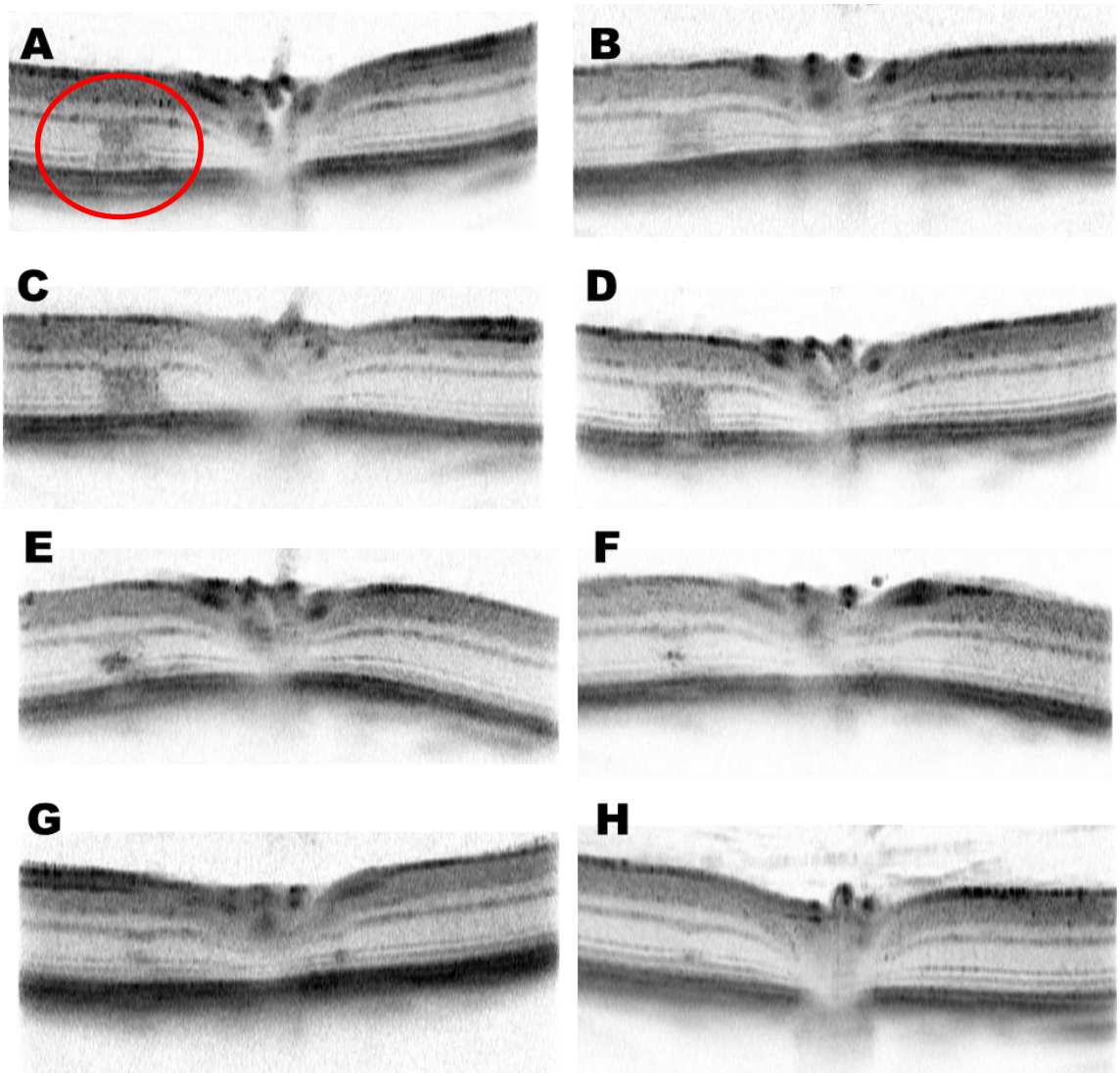

Figure 6-8. Longitudinal SD-OCT images of a single threshold photothermal lesion (circled) in single B-scan cross-sections of the retina (A) Initial laser exposure (B) 6 hours post-exposure (C) 12 hours post-exposure (D) 24 hours post-exposure (E) 4 days post-exposure (F) 1 week post-exposure (G) 2 weeks post-exposure (H) 4 weeks post-exposure.

measurements of lesion area as a function of time. Orthogonal views of the laser lesions were also generated to provide a reference for the retinal layer portrayed in the *en face* projections exhibiting the largest lesion area (Figure 6-10).

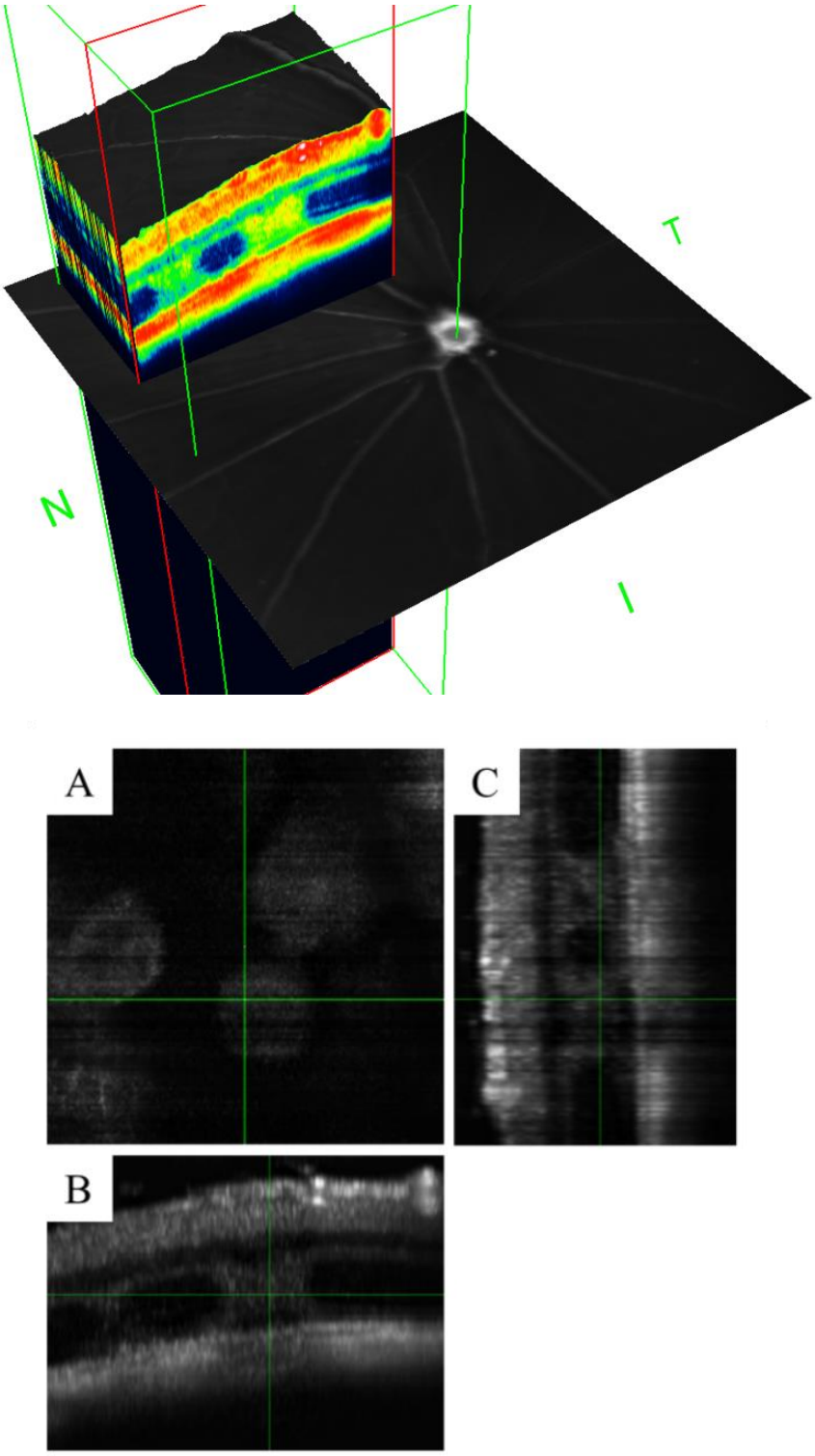

Figure 6-9. (Top) Volumetric SD-OCT scan through a retinal area with multiple photothermal laser lesions co-registered with the NIR-reflectance cSLO image of the fundus. **(Bottom) (A)** *En face* view of the laser lesions in depth shown in the outer nuclear layer. Orthogonal views of the volumetric data representing the *xz*-plane or B-scan **(B)** and the *yz*-plane or the adjacent A-scans **(C)**.

The laser lesion area was measured at 24 hours, 48 hours, 72 hours, 1 week, 2 weeks, and 4 weeks following exposure. The dynamics of the lesion area were plotted for at least 12 lesions (> 3 mice) at each time point. The data is presented as mean lesion area

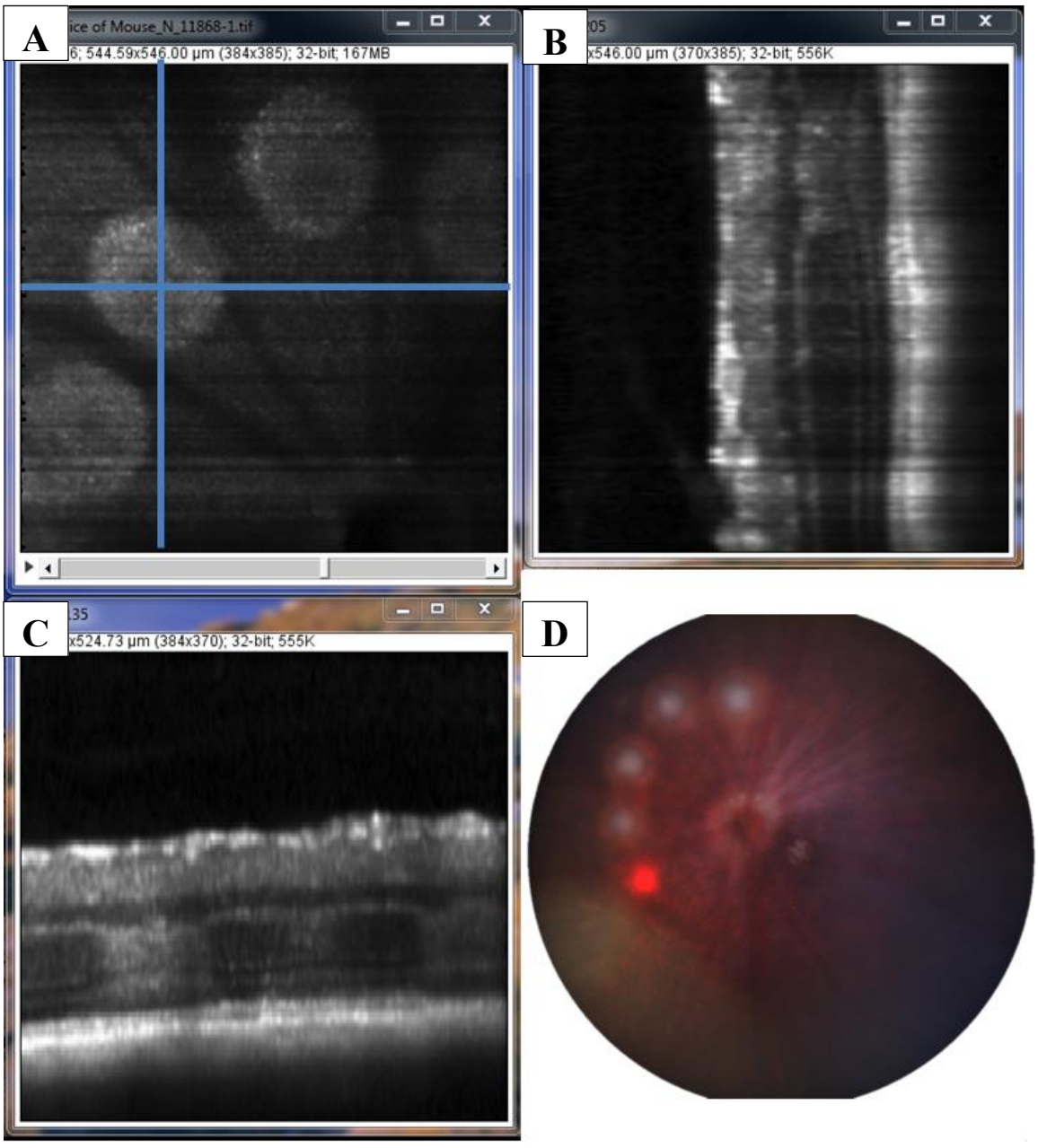

Figure 6-10. (A) *En face* projection of suprathreshold photothermal laser lesions immediately after exposure (B) *yz*-plane through a single lesion (C) *xz*-plane through the same lesion (D) White light fundus photography demonstrating the characteristic circular retinal lesions.

(μm^2) ± SEM. Lesion area decreased 75-80% over the course of 4 weeks with the majority of the lesion regression occurring within the first 7 days based on the SD-OCT measurements. At the 2 week time point, the lesion area appeared to reach a plateau (Figure 6-11).

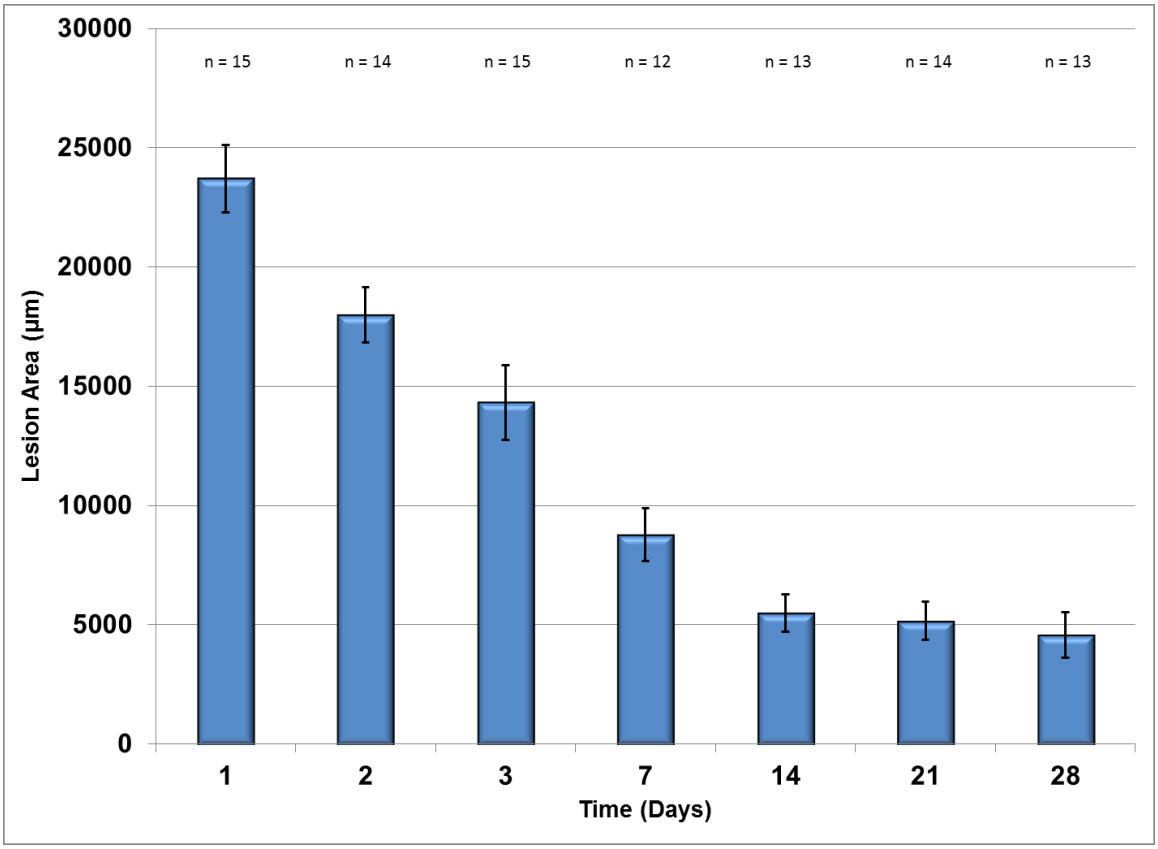

Figure 6-11. Longitudinal imaging of lesion area based on *en face* views of volumetric SD-OCT data sets in *cis*-NF-κβ^{eGFP} mice (n=12).

A small group of mice (n=3) was also used to investigate the lesion size as different focal depths based on the appearance in the *en face* projections and orthogonal views. The ONL, IS/OS junction and RPE were selected based on the preliminary assessments which qualitatively revealed changes in the SD-OCT profile (Figure 6-12).

The lesions appeared to stabilize after one week at each retinal location and the decrease in the lesion area followed the same pattern for all three depths measured.

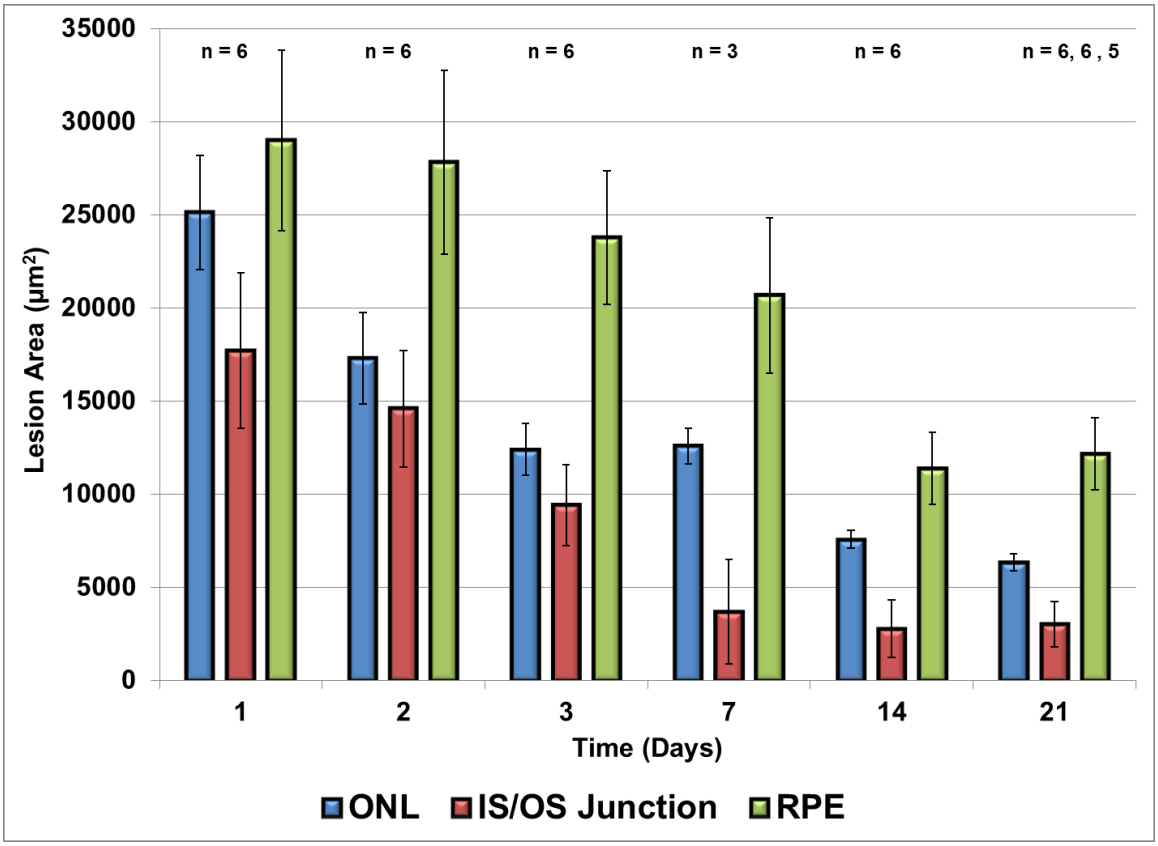

Figure 6-12. Depth resolved photothermal lesion area measured based on *en face* views of volumetric SD-OCT data sets in *cis*-NF-κβ^{eGFP} mice (n=3) at the outer nuclear layer (ONL), inner segment/ outer segment junction (IS/OS), and retinal pigment epithelium (RPE). The number of lesions measured at each time point is noted above the respective bars.

Next a comparison between the structural changes observed with SD-OCT and the molecular changes observed with fluorescence SLO were plotted together to assess similarities in the longitudinal progression (Figure 6-13). With the exception of the initial lag observed with the eGFP fluorescence, the dynamic profiles of each imaging modality were complementary with respect to lesion area and CTCF measurements.

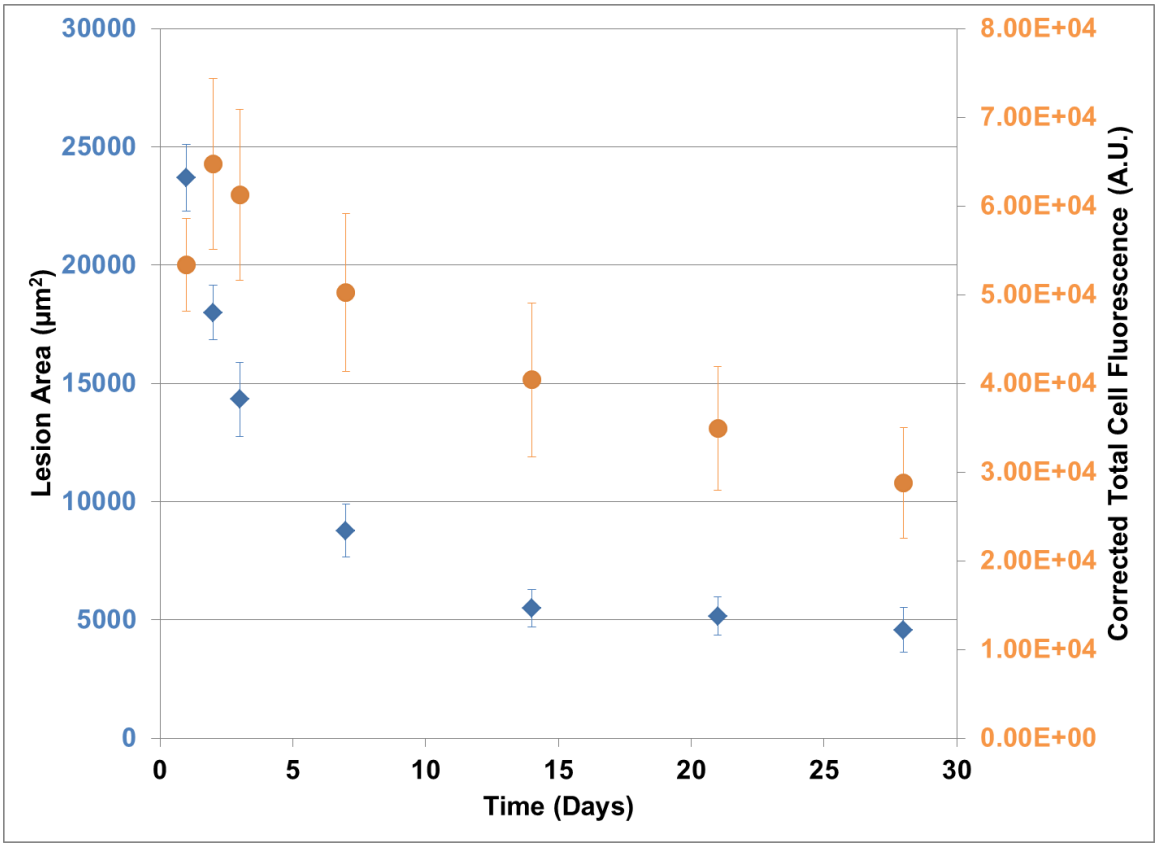

Figure 6-13. Comparison of the longitudinal response to laser induced retinal degeneration measured using SD-OCT (blue) to quantify changes in lesion morphology and fluorescence cSLO to perform molecular imaging of NF-κβ upregulation based on eGFP.

6.3.4 Differential Interference Contrast (DIC) Microscopy

Differential interference contrast (DIC) microscopy was used to provide a morphological assessment of the photoreceptor cells in flatmounts of laser exposed mice. DIC microscopy was well suited for imaging the neurosensory retina due to the transparent properties of the tissue. This technique has traditionally been used in retinal research to visualize the distribution of photoreceptor cells in fixed tissue samples(254, 255). The retinal regions exposed to photothermal damage were readily apparent under normal operating conditions. Although the majority of the laser energy in our

experimental setup was absorbed by the melanin in the underlying RPE cells, thermal diffusion did induce noticeable changes in adjacent cellular layers as demonstrated by the alterations in photoreceptor morphology observed with DIC microscopy. A reduction in the number of photoreceptor cells was noted in the laser exposed regions while the remaining cells exhibited blebbing and general disorganization (Figure 6-14). This would suggest cells were actively undergoing apoptosis.

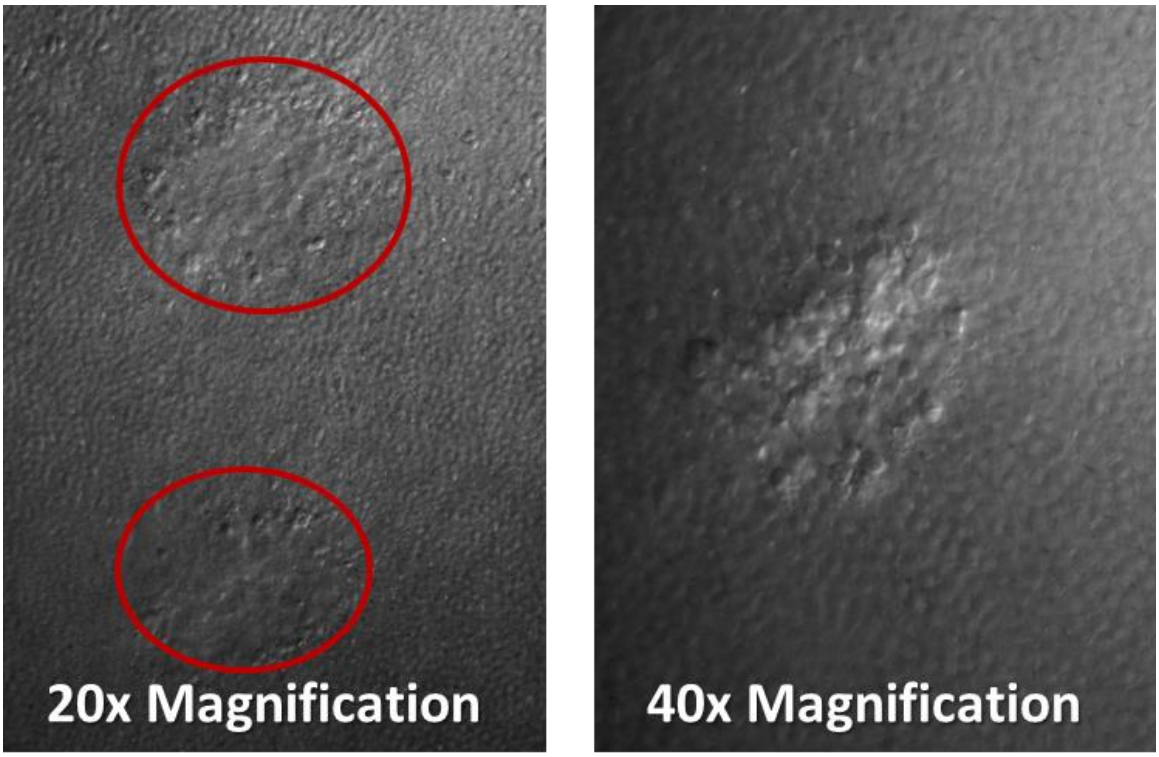

Figure 6-14. Differential interference contrast (DIC) microscopy of murine photoreceptor cells in a retinal flat mount depicting multiple threshold laser lesions.

6.3.5 Fluorescence Microscopy

Retinal flatmounts and cryosections from *cis*-NF-κβ^{eGFP} and wildtype C57BL/6 mice were analyzed to investigate the differences in morphology and molecular

expression related to laser exposure. Focal regions of eGFP observed in flamount preparations with epifluorescence, confocal LSM, or multiphoton microscopy (MPM) corresponded with *in vivo* fluorescence detected with the cSLO. Fluorescence expression was highly variable but basal eGFP was observed throughout the neural retina and along the vasculature with particularly bright expression as vessel branch points. Figure 6-15 shows retinal flatmount samples and corresponding *in vivo* images from transgenic mice receiving suprathreshold laser exposure, threshold laser exposure, naïve, and a naïve wild type C57BL/6 mouse as a control. For the transgenic mice, the eGFP fluorescence is clearly visible and the regions of heightened eGFP expression associated with suprathreshold and threshold laser exposure can be seen clearly in both the flatmount preparations and the *in vivo* images.

Staining of cryosections with GFAP revealed moderate co-localization with eGFP, particularly within the inner retina of laser exposed mice. The Texas red labeled GFAP was observed traversing multiple retinal layers including the GCL, INL, and ONL along eGFP positive cells which were presumably Müller cells (Figure 6-16). Staining of cryosections with the fluorescently labeled p65 antibody demonstrated near complete co-localization with the eGFP signal indicating that the eGFP observed *in vivo* and *ex vivo* was the result of NF-κβ upregulation (Figure 6-17). The fluorescently labeled Iba-1 antibody did not co-localize with the eGFP signal indicating that it does not arise from microglial cells but activated microglia were observed in close proximity to eGFP positive cells traversing the retina around the INL (Figure 6-18). This indicated a relationship between the upregulation in NF-κβ/eGFP and the pro-inflammatory signals initiated by the activated microglial cells to stimulate cytokines, chemokines and

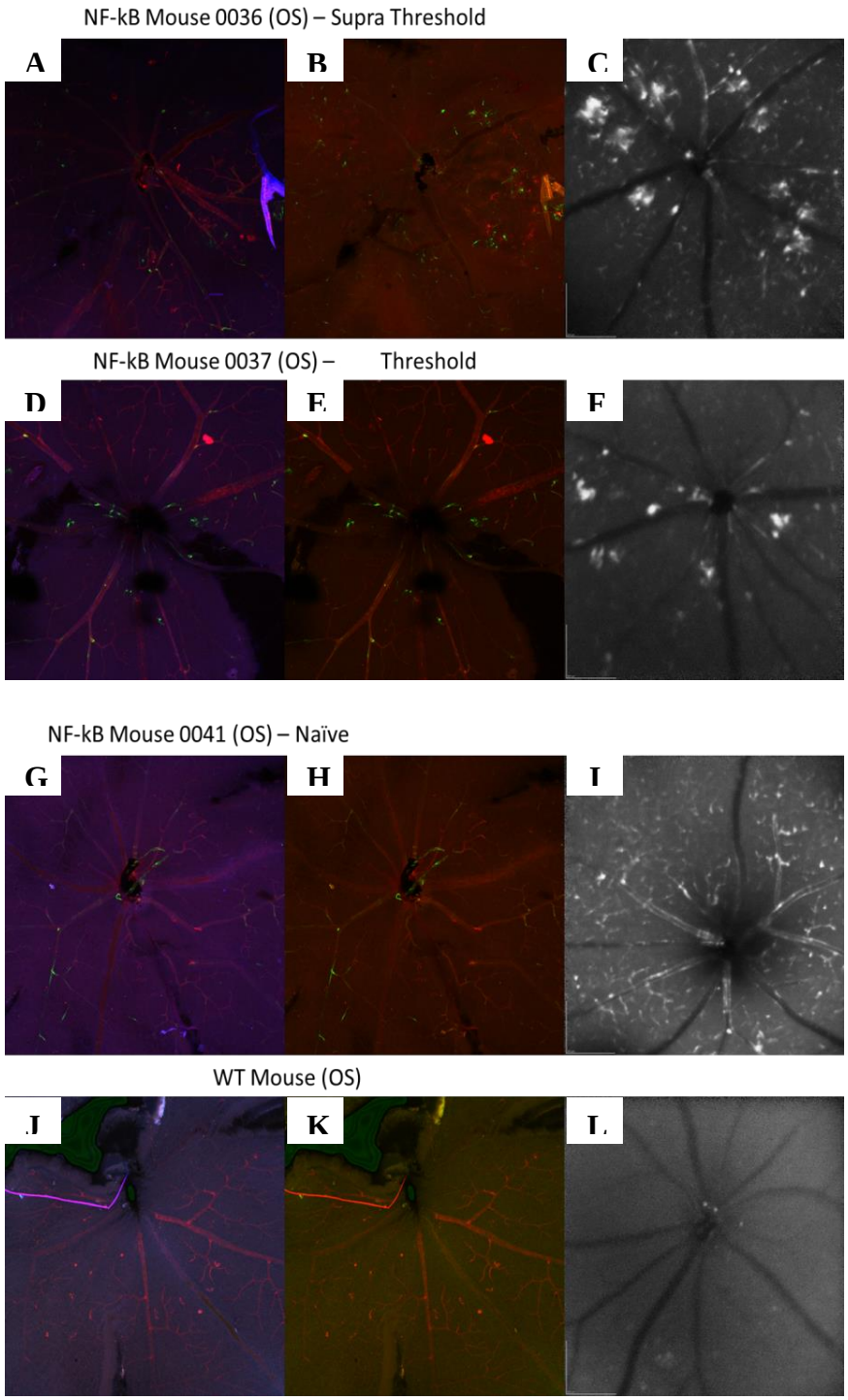

Figure 6-15. Comparison of laser exposed mice with naïve transgenic and wild type mice. (*Left*) Multi-channel fluorescence imaging of retinal flatmount preparations stained with DAPI (blue), isolectin b4 (red) and eGFP (green) (*Center*) Isolectin b4 (red) and eGFP (Green) (*Right*) *in vivo* fluorescence cSLO.

proteases(256). The Isolectin b4 staining of the vasculature provided additional

landmarks to compare retinal features from the *in vivo* imaging data and the retinal flatmount preparations. The stained vasculature also provided reference points with respect to depth during the confocal LSM and MPM 3-D imaging. Interestingly, the majority of the eGFP signal observed in the GLC was adjacent to the blood vessels stained with isolectin b4.

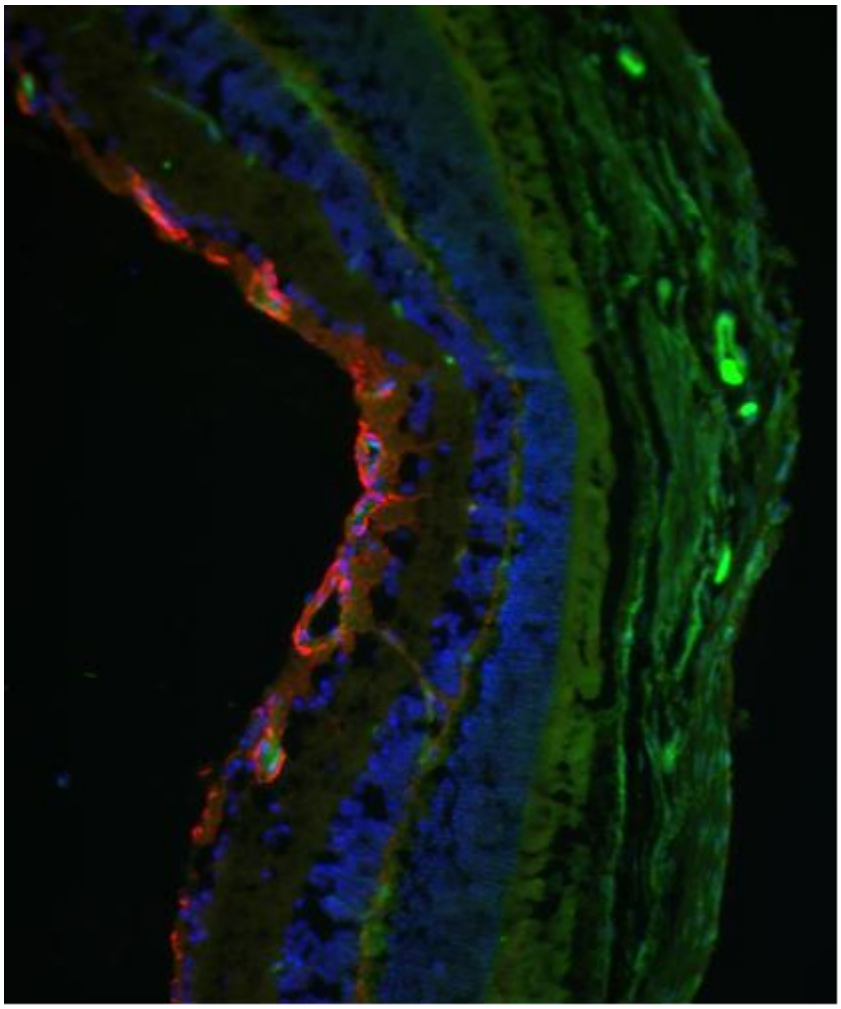

Figure 6-16. IHC staining with GFAP (red), DAPI (blue) and endogenous eGFP (green).

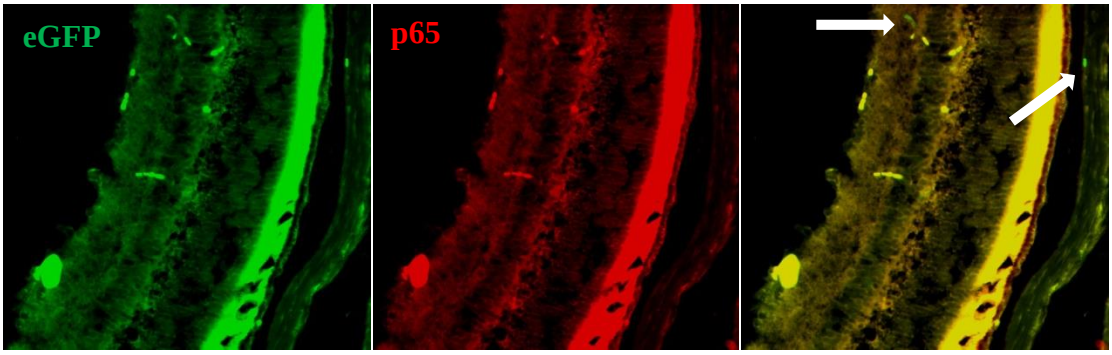

Figure 6-17. Immunostaining of retinal cryosections demonstrating the colocalization of eGFP (green) with the p65 subunit of NF-kB (red). The arrows in the merged image on the right highlight two regions that failed to stain with the p65 antibody.

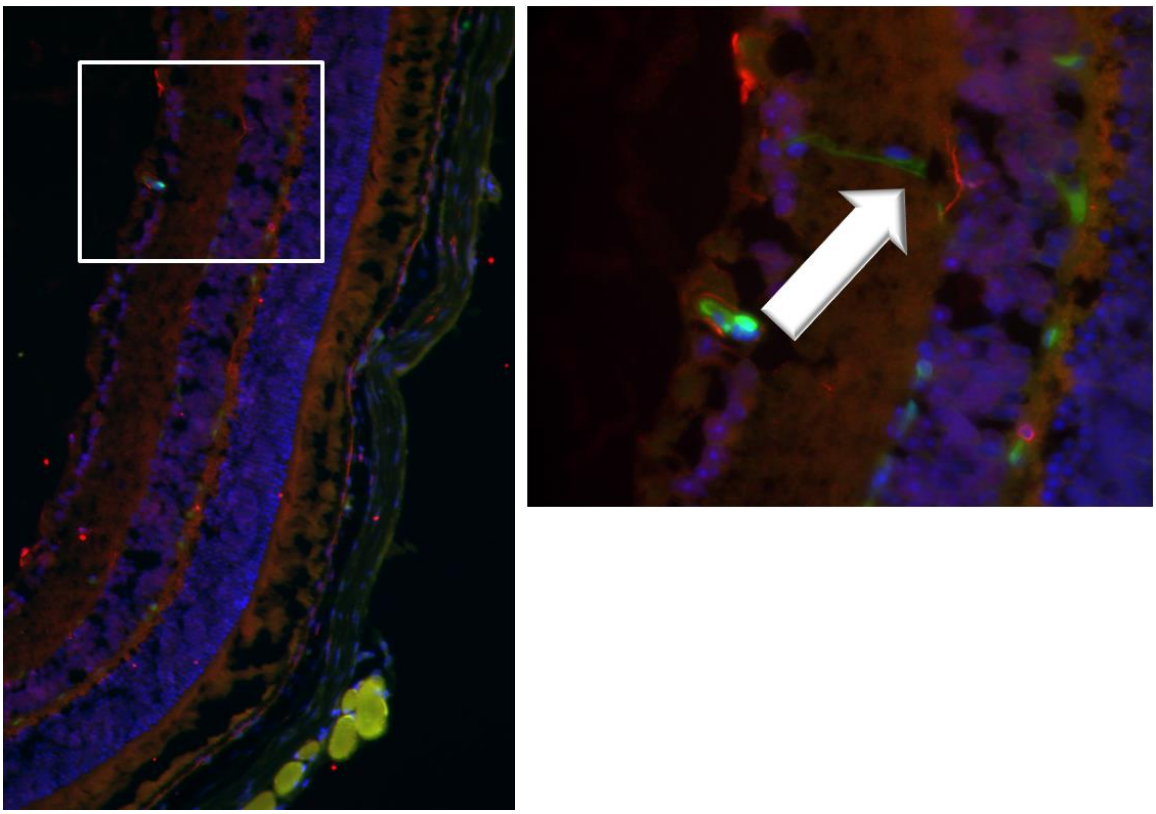

Figure 6-18. IHC of the *cis*-NF-κβ^{eGFP} mouse retina following light-induced injury. The Müller glia expressed the eGFP (green) associated with the upregulation of NF-κβ. The mounting media contained DAPI (blue) which preferentially stained the nuclei in the ganglion cell layer, inner nuclear layer and outer nuclear layer. Microglial cells were stained with Iba-1 (red). The microglial cells did not colocalize with the eGFP signal but activated microglia were observed in close proximity to the fluorescent Müller cells (arrow).

Volumetric fluorescence microscopy was performed using confocal LSM and MPM to determine the 3-D orientation of the eGFP signal in the fixed tissue and examine the cell types responsible for upregulation of NF-κβ in the transgenic model. The fixed retinal flatmounts exhibited continuous eGFP signal traversing the entire thickness of the tissue from the RNFL to the photoreceptor outer segments following laser exposure. Based on the structure of the cells and the characteristic soma within the inner retina, it was concluded that the eGFP positive cells were in fact Müller glial cells. Figure 6-19 depicts a maximum intensity projection from a volumetric confocal LSM data set oriented to show the span of the Müller cells across the retina. Similar to previous light microscopy studies, the endfeet of the Müller cells were observed in the inner retina(257) which may account for the uneven distribution of the basal fluorescence observed in the naïve *cis*-NF-κβ^{eGFP} mice. A top-down view of the eGFP fluorescence highlighted the Müller cell endfeet in the inner retina and demonstrated the convergence of the cells toward the site of injury in the outer retina (Figure 6-20).

A comparison between the *in vivo* cSLO images and the fixed flatmount preparation from the same animal is shown in Figure 6-21. Isolectin b4 was used to visualize the vasculature, DAPI stained the cell nuclei in the GCL, INL and ONL and the eGFP revealed the laser exposed area of the retina. The views of the tissue shown in Figure 6-21 C & D depict the superficial fluorescence signal from the Müller cells while the orthogonal view of the tissue from the 3-D data set clearly shows the extension of the eGFP expressing cells from the inner retina to the outer retina.

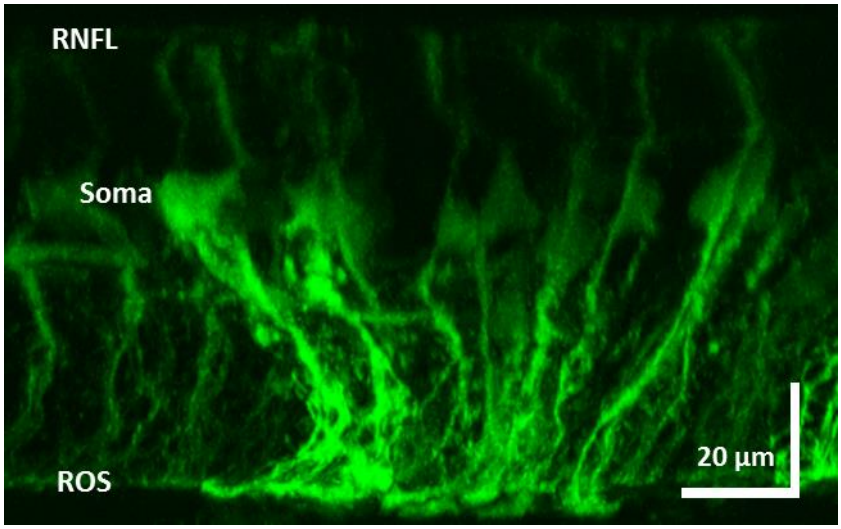

Figure 6-19. Heightened eGFP expression in the transgenic mouse retina observed at a photothermal laser lesion site using confocal microscopy in a fixed flat mount. A maximum intensity projection of the confocal stack (retinal cross-sectional view) demonstrated upregulation in NF-kB activity in the Müller cells extending from the RNFL to the outer retina.

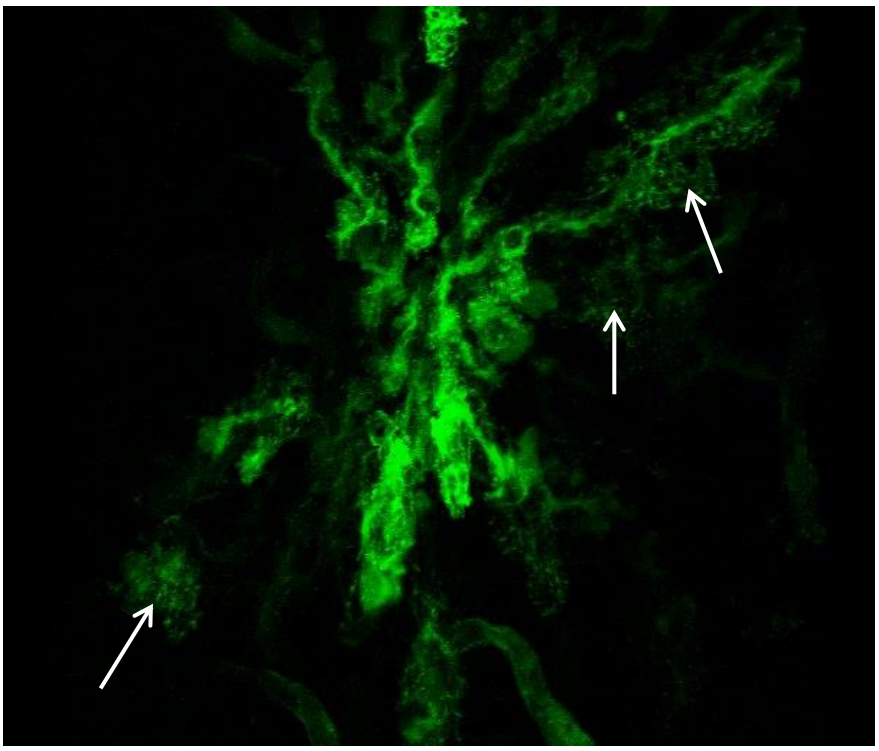

Figure 6-20. Heightened eGFP expression in the transgenic mouse retina observed at a photothermal laser lesion site using confocal microscopy in a fixed flat mount. A top-down view from the GCL revealed the Müller cell endfeet (arrows) and convergence of the cells towards the site of retinal injury.

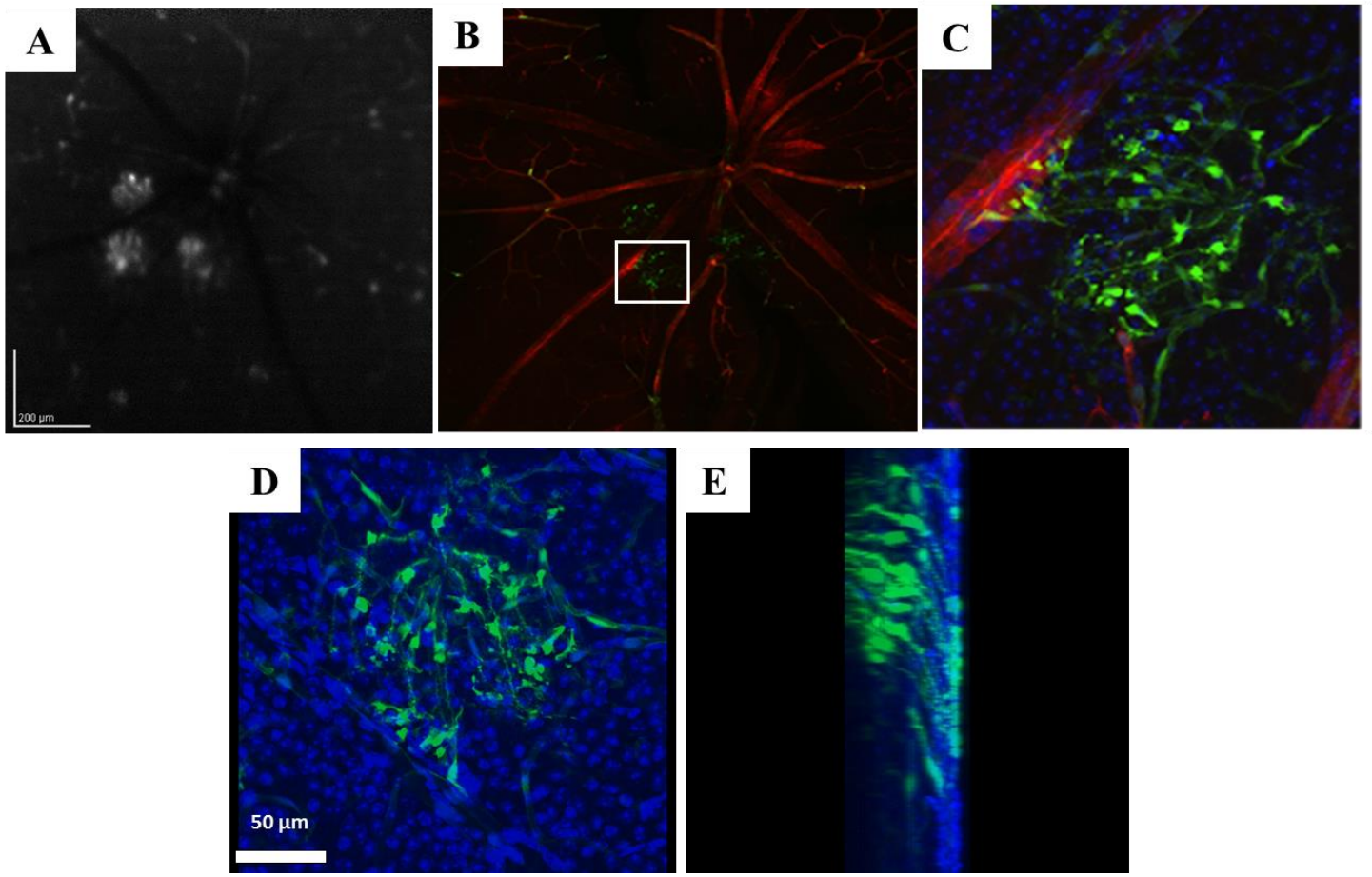

Figure 6-21. Retinal imaging in the *cis*-NF-κβ^{eGFP} transgenic mouse following photothermal laser exposure. **(A)***In vivo* fluorescence cSLO imaging of 3 discernible regions of heightened eGFP expression associated with photothermal lesions. (B) Retinal flat mount preparation 10 days post photothermal laser exposure (C) Enhanced scale of NF-kB activity at photothermal lesion site

MPM was also performed to investigate background autofluorescence signals from the tissue and the spatial distribution of the eGFP signal in fixed retinal flatmounts. Figure 6-22 depicts multiple views of the retina following photothermal laser exposure using 3-dimensinoal *in vivo* and *ex vivo* imaging techniques. Volumetric imaging of the lesions with SD-OCT (Figure 6-22 A, B) viewed in the *en face* plane exhibited structural alterations similar to the 3-D reconstruction of the excised retinal tissue around the lesion sites seen in Figure 6-22 C. The voids in the tissue were presumably the result of ablation of the photoreceptor cells and the 3-D reconstruction of the eGFP signal revealed similar patterns in the fluorescence expression of the Müller cells compared to the confocal LSM.

6.3.6 Histology

Histological evaluation of retinal cryosections was also performed with hematoxylin and eosin (H & E) to investigate changes in the outer retina associated with photothermal laser exposure. As expected, the majority of the perturbations in the retina were located in and around the RPE. Disruption in the continuity of the RPE monolayer, fragments of RPE cells and infiltrating cells were all observed at the site of injury (Figure 6-23). Cryosections from adjacent retinal areas appeared unaffected by the laser exposure and maintained the typical layered organization. Epifluorescence imaging of cryosections stained with DAPI exhibited similar features in the outer retina, particularly the RPE, and appeared to have small focal regions of heightened eGFP signal within the laser lesion locations (Figure 6-24). Both the H & E stained cryosections and the DAPI stained cryosections were obtained within 24 hours of laser exposure to observe acute changes in retinal morphology.

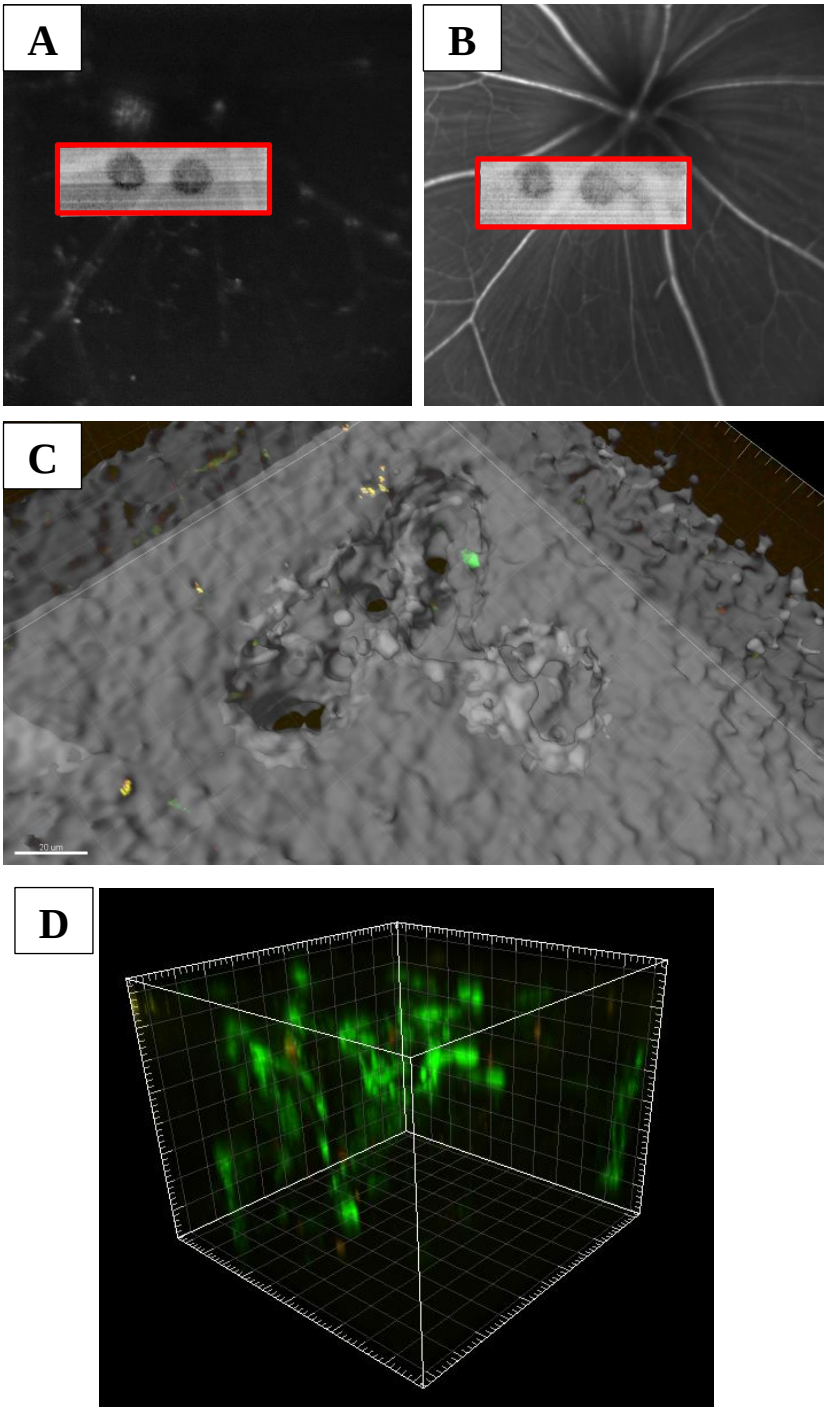

Figure 6-22. *En face* SD-OCT projections from a laser exposed mouse retina simultaneously acquired with **(A)** fluorescence SLO to detect eGFP expression **(B)** reflectance SLO [Red rectangles represent the volumetric OCT scan area encompassing two discrete lesions]. **(C)** 3-D rendering of the volumetric data from the MPM imaging sets depicting the voids in the retinal tissue caused by the photothermal damage. (D) 3-D reconstruction of the eGFP fluorescence signal using MPM.

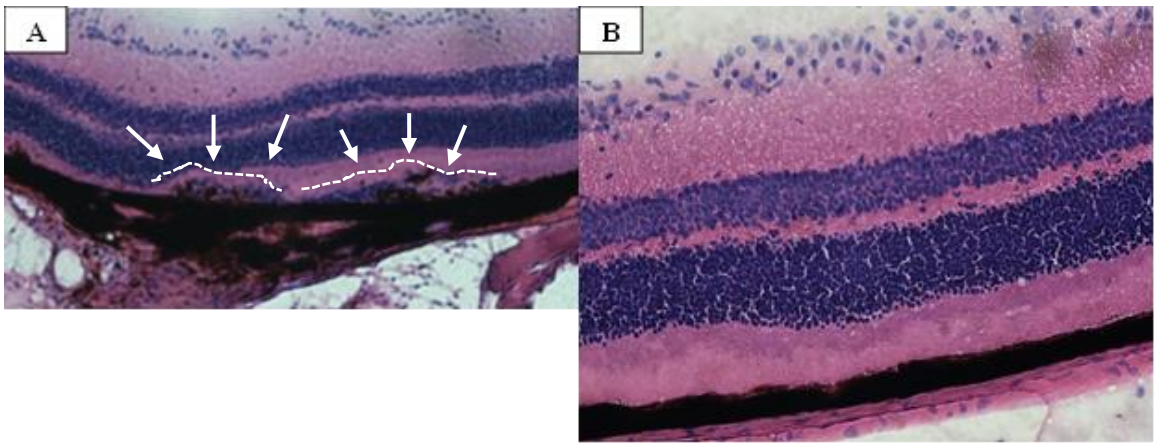

Figure 6-23. H & E staining of the mouse retina. **(A)** Two adjacent laser lesion sites were visible in the retinal section. This animal was sacrificed 8 hours after receiving 4 retinal exposures. The arrows identify the mottling observed along the RPE and the infiltrating cells stained in blue immediately above the RPE monolayer. **(B)** A naïve age-matched mouse was used as a control for comparison with normal retinal architecture.

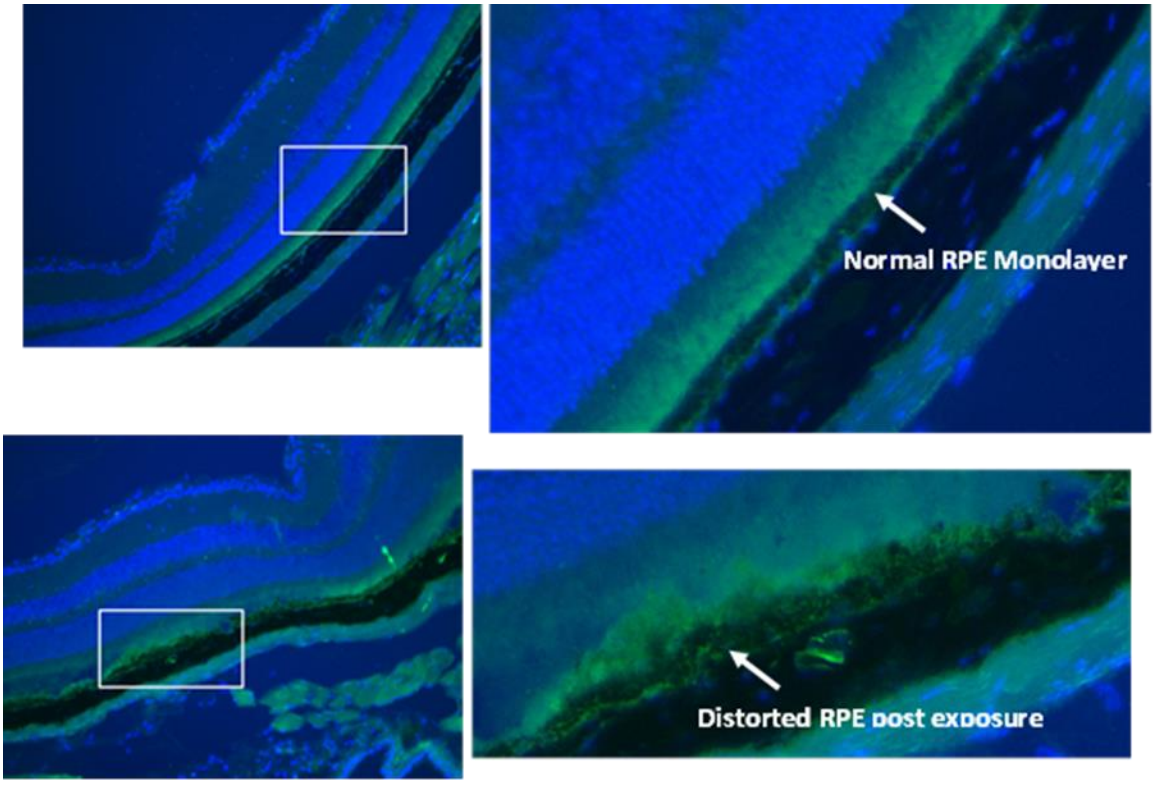

Figure 6-24. Cryosections of the cis-NF-kB^{EGFP} mouse retina. **(Top)** Naïve mouse exhibiting normal retinal structure. **(Bottom)** Distorted RPE and photoreceptor morphology following photothermal exposure to the retina. (Blue – DAPI stained nuclei; Green – eGFP)

6.4 Discussion

In the present study, two non-invasive retinal imaging techniques, cSLO and SD-OCT, were applied to investigate the response to local photothermal injury in a transgenic mouse model. The eGFP reporter gene provided an opportunity to directly visualize the upregulation of NF-κβ in response to low dose photothermal laser exposure. Multiple laser exposure powers were used to demonstrate variability in the molecular expression and morphological perturbations in the outer retina. The spatial and temporal profiles of both molecular and morphological biomarkers were evaluated.

The delayed response observed in the eGFP fluorescence reflects a gene response model of rodent retinal injury recently proposed by Vazquez-Chona et al.(258) The early response to injury included the upregulation of numerous transcription factors, including NF-κβ (p65). Following the early phase, a general inflammatory reaction that lasts for days includes damaged cells releasing pro-inflammatory cytokines and migration of Müller cells to the site of injury. Inflammation generally resolves within the first week as the chronic stage of wound healing begins. During this late phase, Müller glia remain active in the structural remodeling of the damaged tissue(259). These findings are consistent with the observed eGFP fluorescence in the Müller cells visualized using confocal LSM and MPM in fixed tissue samples. The proposed timeline was also consistent with the *in vivo* fluorescence signals and volumetric SD-OCT data.

Although the eGFP response appeared to be highly sensitive to light-induced retinal injury, it is unknown whether the continued presence of eGFP fluorescence is truly indicative of prolonged NF-κβ upregulation and inflammation. An attempt was made to quantify the expression at multiple time points based on western blots but the small

amount of tissue available from the mouse retina coupled with the relatively small regions of light induced damage did not yield significant results when compared with naïve mice. Similarly, it is debatable whether different classes of laser exposure (i.e. threshold vs. suprathreshold) yield measurable differences in fluorescence expression. Recent analysis by our collaborators demonstrated a significant correlation, albeit weak ($r = 0.29$, $P = 0.0017$) between suprathreshold lesion size and eGFP fluorescence in a limited number of mice over 7 days using a mixed model of repeated measures(161). It is likely that additional mice will need to be examined in the future to determine the degree to which this method may be used as an assay to determine upregulation of the transcription factor and overall injury to the retina. Moreover, it would be beneficial to investigate different regimes of laser exposure (i.e. photomechanical and photochemical) and additional wavelengths to assess changes in the spatial and temporal upregulation of NF-κβ based on these parameters.

In addition to the *in vivo* imaging studies, we also examined excised retinal tissue using immunohistochemistry and multiple microscopy techniques including confocal laser scanning, multiphoton (MPM) and differential interference contrast (DIC). The *ex vivo* imaging served to validate our *in vivo* imaging data and provided additional information regarding the localization of the eGFP fluorescent reporter in depth. Hematoxylin and eosin staining and immunostaining were also performed on cryosections and flatmounts of the retinal tissue to investigate to role of specific cell types and molecules in response to the laser-induced injury.

The localized degeneration of the photoreceptor cells seen with DIC may be used to investigate additional mechanisms of cell death following retinal injury or chronic

inflammation. The regions of laser exposure were clearly delineated in the photoreceptor mosaic and the remaining cells exhibited altered morphology. In addition to our DIC microscopy findings, recent studies conducted by our collaborators also demonstrated a similar phenomenon using a TUNEL assay to detect apoptotic cells in retinal cryosections following photothermal damage to the mouse retina(260). The apoptotic cells were largely confined to the outer nuclear layer of the retina. Although the assessment of the photoreceptor mosaic was based on *ex vivo* samples, it will likely be possible to conduct similar experiments *in vivo* in the near future with the use of high resolution adaptive optics scanning laser ophthalmoscopy (AO-SLO) and adaptive optics optical coherence tomography (AO-OCT). Novel imaging systems have been designed or modified to accommodate for the higher optical power and smaller size of the rodent eye while correcting optical aberrations from the ocular tissue of rodents to provide *in vivo* images at a cellular level(147, 261-263). Furthermore, recently developed techniques to effectively mount the rodent RPE(264) may provide additional insight into the photothermal injury incurred from the absorption of high energy light by melanin.

NF-κβ has been linked to increased oxidative stress, inflammation, and angiogenesis. All of these features play a prominent role in the pathogenesis of AMD which makes this transcription factor an intriguing target for therapeutic intervention. A recent phase II clinical trial examined the use of a topical compound to inhibit over-expression of NF-κβ in patients with geographic atrophy(265). Based on the 11 patients studied, this intervention demonstrated a significant preservation in visual acuity but failed to effect enlargement of atrophic area, contrast sensitivity, and extension of drusen.

Therefore, the authors of the study concluded the intervention strategy at the given concentration and route of administration only provided a minor benefit.

The data suggest that the focal depth is an important factor to consider with this transgenic mouse model due to the variability of the eGFP expression throughout the retinal tissue. Likewise, the time course of NF-kB upregulation has a substantial impact on the analysis. Current confocal retinal imaging systems are limited based on axial resolution but recent advancements in *in vivo* MPM and adaptive optics would eliminate many of these issues by providing depth resolved fluorescence data with respect to the localization of NF-κβ(223, 225, 226). The combination of MPM and SD-OCT for *in vivo* imaging would provide highly detailed information regarding the fluorescence (both autofluorescence and eGFP) and the structural alterations associated with injury and tissue remodeling in the light-induced degeneration model.

In conclusion, the combination of light-induced retinal degeneration the *cis*-NF-$\kappa\beta^{eGFP}$ transgenic mouse model provided a novel method to examine the spatial and temporal upregulation of NF-κβ and morphological perturbations. The similarities in the progression of the eGFP fluorescence and morphometric assessment of the SD-OCT data suggest that structural remodeling following injury may be closely related to the inflammatory response of the Müller cells in the retina. This model system may be used to investigate a wide variety of degenerative diseases not only in the retina but throughout the CNS as well. The inhibition of specific inflammatory pathways may also provide insight for the development of new targeted therapies to preserve neuronal cells impacted by injury and disease.

Chapter 7: Adaptive Optics Confocal Scanning Laser Ophthalmoscopy (AO-cSLO) in the Human Retina

7.1 Introduction

Adaptive optics (AO) enhanced retinal imaging is becoming a popular method of non-invasively visualizing cellular morphology in the living eye. Currently, these instruments are limited to research applications but are likely to transition to clinical use in the near future. Numerous research groups have visualized cellular features and retinal ultrastructure including the photoreceptor mosaic, retinal pigmented epithelial cells, capillary networks, and retinal nerve fiber bundles. A number of parameters have been explored in healthy volunteers to characterize variability in the normal population based on traits such as axial length(266, 267), eccentricity(266, 268-270), and age(271). Over the past 5 years, there has also been exponential growth in the number of publications implementing high-resolution AO-SLO to study pathology(272). The photoreceptor cells, particularly cones, are among the easiest features to observe using AO-SLO due to their natural waveguide properties which make them highly reflective. However, the small size (~2 μm) and increased packing density of the foveal cones has limited studies directly visualizing these features(273). Generally, analysis is performed on parafoveal cone photoreceptors for better accuracy and reproducibility with respect to metrics such as density and spacing.

The objectives of this study were to (1) characterize high resolution AO-cSLO imaging data using a custom designed instrument in healthy volunteers and (2) develop analytical methodology to quantitate morphological biomarkers in the retina. The

following sections describe the design of the instrumentation, image acquisition parameters, processing methodology, and algorithms for quantitative image analysis.

7.2 Instrumentation Design

A variety of design strategies may be implemented in AO instrument design. The most common designs use a series of spherical mirrors similar to large scale AO telescopes used for astronomy applications(18, 33, 269, 274, 275). Designs favoring lenses in place of spherical mirrors have also been developed which provide some additional benefits, namely the possibility for more compact instrument design(273). The UTMB AO retinal imaging system implements an all reflective design using 7 spherical mirrors. The system was configured with the optical elements arranged on a 2' x 2' breadboard to minimize the footprint of the instrument while incorporating commercially available optics. The design of the imaging beam path transfers images of the pupil or retina to the appropriate conjugates using paired mirrors (i.e. a telescope). A 2-D representation of the optical configuration and the actual layout of the SLO channel are shown in Figure 7-1. The paired mirrors were separated by the sum of their focal lengths (*f-f*) and the associated magnification was determined by the ratio of the focal lengths. The final unpaired spherical mirror was configured in an *f-2f* relay which contained both pupil and retinal conjugates. The scanning galvanometers, Hartmann-Shack wavefront sensor (HS-WS), and deformable mirror (DM) were all placed at pupil conjugates to effectively sample and correct the wavefront at the pupil of the patient. The magnification of the beam through the system yielded a final beam diameter of 7 mm, which is the approximate diameter of a dilated pupil in patients. The AO control software and associated electronics are located on an additional cart and relayed to optical table.

A custom SLO timing board was used to generate the pixel clock, line sync, and frame sync signals. Additionally, the timing board was responsible for driving the imaging galvanometers and automatically de-warping the SLO images caused by the sinusoidal resonant scanner (RS). The RS (Electro-Optical Products Corporation (EOPC), Ridgewood, NY) operates at a frequency of 12 kHz and provides the fast horizontal scans and slow offsets which permit larger scan areas to be acquired by directing the raster scan to follow a predefined pattern.

The imaging and sensing light source is an 830 nm superluminescent diode (SLD, Superlum, Moscow, Russia) with a bandwidth of 62 nm (Figure 7-2). Utilizing the same light source for both imaging and sensing helped to maintain a small footprint for the system, minimized optical alignment issues, and eliminated the possibility of wavefront correction errors due to chromatic shifts (i.e. longitudinal chromatic aberration (LCA)). The HS-WS used a lenslet array (SussMicroOptics, Neuchatel, Switzerland) and a CCD camera (Uniq Vision Inc., Santa Clara, CA) to sample the wavefront error across the pupil. The focal length of the lenslet array (18 mm) was selected to be compatible with off the shelf optics while providing suitable sensitivity and dynamic range to image a wide variety of patients in a clinical setting. An iris was also placed in front of the lenslet array to block diffuse reflections backscattered from the cornea.

The cSLO component used a confocal pinhole and an avalanche photodiode (APD, Hamamatsu, Japan) to collect the light reflected or backscattered from the retina. The total power of the light, measured at the cornea, was routinely measured and maintained below 500 μW to ensure compliance with safety standards(276). Low light levels reflected from the fundus are difficult to detect even with state-of-the-art sensing

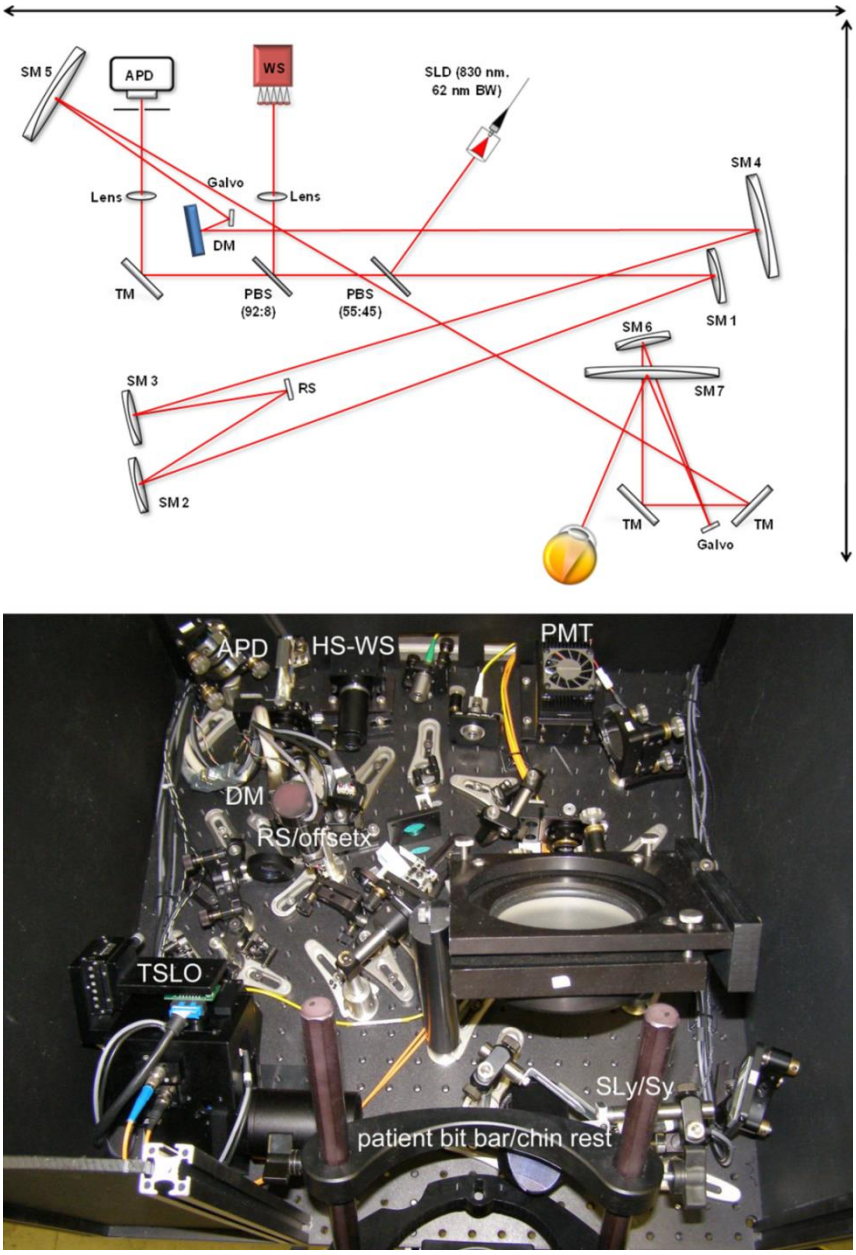

Figure 7-1. (Top) Cartoon diagram of the AO-SLO beampath including all of the optical and sensing elements. *The flattened 2-D representation is not to scale. (Bottom) Actual configuration of all elements arranged on the 2' x 2' optical breadboard.

elements like avalanche photodiodes (APD) and photomultiplier tubes (PMT). There is also a need to minimize the amount of light delivered to the retina to mitigate the risk of adverse effects from phototoxicity. Achieving a balance between the power of the illumination source and the detector sensitivity is a fundamental component of any AO

system design. A comparison of high resolution, small FOV SLO images with and without adaptive optics correction is shown in Figure 7-3. The accompanying wavefront sensor display and wavefront error maps are also shown. The pinhole diameter was adjustable (25 – 400 μm diameter) by manually changing the size to reject out of focus light from the retinal plane based on the desired experimental conditions.

Generally, the larger confocal pinholes (200 and 400 μm) were used for imaging patients with dim fundus reflectance or undilated patients. Smaller pinholes yielded better contrast but this came at the expense of collection efficiency of the backscattered photons. A large-stroke, 50 μm, deformable mirror with 52 actuators (Imagine Eyes Mirao 52-d, Orsay, France) was used to correct distortions in the wavefront. Videos were recorded at a rate of 12 frames per second (fps) in sequences of approximately 10-30 seconds for each retinal location and saved as 8-bit .avi files for further processing. Each SLO image in the video sequence was collected at 1024 x 1024 pixel resolution and an estimated optical resolution of approximately 2.5 μm.

The custom control software for the electronic components and active AO correction were developed by Physical Sciences, Inc. (Andover, MA). Each module was independently controlled through a graphical user interface (GUI) in LabVIEW (National Instruments Corporation, Austin, TX).

Patients were positioned relative to the beam path to align the pupil with the incident light source. A chin rest and forehead rest provided the appropriate angular alignment while a micrometer controlled 3-axis stage was used to guide the fine position thereby aligning the center of the patient's pupil. The custom position for each patient was documented to enable easier realignment during subsequent imaging sessions.

Fixation was maintained using an 8 x 8 array of LED lights. Each LED could be selectively illuminated to steer the patient's fixation and raster scan specific regions on the retina.

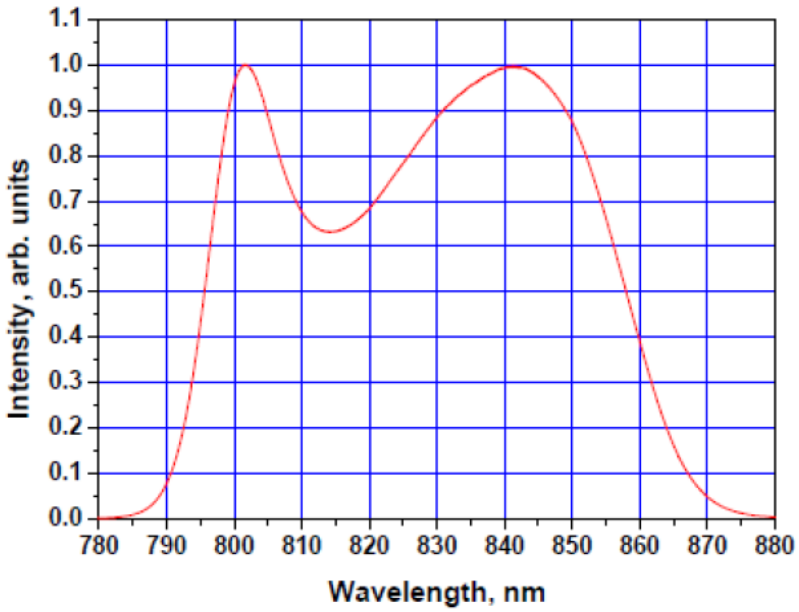

Figure 7-2. Spectrum for the Superlum SLD used for wavefront sensing and reflectance image acquisition.

7.3 Image Processing Methods

Distortions in retinal images are a common source of error which can have a negative impact on registration. Despite a patient's best efforts, there is always at least a small degree of motion when acquiring images of the retina on such a small scale. Three of the most common sources of image distortion are saccades, blinking, and focal alignment which are depicted in Figure 7-4. For each video sequence, a frame-by-frame assessment of the data was performed to eliminate images exhibiting extensive distortions or suboptimal quality. These features were particularly prominent in patients with impaired vision caused by ocular pathology but were also common in young healthy

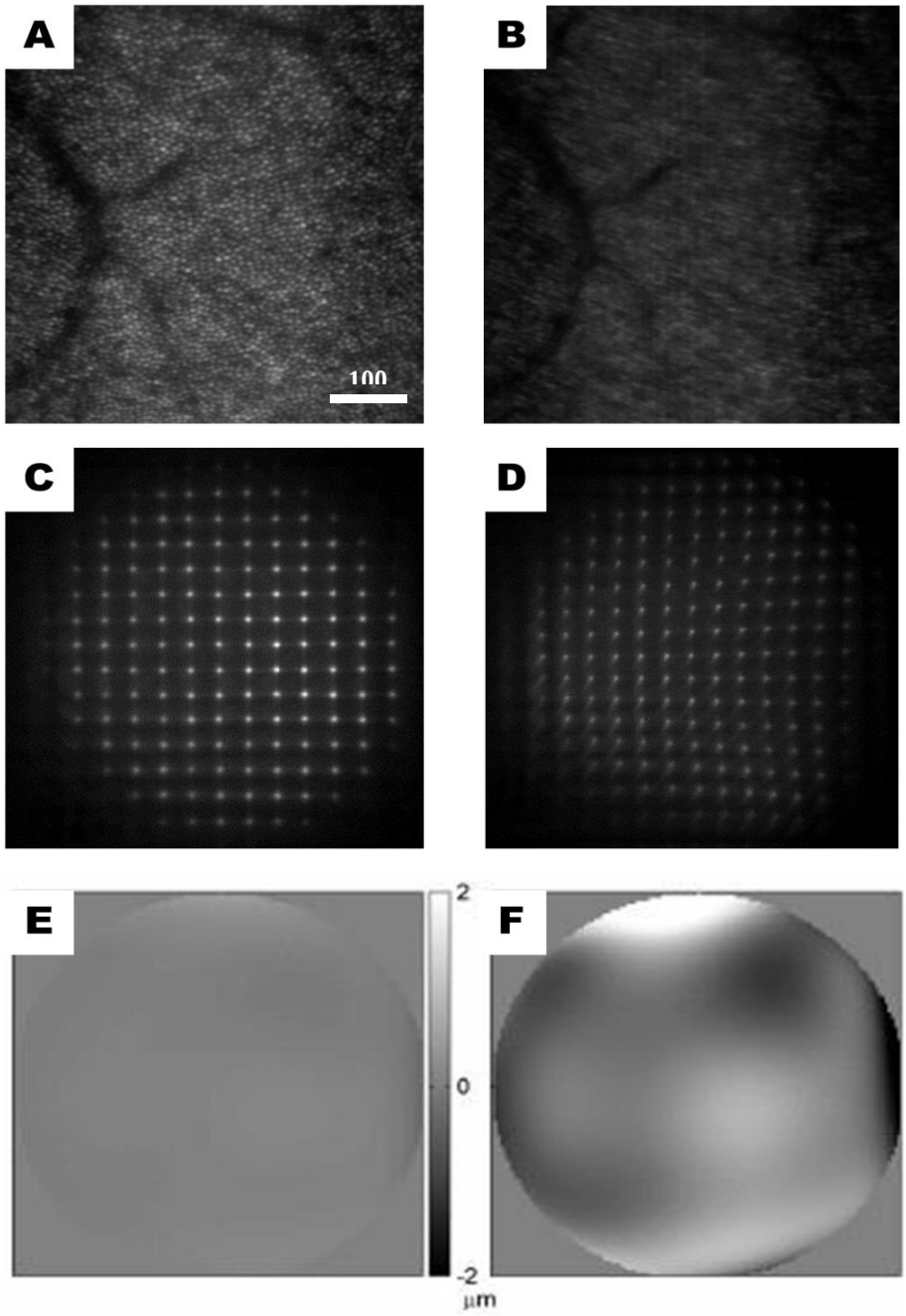

Figure 7-3. High resolution, 1.5° x 1.5° (~435 µm x 435 µm) field of view SLO image of a healthy emmetrope with (A) adaptive optics closed loop correction on and (B) corresponding image without AO correction. (C) Corrected wavefront (D) original wavefront sampling of ocular aberrations without correction. Wavefront error maps for the corrected (E) and the native (F) images depicting the magnitude of the wavefront error. With the closed loop correction active, minute features are easily discernable due to the increased brightness and contrast of each image.

volunteers. In general, the elimination of extensive motion artifacts improved the overall image quality for subsequent image processing steps.

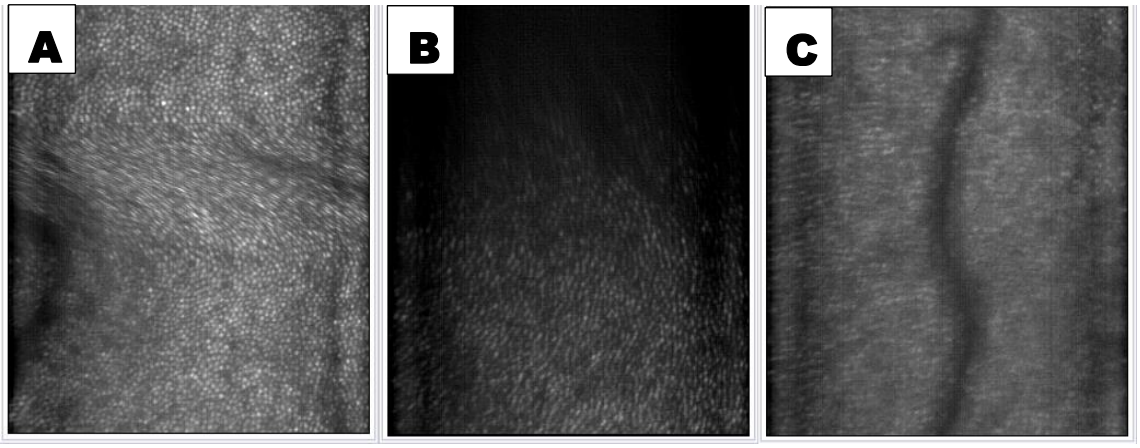

Figure 7-4. Examples of imaging artifacts due to (A) saccades, (B) blinking and (C) focal alignment. Each frame was removed from the data set prior to registration and averaging.

7.3.1 Image Registration

A variety of registration techniques have been described in the literature but there is no universally accepted methodology for AO-SLO image sequences. Much of this variability arises from the differences in the methods used in data acquisition and acquisition speed. Perhaps the most commonly cited technique involves selecting a template image and subsequently matching the remaining images based on predefined descriptors, generally local intensity minima and maxima. This method can be further improved by dividing each image into blocks or subsets which help account for intra-frame motion(277, 278).

We employed a method developed by Saalafeld *et al.*(279) which is freely available as a plugin for ImageJ (Wayne Rasband, NIH, Bethesda, MD). The program was originally developed to register 3-D data sets of electron microscopy but we found that the robust feature identification and registration pairing is also well suited for AO-

SLO image sequences. The basis of this registration technique is the Scale Invariant Feature Transform (S.I.F.T)(280) which identifies unique features in each frame and performs a cross-correlation among successive frames to align the data set (Figure 7-5). Variations on the S.I.F.T. registration technique have also been demonstrated by other groups in the context of high resolution retinal imaging(281, 282). A combination of transformations was also used to accommodate for different types of motion. In general, rigid transformations were used to account for inter-frame motion due to bulk movements and affine transformations were used to account for intra-frame motion. Following the registration stage of the video sequences, the images were averaged to improve the

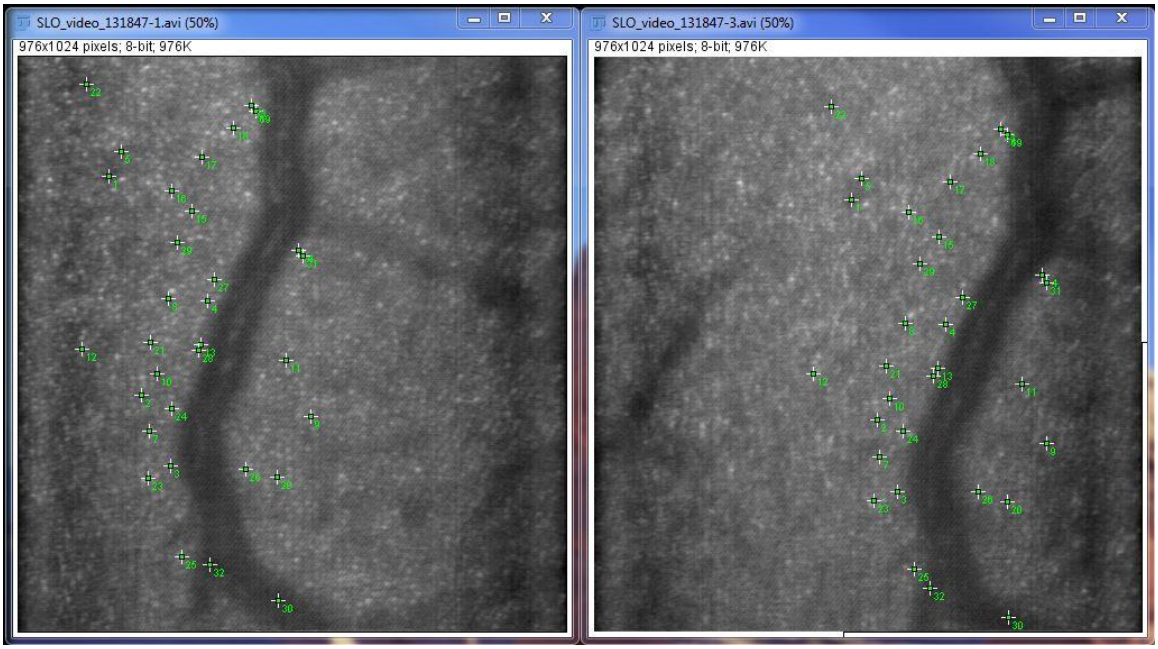

Figure 7-5. Sequential frames from an AO-SLO video demonstrating lateral motion. The S.I.F.T. registration method was able to identify features in each frame and perform cross-correlation of these structures to align images in each data set.

overall signal to noise ratio and make features more discernable. Ten to twenty registered images were typically averaged for each retinal location. The resultant improvements in SNR can be seen in Figure 7-6. When available, larger mosaics were also reconstructed

by stitching averaged images together with Adobe Photoshop (Adobe Systems Inc., Mountain View, CA) to create a composite of the photoreceptor morphology throughout the macula. A mosaic of averaged images from the parafoveal retina of a healthy volunteer is shown in Figure 7-7.

7.4 Image Analysis Methods and Results

Although the processing steps are an important part in obtaining high quality images, it is still necessary to establish quantitative metrics to analyze the imaging data. The identification of clinically relevant parameters is vital in transitioning new diagnostic and therapeutic devices to widespread clinical use. The ability to image individual cells *in vivo* provides a unique opportunity to characterize the variability of anatomical parameters within individual patients and among larger populations. This information may be used to help distinguish irregularities which are indicative of pathology.

The most common analytical metrics for AO-SLO images involve the photoreceptor cells because they are among the easiest features to detect and play a key role in the transduction of visual signals. Photoreceptor density, spacing, and packing arrangement are quantitative benchmarks commonly cited in the literature. A variety of methods may be used to extract these features from high resolution images. The following sections detail the custom applications designed at UTMB to quantitative assess the cone photoreceptor cells.

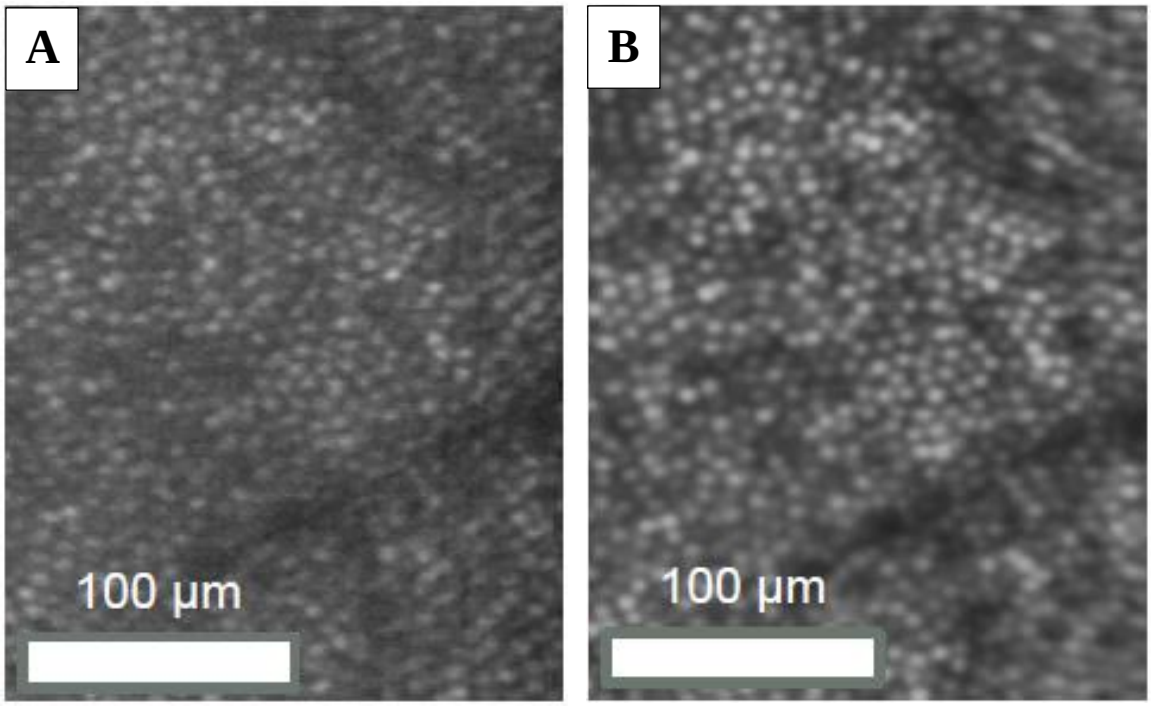

Figure 7-6. Improvements in image quality from registration and averaging aligned frames **(A)** Raw image obtained with AO-cSLO **(B)** Average of 20 frames from the same retinal location demonstrating an improved signal-to-noise-ratio.

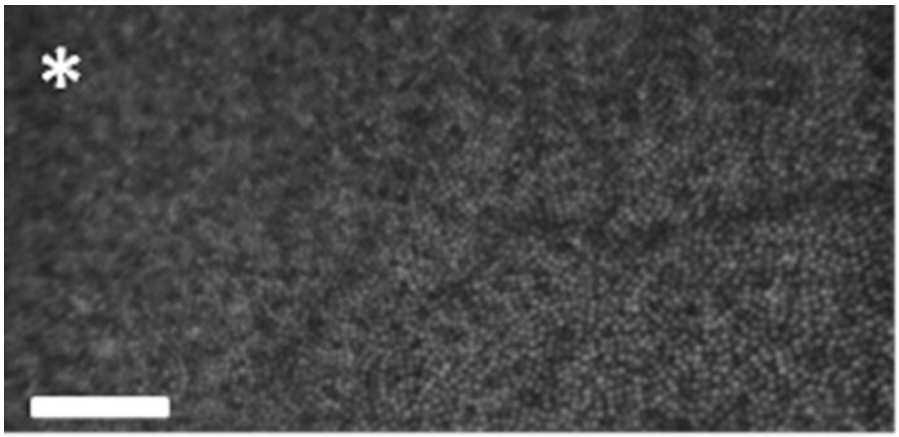

Figure 7-7. Cone photoreceptor image (2° x 1°, ~0.58 mm x 0.29 mm) acquired from a healthy volunteer using the AO-SLO at the University of Texas Medical Branch. The cone photoreceptors immediately adjacent to the fovea exhibit normal packing density and show no signs of disruption [Scale bar = 0.1mm, asterisk marks the center of the fovea] *Figure modified from Boretsky et al. 2012*

There are numerous challenges in developing quantitative algorithms and analytical techniques for AO-SLO data. First, the retina is densely populated with millions of photoreceptor cells which require automated methods to thoroughly characterize morphological parameters. Alternative methods include sparse sampling throughout the retina and manual identification of features, but these processes are time consuming and rely heavily on interpolation of the data. Second, the reflectivity of individual photoreceptors may be variable depending parameters such as on the incident angle of the incoming light(283) and the turnover of photoreceptor outer segments(284, 285). To account for these variables, it is necessary to evaluate metrics like spacing, density and packing arrangement in multiple regions and assess local changes with respect to retinal eccentricity.

7.4.1 Photoreceptor Identification

We employed a Laplacian of Gaussian (LoG) technique which combines a Laplacian derivative filter and a Gaussian smoothing filter to identify the photoreceptor cells in each image. The Gaussian filter was first used to smooth the image thereby reducing background noise and minimizing false positive identification of features. The Laplacian derivative filter was then used to identify edges caused by a sharp transition in local intensity values. The *LoG* filter may be represented mathematically using the following equation:

$$LoG(x,y) = -\frac{1}{\pi\sigma^4}\left[1 - \frac{x^2+y^2}{2\sigma^2}\right]e^{-\frac{x^2+y^2}{2\sigma^2}}$$

We also applied a technique described by Byun *et al.*(286) to help expedite the calculation by providing an approximation of the cell size and spacing prior to the

calculation. Threshold intensity values were also set to minimize the detection of erroneous extrema. This step was often necessary to eliminate features such as blood vessels which may exhibit reflections at the surface. The centroid of each photoreceptor identified in the images was reduced to a single point and the coordinate locations were saved. Once the location of each photoreceptor was mapped, an overlay of each position was applied to the original image. This served as a final quality control step in which cells that were not identified in the automated detection were manually added or false positive identification of cells were removed before further analysis. Based on the orientation of the identified photoreceptors, Voronoi diagrams were generated as a geometric representation of the relationships among neighboring cells (Figure 7-8).

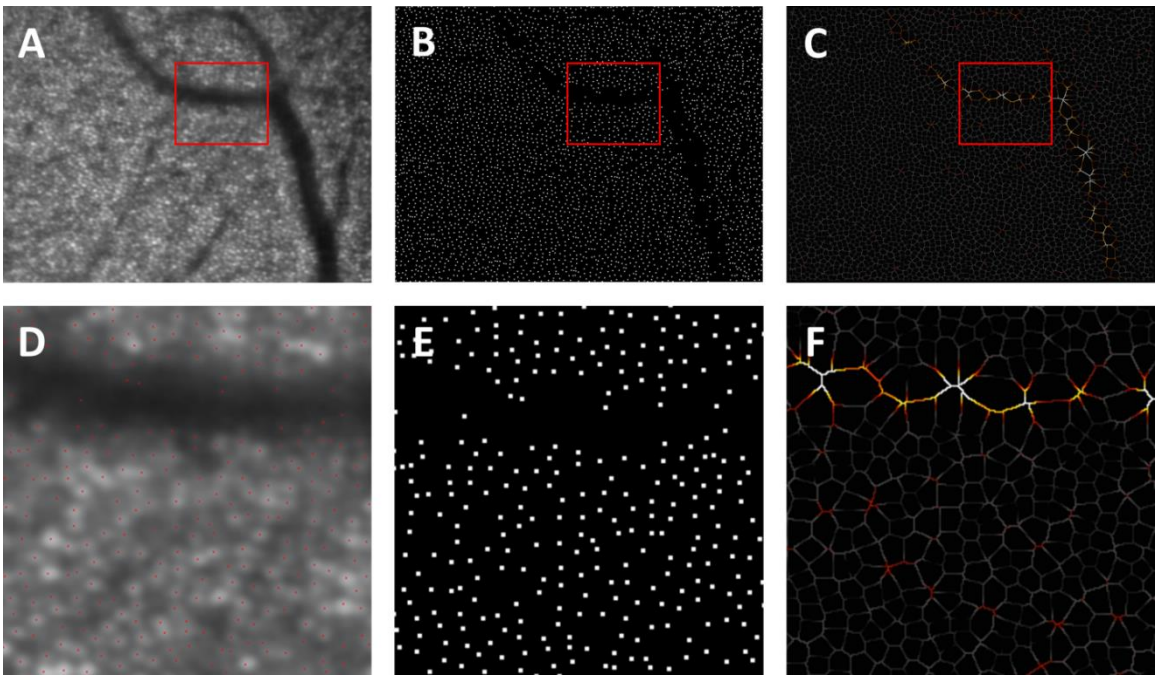

Figure 7-8. Identification of cone photoreceptor cells in high resolution AO-SLO images (A, D) Averaged imaging frame of the parafoveal cone mosaic in a healthy volunteer measuring 2° x 1.5° (B, E) Location of the centroid for each cone photoreceptor cell. (C, F) Voronoi diagram depicting the relationships among neighboring cells. D, E, and F provide an enhanced view of the image details in the 0.5° x 0.5° subsets outlined in red.

7.4.2 Photoreceptor Density Measurements

Once the cone photoreceptors were identified, the images were divided into smaller regions of interest (ROIs). Each ROI had a specified area which enabled us to calculate the local photoreceptor density and represent this value in the conventional term of Cones/mm^2. The ROI size was user defined so it could be modified to suit any particular study. Analysis of the photoreceptor density measurements based on the ROI size was performed using data from healthy volunteers to identify the appropriate conditions for our system. This allowed us to compare our findings with similar imaging studies utilizing AO instruments(271) and earlier microscopy studies of post mortem donor tissue(287, 288).

The semi-automated density measurements were compared to the "gold standard" method of manually counting each cell. Obviously, the manual counting approach would be prohibitive on a large scale due to the amount of time it would take to analyze each image so a fully automated method would be preferable. We evaluated 22 images from healthy volunteers to test both methods. A few of these images are shown in Figure 7-9. Each image represented a 0.5° x 0.5° FOV (~145 μm x 145 μm) from various parafoveal locations. A comparison of both methods is shown in the Bland-Altman plot in Figure 7-10. For this plot, the x-axis represents the mean value of the two measurement methods while the y-axis represents the difference between the two methods. The solid line is the linear regression plot of the data set and the dashed lines signify the 95% confidence interval (95% CI = 1.96*SD). In general, the difference between the cone counting methods was less than 10% for a given area, but excessively dark or noisy images yielded

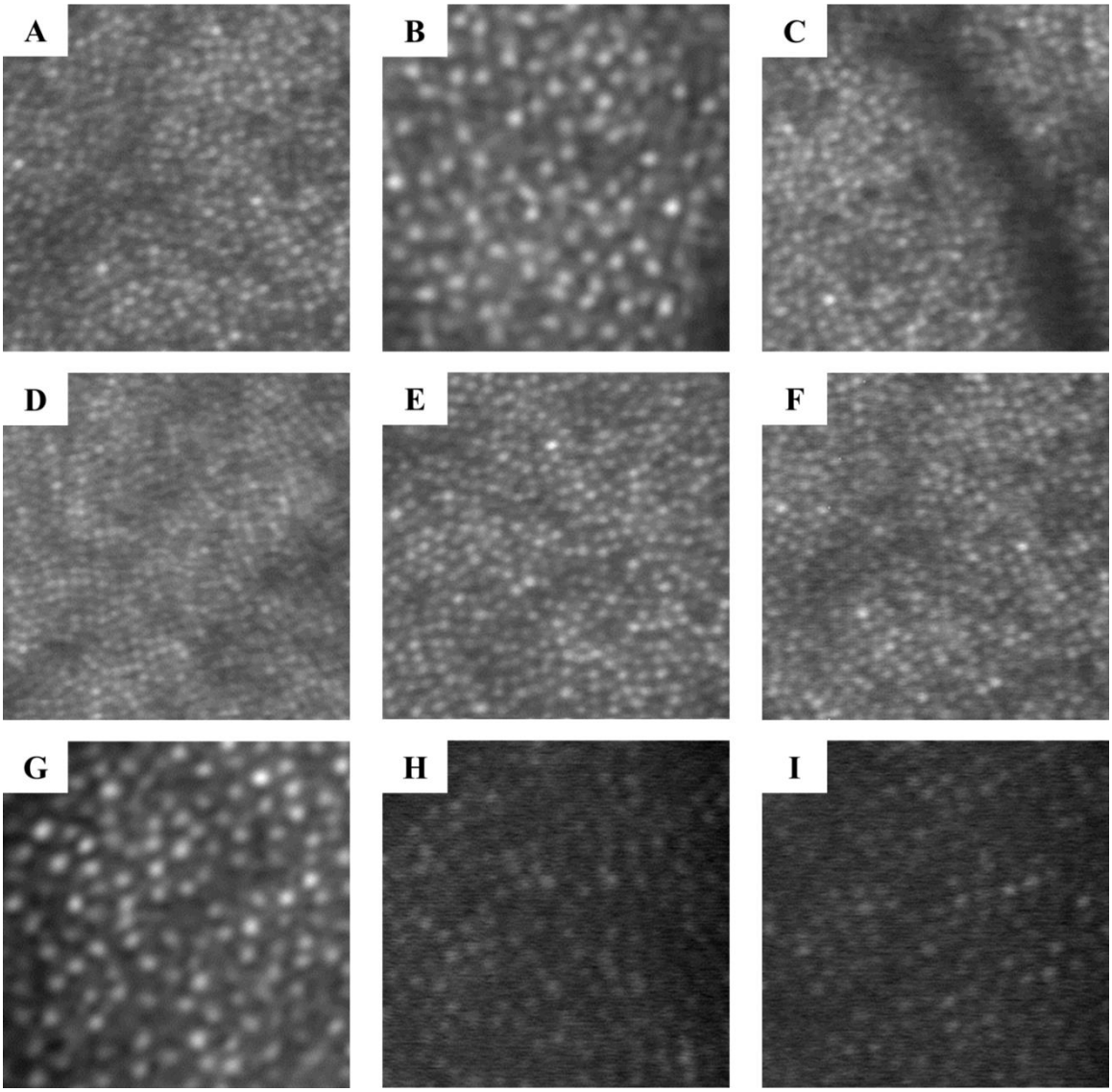

Figure 7-9. *In vivo* AO-cSLO images from 3 healthy volunteers depicting variable photoreceptor density based on retinal eccentricity and image intensity. Each image represents a video frame cropped to 0.5° x 0.5°. Comparative analysis of the manual cone counting method and the semi-automated LoG algorithm was performed to assess the agreement between methods.

poorer results due to the presence of ambiguous features. The data analysis, regardless of methodology, appeared to be highly dependent on the initial image quality.

In addition to identifying the photoreceptor cells in a given image, we tested the variability in density measurements based on the size of the ROI selected by the user. For

flood illuminated AO fundus cameras, the size and orientation of the sampling window can have a significant impact on photoreceptor density and spacing measurements(289). The region selected for analysis was adjacent to the fovea (*parafoveal*) where cone packing density is relatively high but decreases exponentially as a function of eccentricity. This permitted us to evaluate a wide range of density values over a small area (2° x 2° FOV). In Figure 7-11 the same image was analyzed using 5 different sampling window sizes to demonstrate the influence of sampling window on the density measurements.

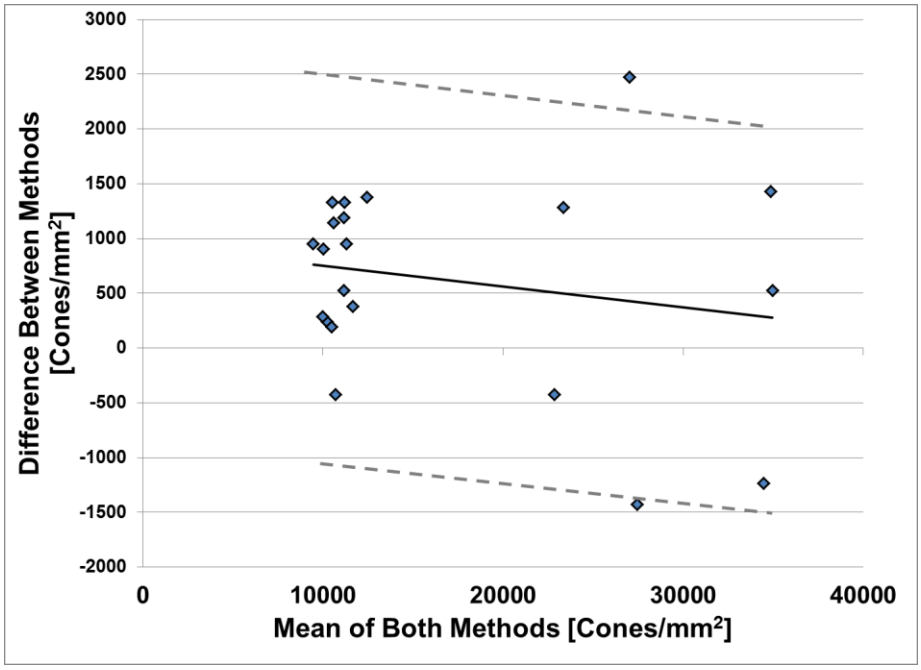

Figure 7-10. Bland-Altman plot showing the agreement between parafoveal cone density values in healthy volunteers counted manually vs. the semi-automated LoG technique. The x-axis represents the mean of both methods while the y-axis portrays the difference between the methods. The dashed lines represent the 95 % confidence interval for agreement between both methods.

An additional test was performed on an image of the peripheral (*perifoveal*) cone mosaic to determine the variability in a region where the density values were not expected to vary more than 10-20% based prior AO-SLO(266, 270, 271, 290) and histological studies(255, 288). Box-and-whisker plots for the density distribution of the parafoveal and perifoveal images based on sampling window are shown in Figure 7-12. Regions with zero photoreceptor counts were found in the analysis of the perifoveal image when the ROI size was limited to 16 x 16 or 32 x 32 pixels. This indicated an undersampling error which was dependent on the analytical window size. A summary of the mean density values, standard deviation and undersampling percentage is displayed in Table 7-1.

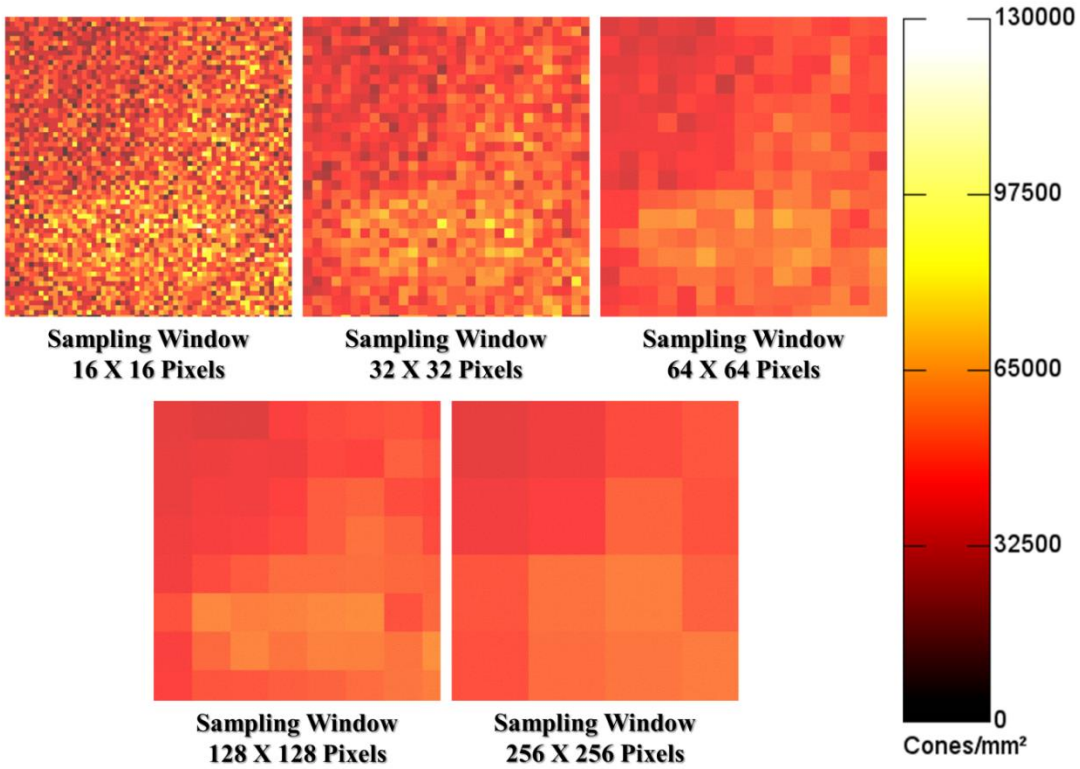

Figure. 7-11. Analysis of sampling window size on photoreceptor density counts on a 2° x 2° parafoveal AO-SLO image from a healthy volunteer.

Photoreceptor density is a useful method of quantifying the cone mosaic which is why it has been used as a fundamental metric to assess AO-SLO images in numerous studies. However, density measurements must be interpreted with caution since they can vary substantially based on the type of imaging system used to acquire the data, the method of identifying photoreceptors and the overall quality of the images. Inter-subject variability of up to 20% has been documented within 10° of eccentricity from the fovea(266, 268, 271, 290). Recent studies have also described abnormalities in the photoreceptor mosaic despite density measurements within the accepted normal range (291, 292).

Additionally, density measurements may be skewed by the presence of retinal vasculature which obscures reflectance from the photoreceptors. This results in an underestimation of the true cell count and potential false positive indication of pathology. Rod photoreceptors may also be misidentified as cones which would provide an overestimation of the cell count. Current research is underway to help discriminate between different photoreceptor types(293) (i.e. rods versus cones), which is of particular interest in diseases such as rod-cone dystrophy and age-related macular degeneration.

7.4.3 Photoreceptor Spacing Measurements

Photoreceptor spacing represents a more conservative assessment of the cell population and may therefore be used to complement the density analysis. Based on the photoreceptor locations that were previously mapped, we were able to perform Delaunay triangulation to determine the center-to-center spacing of neighboring cells and calculate the mean spacing for a given ROI. The Delaunay triangulation method determines spatial

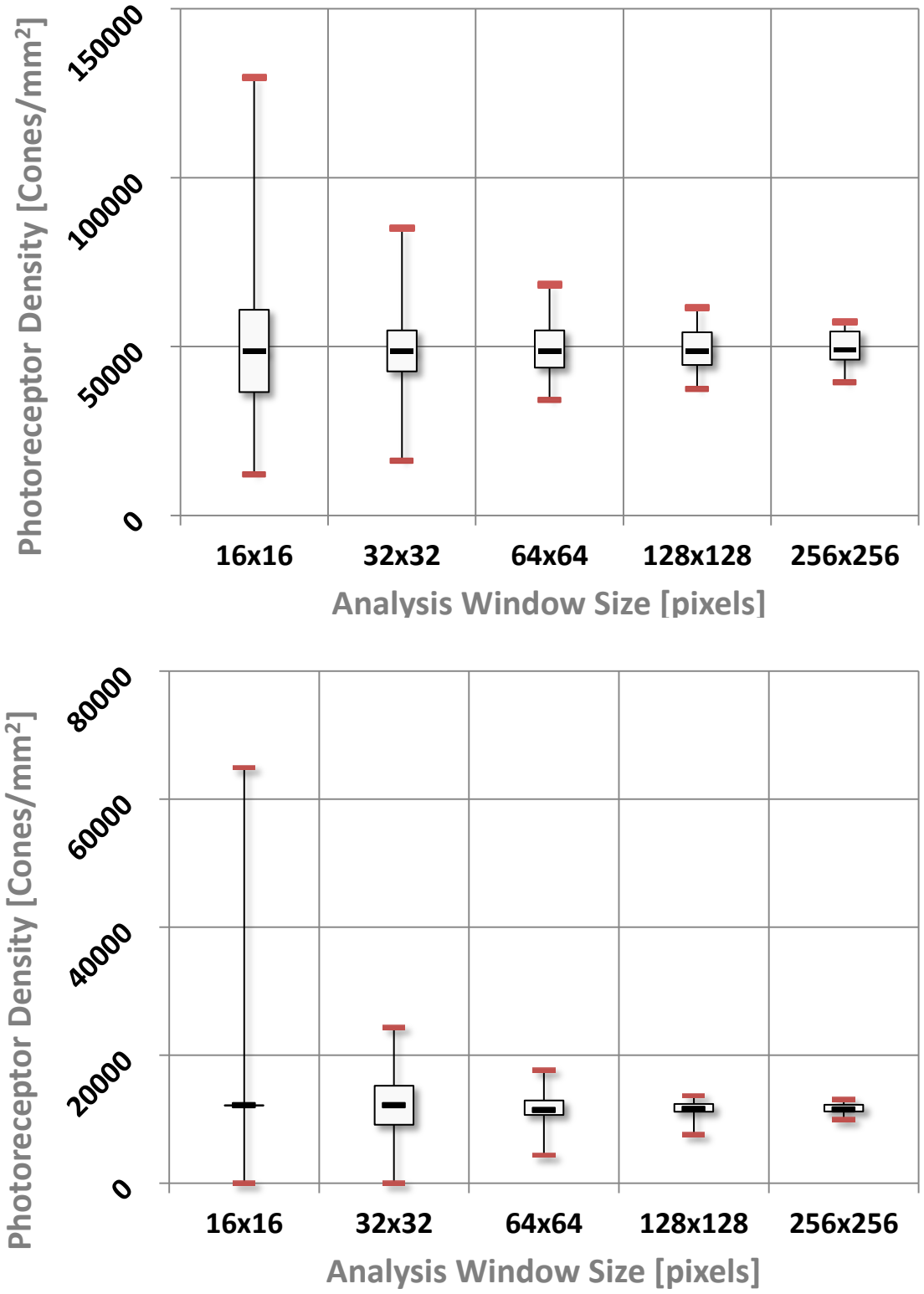

Figure 7-12. Box and whisker plot of the photoreceptor density distribution based on sampling window size in *(Top)* parafoveal region *(Bottom)* perifoveal region.

Table 7-1. Analysis of sampling window size

	Sampling Window [pixels]	Mean ± SD	Minimum Count	Maximum Count	Undersampling [% of total ROIs]
Parafoveal Cone Mosaic	16 x 16	49362 ± 17234	12176	129877	-
	32 x 32	49181 ± 10353	16235	85232	-
	64 x 64	49274 ± 7221	34245	68490	-
	128 x 128	49409 ± 6346	37479	61692	-
	256 x 256	49463 ± 5745	39477	57360	-
Perifoveal Cone Mosaic	16 x 16	11620 ± 7942	0	36528	22.7
	32 x 32	11730 ± 3447	0	24352	0.42
	64 x 64	11547 ± 2187	4428	17711	-
	128 x 128	11588 ± 1293	7645	13698	-
	256 x 256	11651 ± 877	10005	13127	-

Mean ± SD, Min and Max values are in Cones/mm^2

orientation by creating a circumcircle from the 3 vertices of a triangle such that no additional points lie within the circumcircle. An illustration of Delaunay triangulation and the related Voronoi diagram is shown in Figure 7-13. This method limited overestimation of the spacing between cells by maximizing the minimum angle of each triangle.

Additionally, measuring the center-to-center distance eliminated the need to delineate each cell boundary to measure the gaps between cells.

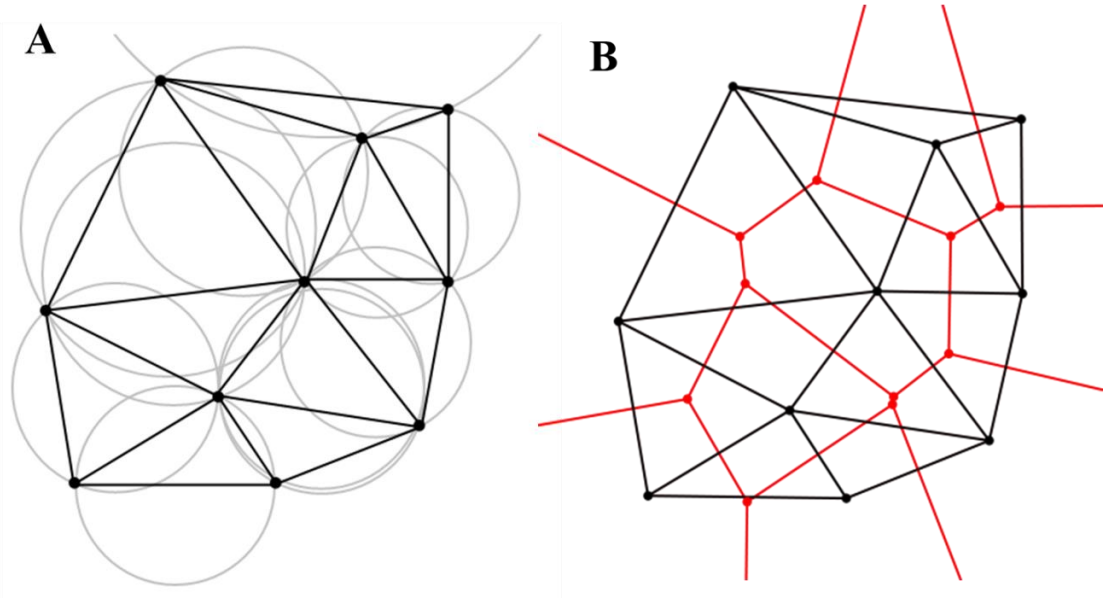

Figure 7-13. (A) Depiction of Deluanay Triangulation with a random array of points. The Euclidian distance between points forms the vertices of the triangles. The circumcircles are shown in gray. **(B)** Illustration of the relationship between Delaunay Triangulation and the corresponding Voronoi diagram shown in red.

The ROI size selected for analysis of both density and spacing measurements was matched to provide complementary information regarding the morphology of the photoreceptor mosaic. As stated previously, each method has its own strengths and weaknesses so the graphical representations for each measurement strategy served to balance the interpretation of the data and provide complementary views. Prior studies have demonstrated that sampling windows larger than 60 x 60 µm provide a more comprehensive assessment of local photoreceptor density, spacing and packing arrangement (270, 289, 292, 294) We selected image subsets of 0.25° x 0.25° (~73 x 73 µm), which is consistent with these previously published reports (Figure 7-14).

Moreover, this allowed us to investigate local perturbations in the context of larger scan areas, including regions which appeared morphologically normal.

Alternate methods of calculating the average cone spacing have also been described in the literature. For example, Lombardo *et al.*(270) labeled the coordinate locations of the photoreceptors and calculated the center-to-center cone distance (Inter-cone distance, ICD) based on the formula:

$$ICD = 1000\left[\frac{2}{\sqrt{3}D}\right]^{1/2}$$

where D represents the photoreceptor density measured in cones/mm^2. This method works under the assumption that the cones are arranged in a hexagonal pattern. However, only approximately 35-50 % of the cones may be found in this orientation, depending on retinal eccentricity. Our approach does not make this assumption in the calculation of the mean spacing so is therefore less prone to bias based on eccentricity-dependent changes in density.

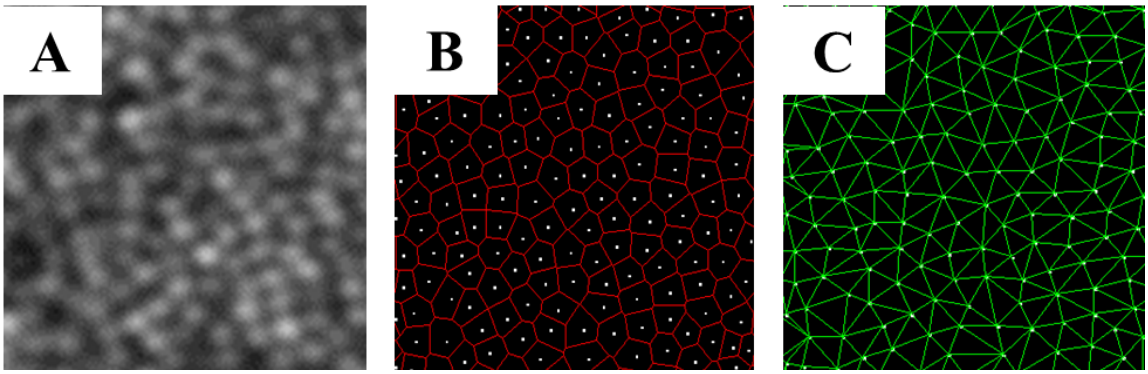

Figure 7-14. (A) Enhanced view (0.25° x 0.25°) of the perifoveal cone photoreceptors **(B)** Voronoi diagram with the centroid of each cell mapped **(C)** Delaunay triangulation based on the coordinates of the cones used to measure center-to-center spacing.

The relationship between the density and spacing measurements along the nasal-temporal axis is shown in Figure 7-15. For cone density and spacing measurements,

retinal eccentricity is referenced with respect to the anatomical fovea of each patient. This enabled us to compare groups of patients based on a common scale of degrees of arc

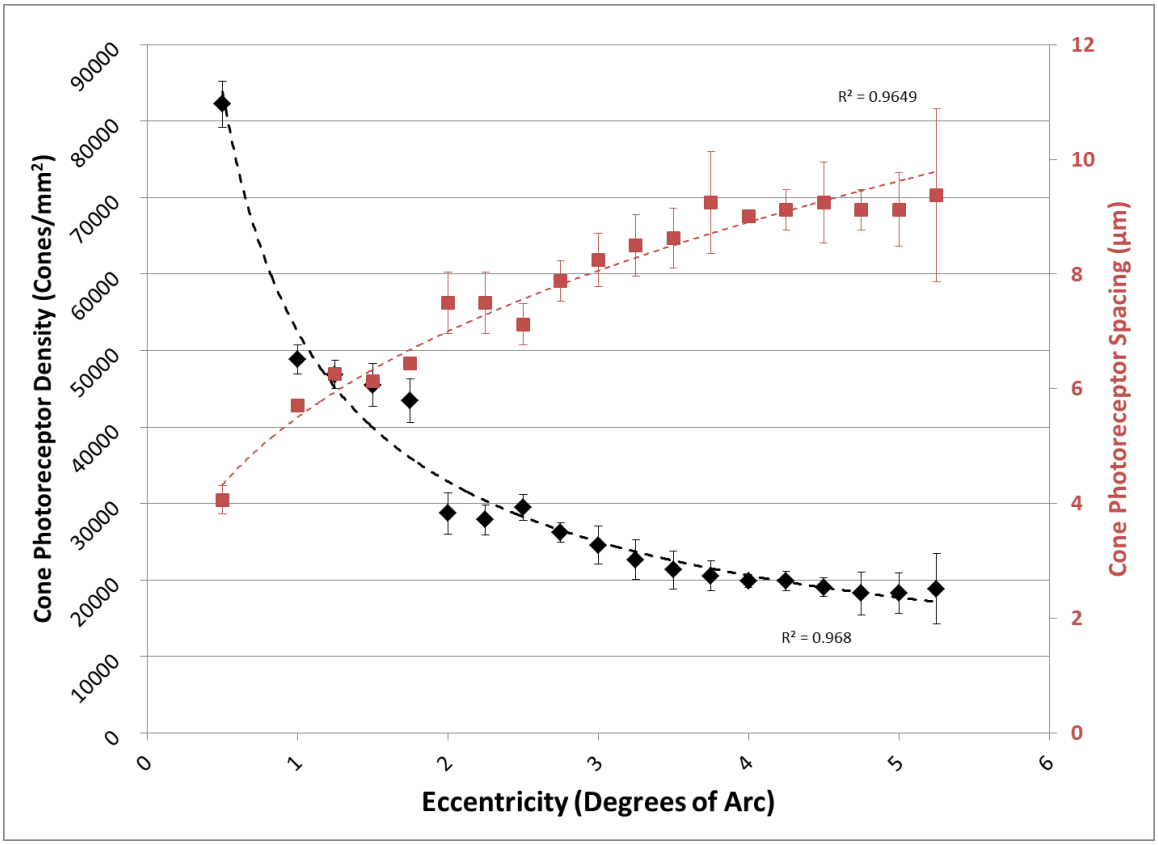

Figure 7-15. Relationship between cone photoreceptor density (*black*) and spacing (*red*) as a function of retinal eccentricity in healthy volunteers. The R^2 values for the density and spacing measurements were 0.968 and 0.965, respectively.

instead of absolute distance measured in micrometers. Although we were unable to resolve the smallest foveal cones at the center of the foveola to identify the exact location, we believe our approach represents a reasonable estimation based on the correlation between our finding and similar reports.

7.4.4 Photoreceptor Packing Arrangement

Documenting the preferred packing arrangement of photoreceptors cells throughout the eye represents another analytical parameter which may have diagnostic implications. Packing arrangement was determined based on the nearest neighbor analysis of each Voronoi region. The number of adjacent cells determines the preferred arrangement for a given location and is denoted based on the corresponding geometric shape (i.e. 4*n* = rectangular, 5*n* = pentagonal, 6*n* = hexagonal, etc.). The results of the nearest neighbor analysis were represented by color coding each Voronoi region to display the given geometric configuration (Figure 7-16). The data was then exported to excel for further analysis of the preferred arrangement based on retinal eccentricity. Generally, a hexagonal (6*n*) arrangement constitutes the largest proportion of the preferred packing arrangement with approximately 35-50% and 4*n* – 8*n* arrangements comprise over 95%. Therefore, divergence in the expected orientation of the packing arrangement may indicate underlying pathology directly affecting the photoreceptor cells.

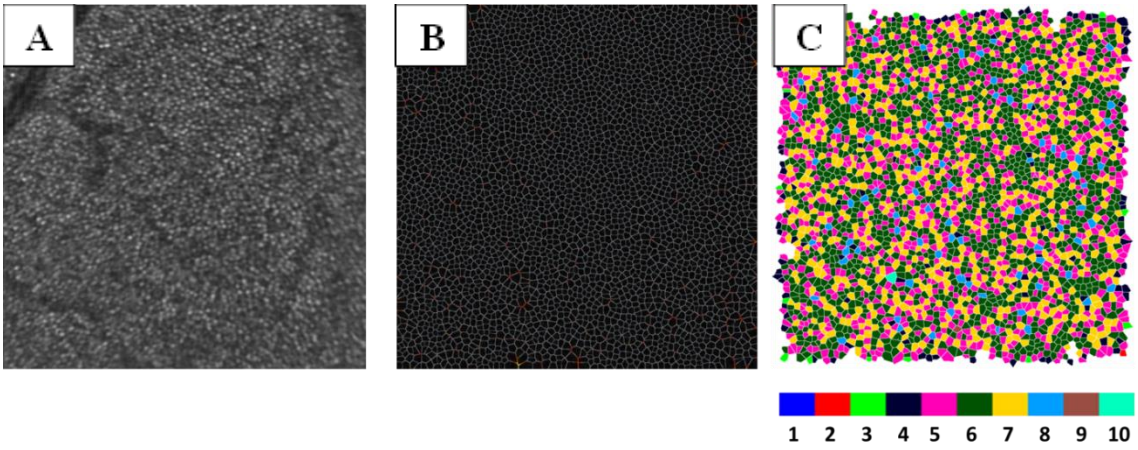

Figure 7-16. (A) 2° x 2° image of the cone photoreceptor mosaic in a healthy patient approximately 5° from the fovea along the temporal meridian. **(B)** Voronoi diagram of the geometric orientation of the cones. **(C)** Color-coded diagram depicting the photoreceptor packing arrangement with respect to the number of nearest neighbors. The scale bar represents the number of adjacent cones for each Voronoi region.

We performed analysis on the macular packing arrangement of 3 healthy volunteers to determine the preferred geometry of the cone photoreceptors with respect to eccentricity within 5° of the fovea. As expected, the 6*n* orientation was the most prominent for each patient and at every eccentricity tested along the nasal-temporal axis (Figure 7-17).

7.5 Conclusion

The development of retinal imaging systems enhanced with adaptive optics has provided an unprecedented view of microstructure within the living eye. The development and refinement of processing algorithms is a fundamental step in translating new devices into a clinical setting. The low light levels reflected back from the fundus, ocular motion, and limitations on the amount of light energy that may be safely delivered to the retina were the primary obstacles to obtaining high quality images of retinal cells *in vivo.* A preprocessing step was necessary to inspect each data set and remove extensive motion artifacts. The registration technique implemented to align sequential images in a series provided the basis for subsequent processing and analysis. The S.I.F.T. technique followed by block matching was able to account for the vast majority of the involuntary motion observed during acquisition. Averaging the resultant images improved the SNR and provided heightened structural detail. Alternative methods of image analysis are able to take advantage of this dynamic image acquisition process by evaluating motion to calculate features such as leukocyte velocity(295) or vascular networks(20, 22).

The clinical implications for AO technology are widespread and have been reviewed in great detail in the literature(272, 296). Qualitatively, the high-resolution

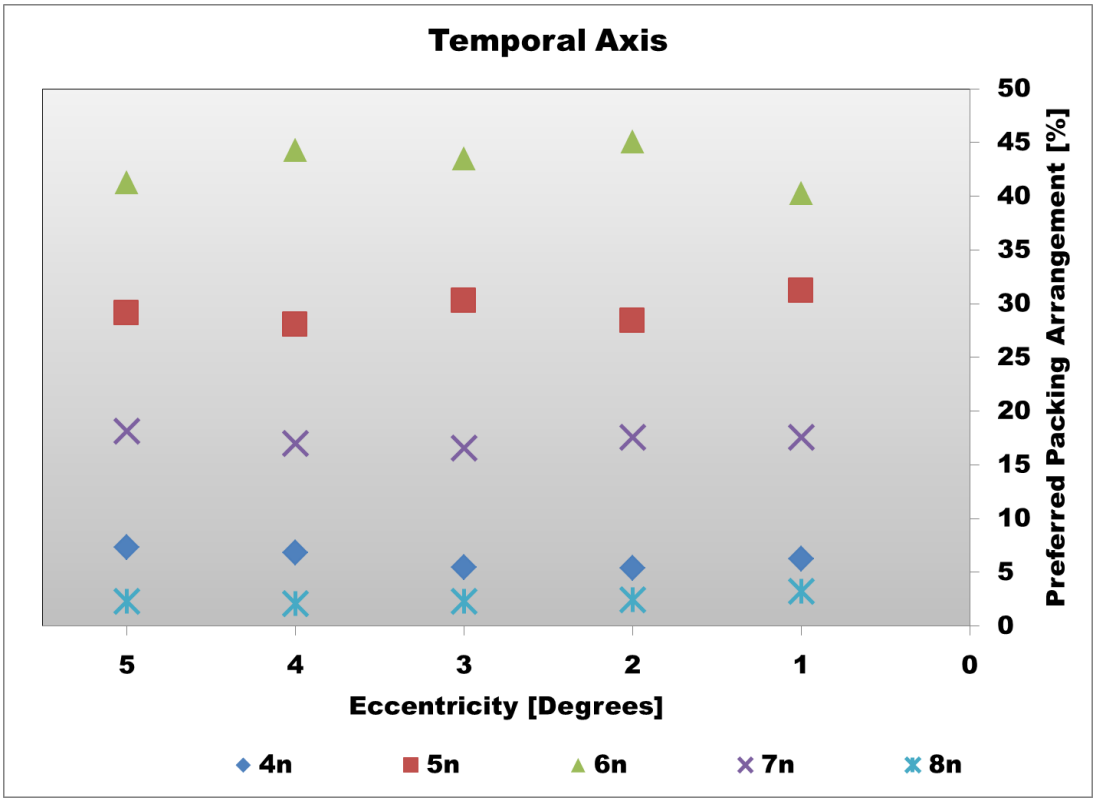

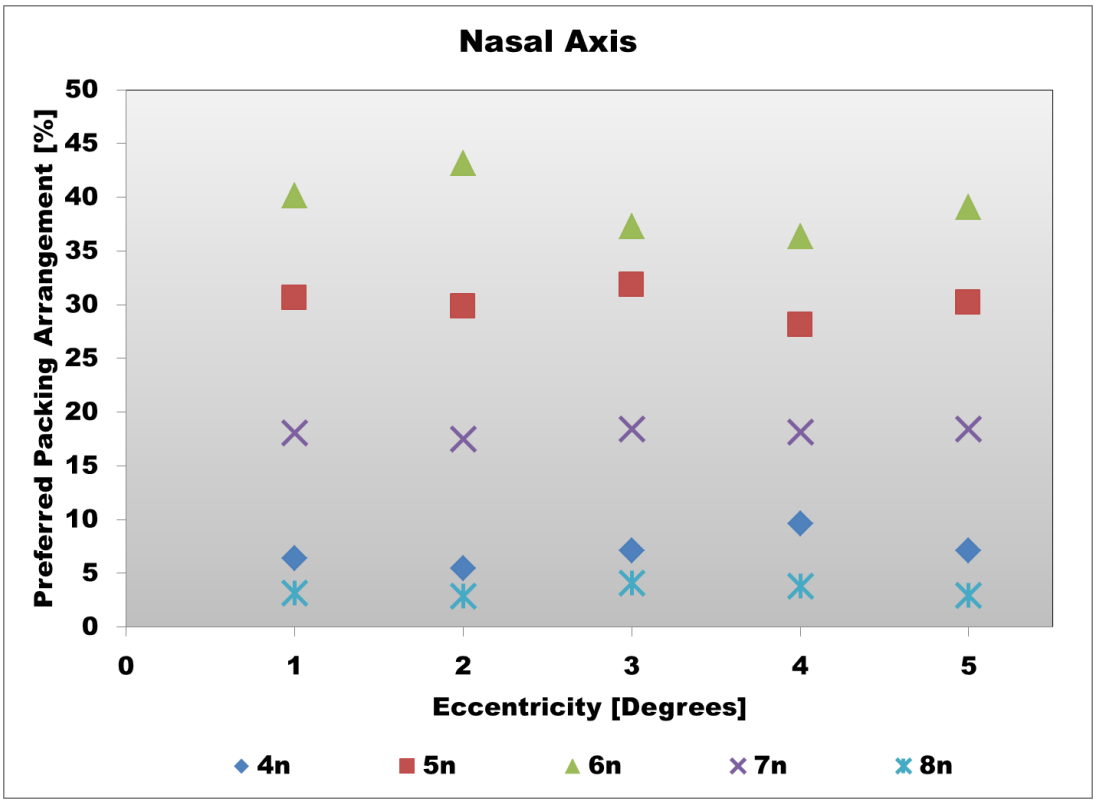

Figure 7-17. Preferred packing arrangement along the nasal-temporal axis compiled from 3 healthy volunteers.

images help reveal clinically relevant signs of pathology like altered cellular morphology. However, the identification of quantitative biomarkers of disease is equally important to justify the routine use of AO in a diagnostic capacity. It is doubtful that one metric alone will be suitable to ascertain the health of the retina or even just the photoreceptor cells. It is likely that the relationships among multiple complementary parameters will provide a more accurate characterization of tissue. Each analytical technique demonstrated in this chapter had its own limitations which could potentially be counterbalanced by incorporating additional metrics to improve the diagnostic capabilities of AO-SLO instruments.

Chapter 8: High Resolution Imaging in Patients with Age-Related Macular Degeneration

High resolution imaging techniques provide the basis for differential diagnoses of retinal diseases. Each new innovation has the potential to further our understanding of retinal diseases by providing a new way of assessing structural, functional or molecular changes associated with pathology. Adaptive optics (AO) represents the next stage in the evolution of diagnostic retinal imaging. A recent review by Carroll et al. highlighted the increase in scientific publications referencing AO enhanced imaging to investigate pathology, particularly over the past 5 years(272). This upward trajectory is likely to continue for the foreseeable future as AO retinal imaging enters the mainstream with commercially available diagnostic instruments.

As one of the leading causes of irreversible visual impairment throughout the world, age-related macular degeneration (AMD) represents a global health crisis that is only projected to rise as life expectancy increases(36-38). This progressive disease targets the specialized region of the retina which is primarily responsible for color vision and sharp central fixation. AMD can have a profound impact on quality of life and represents a tremendous financial burden associated with healthcare costs. In the United States alone, AMD is attributed to billions of dollars in direct health care cost annually(297-299).

8.1 Introduction

The epidemiology and proposed mechanisms of AMD pathogenesis were outlined in Chapter 3 of this dissertation. Despite the uncertainty in our current understanding of

AMD pathogenesis, it is known that vision loss is the result of photoreceptor degeneration. Specifically, the loss of cone photoreceptors within the macula leads to decreased central visual acuity. This inability to discern objects in the central visual field has a negative impact on nearly every aspect of a patient's life by compromising everyday tasks such as driving, reading or even recognizing faces.

Despite the prevalence of AMD and the increasing prominence of adaptive optics (AO) retinal imaging research, only a few publications have demonstrated the use of AO in patients with AMD(1, 300-303). The best quality AO enhanced images are acquired in patients with stable fixation and clear ocular media. Unfortunately, this is rarely the case with elderly patients exhibiting the degenerative effects of AMD within the macula. Stable fixation helps minimize inter- and intra-frame motion distortions which reduce the quality of the retinal images. The use of near-infrared light sources can mitigate some of the effects of ocular opacities due to decreased scattering but features such as dense cataracts can still have a substantial impact on the amount of light reflected back from the fundus. Likewise, advanced retinal tracking software(278) or hardware(31, 275) is often incorporated into AO retinal imaging systems to mitigate the effects of minor, involuntary eye movements. Furthermore, patient cooperation is crucial because of the length of time, generally up to an hour, required to scan a substantial retinal area with most research instruments.

Although there are numerous obstacles in acquiring high resolution images in low vision patients, a variety of techniques may be used to help circumvent these common problems. In this study, we acquired AO-SLO data in patients with each clinical stage of non-exudative AMD and applied quantitative analytical tools to characterize image-based

biomarkers based on retinal morphology. The application of novel image processing techniques and identification of benchmarks for disease progression may provide a greater understanding of pathogenesis and establish new criteria for the evaluation of emerging therapeutic intervention strategies.

8.2 Methods

All procedures in this study were performed in accordance with the Declaration of Helsinki. A detailed protocol was approved by the University of Texas Medical Branch Institutional Review Board and informed consent was obtained for all study participants. Exclusion criteria for patients included retinal complications from diabetes mellitus, cataracts, and history of ocular surgery, with the exception of intraocular lens (IOL) implantation. Likewise, patients that were unable to maintain suitable fixation were excluded from analysis.

8.2.1 Pilot Study

A pilot study was conducted to test the feasibility of high resolution AO-SLO imaging in patients with known indications of pathology. Four representative patients were selected to encompass each clinical stage of AMD progression according to the Age-Related Eye Disease Study (AREDS) classification system (Table 8-1). One eye per patient was selected for AO-SLO imaging. The participants in the pilot study were all female and ranged in age from 65 to 86 years old (Mean age: 75 ± 8.7 years). The age of each patient, eye imaged, and Snellen visual acuity may be found in Table 8-2. We anticipated increasing difficulty in obtaining quality imaging data suitable for analysis to correlate with more advanced stages of the disease. For the advanced stage of AMD (Category IV),

a patient with extensive central geographic atrophy was selected to represent the worst case scenario. Each patient received a comprehensive retinal examination including multimodal clinical imaging (SD-OCT, NIR, FAF, & fundus photography) prior to AO-SLO imaging. Wide field NIR reflectance images (30° x 30°, λ = 830 nm, 1536 x 1536 pixel resolution), FAF (ex: λ = 488 nm; em: λ >500 nm) and SD-OCT (λ =870, acquisition speed 20,000 A-scans/s; axial resolution ~7 μm) were all obtained with the Spectralis™ HRA+OCT (Heidelberg Engineering, Heidelberg, Germany). The wide field clinical imaging data and SD-OCT cross-sections were used to help direct the AO-SLO imaging window to regions exhibiting signs of pathology and control regions which appeared morphologically normal. The AO-SLO acquisition parameters previously described in Chapter 7 were used to collect the pilot study data as well. The only exception to the previously described acquisition procedure was the use of a larger confocal pinhole when imaging AMD patients. A 400 μm pinhole (~6 Airy discs) was used to enhance the collection efficiency at the avalanche photodiode (APD). Fundus images of the 4 pilot patients are shown in Figure 8-1.

Table 8-1. Age-related eye disease study (AREDS) classification levels for AMD.

Age-Related Eye Disease Study (AREDS) Stages of AMD	
Category I	**No or few small drusen (< 63 μm)**
Category II	**Intermediate drusen (< 125 μm)**
Category III	**Extensive intermediate or large drusen (> 125 μm)**
Category IV	**Neovascular AMD or Central Geographic Atrophy (GA)**

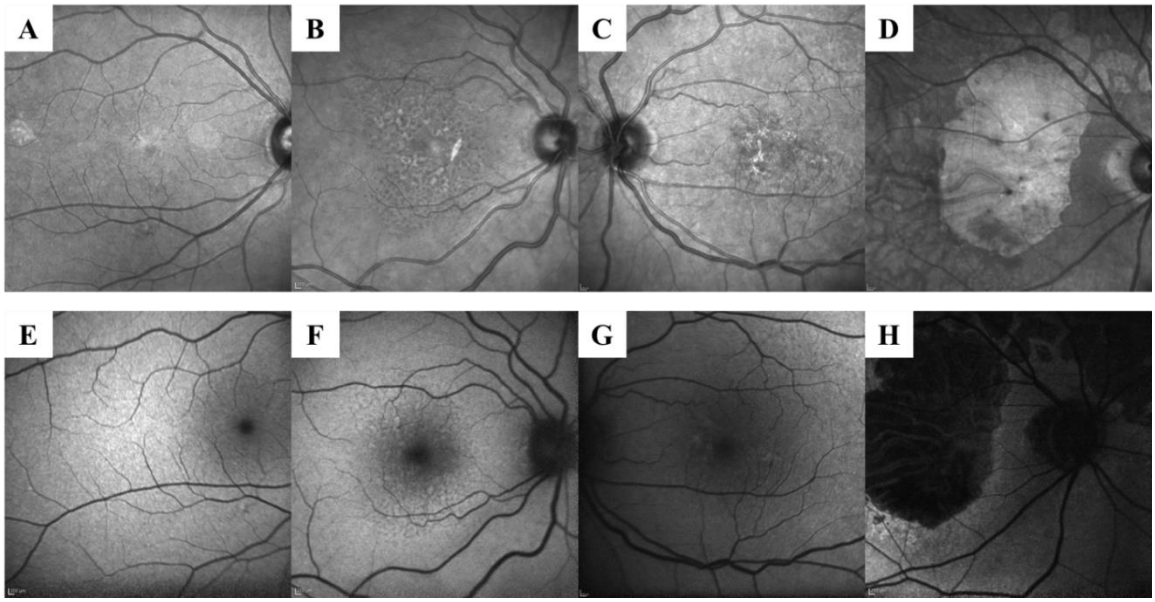

Figure 8-1. Wide field NIR reflectance SLO images from each pilot patient with the corresponding FAF image below **(A,E)** Category I **(B,F)** Category II **(C,G)** Category III **(D,H)** Category IV.

Table 8-2. Summary of Pilot Study Patient Information

Pilot Study Patient Population			
	Eye Imaged	*Age*	*Visual Acuity*
Patient 1 (Category I)	OD	74	20/25
Patient 2 (Category II)	OD	77	20/30
Patient 3 (Category III)	OS	65	20/25
Patient 4 (Category IV)	OD	86	CF 2 ft*

OD – right eye, OS – left eye. *Patient was only able to count the examiners fingers at a distance of two feet. (modified from *Boretsky et al. 2012(1)*)

8.2.2 Expanded Study

Based on the early success of the pilot study, additional patients were recruited for a larger study which included a total of 20 patients (22 eyes). The participants in the expanded study were selected to provide a balance between male and female patients and ranged in age from 54 to 92 years old (Mean age: 76 ± 9.5 years). The age of each patient, eye(s) imaged, and Snellen visual acuity may be found in Table 8-3. A further breakdown of the patient demographics based on category is shown in Table 8-4. The image acquisition procedures remained consistent throughout the study. Typically, image sequences were acquired for 10-30 seconds while scanning the raster over a small region of the retina to oversample the imaged area. This aided in subsequent image registration and processing steps. The relatively short duration of the acquisition for each area allowed the patients to take frequent breaks to minimize eye fatigue. Each AO-SLO imaging session lasted approximately 30-45 minutes. Similar to all of the other AO imaging studies, patients were screened with a multimodal clinical imaging system (Spectralis™ HRA+OCT, Heidelberg Engineering) to identify specific regions of interest and provide a general assessment of AMD-related pathology.

8.2.3 Image Analysis

The primary image analysis metrics were cone photoreceptor density and spacing measurements. Detailed methodology on the semi-automated AO-SLO image analysis techniques may be found in Chapter 7 of this dissertation. Briefly, a Laplacian of Gaussian (*LoG*) filter was used to identify the location of each cell and reduce it to a single point based on the centroid and the coordinate locations were mapped. Voronoi

diagrams were generated to provide a geometric representation of cellular arrangement and scaled look up tables (LUTs) were used to highlight regions of divergent orientation by manually thresholding the 8-bit images. Finally, the coordinate locations of each photoreceptor were used to measure mean center-to-center spacing based on Delaunay triangulation. The corresponding data was then displayed as a heatmap overlay on the original image with each of the analytical regions of interest (ROI) color coded based on the custom spacing or density scale. For each Heatmap, a color coded gradient was used to display the density measurements while a standard deviation scale was used for the spacing measurements.

Table 8-3. Summary of AMD Patients Enrolled in the Imaging Study

AMD Category	Patient ID	Age	Sex	Eye	Snellen Visual Acuity
I	AB_0001	74	F	OD	20/25
I	AB_0006	66	F	OD	20/20
I	AB_0015	66	F	OS	20/25
I	AB_0019	84	M	OD	20/30
I	AB_0020	71	M	OD	20/25
II	AB_0005	77	F	OD	20/25
II	AB_0008	68	F	OD	-
II	AB_0011	83	M	OD	-
	AB_0011			OS	-
II	AB_0013	72	M	OD	20/20
II	AB_0016	54	M	OD	-
III	AB_0002	65	F	OS	20/40
III	AB_0007	77	F	OD	20/25
III	AB_0010	77	M	OD	
III	AB_0014	92	M	OD	20/40
III	AB_0018	72	M	OD	20/25
	AB_0018			OS	20/25
IV	AB_0003	86	F	OD	CF
IV	AB_0004	80	F	OD	20/40
IV	AB_0009	71	M	OD	20/40

IV	AB_0012	88	F	OS	20/25
IV	AB_0017	77	M	OD	20/25

Table 8-4. Summary of Patients Based on AMD Category

AMD Category	Mean Age ± St. Dev.	Male : Female Ratio
Category I	72.2 ± 7.4	2 : 3
Category II	70.8 ± 10.9	3 : 2
Category III	76.6 ± 9.9	3 : 2
Category IV	80.4 ± 6.9	2 : 3

8.3 Results

8.3.1 Pilot Study Patients

The pilot study consisted of 4 female patients as representative cases for each clinical category of AMD. The cone photoreceptor mosaic was evaluated in registered and averaged composite images to assess the integrity of the macular morphology. A qualitative comparison of the high resolution images acquired with the investigational AO-SLO system was compared with standard clinical diagnostic techniques. The smaller FOV of the AO-SLO enabled photoreceptor cells to be readily identified throughout the macula. In some cases, photoreceptor cells were discernable without AO. The active closed-loop AO correction provided heightened contrast with respect to the vasculature and distortions in the photoreceptor mosaic attributed to drusen. AO-SLO imaging in the Category I AMD patient exhibited minimal disruption in the photoreceptor mosaic which we attributed to focal hard drusen. Multiple punctate features were also observed which may be early subclinical indications of drusen. FAF revealed isolated regions of increased fluorescence signal in the perifovea and SD-OCT imaging was able to detect a few isolated deposits in the outer retina. Overall, the AO-SLO images helped visualize

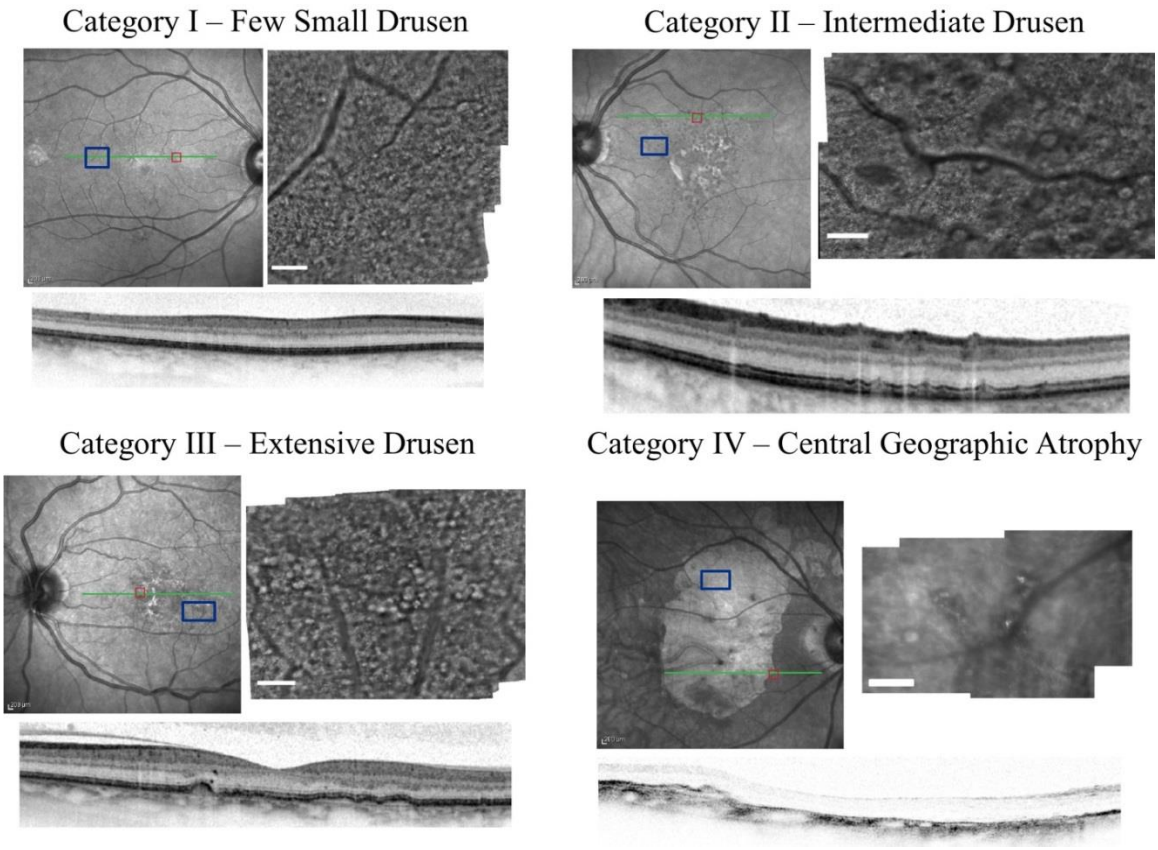

Figure 8-2. Wide field (30° x 30°) near infrared fundus reflectance images with corresponding Spectral Domain Optical Coherence Tomography cross-sections (position noted by the horizontal green line) provides an overview of the retinal morphology for each patient. AO–SLO cone photoreceptor mosaics shown are represented by the blue rectangles. The small scale of the images demonstrates the effect of disease progression on cone photoreceptors for a representative patient from each category (red rectangles represent additional scan areas—not shown). Scale bars represent 200 mm. (modified from *Boretsky et al. 2012(1)*)

these features in greater detail and identified potential subclinical indications of aging and pathology. The Category II AMD patient exhibited multiple discontinuities in the cone mosaic which correlated with drusen observed using SD-OCT. Typical sub-RPE drusen (approximately 120 µm in diameter based on SD-OCT measurements) resulted in dark circular shapes in the cone mosaic with a few bright features within the ring shape. Presumably, disruption of the alignment of the photoreceptors with respect to the incident

light led to the reduced reflectance observed with AO-SLO. The category III AMD patient exhibited large confluent drusen which were evident on using multimodal clinical imaging. Finally, the category IV patient had extensive central GA as shown in Figure 8-1 D & H. Regions along the marginal zones of the atrophy exhibited morphologically intact cone photoreceptor cells although the population of cones appeared sparse. Presumably, this was due to the retinal eccentricity but the progression of AMD may also play a role in the photoreceptor density and spacing at these locations. An overview of the wide filed clinical SLO images with corresponding SD-OCT cross sections through regions exhibiting pathology and AO-SLO images for each of the pilot patients are shown in Figure 8-2.

Quantitative analysis of the photoreceptor mosaic was performed for each of the pilot study patients to assess changes in cone density based on disease category. For this analysis, a 3° x 1° retinal area was selected along the temporal axis (~5° - 7° from the foveal center) to measure cone photoreceptor density. This region was selected because the imaging area was acquired for each patient and density measurements within this region are less likely to be biases by the presence of large blood vessels along the major arcades. The mosaics were divided into smaller regions of interest (0.25° x 0.25°) to measure the variability of the density in the perifovea. Voronoi diagrams and grayscale heatmaps were generated to provide a visual representation of the density of each ROI in the context of the larger mosaic (Figure 8-3).

A One-way analysis of variance (ANOVA) was used to test for significant differences in cone density among the four pilot patients from each AREDS category. The density values were significantly different among the clinical stages ($P < 0.001$).

Pairwise multiple comparisons among the individual stages (Tukey Test) were also performed. Differences between groups were deemed significant at $P < 0.05$ during the multiple comparisons tests. The Category I and II patients did not exhibit significant differences in cone density. Similarly, Category III and IV measurements were not statistically different. However, both Category I and Category II density values were significantly different from the Category III and Category IV measurements. This would indicate the ability to distinguish between earlier and later stages of the disease based on cone photoreceptor density measurements. A summary of these results may be found in

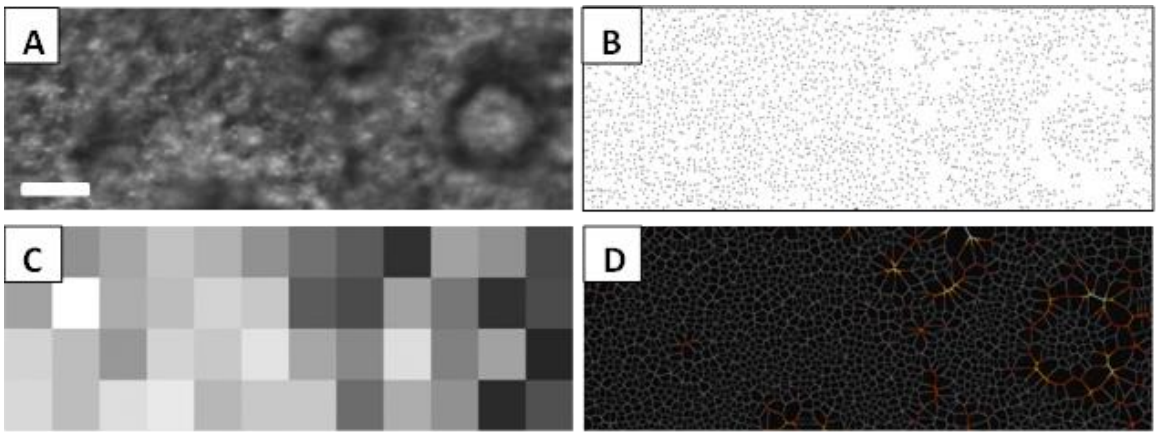

Figure 8-3. Example of cone photoreceptor density analysis from a Category II dry AMD patient (A) cone photoreceptor mosaic (3° x 1°, ~ 0.87 mm x 0.29 mm) (B) Automated identification of cone photoreceptor locations (C) Heat map of localized photoreceptor densities in 0.25° x 0.25° regions, dark regions represent lower photoreceptor density [values range from 2568 – 13983 cones/mm^2; mean value ± SD: 8698 ± 2964] (D) Voronoi diagram demonstrating the relationship between photoreceptor packing density and alterations caused by drusen formation. [Scale bar = 0.1 mm] (modified from *Boretsky et al. 2012*(1))

Table 8-5.

The findings from the density measurements may also be observed qualitatively based on the increasing prevalence of regions demonstrating decreased cone reflectance as a function of disease progression. These features are noted by the arrows in Figure 8-4.

Table 8-5. Cone photoreceptor density analysis for a representative patient from each AMD category

	n	Mean Cone Density [Cones/mm^2]	Standard Deviation	Min	Max
Category I	48	9128	± 1612	4946	14269
Category II	48	8698	± 2965	2568	13983
Category III	48	5443	± 1259	3234	8371
Category IV	48	4744	± 1377	1141	7420

Multiple Comparisons (Tukey Test)	
Category I vs Category IV	P < 0.05
Category I vs Category III	P < 0.05
Category I vs Category II	No
Category II vs Category IV	P < 0.05
Category II vs Category III	P < 0.05
Category III vs Category IV	No

One-way ANOVA was used to test differences in photoreceptor density among the four clinical stages of AMD. Photoreceptor density was significantly different among the 4 groups ($P < 0.001$). Post-hoc comparison of the groups (Tukey Test) found Category I to have a significantly higher cone density than both Category III & IV. Likewise, Category II demonstrated significantly higher cone density than both Category III & IV. No significant differences were observed between Category I & II or between Category III & IV (values were deemed significant at $P < 0.05$).Composite images for each patient represent ~5-7° from the central fovea along the temporal meridian. Each data point represents a 0.25° x 0.25° region to assess local variations in cone density. (modified from *Boretsky et al. 2012(1)*)

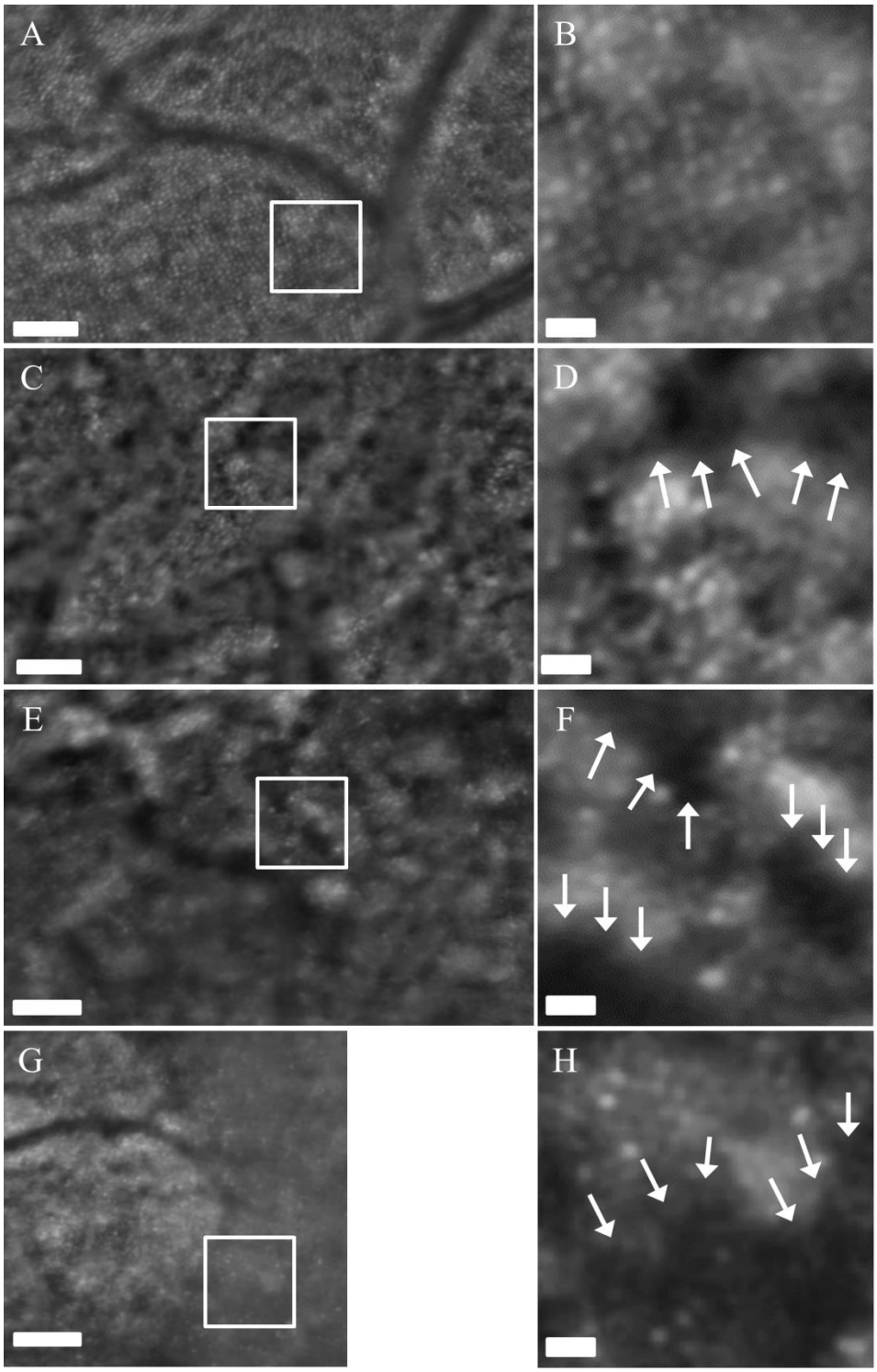

Figure 8-4. AO-SLO composite images from Category I patient **(A, B)**, Category II **(C, D)**, Category III **(E, F)** and Category IV **(G, H)**. White boxes represent the 0.5°×0.5° regions shown in B, D, F & H. An increase in photoreceptor disruption can be observed as a function of disease progression. The arrows denote regions with decreased reflectance possibly indicating loss of functionality or atrophy of cone photoreceptors. Scale bars (A, C, E, & G) = 0.1 mm. Scale bars (B, D, F, & H) = 0.02 mm (modified from *Boretsky et al. 2012(1)*)

8.3.2 Expanded Study Patients

The pilot study demonstrated the ability to visualize the retinae of AMD patients with great detail. However, the pilot study only included a single patient from each category and all four patients were female. In an effort to expand the scope of the study, analysis of multiple patients for each category was performed. The age range for these patients spanned nearly 5 decades and a nearly even gender distribution. The analysis also included the addition of spacing measurements using Delaunay triangulation as described in the previous chapter. A demonstration of multiple analytical metrics including density, Voronoi orientation, and spacing over a typical sub-RPE druse is shown in Figure 8-5.

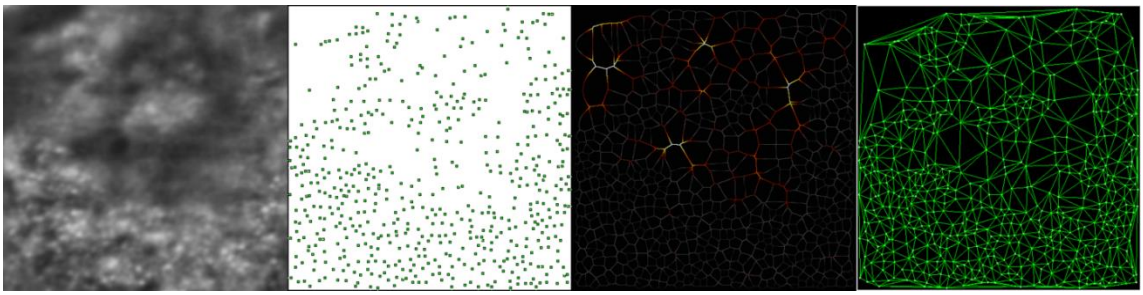

Figure 8-5. (A) Analysis window from an early AMD patient (Category II) exhibiting a typical sub-RPE druse. **(B)** Corresponding cone photoreceptor map based on the LoG technique **(C)** Voronoi diagram highlighting regions of distorted packing arrangement **(D)** tessellation diagram graphically depicting spacing results from Delaunay triangulation analysis.

Imaging in patients with early and intermediate stages of AMD often provided the opportunity to create larger composites of the photoreceptor mosaic throughout the macular region, but this was generally not possible in cases of advanced AMD due to reduced fixation. Composites of early and intermediate AMD patients are shown in

Figure 8-6 as an overlay on wide field (30° x 30°) SLO images taken with the clinical system to provide a comparison of scale (Figure 8-6).

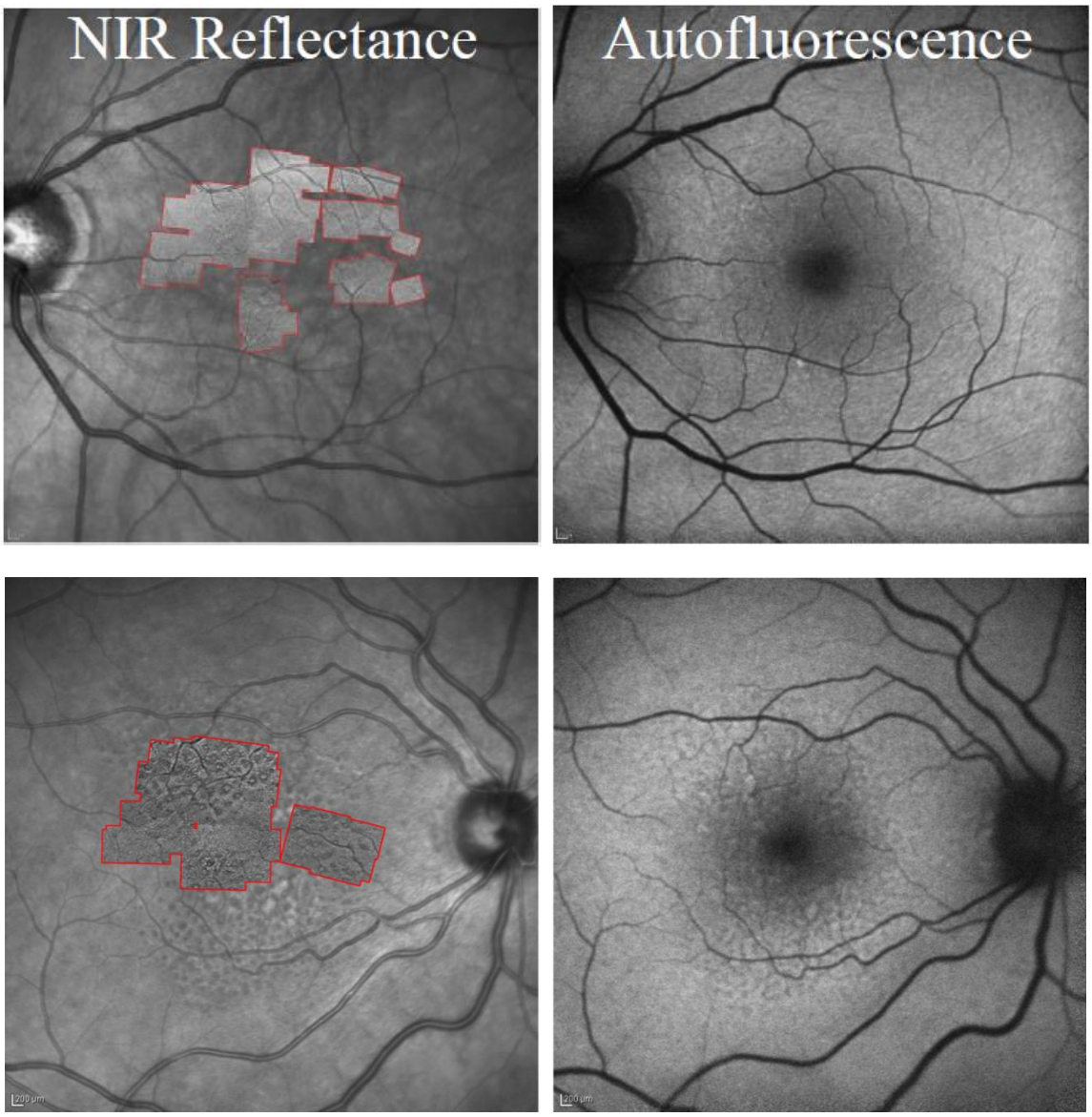

Figure 8-6. NIR-reflectance SLO images with the accompanying FAF images. Areas outlined in red represent the composite AO-SLO scan regions from the registered 2° x 2° data sets.

8.3.3 Photoreceptor Density and Spacing Analysis

The photoreceptor density and spacing analysis was performed visualize local perturbations in the cone mosaic based on averaged images and to assess changes in these

metrics across multiple patients within AMD categories. The local changes in the mosaic were easily discernable in both the density and spacing measurements. However, the density measurements were more likely to be influenced by the presence of normal anatomical features such as blood vessels which yielded numerous regions that appeared below the expected mean photoreceptor density. Alternatively, the spacing measurements provided a more conservative assessment of the integrity and continuity of the cone mosaic. This is aptly demonstrated in Figure 8-7. An alternative view of the processed overlay images in shown in Figure 8-8. This representation highlights the aberrant features, namely distortion of the cone mosaic due to confluent drusen, using the Voronoi diagram and the cone density heatmap.

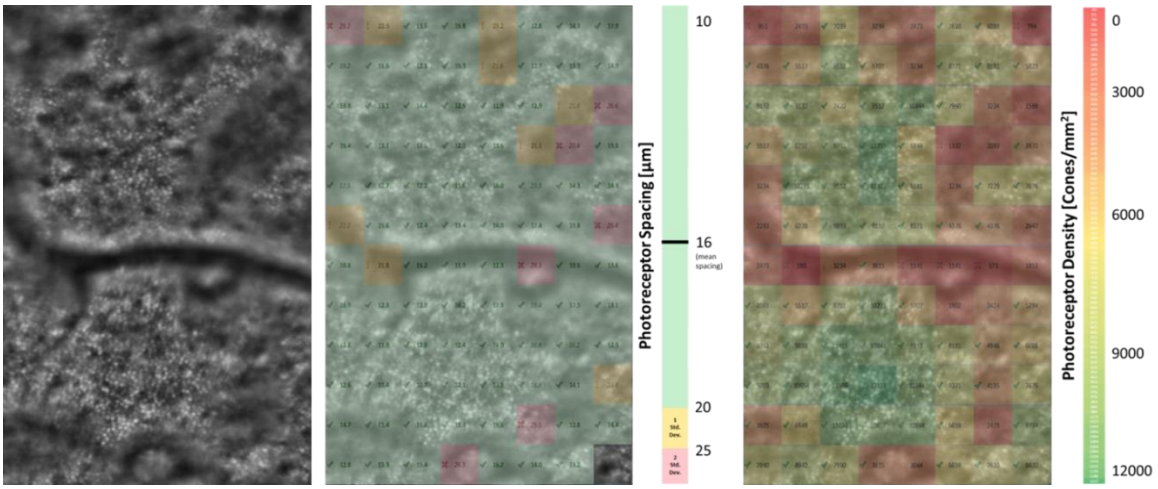

Figure 8-7. Parafoveal photoreceptor mosaic from a stage II (early) AMD patient demonstrating pronounced disruption in the continuity of the cones. The dark circular shapes correspond with typical sub-RPE drusen while the irregular dark patches appear to be regions impacted by reticular pseudodrusen. SD-OCT scans through each region are shown below. Each image panel represents a clinically applicable assessment of the viewable retinal region. **(Left)** Summary of the imaging area highlighting photoreceptor density characteristics **(Center)** Heatmap depicting regional variations in photoreceptor spacing in subdivided regions of the image where green is within 1 standard deviation of the expected spacing for a given retinal eccentricity, yellow is greater than 1 standard deviation, and red is greater than 2 standard deviations. **(Right)** Heatmap of the photoreceptor density in each 0.25° x 0.25° region of interest.

The data from the density and spacing measurements was plotted with respect to retinal eccentricity for each stage of the disease to evaluate and discernable patters associated with progression. The nasal and temporal meridians were selected in an effort to standardize the regions evaluated to better compare multiple patients within and across each disease category. Trends toward decreased photoreceptor density and increased spacing were observed but the high degree of variability in the measurements did not yield statistically significant results. Additionally, the data points from the category IV patients with extensive GA were limited to the regions outside of the atrophic lesions so measurements near the fovea were not available. The plots for the density and spacing measurements may be found in Figures 8-9 through 8-12.

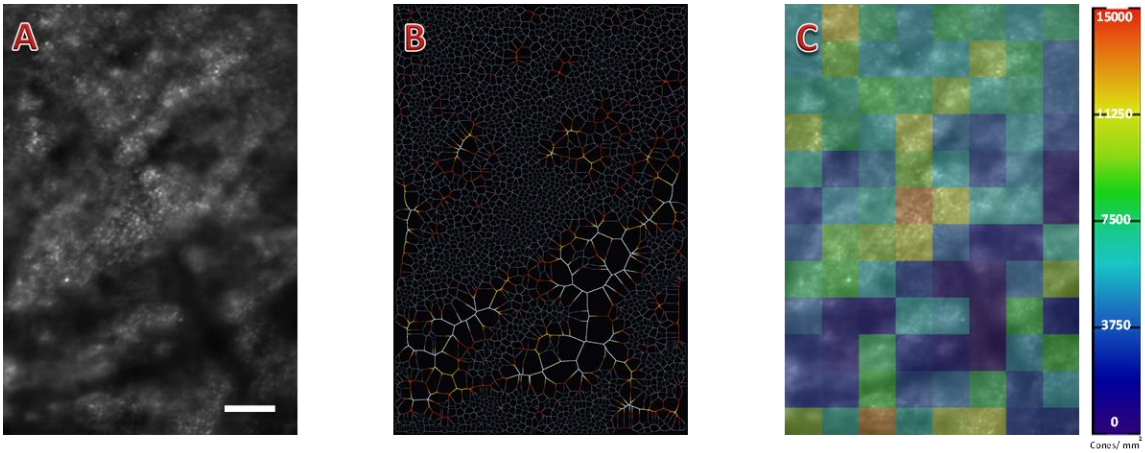

Figure 8-8. Category III AMD patient (77 year old female) with intermediate drusen throughout the macula. (A) 2°x3° mosaic along the superior meridian (B) Voronoi diagram highlighting regions of the PR mosaic affected by underlying drusen. (C) Heatmap of the local PR density. Scale bar = 100 μm

Ultimately, multimodal imaging with the clinical instruments and the investigational AO-SLO provided the most comprehensive assessment of the retina. The combination of fundus photography, wide field SLO, SD-OCT, and AO-SLO gave us

complimentary views of the tissue. The use of SD-OCT to identify morphological abnormalities in the outer retina helped guide the regions of interest for AO-SLO imaging, specifically in the investigation of the macular cone photoreceptor cells. The FAF images also helped to define the atrophic margins which could then be viewed in greater detail with the AO imaging system (Figure 8-15). Similarly, regions of hyper- or hypo-pigmentation may be seen with enhanced detail to highlight early signs of AMD pathogenesis (Figure 8-16)

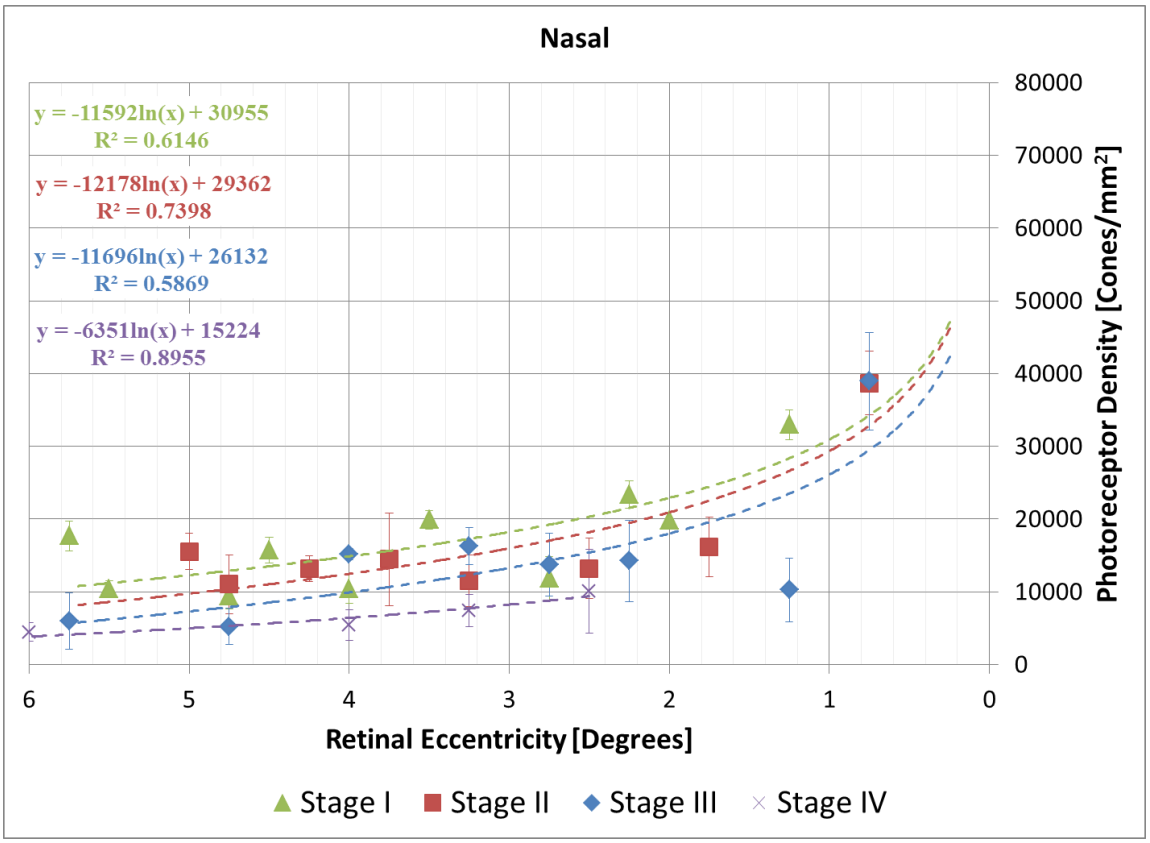

Figure 8-9. Photoreceptor density plot with respect to retinal eccentricity along the nasal meridian. The dashed lines represent the best fit logarithmic plot for each category based on the data set. The equations for the best fit plots and their respective correlation coefficients are shown.

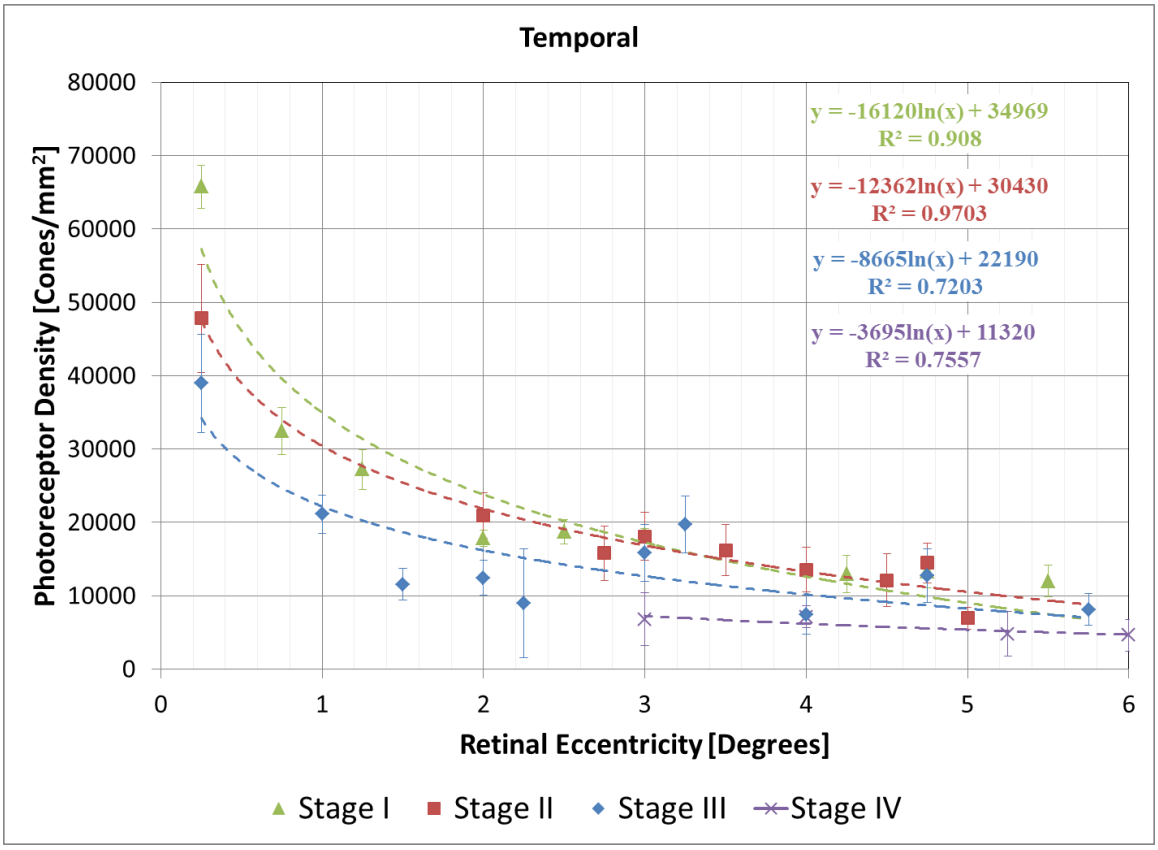

Figure 8-10. Photoreceptor density plot with respect to retinal eccentricity along the temporal meridian. The dashed lines represent the best fit logarithmic plot for each category based on the data set. The equations for the best fit plots and their respective correlation coefficients are shown.

8.3.4 Subretinal Drusenoid Deposits (Reticular Pseudodrusen)

Although we did not explicitly seek out patients with subretinal drusenoid deposits (SDD, also known as reticular pseudodrusen), a *post hoc* assessment of these features was noted based on the SD-OCT data. Specifically, the subretinal drusenoid deposits/debris (SDD) demonstrated a pronounced decrease in the hyper-reflectivity of the IS/OS junction. In one patient (Patient AB_008; Category II non-exudative AMD), we were able to observe typical sub-RPE drusen and subretinal drusenoid deposits in the same data set (Figure 8-13). Future AO-SLO imaging of such patients may be able to reveal whether or not SDD actually confer lower risk for advanced AMD when compared

with conventional drusen as proposed by Zweifel *et al(97)*. Additional imaging of this subject was viewed with SD-OCT to examine the integrity of the IS/OS junction (also currently referred to as the *ellipsoid zone* of the inner segments(304)) within the region of SDD. The intensity profiles of a control region and the SDD zone were plotted together to demonstrate the loss of the hyper-reflective band typically associated with the IS/OS junction (Figure 8-14). Additionally, similar techniques could be used to investigate features such as outer retinal tubulations with AO as demonstrated by Panorgias et al(305).

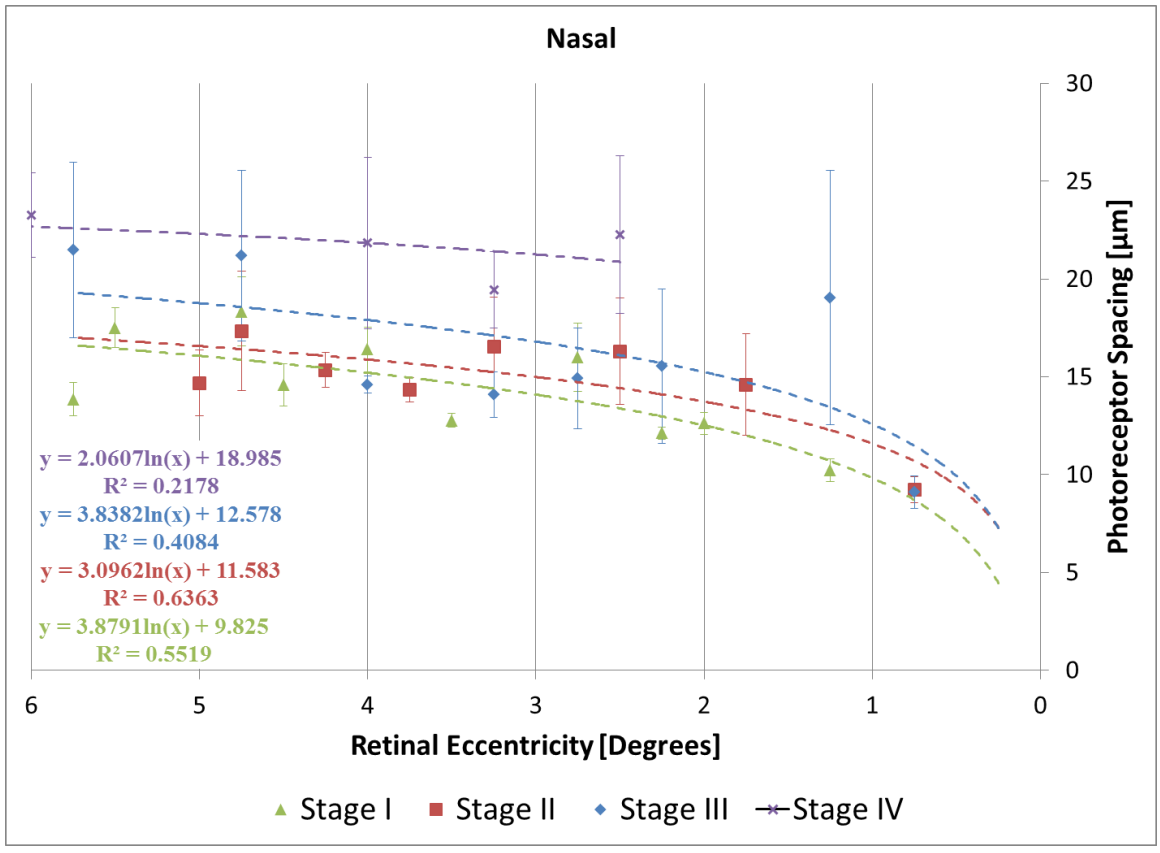

Figure 8-11. Photoreceptor spacing plot with respect to retinal eccentricity along the nasal meridian. The dashed lines represent the best fit logarithmic plot for each category based on the data set. The equations for the best fit plots and their respective correlation coefficients are shown.

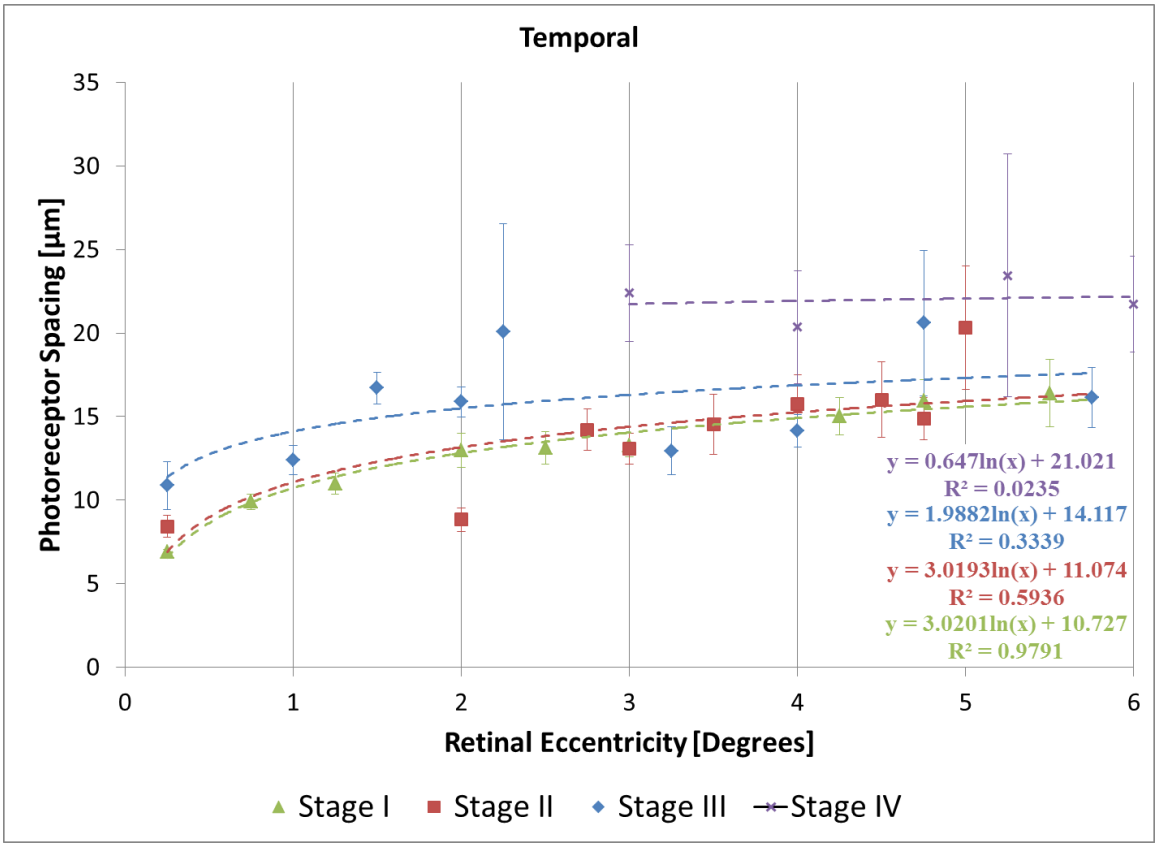

Figure 8-12. Photoreceptor spacing plot with respect to retinal eccentricity along the temporal meridian. The dashed lines represent the best fit logarithmic plot for each category based on the data set. The equations for the best fit plots and their respective correlation coefficients are shown.

8.4 Discussion

In the pilot study, we were able to demonstrate the application of high resolution imaging at a cellular level in patients representing each clinical stage of non-exudative AMD. This study was the first of its kind to visualize the cone photoreceptor mosaic *in vivo* in patients encompassing each clinical stage of AMD with AO-SLO. Detailed morphological data regarding the health of the macular photoreceptor cells established an additional clinical benchmark for the diagnosis of AMD, criteria for disease progression,

Figure 8-13. Category IV AMD patient (71 year old male) with extensive central GA. Green line represents the SD-OCT scan and the yellow rectangle corresponds to the AO-cSLO imaging area (A) Wide field fundus reflectance (B) Fundus autofluorescence (C) White light fundoscopy (D) AO-cSLO of atrophic region (E) Corresponding SD-OCT cross-section demonstrating enhanced light penetration in areas of atrophy indicated by the red lines. The Intensity v. Depth profile through a region of atrophy is shown in the plot on the right.

and the potential to evaluate therapeutic intervention. Local anomalies in the integrity of

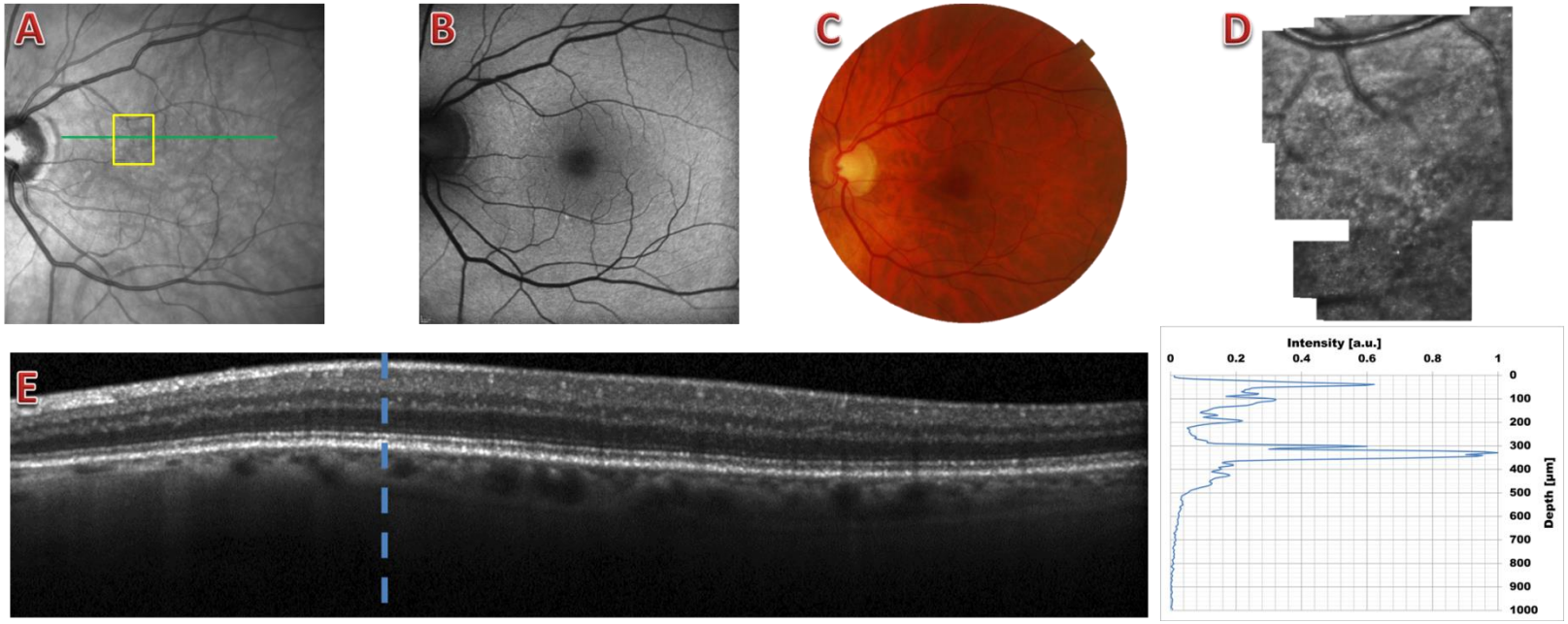

Figure 8-14. Category I AMD patient (66 year old female) with small drusen distributed sparingly throughout the macula. Green line represents the SD-OCT scan and the yellow rectangle corresponds to the AO-cSLO imaging area (A) Wide field fundus reflectance (B) Fundus autofluorescence (C) White light fundoscopy (D) AO-cSLO mosaic of a region photoreceptor disruption due to drusen in the macula (E) SD-OCT cross-section through the AO-cSLO scan area. The Intensity v. Depth profile is shown in the plot on the right.

By quantifying metrics such as density and spacing, early biomarkers of AMD which are currently deemed subclinical may be identified.

Qualitatively, the images acquired for the AMD patients were generally poorer than young, healthy volunteers. This was expected based on the dim fundus reflectance in the aged patients and problems maintaining fixation for extended periods of time. Despite these complications, the quantitative analysis of our data yielded comparable results to previous *ex vivo* and *in vivo* characterization of the photoreceptor mosaic in aged and AMD patients(255, 271, 287, 303). Interestingly, the analysis of cone density was able to discern statistically significant differences between early stages of AMD (Category I & II) and later stages (Category III & IV).

The combined data from each AMD category provided an intriguing problem from an analytical standpoint. The unpredictable nature of drusen accumulation and the formation of GA yielded wide variability when density or spacing measurements were plotted with respect to retinal eccentricity. Even the addition of hundreds or thousands of patients to generate a normative database would be unlikely to produce a predictive assessment of photoreceptor metrics. Therefore, local perturbations were evaluated within the context of the surrounding tissue to identify deviations in the pattern of the photoreceptor mosaic. This approach used retinal regions which appeared morphologically normal as innate controls. In the absence of a more complex model, this technique has been used to assess AMD patients in one other AO study(302). Admittedly, this approach will not provide much additional diagnostic benefit to late stage patients with extensive morphological alterations which can already be detected using current

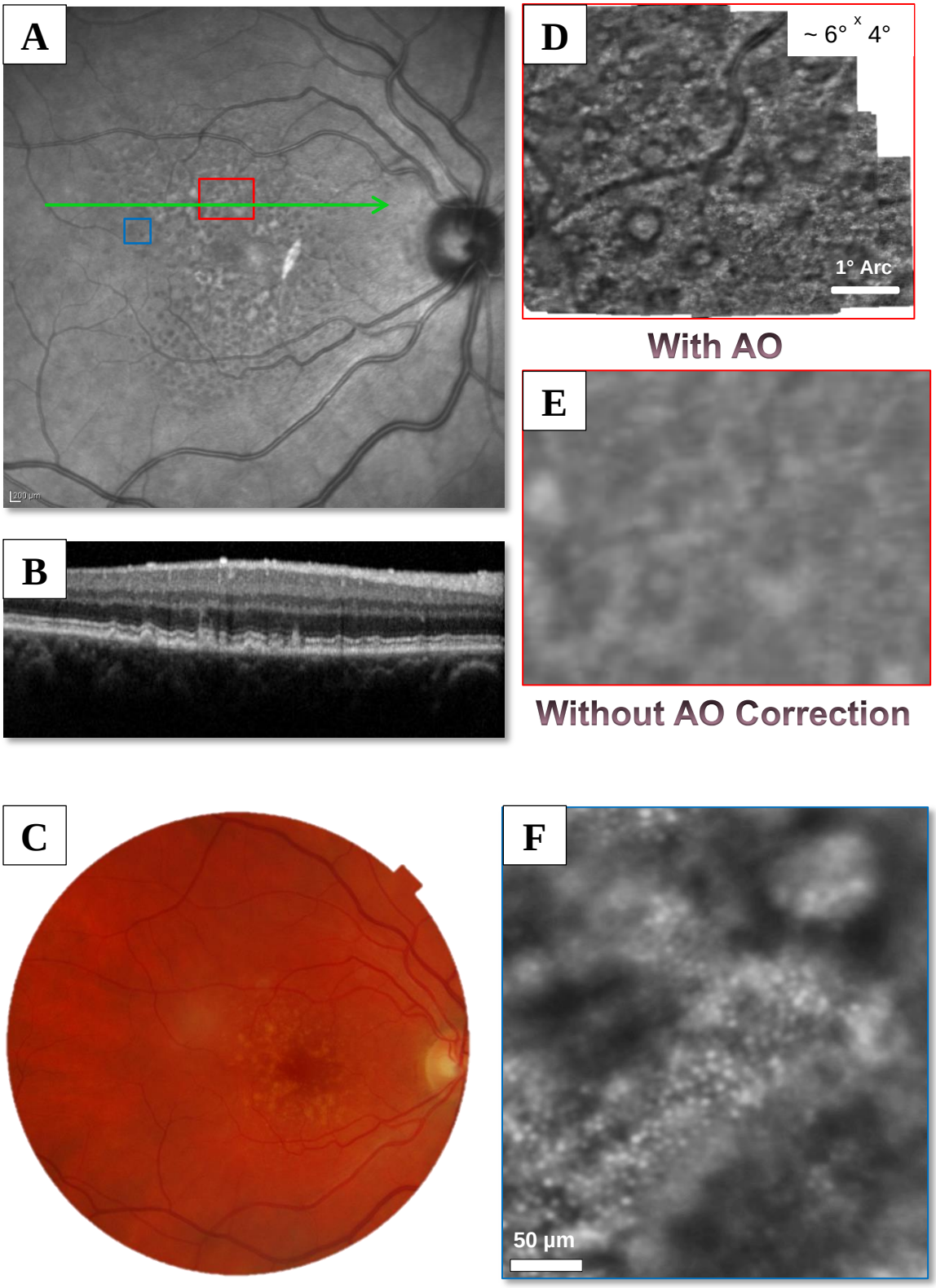

Figure 8-15. Category II non-exudative AMD patient. (A) Wide field SLO fundus image (B) SD-OCT cross section through a retinal region exhibiting sub-RPE drusen (C) Color fundus photography (D) Composite AO-SLO image of the cone photoreceptor mosaic with closed loop correction (E) High resolution SLO without AO correction (F) Enhanced view of photoreceptor disruption associated with drusen.

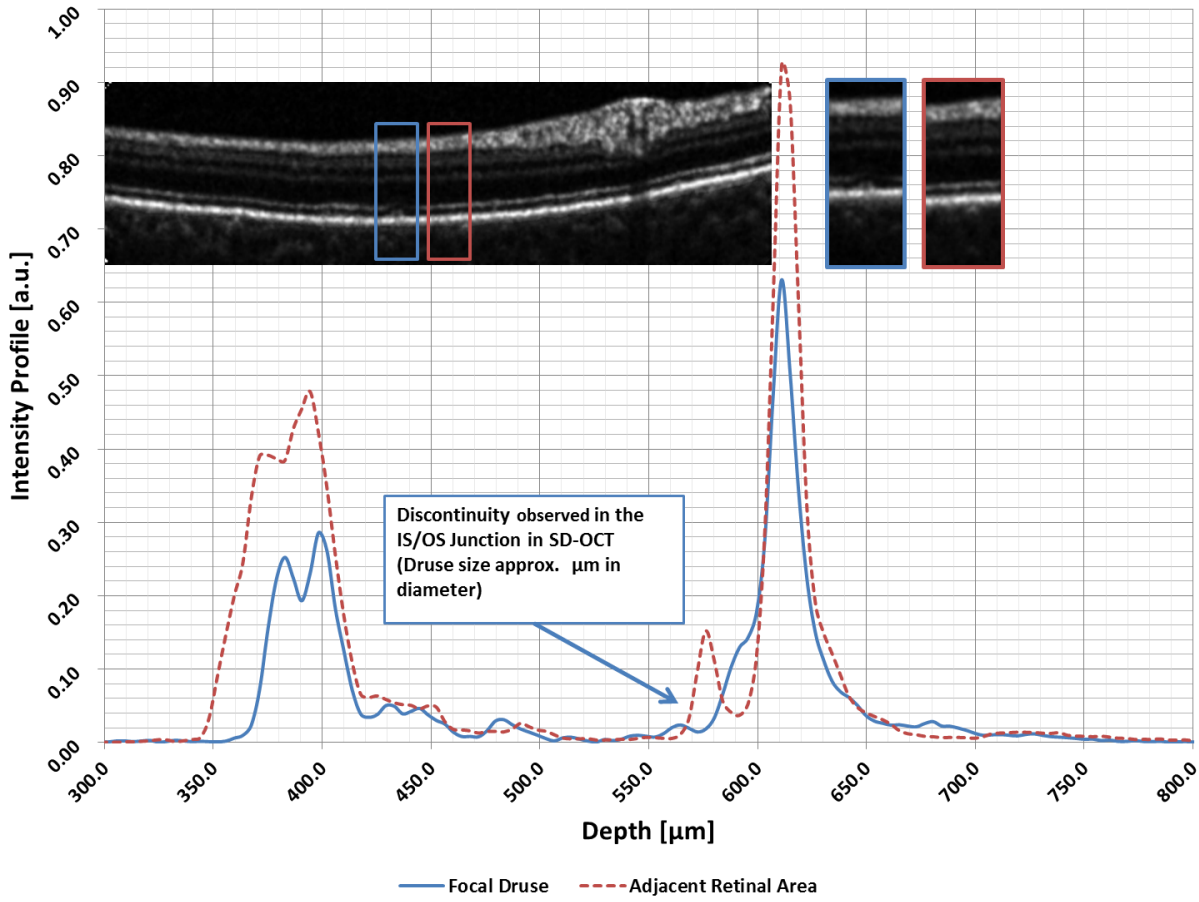

Figure 8-16. Intensity versus depth plot of adjacent retinal regions in a patient exhibiting characteristic signs of reticular pseudodrusen/subretinal dursenoid deposits (SDD). The SDD region lacks the hyper-reflective SD-OCT band typically associated with the IS/OS junction (also referred to as the *ellipsoid zone).*

clinical instrumentation. However, as shown here, this technique may still be used to investigate the marginal zones of GA or the progressive enlargement of drusen.

Recently, another research group demonstrated similar findings in the displacement of the cone mosaic attributed to drusen(303). One plausible explanation of the dark regions observed in the AO-SLO mosaics is the displacement of the photoreceptor layer by the underlying drusen. This effect would alter the angle of the photoreceptors with respect to

the incident light. Photoreceptors have a well characterized directional sensitivity whereby light entering the eye at the edge of the pupil elicits a smaller response compared to an equivalent stimulus directed near the center of the pupil. This

was first described in 1933 by Walter Stiles and Brian Crawford(306) and is known today as the Stiles-Crawford effect. Based on observations with OCT and histology, we know punctate drusen elevate the RPE and photoreceptor layer resulting in axial displacement at the apex of each druse and an angular shift in the alignment of the photoreceptors along the edge of the druse. This is consistent with our observations of dark halos throughout the photoreceptor mosaic in patients with AMD. It should be noted that these features are not seen in young healthy patients or age-matched patients without visible perturbations in the outer retina. The shift in the alignment of photoreceptor cells would alter the acceptance angle of the cones with respect to the incident light projected onto the retina.

Although we were unable to demonstrate off-axis imaging in our AMD patients to test this theory, it is conceivable that some or all of the displaced photoreceptors may retain waveguide functionality. Likewise, we cannot state definitively that the reflective regions within the dark halos are viable cones. The separation of the RPE and photoreceptors from the choroidal blood supply almost certainly has a detrimental effect on the metabolic regulation of the outer retina and the turnover of the photoreceptor outer segments. Functional tests would likely reveal further information regarding the viability of these cells. Recent work by Tuten et al. utilized AO-SLO guided microperimetry to measure the response of individual photoreceptor cells which could be useful in determining the functionality of displaced cones(35).

Within the areas of GA, hyper-reflective features were noted but they did not exhibit characteristics generally attributed to photoreceptor cells. It is unlikely that cones would be able to survive without the underlying RPE to provide metabolic support. However, changes in the reflectance patter may provide some indication of tissue remodeling associated with the progressive enlargement of GA. Interestingly, we did not observe the hypo-reflective clusters (HRCs) recently described by Gocho et al(301). This may be the result of differing acquisition techniques (Flood Illumination vs. SLO) or the lack of longitudinal data in our analysis. Regardless, AO enhanced retinal imaging would provide an opportunity to investigate emerging therapies to recover the RPE and photoreceptor cells with tissue grafts or stem cell implants.

The analysis of local perturbations is a highly useful method of identifying tissue abnormalities, particularly within the perifovea where the density of the cone photoreceptors changes gradually as a function of eccentricity. This may limit the applications of the specified metrics within the cone-dense fovea but trade-offs in the optical design of the UTMB system prohibit reliably visualizing individual foveal cones. Future systems with the ability resolve the smallest foveal cones and peripheral rods may require more advanced analytical models to generate standard curves which accommodate for variations in factors such as axial length, refractive error, and eccentricity.

Chapter 9: Future Directions

9.1 Introduction

The advancement of ophthalmic imaging instrumentation has seen tremendous development over the past three decades. Many of the cutting-edge devices currently being tested have been adapted from existing technology and optimized for use in the eye. Adaptive optics (AO) is a prime example of implementing existing technology for biomedical applications. Much of the AO enhanced retinal imaging thus far has focused on the analysis of the photoreceptor mosaic. However, novel system designs and image processing techniques have revealed a wealth of information which may be beneficial for clinical diagnostics. For example, modifications to the configuration of the confocal pinhole or utilizing dark field aperture designs may be used to highlight specific features within the retina such as microvascular networks(22) and RPE cells(26). Characterization of the foveal avascular zone (FAZ) and the retinal capillary networks has been shown without introducing contrast agents by plotting standard error maps of the registered image sequences to reveal blood flow(20-22). Creative modifications to existing diagnostic techniques and improved analytical methodology have the potential to provide additional insight into pathogenesis of ocular disease. These emerging applications of AO could conceivably be used to investigate a variety of conditions affecting retinal vasculature such as capillary dropout in diabetic retinopathy (DR) and branch retinal vein occlusion (BRVO).

9.2 - Investigations into Normal Physiology and Retinal Pathology

A multitude of retinal diseases have already been explored using imaging systems enhanced by adaptive optics (AO) but most of these studies are limited to only a handful of cases. Efforts are also underway to compile data from multiple institutions, each utilizing custom instrumentation, to determine variability in morphometric parameters across a wider population. To date, variability in the cone photoreceptor population based on retinal eccentricity(270, 274, 290, 294), axial length of the eye (266), sampling window size(289), and age of the patient(271) have all been reported. The cone photoreceptors have been the natural target for AO retinal imaging investigations since they are instrumental in the transduction of visual signals, act as natural waveguides, and exhibit a bright reflectance pattern. Some examples of novel investigations into changes in the photoreceptor mosaic associated with multiple evanescent white dot syndrome (MEWDS) and cone-rod dystrophy are shown in Figure 9-1 and Figure 9-2, respectively.

Additional retinal features are also being investigated at a rapid pace. As mentioned previously, the RPE plays a prominent role in maintaining overall retinal health and regulation of the visual cycle. Therefore, this monolayer of cells is another desirable target for non-invasive, high-resolution imaging techniques. Recent studies have highlighted the potential for AO-SLO imaging of the RPE by capitalizing on the endogenous autofluorescence from lipofuscin in non-human primate models(24, 25), healthy volunteers(26), and patients with AMD(27). Similarly, high resolution images of the lamina cribrosa enhanced with AO(29, 307) are being used to investigate patients and animal models of glaucoma. We recently reported on the dynamics of a case of multiple evanescent white dot syndrome (MEWDS) utilizing a multimodal imaging approach

which included AO-SLO(308). Similar investigations will undoubtedly provide a better understanding of pathological processes associated with numerous ocular diseases.

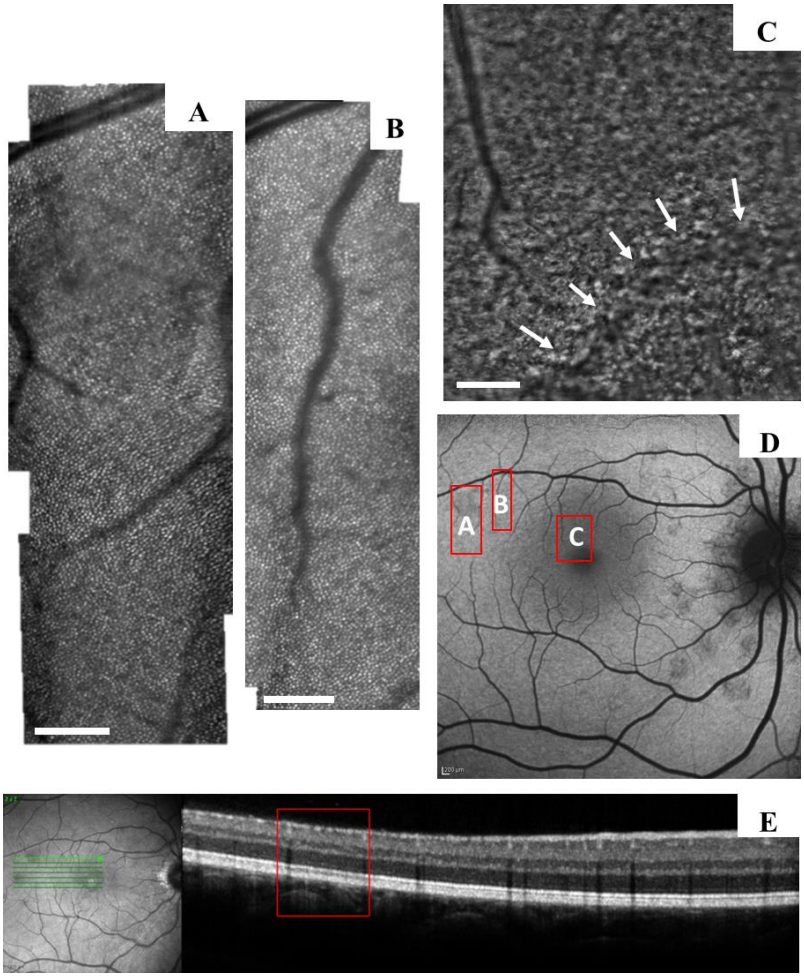

Figure 9-1. High resolution composite AO-SLO images of **(A)** perifoveal lesion [2.1° x 6.3°] **(B)** adjacent unaffected area [1.7° x 5.9°] **(C)** boundary of the foveal granularity observed during recurrent episode [3.9° x 4.3°]. **(D)** Overlay of the corresponding AO-SLO imaging regions on a wide field (30° x 30°) FAF image taken during initial clinical presentation. **(E)** SD-OCT cross-section at the perifoveal lesion site taken prior to AO-SLO imaging [width of red box corresponds to the width of the AO-SLO scan of the perifoveal lesion site from (A)]. All scale bars = 200 µm *(Figure modified from Boretsky et al 2013)*

Functional imaging is another promising direction for AO. The visualization of photoreceptors provides an opportunity to deliver a stimulus to an individual cell and measure the response to determine functional viability. Tuten *et al.*(35) recently reported

the development of an AO-SLO based microperimetry system which could be used to simultaneously investigate structure and function at a cellular level. Other aspects of retinal function and anatomy, such as the arrangement and distribution among different classes of cone photoreceptor cells(309, 310), have also been studied. These advancements have led to a much greater understanding of the underlying genes responsible for normal color vision in humans.

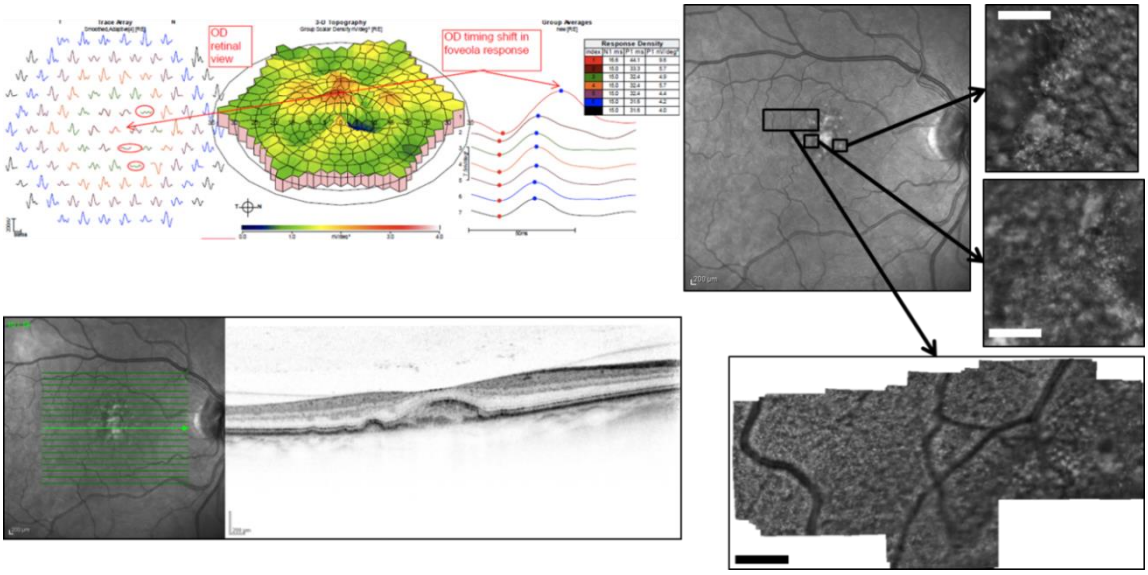

Figure 9-2. Multimodal imaging of a patient with Rod-cone dystrophy. Functional deficits noted using multifocal electroretinography were investigated with a clinical SD-OCT system and AO-SLO to correlate morphological alterations at a cellular level with reduced functional response in the macula.

9.3 – Next Frontier of Diagnostic Retinal Imaging

New techniques, collectively named super-resolution microscopy, have also been developed to go beyond the traditional diffraction limit which has long been held as a fundamental limitation in achievable resolution of optical imaging systems. Among these super-resolution techniques, structured illumination microscopy has already shown promise in *ex vivo* applications to visualize nano-scale features in retinal tissue such as

individual lipofuscin and melanolipofuscin granules(311, 312). As acquisition speed improves and effects of patient motion are mitigated, it is conceivable that structured illumination could provide an additional solution for *in vivo* cellular imaging without the complex optical components required for AO.

Non-linear optical imaging techniques have also shown great promise in the investigation of ocular tissue. The endogenous fluorophores present in the retina are well suited for detection using two-photon excited fluorescence microscopy which has recently been demonstrated in frog retinal tissue(228), mouse retinal tissue(227), and even *in vivo* in a non-human primate model(225). Monitoring changes in retinal autofluorescence properties is already used as a biomarker for certain disease but clinical imaging systems are limited to a 2 dimensional assessment of the FAF pattern. Multiphoton microscopy techniques would provide additional information regarding spatial orientation of retinal fluorophores seen in aging and disease.

9.4 – Adapting Instrumentation for Small Animal Models of Injury and Disease

As we have already demonstrated in our studies, small animal models of retinal injury and disease are particularly useful for investigating complex biological interactions and subtle changes in tissue morphology. Moreover, the rodent genome can be manipulated to help investigate the influence of specific molecules and the cellular response to an inducible disease state.

Clinical instruments and research instruments have been modified for use in small animal models. This will help characterize injury and disease non-invasively to ascertain the degree to which commonly used experimental models mimic human pathology. The

market for this technology has actually led to the development of companies devoted to the design of manufacture of small animal imaging instrumentation. Multiple reports have demonstrated a strong correlation between high resolution *in vivo* imaging data and traditional methods such as histology(121, 124). Additionally, the degree of detail visible in small animal models will continue to improve with the incorporation of AO as two groups recently demonstrated(261, 262).

9.5 – Characterization of emerging therapeutic intervention

The ultimate goal in translational research is the development of new techniques or strategies that can have an immediate impact on the wellbeing of patients. To that end, I believe that high resolution imaging of the retina will greatly improve early stage diagnosis of AMD prior to widespread vision loss. Furthermore, these new tools also have the ability to provide feedback on the efficacy of therapeutic intervention to identify the optimal course of treatment for each patient. Recent work by Talcott et al.(313) demonstrated this capability by utilizing AO-SLO to investigate the longitudinal effects of ciliary neurotrophic factor on patients with inherited retinal degenerations (retinitis pigmentosa and Usher syndrome type 2). Such investigations may also help expedite the clinical trial process by identifying early changes at a cellular level which would otherwise go undetected.

References

1. Boretsky A, Khan F, Burnett G, Hammer DX, Ferguson RD, van Kuijk F, Motamedi M. In vivo imaging of photoreceptor disruption associated with age-related macular degeneration: A pilot study. Lasers in Surgery and Medicine. 2012;44(8):603-10. doi: 10.1002/lsm.22070. PubMed PMID: WOS:000308885000001.

2. Helmholtz Hv. Beschreibung eines Augen-Spiegels zur Untersuchung der Netzhaut im lebenden Auge. Berlin,: Förstner; 1851. 43 p. p.

3. Webb RH, Hughes GW, Pomerantzeff O. Flying spot TV ophthalmoscope. Appl Opt. 1980;19(17):2991-7. PubMed PMID: 20234539.

4. Webb RH, Hughes GW. Scanning laser ophthalmoscope. IEEE Trans Biomed Eng. 1981;28(7):488-92. doi: 10.1109/TBME.1981.324734. PubMed PMID: 7275128.

5. Webb RH, Hughes GW, Delori FC. Confocal scanning laser ophthalmoscope. Appl Opt. 1987;26(8):1492-9. PubMed PMID: 20454349.

6. Delori FC, Dorey CK, Staurenghi G, Arend O, Goger DG, Weiter JJ. In vivo fluorescence of the ocular fundus exhibits retinal pigment epithelium lipofuscin characteristics. Invest Ophthalmol Vis Sci. 1995;36(3):718-29. PubMed PMID: 7890502.

7. Kennedy CJ, Rakoczy PE, Constable IJ. Lipofuscin of the retinal pigment epithelium: a review. Eye (Lond). 1995;9 (Pt 6):763-71. doi: 10.1038/eye.1995.192. PubMed PMID: 8849547.

8. Keilhauer CN, Delori FC. Near-infrared autofluorescence imaging of the fundus: visualization of ocular melanin. Invest Ophthalmol Vis Sci. 2006;47(8):3556-64. doi: 10.1167/iovs.06-0122. PubMed PMID: 16877429.

9. Weinberger AW, Lappas A, Kirschkamp T, Mazinani BA, Huth JK, Mohammadi B, Walter P. Fundus near infrared fluorescence correlates with fundus near infrared reflectance. Invest Ophthalmol Vis Sci. 2006;47(7):3098-108. doi: 10.1167/iovs.05-1104. PubMed PMID: 16799056.

10. Huang D, Wang J, Lin CP, Puliafito CA, Fujimoto JG. Micron-resolution ranging of cornea anterior chamber by optical reflectometry. Lasers Surg Med. 1991;11(5):419-25. PubMed PMID: 1816476.

11. Fercher AF, Hitzenberger CK, Drexler W, Kamp G, Sattmann H. In vivo optical coherence tomography. Am J Ophthalmol. 1993;116(1):113-4. PubMed PMID: 8328536.

12. Swanson EA, Izatt JA, Hee MR, Huang D, Lin CP, Schuman JS, Puliafito CA, Fujimoto JG. In vivo retinal imaging by optical coherence tomography. Opt Lett. 1993;18(21):1864-6. PubMed PMID: 19829430.

13. Swanson EA, Huang D, Hee MR, Fujimoto JG, Lin CP, Puliafito CA. High-speed optical coherence domain reflectometry. Opt Lett. 1992;17(2):151-3. PubMed PMID: 19784259.

14. Drexler W, Fujimoto JG. State-of-the-art retinal optical coherence tomography. Prog Retin Eye Res. 2008;27(1):45-88. doi: 10.1016/j.preteyeres.2007.07.005. PubMed PMID: 18036865.

15. Wang XJ, Milner TE, Nelson JS. Characterization of fluid flow velocity by optical Doppler tomography. Opt Lett. 1995;20(11):1337-9. PubMed PMID: 19859518.

16. Hee MR, Izatt JA, Swanson EA, Huang D, Schuman JS, Lin CP, Puliafito CA, Fujimoto JG. Optical coherence tomography of the human retina. Arch Ophthalmol. 1995;113(3):325-32. PubMed PMID: 7887846.

17. Liang J, Williams DR, Miller DT. Supernormal vision and high-resolution retinal imaging through adaptive optics. J Opt Soc Am A Opt Image Sci Vis. 1997;14(11):2884-92. PubMed PMID: 9379246.

18. Roorda A, Romero-Borja F, Donnelly Iii W, Queener H, Hebert T, Campbell M. Adaptive optics scanning laser ophthalmoscopy. Opt Express. 2002;10(9):405-12. doi: 68843 [pii]. PubMed PMID: 19436374.

19. Schwiegerling J. Field guide to visual and ophthalmic optics. Bellingham, Wash.: SPIE Press; 2004. xiii, 109 p. p.

20. Tam J, Martin JA, Roorda A. Noninvasive visualization and analysis of parafoveal capillaries in humans. Invest Ophthalmol Vis Sci. 2010;51(3):1691-8. doi: 10.1167/iovs.09-4483. PubMed PMID: 19907024; PubMed Central PMCID: PMCPMC2868418.

21. Tam J, Dhamdhere KP, Tiruveedhula P, Lujan BJ, Johnson RN, Bearse MA, Adams AJ, Roorda A. Subclinical capillary changes in non-proliferative diabetic retinopathy. Optom Vis Sci. 2012;89(5):E692-703. doi: 10.1097/OPX.0b013e3182548b07. PubMed PMID: 22525131; PubMed Central PMCID: PMCPMC3348374.

22. Chui TY, Vannasdale DA, Burns SA. The use of forward scatter to improve retinal vascular imaging with an adaptive optics scanning laser ophthalmoscope. Biomed Opt Express. 2012;3(10):2537-49. doi: 10.1364/BOE.3.002537. PubMed PMID: 23082294; PubMed Central PMCID: PMCPMC3470005.

23. Chui TY, Gast TJ, Burns SA. Imaging of vascular wall fine structure in the human retina using adaptive optics scanning laser ophthalmoscopy. Invest Ophthalmol Vis Sci. 2013;54(10):7115-24. doi: 10.1167/iovs.13-13027. PubMed PMID: 24071955; PubMed Central PMCID: PMCPMC3813321.

24. Morgan J, Hunter J, Masella B, Wolfe R, Gray D, Merigan W, Delori F, Williams D. Light-induced retinal changes observed with high-resolution autofluorescence imaging of the retinal pigment epithelium. Investigative Ophthalmology & Visual Science. 2008:3715-29. doi: DOI 10.1167/iovs.07-1430. PubMed PMID: ISI:000257951100060.

25. Morgan J, Hunter J, Merigan W, Williams D. The Reduction of Retinal Autofluorescence Caused by Light Exposure. Investigative Ophthalmology & Visual Science. 2009:6015-22. doi: DOI 10.1167/iovs.09-3643. PubMed PMID: ISI:000272355900067.

26. Scoles D, Sulai YN, Dubra A. In vivo dark-field imaging of the retinal pigment epithelium cell mosaic. Biomed Opt Express. 2013;4(9):1710-23. doi: 10.1364/BOE.4.001710. PubMed PMID: 24049692; PubMed Central PMCID: PMCPMC3771842.

27. Rossi EA, Rangel-Fonseca P, Parkins K, Fischer W, Latchney LR, Folwell MA, Williams DR, Dubra A, Chung MM. In vivo imaging of retinal pigment epithelium cells in age related macular degeneration. Biomed Opt Express. 2013;4(11):2527-39. doi: 10.1364/BOE.4.002527. PubMed PMID: 24298413; PubMed Central PMCID: PMCPMC3829547.

28. Akagi T, Hangai M, Takayama K, Nonaka A, Ooto S, Yoshimura N. In vivo imaging of lamina cribrosa pores by adaptive optics scanning laser ophthalmoscopy. Invest Ophthalmol Vis Sci. 2012;53(7):4111-9. doi: 10.1167/iovs.11-7536. PubMed PMID: 22669726.

29. Sredar N, Ivers KM, Queener HM, Zouridakis G, Porter J. 3D modeling to characterize lamina cribrosa surface and pore geometries using in vivo images from normal and glaucomatous eyes. Biomed Opt Express. 2013;4(7):1153-65. doi: 10.1364/BOE.4.001153. PubMed PMID: 23847739; PubMed Central PMCID: PMCPMC3704095.

30. Lai TY, Chan WM, Lai RY, Ngai JW, Li H, Lam DS. The clinical applications of multifocal electroretinography: a systematic review. Surv Ophthalmol. 2007;52(1):61-96. doi: 10.1016/j.survophthal.2006.10.005. PubMed PMID: 17212991.

31. Ferguson RD, Zhong Z, Hammer DX, Mujat M, Patel AH, Deng C, Zou W, Burns SA. Adaptive optics scanning laser ophthalmoscope with integrated wide-field retinal imaging and tracking. J Opt Soc Am A Opt Image Sci Vis. 2010;27(11):A265-77. doi: 206667 [pii]. PubMed PMID: 21045887; PubMed Central PMCID: PMCPMC3071649.

32. Hammer DX, Ferguson RD, Mujat M, Patel A, Plumb E, Iftimia N, Chui TY, Akula JD, Fulton AB. Multimodal adaptive optics retinal imager: design and performance. J Opt Soc Am A Opt Image Sci Vis. 2012;29(12):2598-607. PubMed PMID: 23455909.

33. Mujat M, Ferguson RD, Patel AH, Iftimia N, Lue N, Hammer DX. High resolution multimodal clinical ophthalmic imaging system. Opt Express. 2010;18(11):11607-21. doi: 199594 [pii]. PubMed PMID: 20589021; PubMed Central PMCID: PMCPMC2958093.

34. Zawadzki RJ, Jones SM, Pilli S, Balderas-Mata S, Kim DY, Olivier SS, Werner JS. Integrated adaptive optics optical coherence tomography and adaptive optics scanning laser ophthalmoscope system for simultaneous cellular resolution in vivo retinal imaging. Biomed Opt Express. 2011;2(6):1674-86. doi: 10.1364/BOE.2.001674. PubMed PMID: 21698028; PubMed Central PMCID: PMCPMC3114233.

35. Tuten WS, Tiruveedhula P, Roorda A. Adaptive optics scanning laser ophthalmoscope-based microperimetry. Optom Vis Sci. 2012;89(5):563-74. doi: 10.1097/OPX.0b013e3182512b98. PubMed PMID: 22446720; PubMed Central PMCID: PMCPMC3348404.

36. Resnikoff S, Pascolini D, Etya'ale D, Kocur I, Pararajasegaram R, Pokharel GP, Mariotti SP. Global data on visual impairment in the year 2002. Bull World Health Organ. 2004;82(11):844-51. doi: /S0042-96862004001100009. PubMed PMID: 15640920; PubMed Central PMCID: PMCPMC2623053.

37. Friedman DS, O'Colmain BJ, Muñoz B, Tomany SC, McCarty C, de Jong PT, Nemesure B, Mitchell P, Kempen J, Group EDPR. Prevalence of age-related macular degeneration in the United States. Arch Ophthalmol. 2004;122(4):564-72. doi: 10.1001/archopht.122.4.564. PubMed PMID: 15078675.

38. Klein R, Chou CF, Klein BE, Zhang X, Meuer SM, Saaddine JB. Prevalence of age-related macular degeneration in the US population. Arch Ophthalmol. 2011;129(1):75-80. doi: 129/1/75 [pii] 10.1001/archophthalmol.2010.318. PubMed PMID: 21220632.

39. Group A-REDSR. A randomized, placebo-controlled, clinical trial of high-dose supplementation with vitamins C and E, beta carotene, and zinc for age-related macular degeneration and vision loss: AREDS report no. 8. Arch Ophthalmol. 2001;119(10):1417-36. PubMed PMID: 11594942; PubMed Central PMCID: PMCPMC1462955.

40. Barker FM. Dietary supplementation: effects on visual performance and occurrence of AMD and cataracts. Curr Med Res Opin. 2010;26(8):2011-23. doi: 10.1185/03007995.2010.494549. PubMed PMID: 20590393.

41. Access Economics 2010. The Global Economic Cost of Visual Impairment, report prepared for AMD Alliance International. 2010.

42. Leske MC, Wu SY, Hennis A, Nemesure B, Yang L, Hyman L, Schachat AP, Group BES. Nine-year incidence of age-related macular degeneration in the Barbados Eye Studies. Ophthalmology. 2006;113(1):29-35. doi: 10.1016/j.ophtha.2005.08.012. PubMed PMID: 16290049.

43. Kawasaki R, Wang JJ, Ji GJ, Taylor B, Oizumi T, Daimon M, Kato T, Kawata S, Kayama T, Tano Y, Mitchell P, Yamashita H, Wong TY. Prevalence and risk factors for age-related macular degeneration in an adult Japanese population: the Funagata study. Ophthalmology. 2008;115(8):1376-81, 81.e1-2. doi: 10.1016/j.ophtha.2007.11.015. PubMed PMID: 18222000.

44. Krishnaiah S, Das T, Nirmalan PK, Nutheti R, Shamanna BR, Rao GN, Thomas R. Risk factors for age-related macular degeneration: findings from the Andhra Pradesh eye disease study in South India. Invest Ophthalmol Vis Sci. 2005;46(12):4442-9. doi: 10.1167/iovs.05-0853. PubMed PMID: 16303932.

45. You QS, Xu L, Yang H, Li YB, Wang S, Wang JD, Zhang JS, Wang YX, Jonas JB. Five-year incidence of age-related macular degeneration: the Beijing Eye Study. Ophthalmology. 2012;119(12):2519-25. doi: 10.1016/j.ophtha.2012.06.043. PubMed PMID: 22921389.

46. Andersen MV, Rosenberg T, la Cour M, Kiilgaard JF, Prause JU, Alsbirk PH, Borch-Johnsen K, Peto T, Carstensen B, Bird AC. Prevalence of age-related maculopathy and age-related macular degeneration among the inuit in Greenland. The Greenland Inuit Eye Study. Ophthalmology. 2008;115(4):700-7.e1. doi: 10.1016/j.ophtha.2007.12.013. PubMed PMID: 18267341.

47. Beatty S, Koh H, Phil M, Henson D, Boulton M. The role of oxidative stress in the pathogenesis of age-related macular degeneration. Surv Ophthalmol. 2000;45(2):115-34. PubMed PMID: 11033038.

48. Algvere PV, Marshall J, Seregard S. Age-related maculopathy and the impact of blue light hazard. Acta Ophthalmol Scand. 2006;84(1):4-15. doi: 10.1111/j.1600-0420.2005.00627.x. PubMed PMID: 16445433.

49. Delcourt C, Carrière I, Delage M, Barberger-Gateau P, Schalch W, Group PS. Plasma lutein and zeaxanthin and other carotenoids as modifiable risk factors for age-related maculopathy and cataract: the POLA Study. Invest Ophthalmol Vis Sci. 2006;47(6):2329-35. doi: 10.1167/iovs.05-1235. PubMed PMID: 16723441.

50. Wang L, Gaziano JM, Norkus EP, Buring JE, Sesso HD. Associations of plasma carotenoids with risk factors and biomarkers related to cardiovascular disease in middle-aged and older women. Am J Clin Nutr. 2008;88(3):747-54. PubMed PMID: 18779292; PubMed Central PMCID: PMCPMC2559966.

51. Parekh N, Voland RP, Moeller SM, Blodi BA, Ritenbaugh C, Chappell RJ, Wallace RB, Mares JA, Group CRS. Association between dietary fat intake and age-related macular degeneration in the Carotenoids in Age-Related Eye Disease Study (CAREDS): an ancillary study of the Women's Health Initiative. Arch Ophthalmol. 2009;127(11):1483-93. doi: 10.1001/archophthalmol.2009.130. PubMed PMID: 19901214; PubMed Central PMCID: PMCPMC3144752.

52. SanGiovanni JP, Chew EY. The role of omega-3 long-chain polyunsaturated fatty acids in health and disease of the retina. Prog Retin Eye Res. 2005;24(1):87-138. doi: 10.1016/j.preteyeres.2004.06.002. PubMed PMID: 15555528.

53. Sangiovanni JP, Agrón E, Meleth AD, Reed GF, Sperduto RD, Clemons TE, Chew EY, Group A-REDSR. {omega}-3 Long-chain polyunsaturated fatty acid intake and 12-y incidence of neovascular age-related macular degeneration and central geographic atrophy: AREDS report 30, a prospective cohort study from the Age-Related Eye Disease Study. Am J Clin Nutr. 2009;90(6):1601-7. doi: 10.3945/ajcn.2009.27594. PubMed PMID: 19812176; PubMed Central PMCID: PMCPMC2777471.

54. Klein BE, Knudtson MD, Lee KE, Reinke JO, Danforth LG, Wealti AM, Moore E, Klein R. Supplements and age-related eye conditions the beaver dam eye study. Ophthalmology. 2008;115(7):1203-8. doi: 10.1016/j.ophtha.2007.09.011. PubMed PMID: 17997484.

55. Goverdhan SV, Hannan S, Newsom RB, Luff AJ, Griffiths H, Lotery AJ. An analysis of the CFH Y402H genotype in AMD patients and controls from the UK, and response to PDT treatment. Eye (Lond). 2008;22(6):849-54. doi: 10.1038/sj.eye.6702830. PubMed PMID: 17464302.

56. Brantley MA, Edelstein SL, King JM, Plotzke MR, Apte RS, Kymes SM, Shiels A. Association of complement factor H and LOC387715 genotypes with response of exudative age-related macular degeneration to photodynamic therapy. Eye (Lond). 2009;23(3):626-31. doi: 10.1038/eye.2008.28. PubMed PMID: 18292785.

57. Hageman GS, Anderson DH, Johnson LV, Hancox LS, Taiber AJ, Hardisty LI, Hageman JL, Stockman HA, Borchardt JD, Gehrs KM, Smith RJ, Silvestri G, Russell SR, Klaver CC, Barbazetto I, Chang S, Yannuzzi LA, Barile GR, Merriam JC, Smith RT, Olsh AK, Bergeron J, Zernant J, Merriam JE, Gold B, Dean M, Allikmets R. A common haplotype in the complement regulatory gene factor H (HF1/CFH) predisposes individuals to age-related macular degeneration. Proc Natl Acad Sci U S A. 2005;102(20):7227-32. doi: 10.1073/pnas.0501536102. PubMed PMID: 15870199; PubMed Central PMCID: PMCPMC1088171.

58. Edwards AO, Ritter R, Abel KJ, Manning A, Panhuysen C, Farrer LA. Complement factor H polymorphism and age-related macular degeneration.

Science. 2005;308(5720):421-4. doi: 10.1126/science.1110189. PubMed PMID: 15761121.

59. Klein RJ, Zeiss C, Chew EY, Tsai JY, Sackler RS, Haynes C, Henning AK, SanGiovanni JP, Mane SM, Mayne ST, Bracken MB, Ferris FL, Ott J, Barnstable C, Hoh J. Complement factor H polymorphism in age-related macular degeneration. Science. 2005;308(5720):385-9. doi: 10.1126/science.1109557. PubMed PMID: 15761122; PubMed Central PMCID: PMCPMC1512523.

60. Haines JL, Hauser MA, Schmidt S, Scott WK, Olson LM, Gallins P, Spencer KL, Kwan SY, Noureddine M, Gilbert JR, Schnetz-Boutaud N, Agarwal A, Postel EA, Pericak-Vance MA. Complement factor H variant increases the risk of age-related macular degeneration. Science. 2005;308(5720):419-21. doi: 10.1126/science.1110359. PubMed PMID: 15761120.

61. Rodríguez de Córdoba S, Esparza-Gordillo J, Goicoechea de Jorge E, Lopez-Trascasa M, Sánchez-Corral P. The human complement factor H: functional roles, genetic variations and disease associations. Mol Immunol. 2004;41(4):355-67. doi: 10.1016/j.molimm.2004.02.005. PubMed PMID: 15163532.

62. Gold B, Merriam JE, Zernant J, Hancox LS, Taiber AJ, Gehrs K, Cramer K, Neel J, Bergeron J, Barile GR, Smith RT, Hageman GS, Dean M, Allikmets R, Group AGCS. Variation in factor B (BF) and complement component 2 (C2) genes is associated with age-related macular degeneration. Nat Genet. 2006;38(4):458-62. doi: 10.1038/ng1750. PubMed PMID: 16518403; PubMed Central PMCID: PMCPMC2921703.

63. van de Ven JP, Nilsson SC, Tan PL, Buitendijk GH, Ristau T, Mohlin FC, Nabuurs SB, Schoenmaker-Koller FE, Smailhodzic D, Campochiaro PA, Zack DJ, Duvvari MR, Bakker B, Paun CC, Boon CJ, Uitterlinden AG, Liakopoulos S, Klevering BJ, Fauser S, Daha MR, Katsanis N, Klaver CC, Blom AM, Hoyng CB, den Hollander AI. A functional variant in the CFI gene confers a high risk of age-related macular degeneration. Nat Genet. 2013;45(7):813-7. doi: 10.1038/ng.2640. PubMed PMID: 23685748.

64. Sun C, Zhao M, Li X. CFB/C2 gene polymorphisms and risk of age-related macular degeneration: a systematic review and meta-analysis. Curr Eye Res. 2012;37(4):259-71. doi: 10.3109/02713683.2011.635401. PubMed PMID: 22440158.

65. Yates JR, Sepp T, Matharu BK, Khan JC, Thurlby DA, Shahid H, Clayton DG, Hayward C, Morgan J, Wright AF, Armbrecht AM, Dhillon B, Deary IJ, Redmond E, Bird AC, Moore AT, Group GFiAS. Complement C3 variant and the risk of age-related macular degeneration. N Engl J Med. 2007;357(6):553-61. doi: 10.1056/NEJMoa072618. PubMed PMID: 17634448.

66. Kanda A, Chen W, Othman M, Branham KE, Brooks M, Khanna R, He S, Lyons R, Abecasis GR, Swaroop A. A variant of mitochondrial protein

LOC387715/ARMS2, not HTRA1, is strongly associated with age-related macular degeneration. Proc Natl Acad Sci U S A. 2007;104(41):16227-32. doi: 10.1073/pnas.0703933104. PubMed PMID: 17884985; PubMed Central PMCID: PMCPMC1987388.

67. Fritsche LG, Loenhardt T, Janssen A, Fisher SA, Rivera A, Keilhauer CN, Weber BH. Age-related macular degeneration is associated with an unstable ARMS2 (LOC387715) mRNA. Nat Genet. 2008;40(7):892-6. doi: 10.1038/ng.170. PubMed PMID: 18511946.

68. Barron MJ, Johnson MA, Andrews RM, Clarke MP, Griffiths PG, Bristow E, He LP, Durham S, Turnbull DM. Mitochondrial abnormalities in ageing macular photoreceptors. Invest Ophthalmol Vis Sci. 2001;42(12):3016-22. PubMed PMID: 11687550.

69. Feher J, Kovacs I, Artico M, Cavallotti C, Papale A, Balacco Gabrieli C. Mitochondrial alterations of retinal pigment epithelium in age-related macular degeneration. Neurobiol Aging. 2006;27(7):983-93. doi: 10.1016/j.neurobiolaging.2005.05.012. PubMed PMID: 15979212.

70. Liang FQ, Godley BF. Oxidative stress-induced mitochondrial DNA damage in human retinal pigment epithelial cells: a possible mechanism for RPE aging and age-related macular degeneration. Exp Eye Res. 2003;76(4):397-403. PubMed PMID: 12634104.

71. Jarrett SG, Lin H, Godley BF, Boulton ME. Mitochondrial DNA damage and its potential role in retinal degeneration. Prog Retin Eye Res. 2008;27(6):596-607. doi: 10.1016/j.preteyeres.2008.09.001. PubMed PMID: 18848639.

72. Wang AL, Lukas TJ, Yuan M, Neufeld AH. Increased mitochondrial DNA damage and down-regulation of DNA repair enzymes in aged rodent retinal pigment epithelium and choroid. Mol Vis. 2008;14:644-51. PubMed PMID: 18392142; PubMed Central PMCID: PMCPMC2288587.

73. Wang AL, Lukas TJ, Yuan M, Neufeld AH. Age-related increase in mitochondrial DNA damage and loss of DNA repair capacity in the neural retina. Neurobiol Aging. 2010;31(11):2002-10. doi: 10.1016/j.neurobiolaging.2008.10.019. PubMed PMID: 19084291.

74. Conley YP, Jakobsdottir J, Mah T, Weeks DE, Klein R, Kuller L, Ferrell RE, Gorin MB. CFH, ELOVL4, PLEKHA1 and LOC387715 genes and susceptibility to age-related maculopathy: AREDS and CHS cohorts and meta-analyses. Hum Mol Genet. 2006;15(21):3206-18. doi: 10.1093/hmg/ddl396. PubMed PMID: 17000705.

75. Ramrattan RS, van der Schaft TL, Mooy CM, de Bruijn WC, Mulder PG, de Jong PT. Morphometric analysis of Bruch's membrane, the choriocapillaris, and the

choroid in aging. Invest Ophthalmol Vis Sci. 1994;35(6):2857-64. PubMed PMID: 8188481.

76. Grunwald JE, Hariprasad SM, DuPont J. Effect of aging on foveolar choroidal circulation. Arch Ophthalmol. 1998;116(2):150-4. PubMed PMID: 9488265.

77. Grunwald JE, Hariprasad SM, DuPont J, Maguire MG, Fine SL, Brucker AJ, Maguire AM, Ho AC. Foveolar choroidal blood flow in age-related macular degeneration. Invest Ophthalmol Vis Sci. 1998;39(2):385-90. PubMed PMID: 9477998.

78. Guymer R, Luthert P, Bird A. Changes in Bruch's membrane and related structures with age. Prog Retin Eye Res. 1999;18(1):59-90. PubMed PMID: 9920499.

79. Booij JC, Baas DC, Beisekeeva J, Gorgels TG, Bergen AA. The dynamic nature of Bruch's membrane. Prog Retin Eye Res. 2010;29(1):1-18. doi: 10.1016/j.preteyeres.2009.08.003. PubMed PMID: 19747980.

80. Handa JT, Verzijl N, Matsunaga H, Aotaki-Keen A, Lutty GA, te Koppele JM, Miyata T, Hjelmeland LM. Increase in the advanced glycation end product pentosidine in Bruch's membrane with age. Invest Ophthalmol Vis Sci. 1999;40(3):775-9. PubMed PMID: 10067983.

81. Chong NH, Keonin J, Luthert PJ, Frennesson CI, Weingeist DM, Wolf RL, Mullins RF, Hageman GS. Decreased thickness and integrity of the macular elastic layer of Bruch's membrane correspond to the distribution of lesions associated with age-related macular degeneration. Am J Pathol. 2005;166(1):241-51. doi: 10.1016/S0002-9440(10)62248-1. PubMed PMID: 15632016; PubMed Central PMCID: PMCPMC1602307.

82. Bergmann M, Schütt F, Holz FG, Kopitz J. Inhibition of the ATP-driven proton pump in RPE lysosomes by the major lipofuscin fluorophore A2-E may contribute to the pathogenesis of age-related macular degeneration. FASEB J. 2004;18(3):562-4. doi: 10.1096/fj.03-0289fje. PubMed PMID: 14715704.

83. Hageman GS, Luthert PJ, Victor Chong NH, Johnson LV, Anderson DH, Mullins RF. An integrated hypothesis that considers drusen as biomarkers of immune-mediated processes at the RPE-Bruch's membrane interface in aging and age-related macular degeneration. Prog Retin Eye Res. 2001;20(6):705-32. doi: S1350946201000106 [pii]. PubMed PMID: 11587915.

84. Buschini E, Piras A, Nuzzi R, Vercelli A. Age related macular degeneration and drusen: Neuroinflammation in the retina. Progress in Neurobiology. 2011;95(1):14-25. doi: 10.1016/j.pneurobio.2011.05.011. PubMed PMID: WOS:000294943600002.

85. Xu H, Chen M, Forrester JV. Para-inflammation in the aging retina. Prog Retin Eye Res. 2009;28(5):348-68. doi: S1350-9462(09)00034-2 [pii]

10.1016/j.preteyeres.2009.06.001. PubMed PMID: 19560552.

86. Anderson DH, Mullins RF, Hageman GS, Johnson LV. A role for local inflammation in the formation of drusen in the aging eye. Am J Ophthalmol. 2002;134(3):411-31. PubMed PMID: 12208254.

87. Parmeggiani F, Romano MR, Costagliola C, Semeraro F, Incorvaia C, D'Angelo S, Perri P, De Palma P, De Nadai K, Sebastiani A. Mechanism of inflammation in age-related macular degeneration. Mediators Inflamm. 2012;2012:546786. doi: 10.1155/2012/546786. PubMed PMID: 23209345; PubMed Central PMCID: PMCPMC3504473.

88. Pauleikhoff D, Barondes MJ, Minassian D, Chisholm IH, Bird AC. Drusen as risk factors in age-related macular disease. Am J Ophthalmol. 1990;109(1):38-43. PubMed PMID: 1688685.

89. Bressler NM, Silva JC, Bressler SB, Fine SL, Green WR. Clinicopathologic correlation of drusen and retinal pigment epithelial abnormalities in age-related macular degeneration. Retina. 1994;14(2):130-42. PubMed PMID: 8036323.

90. Klein ML, Ferris FL, Armstrong J, Hwang TS, Chew EY, Bressler SB, Chandra SR, Group AR. Retinal precursors and the development of geographic atrophy in age-related macular degeneration. Ophthalmology. 2008;115(6):1026-31. doi: S0161-6420(07)00933-5 [pii] 10.1016/j.ophtha.2007.08.030. PubMed PMID: 17981333.

91. Curcio CA, Presley JB, Malek G, Medeiros NE, Avery DV, Kruth HS. Esterified and unesterified cholesterol in drusen and basal deposits of eyes with age-related maculopathy. Exp Eye Res. 2005;81(6):731-41. doi: 10.1016/j.exer.2005.04.012. PubMed PMID: 16005869.

92. Mullins RF, Russell SR, Anderson DH, Hageman GS. Drusen associated with aging and age-related macular degeneration contain proteins common to extracellular deposits associated with atherosclerosis, elastosis, amyloidosis, and dense deposit disease. FASEB J. 2000;14(7):835-46. PubMed PMID: 10783137.

93. Ferris FL, Davis MD, Clemons TE, Lee LY, Chew EY, Lindblad AS, Milton RC, Bressler SB, Klein R, Group A-REDSAR. A simplified severity scale for age-related macular degeneration: AREDS Report No. 18. Arch Ophthalmol. 2005;123(11):1570-4. doi: 10.1001/archopht.123.11.1570. PubMed PMID: 16286620; PubMed Central PMCID: PMCPMC1473206.

94. Klein R, Klein BE, Tomany SC, Meuer SM, Huang GH. Ten-year incidence and progression of age-related maculopathy: The Beaver Dam eye study. Ophthalmology. 2002;109(10):1767-79. PubMed PMID: 12359593.

95. Curcio CA, Millican CL. Basal linear deposit and large drusen are specific for early age-related maculopathy. Arch Ophthalmol. 1999;117(3):329-39. PubMed PMID: 10088810.

96. Schmitz-Valckenberg S, Steinberg JS, Fleckenstein M, Visvalingam S, Brinkmann CK, Holz FG. Combined confocal scanning laser ophthalmoscopy and spectral-domain optical coherence tomography imaging of reticular drusen associated with age-related macular degeneration. Ophthalmology. 2010;117(6):1169-76. doi: 10.1016/j.ophtha.2009.10.044. PubMed PMID: 20163861.

97. Zweifel SA, Imamura Y, Spaide TC, Fujiwara T, Spaide RF. Prevalence and significance of subretinal drusenoid deposits (reticular pseudodrusen) in age-related macular degeneration. Ophthalmology. 2010;117(9):1775-81. doi: 10.1016/j.ophtha.2010.01.027. PubMed PMID: 20472293.

98. Klein R, Davis MD, Magli YL, Segal P, Klein BE, Hubbard L. The Wisconsin age-related maculopathy grading system. Ophthalmology. 1991;98(7):1128-34. PubMed PMID: 1843453.

99. Curcio CA, Medeiros NE, Millican CL. The Alabama Age-Related Macular Degeneration Grading System for donor eyes. Invest Ophthalmol Vis Sci. 1998;39(7):1085-96. PubMed PMID: 9620067.

100. Olsen TW, Feng X. The Minnesota Grading System of eye bank eyes for age-related macular degeneration. Invest Ophthalmol Vis Sci. 2004;45(12):4484-90. doi: 10.1167/iovs.04-0342. PubMed PMID: 15557458.

101. van der Schaft TL, de Bruijn WC, Mooy CM, Ketelaars DA, de Jong PT. Element analysis of the early stages of age-related macular degeneration. Arch Ophthalmol. 1992;110(3):389-94. PubMed PMID: 1543459.

102. Crabb JW, Miyagi M, Gu X, Shadrach K, West KA, Sakaguchi H, Kamei M, Hasan A, Yan L, Rayborn ME, Salomon RG, Hollyfield JG. Drusen proteome analysis: an approach to the etiology of age-related macular degeneration. Proc Natl Acad Sci U S A. 2002;99(23):14682-7. doi: 10.1073/pnas.222551899. PubMed PMID: 12391305; PubMed Central PMCID: PMCPMC137479.

103. Curcio CA, Presley JB, Millican CL, Medeiros NE. Basal deposits and drusen in eyes with age-related maculopathy: evidence for solid lipid particles. Exp Eye Res. 2005;80(6):761-75. doi: 10.1016/j.exer.2004.09.017. PubMed PMID: 15939032.

104. Wang L, Clark ME, Crossman DK, Kojima K, Messinger JD, Mobley JA, Curcio CA. Abundant lipid and protein components of drusen. PLoS One. 2010;5(4):e10329. doi: 10.1371/journal.pone.0010329. PubMed PMID: 20428236; PubMed Central PMCID: PMCPMC2859054.

105. Johnson LV, Leitner WP, Staples MK, Anderson DH. Complement activation and inflammatory processes in Drusen formation and age related macular degeneration. Exp Eye Res. 2001;73(6):887-96. doi: 10.1006/exer.2001.1094. PubMed PMID: 11846519.

106. Sunness JS, Gonzalez-Baron J, Applegate CA, Bressler NM, Tian Y, Hawkins B, Barron Y, Bergman A. Enlargement of atrophy and visual acuity loss in the geographic atrophy form of age-related macular degeneration. Ophthalmology. 1999;106(9):1768-79. doi: S0161-6420(99)90340-8 [pii] 10.1016/S0161-6420(99)90340-8. PubMed PMID: 10485549.

107. Sunness JS, Bressler NM, Tian Y, Alexander J, Applegate CA. Measuring geographic atrophy in advanced age-related macular degeneration. Invest Ophthalmol Vis Sci. 1999;40(8):1761-9. PubMed PMID: 10393046.

108. Lutty G, Grunwald J, Majji AB, Uyama M, Yoneya S. Changes in choriocapillaris and retinal pigment epithelium in age-related macular degeneration. Mol Vis. 1999;5:35. PubMed PMID: 10562659.

109. Holz FG, Bindewald-Wittich A, Fleckenstein M, Dreyhaupt J, Scholl HP, Schmitz-Valckenberg S, Group F-S. Progression of geographic atrophy and impact of fundus autofluorescence patterns in age-related macular degeneration. Am J Ophthalmol. 2007;143(3):463-72. doi: 10.1016/j.ajo.2006.11.041. PubMed PMID: 17239336.

110. Klein ML, Ferris FL, Francis PJ, Lindblad AS, Chew EY, Hamon SC, Ott J. Progression of geographic atrophy and genotype in age-related macular degeneration. Ophthalmology. 2010;117(8):1554-9, 9.e1. doi: 10.1016/j.ophtha.2009.12.012. PubMed PMID: 20381870; PubMed Central PMCID: PMCPMC2904435.

111. Lindblad AS, Lloyd PC, Clemons TE, Gensler GR, Ferris FL, Klein ML, Armstrong JR, Group A-REDSR. Change in area of geographic atrophy in the Age-Related Eye Disease Study: AREDS report number 26. Arch Ophthalmol. 2009;127(9):1168-74. doi: 10.1001/archophthalmol.2009.198. PubMed PMID: 19752426.

112. Fleckenstein M, Schmitz-Valckenberg S, Adrion C, Visvalingam S, Göbel AP, Mössner A, von Strachwitz CN, Mackensen F, Pauleikhoff D, Wolf S, Mansmann U, Holz FG, Group FS. Progression of age-related geographic atrophy: role of the fellow eye. Invest Ophthalmol Vis Sci. 2011;52(9):6552-7. doi: 10.1167/iovs.11-7298. PubMed PMID: 21757586.

113. Solbach U, Keilhauer C, Knabben H, Wolf S. Imaging of retinal autofluorescence in patients with age-related macular degeneration. Retina. 1997;17(5):385-9. PubMed PMID: 9355185.

114. von Rückmann A, Fitzke FW, Bird AC. Fundus autofluorescence in age-related macular disease imaged with a laser scanning ophthalmoscope. Invest Ophthalmol Vis Sci. 1997;38(2):478-86. PubMed PMID: 9040481.

115. Holz FG, Bellman C, Staudt S, Schütt F, Völcker HE. Fundus autofluorescence and development of geographic atrophy in age-related macular degeneration. Invest Ophthalmol Vis Sci. 2001;42(5):1051-6. PubMed PMID: 11274085.

116. Yehoshua Z, Rosenfeld PJ, Albini TA. Current Clinical Trials in Dry AMD and the Definition of Appropriate Clinical Outcome Measures. Semin Ophthalmol. 2011;26(3):167-80. doi: 10.3109/08820538.2011.577132. PubMed PMID: 21609230.

117. Schwartz SD, Hubschman JP, Heilwell G, Franco-Cardenas V, Pan CK, Ostrick RM, Mickunas E, Gay R, Klimanskaya I, Lanza R. Embryonic stem cell trials for macular degeneration: a preliminary report. Lancet. 2012;379(9817):713-20. doi: 10.1016/S0140-6736(12)60028-2. PubMed PMID: 22281388.

118. Ding JD, Johnson LV, Herrmann R, Farsiu S, Smith SG, Groelle M, Mace BE, Sullivan P, Jamison JA, Kelly U, Harrabi O, Bollini SS, Dilley J, Kobayashi D, Kuang B, Li W, Pons J, Lin JC, Bowes Rickman C. Anti-amyloid therapy protects against retinal pigmented epithelium damage and vision loss in a model of age-related macular degeneration. Proc Natl Acad Sci U S A. 2011;108(28):E279-87. doi: 10.1073/pnas.1100901108. PubMed PMID: 21690377; PubMed Central PMCID: PMCPMC3136266.

119. Troutbeck R, Al-Qureshi S, Guymer RH. Therapeutic targeting of the complement system in age-related macular degeneration: a review. Clin Experiment Ophthalmol. 2012;40(1):18-26. doi: 10.1111/j.1442-9071.2011.02581.x. PubMed PMID: 22304025.

120. Koss MJ, Kurz P, Tsobanelis T, Lehmacher W, Fassbender C, Klingel R, Koch FH. Prospective, randomized, controlled clinical study evaluating the efficacy of Rheopheresis for dry age-related macular degeneration. Dry AMD treatment with Rheopheresis Trial-ART. Graefes Arch Clin Exp Ophthalmol. 2009;247(10):1297-306. doi: 10.1007/s00417-009-1113-7. PubMed PMID: 19629514.

121. Fischer MD, Huber G, Beck SC, Tanimoto N, Muehlfriedel R, Fahl E, Grimm C, Wenzel A, Remé CE, van de Pavert SA, Wijnholds J, Pacal M, Bremner R, Seeliger MW. Noninvasive, in vivo assessment of mouse retinal structure using optical coherence tomography. PLoS One. 2009;4(10):e7507. doi: 10.1371/journal.pone.0007507. PubMed PMID: 19838301; PubMed Central PMCID: PMCPMC2759518.

122. Knott EJ, Sheets KG, Zhou Y, Gordon WC, Bazan NG. Spatial correlation of mouse photoreceptor-RPE thickness between SD-OCT and histology. Exp Eye

Res. 2011;92(2):155-60. doi: 10.1016/j.exer.2010.10.009. PubMed PMID: 21035444; PubMed Central PMCID: PMCPMC3169798.

123. Gabriele ML, Ishikawa H, Schuman JS, Bilonick RA, Kim J, Kagemann L, Wollstein G. Reproducibility of spectral-domain optical coherence tomography total retinal thickness measurements in mice. Invest Ophthalmol Vis Sci. 2010;51(12):6519-23. doi: iovs.10-5662 [pii] 10.1167/iovs.10-5662. PubMed PMID: 20574022.

124. Huber G, Beck SC, Grimm C, Sahaboglu-Tekgoz A, Paquet-Durand F, Wenzel A, Humphries P, Redmond TM, Seeliger MW, Fischer MD. Spectral domain optical coherence tomography in mouse models of retinal degeneration. Invest Ophthalmol Vis Sci. 2009;50(12):5888-95. doi: iovs.09-3724 [pii] 10.1167/iovs.09-3724. PubMed PMID: 19661229; PubMed Central PMCID: PMCPMC2800101.

125. Li Q, Zemel E, Miller B, Perlman I. Early retinal damage in experimental diabetes: electroretinographical and morphological observations. Exp Eye Res. 2002;74(5):615-25. doi: 10.1006/exer.2002.1170. PubMed PMID: 12076083.

126. Martin PM, Roon P, Van Ells TK, Ganapathy V, Smith SB. Death of retinal neurons in streptozotocin-induced diabetic mice. Invest Ophthalmol Vis Sci. 2004;45(9):3330-6. doi: 45/9/3330 [pii] 10.1167/iovs.04-0247. PubMed PMID: 15326158.

127. Park SH, Park JW, Park SJ, Kim KY, Chung JW, Chun MH, Oh SJ. Apoptotic death of photoreceptors in the streptozotocin-induced diabetic rat retina. Diabetologia. 2003;46(9):1260-8. doi: 10.1007/s00125-003-1177-6. PubMed PMID: 12898017.

128. Kern TS. Contributions of inflammatory processes to the development of the early stages of diabetic retinopathy. Exp Diabetes Res. 2007;2007:95103. doi: 10.1155/2007/95103. PubMed PMID: 18274606; PubMed Central PMCID: PMCPMC2216058.

129. Tirgan N, Boretsky A, Gupta P, Godley BF, Tilton RG, Motamedi M. Non-Invasive Monitoring of Changes in the Rat Retina Induced by Nicotine Toxicity and Diabetes Mellitus. Invest Ophthalmol Vis Sci. 2012;53(6):5361-.

130. Zhou X, Li F, Kong L, Tomita H, Li C, Cao W. Involvement of inflammation, degradation, and apoptosis in a mouse model of glaucoma. J Biol Chem. 2005;280(35):31240-8. doi: M502641200 [pii] 10.1074/jbc.M502641200. PubMed PMID: 15985430.

131. Wang AL, Carroll RC, Nawy S. Down-regulation of the RNA editing enzyme ADAR2 contributes to RGC death in a mouse model of glaucoma. PLoS One. 2014;9(3):e91288. doi: 10.1371/journal.pone.0091288. PubMed PMID: 24608178; PubMed Central PMCID: PMCPMC3946738.

132. Zhu Y, Zhang L, Schmidt JF, Gidday JM. Glaucoma-induced degeneration of retinal ganglion cells prevented by hypoxic preconditioning: a model of glaucoma tolerance. Mol Med. 2012;18:697-706. doi: 10.2119/molmed.2012.00050. PubMed PMID: 22396016; PubMed Central PMCID: PMCPMC3388129.

133. Zhao Z, Chen Y, Wang J, Sternberg P, Freeman ML, Grossniklaus HE, Cai J. Age-related retinopathy in NRF2-deficient mice. PLoS One. 2011;6(4):e19456. doi: 10.1371/journal.pone.0019456. PubMed PMID: 21559389; PubMed Central PMCID: PMCPMC3084871.

134. Begum R, Powner MB, Hudson N, Hogg C, Jeffery G. Treatment with 670 nm light up regulates cytochrome C oxidase expression and reduces inflammation in an age-related macular degeneration model. PLoS One. 2013;8(2):e57828. doi: 10.1371/journal.pone.0057828. PubMed PMID: 23469078; PubMed Central PMCID: PMCPMC3585189.

135. Elizabeth Rakoczy P, Yu MJ, Nusinowitz S, Chang B, Heckenlively JR. Mouse models of age-related macular degeneration. Exp Eye Res. 2006;82(5):741-52. doi: 10.1016/j.exer.2005.10.012. PubMed PMID: 16325179.

136. Justilien V, Pang JJ, Renganathan K, Zhan X, Crabb JW, Kim SR, Sparrow JR, Hauswirth WW, Lewin AS. SOD2 knockdown mouse model of early AMD. Invest Ophthalmol Vis Sci. 2007;48(10):4407-20. doi: 10.1167/iovs.07-0432. PubMed PMID: 17898259.

137. Rakoczy PE, Zhang D, Robertson T, Barnett NL, Papadimitriou J, Constable IJ, Lai CM. Progressive age-related changes similar to age-related macular degeneration in a transgenic mouse model. Am J Pathol. 2002;161(4):1515-24. doi: 10.1016/S0002-9440(10)64427-6. PubMed PMID: 12368224; PubMed Central PMCID: PMCPMC1867306.

138. Ramkumar HL, Zhang J, Chan CC. Retinal ultrastructure of murine models of dry age-related macular degeneration (AMD). Prog Retin Eye Res. 2010;29(3):169-90. doi: 10.1016/j.preteyeres.2010.02.002. PubMed PMID: 20206286; PubMed Central PMCID: PMCPMC2854213.

139. Weikel KA, Fitzgerald P, Shang F, Caceres MA, Bian Q, Handa JT, Stitt AW, Taylor A. Natural history of age-related retinal lesions that precede AMD in mice fed high or low glycemic index diets. Invest Ophthalmol Vis Sci. 2012;53(2):622-32. doi: 10.1167/iovs.11-8545. PubMed PMID: 22205601; PubMed Central PMCID: PMCPMC3317410.

140. Zeiss CJ. Animals as models of age-related macular degeneration: an imperfect measure of the truth. Vet Pathol. 2010;47(3):396-413. doi: 10.1177/0300985809359598. PubMed PMID: 20382825.

141. Edwards AO, Malek G. Molecular genetics of AMD and current animal models. Angiogenesis. 2007;10(2):119-32. doi: 10.1007/s10456-007-9064-2. PubMed PMID: 17372852.

142. Pennesi ME, Neuringer M, Courtney RJ. Animal models of age related macular degeneration. Mol Aspects Med. 2012;33(4):487-509. doi: 10.1016/j.mam.2012.06.003. PubMed PMID: 22705444; PubMed Central PMCID: PMCPMC3770531.

143. Remtulla S, Hallett PE. A schematic eye for the mouse, and comparisons with the rat. Vision Res. 1985;25(1):21-31. PubMed PMID: 3984214.

144. Hughes A. Schematic Eye For The Rat. Vision Research. 1979:569-88. PubMed PMID: ISI:A1979GT89900013.

145. Gross H. Handbook of optical systems. Weinheim: Wiley-VCH; 2005. v. <2, 5> p.

146. Geng Y, Schery LA, Sharma R, Dubra A, Ahmad K, Libby RT, Williams DR. Optical properties of the mouse eye. Biomed Opt Express. 2011;2(4):717-38. doi: 10.1364/BOE.2.000717. PubMed PMID: 21483598; PubMed Central PMCID: PMCPMC3072116.

147. Geng Y, Dubra A, Yin L, Merigan WH, Sharma R, Libby RT, Williams DR. Adaptive optics retinal imaging in the living mouse eye. Biomed Opt Express. 2012;3(4):715-34. Epub 2012/05/11. doi: 10.1364/boe.3.000715. PubMed PMID: 22574260; PubMed Central PMCID: PMCPmc3345801.

148. Woodell A, Coughlin B, Kunchithapautham K, Casey S, Williamson T, Ferrell WD, Atkinson C, Jones BW, Rohrer B. Alternative complement pathway deficiency ameliorates chronic smoke-induced functional and morphological ocular injury. PLoS One. 2013;8(6):e67894. doi: 10.1371/journal.pone.0067894. PubMed PMID: 23825688; PubMed Central PMCID: PMCPMC3692454.

149. Weng J, Mata NL, Azarian SM, Tzekov RT, Birch DG, Travis GH. Insights into the function of Rim protein in photoreceptors and etiology of Stargardt's disease from the phenotype in abcr knockout mice. Cell. 1999;98(1):13-23. doi: 10.1016/S0092-8674(00)80602-9. PubMed PMID: 10412977.

150. Karan G, Lillo C, Yang Z, Cameron DJ, Locke KG, Zhao Y, Thirumalaichary S, Li C, Birch DG, Vollmer-Snarr HR, Williams DS, Zhang K. Lipofuscin accumulation, abnormal electrophysiology, and photoreceptor degeneration in mutant ELOVL4 transgenic mice: a model for macular degeneration. Proc Natl Acad Sci U S A. 2005;102(11):4164-9. doi: 10.1073/pnas.0407698102. PubMed PMID: 15749821; PubMed Central PMCID: PMCPMC554798.

151. Charbel Issa P, Chong NV, Scholl HP. The significance of the complement system for the pathogenesis of age-related macular degeneration - current

evidence and translation into clinical application. Graefes Arch Clin Exp Ophthalmol. 2011;249(2):163-74. doi: 10.1007/s00417-010-1568-6. PubMed PMID: 21127893; PubMed Central PMCID: PMCPMC3042099.

152. Ambati J, Anand A, Fernandez S, Sakurai E, Lynn BC, Kuziel WA, Rollins BJ, Ambati BK. An animal model of age-related macular degeneration in senescent Ccl-2- or Ccr-2-deficient mice. Nat Med. 2003;9(11):1390-7. doi: 10.1038/nm950. PubMed PMID: 14566334.

153. Malek G, Johnson LV, Mace BE, Saloupis P, Schmechel DE, Rickman DW, Toth CA, Sullivan PM, Bowes Rickman C. Apolipoprotein E allele-dependent pathogenesis: a model for age-related retinal degeneration. Proc Natl Acad Sci U S A. 2005;102(33):11900-5. doi: 10.1073/pnas.0503015102. PubMed PMID: 16079201; PubMed Central PMCID: PMCPMC1187976.

154. Imamura Y, Noda S, Hashizume K, Shinoda K, Yamaguchi M, Uchiyama S, Shimizu T, Mizushima Y, Shirasawa T, Tsubota K. Drusen, choroidal neovascularization, and retinal pigment epithelium dysfunction in SOD1-deficient mice: a model of age-related macular degeneration. Proc Natl Acad Sci U S A. 2006;103(30):11282-7. doi: 10.1073/pnas.0602131103. PubMed PMID: 16844785; PubMed Central PMCID: PMCPMC1544079.

155. Wu T, Chen Y, Chiang SK, Tso MO. NF-kappaB activation in light-induced retinal degeneration in a mouse model. Invest Ophthalmol Vis Sci. 2002;43(9):2834-40. PubMed PMID: 12202499.

156. Yang LP, Zhu XA, Tso MO. A possible mechanism of microglia-photoreceptor crosstalk. Mol Vis. 2007;13:2048-57. doi: v13/a232 [pii]. PubMed PMID: 18079678.

157. Boretsky A, Motamedi M, Bell B, van Kuijk F. Quantitative Evaluation of Retinal Response to Laser Photocoagulation Using Dual-Wavelength Fundus Autofluorescence Imaging in a Small Animal Model. Investigative Ophthalmology & Visual Science. 2011;52(9):6300-7. doi: 10.1167/iovs.10-7033. PubMed PMID: WOS:000293849400034.

158. Belokopytov M, Belkin M, Dubinsky G, Epstein Y, Rosner M. Development and recovery of laser-induced retinal lesion in rats. Retina. 2010;30(4):662-70. doi: 10.1097/IAE.0b013e3181bd2fa9. PubMed PMID: 19996833.

159. Ben-Shlomo G, Belokopytov M, Rosner M, Dubinsky G, Belkin M, Epstein Y, Ofri R. Functional deficits resulting from laser-induced damage in the rat retina. Lasers in Surgery and Medicine. 2006:689-94. doi: DOI 10.1002/lsm.20351. PubMed PMID: ISI:000240304600007.

160. Jones BW, Marc RE, Watt CB, Vaughan DK, Organisciak DT. Neural plasticity revealed by light-induced photoreceptor lesions. Adv Exp Med Biol. 2006;572:405-10. doi: 10.1007/0-387-32442-9_57. PubMed PMID: 17249603.

161. Pocock GM, Boretsky A, Wang H-C, Golden D, Gupta P, Vargas G, Oliver JW, Motamedi M. NF-kB activation as a biomarker of light injury using a transgenic mouse model2012:822108-. doi: 10.1117/12.908835.

162. Kiuchi K, Yoshizawa K, Shikata N, Moriguchi K, Tsubura A. Morphologic characteristics of retinal degeneration induced by sodium iodate in mice. Curr Eye Res. 2002;25(6):373-9. PubMed PMID: 12789545.

163. Enzmann V, Row BW, Yamauchi Y, Kheirandish L, Gozal D, Kaplan HJ, McCall MA. Behavioral and anatomical abnormalities in a sodium iodate-induced model of retinal pigment epithelium degeneration. Exp Eye Res. 2006;82(3):441-8. doi: 10.1016/j.exer.2005.08.002. PubMed PMID: 16171805.

164. Kielland A, Carlsen H. Molecular imaging of transcriptional regulation during inflammation. J Inflamm (Lond). 2010;7:20. doi: 1476-9255-7-20 [pii] 10.1186/1476-9255-7-20. PubMed PMID: 20420665; PubMed Central PMCID: PMCPMC2883981.

165. Eter N, Engel DR, Meyer L, Helb HM, Roth F, Maurer J, Holz FG, Kurts C. In vivo visualization of dendritic cells, macrophages, and microglial cells responding to laser-induced damage in the fundus of the eye. Invest Ophthalmol Vis Sci. 2008;49(8):3649-58. doi: iovs.07-1322 [pii] 10.1167/iovs.07-1322. PubMed PMID: 18316698.

166. Magness ST, Jijon H, Van Houten Fisher N, Sharpless NE, Brenner DA, Jobin C. In vivo pattern of lipopolysaccharide and anti-CD3-induced NF-kappa B activation using a novel gene-targeted enhanced GFP reporter gene mouse. J Immunol. 2004;173(3):1561-70. doi: 173/3/1561 [pii]. PubMed PMID: 15265883.

167. Capozzi ME, Gordon AY, Penn JS, Jayagopal A. Molecular imaging of retinal disease. J Ocul Pharmacol Ther. 2013;29(2):275-86. doi: 10.1089/jop.2012.0279. PubMed PMID: 23421501; PubMed Central PMCID: PMCPMC3601716.

168. Jayagopal A, Russ PK, Haselton FR. Surface engineering of quantum dots for in vivo vascular imaging. Bioconjug Chem. 2007;18(5):1424-33. doi: 10.1021/bc070020r. PubMed PMID: 17760416; PubMed Central PMCID: PMCPMC2853010.

169. Glickman R. Phototoxicity to the retina: mechanisms of damage. Int J Toxicol. 2002;21(6):473-90. doi: QEKFWK622JVP5L7B [pii] 10.1080/10915810290169909. PubMed PMID: 12537644.

170. Dunsky I, Lappin P. Evaluation Of Retinal Thresholds For Cw Laser Radiation. Vision Research. 1971:733-&. PubMed PMID: ISI:A1971J951100011.

171. Baurmann H, Sasaki K, Chioralia G. Investigations On Laser Coagulated Rat Eyes By Fluorescence Angiography And Microscopy. Albrecht Von Graefes

Archiv Fur Klinische Und Experimentelle Ophthalmologie. 1975:245-52. PubMed PMID: ISI:A1975V732200002.

172. Schmitz-Valckenberg S, Guo L, Maass A, Cheung W, Vugler A, Moss S, Munro P, Fitzke F, Cordeiro M. Real-time in vivo imaging of retinal cell apoptosis after laser exposure. Investigative Ophthalmology & Visual Science. 2008:2773-80. doi: DOI 10.1167/iovs.07-1335. PubMed PMID: ISI:000256306800063.

173. Busch E, Gorgels T, van Norren D. Temporal sequence of changes in rat retina after UV-A and blue light exposure. Vision Research. 1999:1233-47. PubMed PMID: ISI:000078729400001.

174. Gorgels T, Vannorren D. Ultraviolet And Green Light Cause Different Types Of Damage In Rat Retina. Investigative Ophthalmology & Visual Science. 1995:851-63. PubMed PMID: ISI:A1995QQ75600012.

175. Gorgels T, van Norren D. Two spectral types of retinal light damage occur in albino as well as in pigmented rat: No essential role for melanin. Experimental Eye Research. 1998:155-62. PubMed PMID: ISI:000072044700004.

176. Ham W, Ruffolo J, Mueller H, Clarke A, Moon M. Histologic Analysis Of Photo-Chemical Lesions Produced In Rhesus Retina By Short-Wave-Length Light. Investigative Ophthalmology & Visual Science. 1978:1029-35. PubMed PMID: ISI:A1978FS93800010.

177. Wu J, Seregard S, Spangberg B, Oskarsson M, Chen E. Blue light induced apoptosis in rat retina. Eye. 1999:577-83. PubMed PMID: ISI:000082998400015.

178. Lund D, Beatrice E. Ocular Hazard Of Short Pulse Argon-Laser Irradiation. Health Physics. 1979:7-11. PubMed PMID: ISI:A1979GG06000002.

179. Jain A, Blumenkranz M, Paulus Y, Wiltberger M, Andersen D, Huie P, Palanker D. Effect of pulse duration on size and character of the lesion in retinal photocoagulation. Archives of Ophthalmology. 2008:78-85. PubMed PMID: ISI:000252312800011.

180. Paulus Y, Jain A, Gariano R, Stanzel B, Marmor M, Blumenkranz M, Palanker D. Healing of Retinal Photocoagulation Lesions. Investigative Ophthalmology & Visual Science. 2008:5540-5. doi: DOI 10.1167/iovs.08-1928. PubMed PMID: ISI:000261193900049.

181. Rapp L, Williams T. The Role Of Ocular Pigmentation In Protecting Against Retinal Light Damage. Vision Research. 1980:1127-31. PubMed PMID: ISI:A1980LA88100012.

182. Masuda K. Short Wavelength Light-Induced Retinal Damage in Rats. In: Watanabe I, editor. Japanese Journal of Ophthalmology2000. p. 615-9.

183. Glickman RD, Natarajan M, Rockwell B, Denton M, Maswadi S, Kumar N, Nieves-Roldan F, editors. Intracellular signaling mechanisms responsive to laser-induced photochemical and thermal stress. Conference on Optical Interactions with Tissue and Cells XVI; 2005 Jan 24-26; San Jose, CA.

184. Delori F, Goger D, Hammond B, Snodderly D, Burns S. Macular pigment density measured by autofluorescence spectrometry: comparison with reflectometry and heterochromatic flicker photometry. Journal of the Optical Society of America a-Optics Image Science and Vision. 2001:1212-30. PubMed PMID: ISI:000168938900002.

185. Boulton M, Docchio F, Dayhaw-Barker P, Ramponi R, Cubeddu R. Age-related changes in the morphology, absorption and fluorescence of melanosomes and lipofuscin granules of the retinal pigment epithelium. Vision Res. 1990;30(9):1291-303. doi: 0042-6989(90)90003-4 [pii]. PubMed PMID: 2219746.

186. Feeney-Burns L, Hilderbrand ES, Eldridge S. Aging human RPE: morphometric analysis of macular, equatorial, and peripheral cells. Invest Ophthalmol Vis Sci. 1984;25(2):195-200. PubMed PMID: 6698741.

187. Vonruckmann A, Fitzke F, Bird A. Distribution Of Fundus Autofluorescence With A Scanning Laser Ophthalmoscope. British Journal of Ophthalmology. 1995:407-12. PubMed PMID: ISI:A1995RA26000004.

188. Grey AC, Crouch RK, Koutalos Y, Schey KL, Ablonczy Z. Spatial localization of A2E in the retinal pigment epithelium. Invest Ophthalmol Vis Sci. 2011;52(7):3926-33. doi: 10.1167/iovs.10-7020. PubMed PMID: 21357388; PubMed Central PMCID: PMCPMC3175942.

189. Katz ML. Potential role of retinal pigment epithelial lipofuscin accumulation in age-related macular degeneration. Arch Gerontol Geriatr. 2002;34(3):359-70. PubMed PMID: 14764336.

190. Katz ML, Robison WG. What is lipofuscin? Defining characteristics and differentiation from other autofluorescent lysosomal storage bodies. Arch Gerontol Geriatr. 2002;34(3):169-84. PubMed PMID: 14764321.

191. Warburton S, Southwick K, Hardman RM, Secrest AM, Grow RK, Xin H, Woolley AT, Burton GF, Thulin CD. Examining the proteins of functional retinal lipofuscin using proteomic analysis as a guide for understanding its origin. Mol Vis. 2005;11:1122-34. PubMed PMID: 16379024.

192. Ng KP, Gugiu B, Renganathan K, Davies MW, Gu X, Crabb JS, Kim SR, Rózanowska MB, Bonilha VL, Rayborn ME, Salomon RG, Sparrow JR, Boulton ME, Hollyfield JG, Crabb JW. Retinal pigment epithelium lipofuscin proteomics. Mol Cell Proteomics. 2008;7(7):1397-405. doi: 10.1074/mcp.M700525-MCP200. PubMed PMID: 18436525; PubMed Central PMCID: PMCPMC2493379.

193. Sparrow JR, Nakanishi K, Parish CA. The lipofuscin fluorophore A2E mediates blue light-induced damage to retinal pigmented epithelial cells. Invest Ophthalmol Vis Sci. 2000;41(7):1981-9. PubMed PMID: 10845625.

194. Avalle LB, Wang Z, Dillon JP, Gaillard ER. Observation of A2E oxidation products in human retinal lipofuscin. Exp Eye Res. 2004;78(4):895-8. doi: 10.1016/j.exer.2003.10.023. PubMed PMID: 15037123.

195. Dillon J, Wang Z, Avalle LB, Gaillard ER. The photochemical oxidation of A2E results in the formation of a 5,8,5',8'-bis-furanoid oxide. Exp Eye Res. 2004;79(4):537-42. doi: 10.1016/j.exer.2004.06.024. PubMed PMID: 15381037.

196. Gaillard ER, Avalle LB, Keller LM, Wang Z, Reszka KJ, Dillon JP. A mechanistic study of the photooxidation of A2E, a component of human retinal lipofuscin. Exp Eye Res. 2004;79(3):313-9. doi: 10.1016/j.exer.2004.05.005. PubMed PMID: 15336493.

197. Zhou J, Jang YP, Kim SR, Sparrow JR. Complement activation by photooxidation products of A2E, a lipofuscin constituent of the retinal pigment epithelium. Proc Natl Acad Sci U S A. 2006;103(44):16182-7. doi: 10.1073/pnas.0604255103. PubMed PMID: 17060630; PubMed Central PMCID: PMCPMC1637557.

198. Zhou J, Kim SR, Westlund BS, Sparrow JR. Complement activation by bisretinoid constituents of RPE lipofuscin. Invest Ophthalmol Vis Sci. 2009;50(3):1392-9. doi: 10.1167/iovs.08-2868. PubMed PMID: 19029031; PubMed Central PMCID: PMCPMC2669319.

199. Lakkaraju A, Finnemann SC, Rodriguez-Boulan E. The lipofuscin fluorophore A2E perturbs cholesterol metabolism in retinal pigment epithelial cells. Proc Natl Acad Sci U S A. 2007;104(26):11026-31. doi: 10.1073/pnas.0702504104. PubMed PMID: 17578916; PubMed Central PMCID: PMCPMC1904145.

200. Marmorstein AD, Marmorstein LY, Sakaguchi H, Hollyfield JG. Spectral profiling of autofluorescence associated with lipofuscin, Bruch's Membrane, and sub-RPE deposits in normal and AMD eyes. Invest Ophthalmol Vis Sci. 2002;43(7):2435-41. PubMed PMID: 12091448.

201. Delori FC, Fleckner MR, Goger DG, Weiter JJ, Dorey CK. Autofluorescence distribution associated with drusen in age-related macular degeneration. Invest Ophthalmol Vis Sci. 2000;41(2):496-504. PubMed PMID: 10670481.

202. Framme C, Brinkmann R, Birngruber R, Roider J. Autofluorescence imaging after selective RPE laser treatment in macular diseases and clinical outcome: a pilot study. British Journal of Ophthalmology. 2002:1099-106. PubMed PMID: ISI:000178135200010.

203. Kellner U, Kellner S, Weinitz S. Fundus autofluorescence (488 NM) and near-infrared autofluorescence (787 NM) visualize different retinal pigment epithelium

alterations in patients with age-related macular degeneration. Retina. 2010;30(1):6-15. PubMed PMID: 20066766.

204. Delori FC, Staurenghi G, Arend O, Dorey CK, Goger DG, Weiter JJ. In vivo measurement of lipofuscin in Stargardt's disease--Fundus flavimaculatus. Invest Ophthalmol Vis Sci. 1995;36(11):2327-31. PubMed PMID: 7558729.

205. Lois N, Halfyard A, Bird A, Holder G, Fitzke F. Fundus autofluorescence in Stargardt macular dystrophy-fundus flavimaculatus. American Journal of Ophthalmology. 2004:55-63. doi: DOI 10.1016/j.ajo.2004.02.056. PubMed PMID: ISI:000222568200007.

206. Lois N, Halfyard A, Bird A, Fitzke F. Quantitative evaluation of fundus autofluorescence imaged "in vivo" in eyes with retinal disease. British Journal of Ophthalmology. 2000:741-5. PubMed PMID: ISI:000088067000017.

207. Dobi ET, Puliafito CA, Destro M. A new model of experimental choroidal neovascularization in the rat. Arch Ophthalmol. 1989;107(2):264-9. PubMed PMID: 2464985.

208. Frank RN, Das A, Weber ML. A model of subretinal neovascularization in the pigmented rat. Curr Eye Res. 1989;8(3):239-47. PubMed PMID: 2468453.

209. Busch E, Gorgels T, van Norren D. Filling-in after focal loss of photoreceptors in rat retina. Experimental Eye Research. 1999:485-92. PubMed PMID: ISI:000079745000011.

210. Vannorren D, Schellekens P. Blue-Light Hazard In Rat. Vision Research. 1990:1517-20. PubMed PMID: ISI:A1990DX33300013.

211. Framme C, Roider J. Immediate and long-term changes of fundus autofluorescence in continuous wave laser lesions of the retina. Ophthalmic Surgery Lasers & Imaging. 2004:131-8. PubMed PMID: ISI:000220206100006.

212. Denton M, Foltz M, Estlack L, Stolarski D, Noojin G, Thomas R, Eikum D, Rockwell B. Damage thresholds for exposure to NIR and blue lasers in an in vitro RPE cell system. Investigative Ophthalmology & Visual Science. 2006:3065-73. doi: DOI 10.1167/iovs.05-1066. PubMed PMID: ISI:000238688600045.

213. Denton M, Foltz M, Schuster K, Estlack L, Thomas R. Damage thresholds for cultured retinal pigment epithelial cells exposed to lasers at 532 nm and 458 nm. Journal of Biomedical Optics. 2007:-. doi: ARTN 034030 DOI 10.1117/1.2737394. PubMed PMID: ISI:000248504500034.

214. Lund D, Edsall P, Stuck B, Schulmeister K. Variation of laser-induced retinal injury thresholds with retinal irradiated area: 0.1-s duration, 514-nm exposures. J Biomed Opt. 2007;12(2):024023. doi: 10.1117/1.2714810. PubMed PMID: 17477738.

215. Framme C, Walter A, Prahs P, Regler R, Theisen-Kunde D, Alt C, Brinkmann R. Structural changes of the retina after conventional laser photocoagulation and selective retina treatment (SRT) in spectral domain OCT. Curr Eye Res. 2009;34(7):568-79. doi: 10.1080/02713680902964892 [pii]. PubMed PMID: 19899970.

216. Framme C, Schule G, Roider J, Birngruber R, Brinkmann R. Online autofluorescence measurements during selective RPE laser treatment. Graefes Archive For Clinical and Experimental Ophthalmology. 2004:863-9. doi: DOI 10.1007/s00417-004-0938-3. PubMed PMID: ISI:000225104800008.

217. Sarna T, Burke JM, Korytowski W, Rózanowska M, Skumatz CM, Zareba A, Zareba M. Loss of melanin from human RPE with aging: possible role of melanin photooxidation. Exp Eye Res. 2003;76(1):89-98. doi: S0014483502002476 [pii]. PubMed PMID: 12589778.

218. Burke JM, Henry MM, Zareba M, Sarna T. Photobleaching of melanosomes from retinal pigment epithelium: I. Effects on protein oxidation. Photochem Photobiol. 2007;83(4):920-4. doi: PHP081 [pii] 10.1111/j.1751-1097.2007.00081.x. PubMed PMID: 17645664.

219. Marc RE, Jones BW, Watt CB, Vazquez-Chona F, Vaughan DK, Organisciak DT. Extreme retinal remodeling triggered by light damage: implications for age related macular degeneration. Mol Vis. 2008;14:782-806. PubMed PMID: 18483561; PubMed Central PMCID: PMCPMC2375357.

220. Sullivan R, Penfold P, Pow DV. Neuronal migration and glial remodeling in degenerating retinas of aged rats and in nonneovascular AMD. Invest Ophthalmol Vis Sci. 2003;44(2):856-65. PubMed PMID: 12556422.

221. Delori F. Autofluorescence method to measure macular pigment optical densities fluorometry and autofluorescence imaging. Archives of Biochemistry and Biophysics. 2004:156-62. doi: DOI 10.1016/j.abb.2004.05.016. PubMed PMID: ISI:000224104500005.

222. Delori F, Greenberg JP, Woods RL, Fischer J, Duncker T, Sparrow J, Smith RT. Quantitative measurements of autofluorescence with the scanning laser ophthalmoscope. Invest Ophthalmol Vis Sci. 2011;52(13):9379-90. doi: iovs.11-8319 [pii] 10.1167/iovs.11-8319. PubMed PMID: 22016060; PubMed Central PMCID: PMCPMC3250263.

223. Gray D, Merigan W, Wolfing J, Gee B, Porter J, Dubra A, Twietmeyer T, Ahmad K, Tumbar R, Reinholz F, Williams D. In vivo fluorescence imaging of primate retinal ganglion cells and retinal pigment epithelial cells. Optics Express. 2006:7144-58. PubMed PMID: ISI:000239861100018.

224. Delori FC, Webb RH, Sliney DH, Institute ANS. Maximum permissible exposures for ocular safety (ANSI 2000), with emphasis on ophthalmic devices. J

Opt Soc Am A Opt Image Sci Vis. 2007;24(5):1250-65. PubMed PMID: 17429471.

225. Hunter JJ, Masella B, Dubra A, Sharma R, Yin L, Merigan WH, Palczewska G, Palczewski K, Williams DR. Images of photoreceptors in living primate eyes using adaptive optics two-photon ophthalmoscopy. Biomed Opt Express. 2010;2(1):139-48. doi: 10.1364/BOE.2.000139. PubMed PMID: 21326644; PubMed Central PMCID: PMCPMC3028489.

226. Palczewska G, Maeda T, Imanishi Y, Sun W, Chen Y, Williams DR, Piston DW, Maeda A, Palczewski K. Noninvasive multiphoton fluorescence microscopy resolves retinol and retinal condensation products in mouse eyes. Nat Med. 2010;16(12):1444-9. doi: nm.2260 [pii] 10.1038/nm.2260. PubMed PMID: 21076393.

227. Briley D, Boretsky A, Motamedi N, Motamedi M. High resolution volumetric imaging in the murine retina. Journal of Vision. 2013;13(15):P34. doi: 10.1167/13.15.69.

228. Lu RW, Li YC, Ye T, Strang C, Keyser K, Curcio CA, Yao XC. Two-photon excited autofluorescence imaging of freshly isolated frog retinas. Biomed Opt Express. 2011;2(6):1494-503. doi: 10.1364/BOE.2.001494. PubMed PMID: 21698013; PubMed Central PMCID: PMCPMC3114218.

229. Bindewald A, Schmitz-Valckenberg S, Jorzik JJ, Dolar-Szczasny J, Sieber H, Keilhauer C, Weinberger AW, Dithmar S, Pauleikhoff D, Mansmann U, Wolf S, Holz FG. Classification of abnormal fundus autofluorescence patterns in the junctional zone of geographic atrophy in patients with age related macular degeneration. Br J Ophthalmol. 2005;89(7):874-8. doi: 10.1136/bjo.2004.057794. PubMed PMID: 15965170; PubMed Central PMCID: PMCPMC1772741.

230. Bindewald A, Bird AC, Dandekar SS, Dolar-Szczasny J, Dreyhaupt J, Fitzke FW, Einbock W, Holz FG, Jorzik JJ, Keilhauer C, Lois N, Mlynski J, Pauleikhoff D, Staurenghi G, Wolf S. Classification of fundus autofluorescence patterns in early age-related macular disease. Invest Ophthalmol Vis Sci. 2005;46(9):3309-14. doi: 10.1167/iovs.04-0430. PubMed PMID: 16123434.

231. Dorin G. Evolution of retinal laser therapy: minimum intensity photocoagulation (MIP). Can the laser heal the retina without harming it? Semin Ophthalmol. 2004;19(1-2):62-8. doi: K9WYD1P43528DU5K [pii] 10.1080/08820530490884173. PubMed PMID: 15590536.

232. Roider J, Brinkmann R, Wirbelauer C, Laqua H, Birngruber R. Subthreshold (retinal pigment epithelium) photocoagulation in macular diseases: a pilot study. British Journal of Ophthalmology. 2000:40-7. PubMed PMID: ISI:000084886900018.

233. Buschini E, Piras A, Nuzzi R, Vercelli A. Age related macular degeneration and drusen: neuroinflammation in the retina. Prog Neurobiol. 2011;95(1):14-25. doi: S0301-0082(11)00102-X [pii] 10.1016/j.pneurobio.2011.05.011. PubMed PMID: 21740956.

234. Iezzi R, Guru BR, Glybina IV, Mishra MK, Kennedy A, Kannan RM. Dendrimer-based targeted intravitreal therapy for sustained attenuation of neuroinflammation in retinal degeneration. Biomaterials. 2012;33(3):979-88. doi: 10.1016/j.biomaterials.2011.10.010. PubMed PMID: WOS:000298212400027.

235. Jiang B, Harper MM, Kecova H, Adamus G, Kardon RH, Grozdanic SD, Kuehn MH. Neuroinflammation in advanced canine glaucoma. Molecular Vision. 2010;16(225-26):2092-108. PubMed PMID: WOS:000283717000001.

236. Ibrahim AS, El-Remessy AB, Matragoon S, Zhang W, Patel Y, Khan S, Al-Gayyar MM, El-Shishtawy MM, Liou GI. Retinal microglial activation and inflammation induced by amadori-glycated albumin in a rat model of diabetes. Diabetes. 2011;60(4):1122-33. doi: db10-1160 [pii] 10.2337/db10-1160. PubMed PMID: 21317295; PubMed Central PMCID: PMCPMC3064086.

237. Liou GI. Diabetic retinopathy: Role of inflammation and potential therapies for anti-inflammation. World journal of diabetes. 2010;1(1):12-8. PubMed PMID: MEDLINE:21537423.

238. Tang J, Kern TS. Inflammation in diabetic retinopathy. Prog Retin Eye Res. 2011;30(5):343-58. doi: S1350-9462(11)00035-8 [pii] 10.1016/j.preteyeres.2011.05.002. PubMed PMID: 21635964.

239. Kowluru RA, Koppolu P, Chakrabarti S, Chen S. Diabetes-induced activation of nuclear transcriptional factor in the retina, and its inhibition by antioxidants. Free Radic Res. 2003;37(11):1169-80. PubMed PMID: 14703729.

240. Chakraborty JB, Mann DA. NF-kappaB signalling: embracing complexity to achieve translation. J Hepatol. 2010;52(2):285-91. doi: S0168-8278(09)00737-5 [pii] 10.1016/j.jhep.2009.10.030. PubMed PMID: 20022129.

241. Srivastava SK, Ramana KV. Focus on molecules: nuclear factor-kappaB. Exp Eye Res. 2009;88(1):2-3. doi: S0014-4835(08)00099-7 [pii] 10.1016/j.exer.2008.03.012. PubMed PMID: 18472097; PubMed Central PMCID: PMCPMC2606916.

242. Vallabhapurapu S, Karin M. Regulation and function of NF-kappaB transcription factors in the immune system. Annu Rev Immunol. 2009;27:693-733. doi: 10.1146/annurev.immunol.021908.132641. PubMed PMID: 19302050.

243. Kumar A, Takada Y, Boriek AM, Aggarwal BB. Nuclear factor-kappaB: its role in health and disease. J Mol Med (Berl). 2004;82(7):434-48. doi: 10.1007/s00109-004-0555-y. PubMed PMID: 15175863.

244. Hunot S, Brugg B, Ricard D, Michel PP, Muriel MP, Ruberg M, Faucheux BA, Agid Y, Hirsch EC. Nuclear translocation of NF-kappa B is increased in dopaminergic neurons of patients with Parkinson disease. Proceedings of the National Academy of Sciences of the United States of America. 1997;94(14):7531-6. doi: 10.1073/pnas.94.14.7531. PubMed PMID: WOS:A1997XJ87600074.

245. Kaltschmidt B, Uherek M, Volk B, Baeuerle PA, Kaltschmidt C. Transcription factor NF-kappa B is activated in primary neurons by amyloid beta peptides and in neurons surrounding early plaques from patients with Alzheimer disease. Proceedings of the National Academy of Sciences of the United States of America. 1997;94(6):2642-7. doi: 10.1073/pnas.94.6.2642. PubMed PMID: WOS:A1997WP33400100.

246. O'Neill LA, Kaltschmidt C. NF-kappa B: a crucial transcription factor for glial and neuronal cell function. Trends Neurosci. 1997;20(6):252-8. doi: S0166223696010351 [pii]. PubMed PMID: 9185306.

247. Pizzi M, Spano P. Distinct roles of diverse nuclear factor-kappaB complexes in neuropathological mechanisms. Eur J Pharmacol. 2006;545(1):22-8. doi: S0014-2999(06)00645-5 [pii] 10.1016/j.ejphar.2006.06.027. PubMed PMID: 16854410.

248. Fischer F, Martin G, Agostini HT. Activation of retinal microglia rather than microglial cell density correlates with retinal neovascularization in the mouse model of oxygen-induced retinopathy. J Neuroinflammation. 2011;8:120. doi: 1742-2094-8-120 [pii] 10.1186/1742-2094-8-120. PubMed PMID: 21943408; PubMed Central PMCID: PMCPMC3190350.

249. Mandal MN, Patlolla JM, Zheng L, Agbaga MP, Tran JT, Wicker L, Kasus-Jacobi A, Elliott MH, Rao CV, Anderson RE. Curcumin protects retinal cells from light- and oxidant stress-induced cell death. Free Radic Biol Med. 2009;46(5):672-9. doi: S0891-5849(08)00759-4 [pii] 10.1016/j.freeradbiomed.2008.12.006. PubMed PMID: 19121385; PubMed Central PMCID: PMCPMC2810836.

250. Wu T, Handa JT, Gottsch JD. Light-induced oxidative stress in choroidal endothelial cells in mice. Invest Ophthalmol Vis Sci. 2005;46(4):1117-23. doi: 46/4/1117 [pii] 10.1167/iovs.04-0517. PubMed PMID: 15790868.

251. Chen YG, Zhang C, Chiang SK, Wu T, Tso MO. Increased nuclear factor-kappa B p65 immunoreactivity following retinal ischemia and reperfusion injury in mice. J Neurosci Res. 2003;72(1):125-31. doi: 10.1002/jnr.10548. PubMed PMID: 12645086.

252. Yang LP, Zhu XA, Tso MO. Role of NF-kappaB and MAPKs in light-induced photoreceptor apoptosis. Invest Ophthalmol Vis Sci. 2007;48(10):4766-76. doi: 48/10/4766 [pii] 10.1167/iovs.06-0871. PubMed PMID: 17898303.

253. Burgess A, Vigneron S, Brioudes E, Labbé JC, Lorca T, Castro A. Loss of human Greatwall results in G2 arrest and multiple mitotic defects due to deregulation of the cyclin B-Cdc2/PP2A balance. Proc Natl Acad Sci U S A. 2010;107(28):12564-9. doi: 10.1073/pnas.0914191107. PubMed PMID: 20538976; PubMed Central PMCID: PMCPMC2906566.

254. Wikler KC, Williams RW, Rakic P. Photoreceptor mosaic: number and distribution of rods and cones in the rhesus monkey retina. J Comp Neurol. 1990;297(4):499-508. doi: 10.1002/cne.902970404. PubMed PMID: 2384610.

255. Curcio CA, Sloan KR, Kalina RE, Hendrickson AE. Human photoreceptor topography. J Comp Neurol. 1990;292(4):497-523. doi: 10.1002/cne.902920402. PubMed PMID: 2324310.

256. Wood PL. Neuroinflammation : mechanisms and management. 2nd ed. Totowa, N.J.: Humana Press; 2003. 419 p. p.

257. Dreher Z, Wegner M, Stone J. Müller cell endfeet at the inner surface of the retina: light microscopy. Vis Neurosci. 1988;1(2):169-80. PubMed PMID: 3154794.

258. Vázquez-Chona F, Song BK, Geisert EE. Temporal changes in gene expression after injury in the rat retina. Invest Ophthalmol Vis Sci. 2004;45(8):2737-46. doi: 10.1167/iovs.03-1047. PubMed PMID: 15277499; PubMed Central PMCID: PMCPMC2821791.

259. Bringmann A, Reichenbach A. Role of Muller cells in retinal degenerations. Front Biosci. 2001;6:E72-92. PubMed PMID: 11578954.

260. Pocock GM, Boretsky A, Wang H-C, Golden D, Gupta P, Vargas G, Oliver JW, Motamedi M, Jansen E, Thomas R. NF-kB Activation as a Biomarker of Light Injury Using a Transgenic Mouse Model. Optical Interactions With Tissue and Cells Xxiii. 2012;8221. doi: 10.1117/12.908835. PubMed PMID: WOS:000302290100003.

261. Geng Y, Greenberg KP, Wolfe R, Gray DC, Hunter JJ, Dubra A, Flannery JG, Williams DR, Porter J. In vivo imaging of microscopic structures in the rat retina. Invest Ophthalmol Vis Sci. 2009;50(12):5872-9. doi: iovs.09-3675 [pii] 10.1167/iovs.09-3675. PubMed PMID: 19578019; PubMed Central PMCID: PMCPMC2873188.

262. Jian Y, Zawadzki RJ, Sarunic MV. Adaptive optics optical coherence tomography for in vivo mouse retinal imaging. J Biomed Opt. 2013;18(5):56007. doi: 10.1117/1.JBO.18.5.056007. PubMed PMID: 23644903.

263. Sharma R, Yin L, Geng Y, Merigan WH, Palczewska G, Palczewski K, Williams DR, Hunter JJ. In vivo two-photon imaging of the mouse retina. Biomed Opt

Express. 2013;4(8):1285-93. doi: 10.1364/BOE.4.001285. PubMed PMID: 24009992; PubMed Central PMCID: PMCPMC3756587.

264. Claybon A, Bishop AJR. Dissection of a Mouse Eye for a Whole Mount of the Retinal Pigment Epithelium.

265. Wong WT, Kam W, Cunningham D, Harrington M, Hammel K, Meyerle CB, Cukras C, Chew EY, Sadda SR, Ferris FL. Treatment of geographic atrophy by the topical administration of OT-551: results of a phase II clinical trial. Invest Ophthalmol Vis Sci. 2010;51(12):6131-9. doi: 10.1167/iovs.10-5637. PubMed PMID: 20574018; PubMed Central PMCID: PMCPMC3055748.

266. Li KY, Tiruveedhula P, Roorda A. Intersubject variability of foveal cone photoreceptor density in relation to eye length. Invest Ophthalmol Vis Sci. 2010;51(12):6858-67. doi: iovs.10-5499 [pii] 10.1167/iovs.10-5499. PubMed PMID: 20688730; PubMed Central PMCID: PMCPMC3055782.

267. Park SP, Chung JK, Greenstein V, Tsang SH, Chang S. A study of factors affecting the human cone photoreceptor density measured by adaptive optics scanning laser ophthalmoscope. Exp Eye Res. 2013;108:1-9. doi: 10.1016/j.exer.2012.12.011. PubMed PMID: 23276813.

268. Chui TY, Song H, Burns SA. Individual variations in human cone photoreceptor packing density: variations with refractive error. Invest Ophthalmol Vis Sci. 2008;49(10):4679-87. doi: iovs.08-2135 [pii] 10.1167/iovs.08-2135. PubMed PMID: 18552378; PubMed Central PMCID: PMCPMC2710765.

269. Dubra A, Sulai Y, Norris JL, Cooper RF, Dubis AM, Williams DR, Carroll J. Noninvasive imaging of the human rod photoreceptor mosaic using a confocal adaptive optics scanning ophthalmoscope. Biomed Opt Express. 2011;2(7):1864-76. doi: 145204 [pii] 10.1364/BOE.2.001864. PubMed PMID: 21750765; PubMed Central PMCID: PMCPMC3130574.

270. Lombardo M, Serrao S, Ducoli P, Lombardo G. Eccentricity dependent changes of density, spacing and packing arrangement of parafoveal cones. Ophthalmic Physiol Opt. 2013;33(4):516-26. doi: 10.1111/opo.12053. PubMed PMID: 23550537.

271. Song H, Chui TY, Zhong Z, Elsner AE, Burns SA. Variation of cone photoreceptor packing density with retinal eccentricity and age. Invest Ophthalmol Vis Sci. 2011;52(10):7376-84. doi: iovs.11-7199 [pii] 10.1167/iovs.11-7199. PubMed PMID: 21724911; PubMed Central PMCID: PMCPMC3183974.

272. Carroll J, Kay DB, Scoles D, Dubra A, Lombardo M. Adaptive Optics Retinal Imaging - Clinical Opportunities and Challenges. Curr Eye Res. 2013. doi: 10.3109/02713683.2013.784792. PubMed PMID: 23621343.

273. Felberer F, Kroisamer JS, Hitzenberger CK, Pircher M. Lens based adaptive optics scanning laser ophthalmoscope. Opt Express. 2012;20(16):17297-310. PubMed PMID: 23038283.

274. Burns SA, Tumbar R, Elsner AE, Ferguson D, Hammer DX. Large-field-of-view, modular, stabilized, adaptive-optics-based scanning laser ophthalmoscope. J Opt Soc Am A Opt Image Sci Vis. 2007;24(5):1313-26. doi: 132123 [pii]. PubMed PMID: 17429477; PubMed Central PMCID: PMCPMC2443858.

275. Hammer DX, Ferguson RD, Bigelow CE, Iftimia NV, Ustun TE, Burns SA. Adaptive optics scanning laser ophthalmoscope for stabilized retinal imaging. Opt Express. 2006;14(8):3354-67. PubMed PMID: 19516480; PubMed Central PMCID: PMCPMC2923468.

276. Delori F, Webb R, Sliney D. Maximum permissible exposures for ocular safety (ANSI 2000), with emphasis on ophthalmic devices. Journal of the Optical Society of America a-Optics Image Science and Vision. 2007:1250-65. PubMed PMID: ISI:000245933700003.

277. Dubra A, Harvey Z. Registration of 2D Images from Fast Scanning Ophthalmic Instruments. In: Fischer B, Dawant B, Lorenz C, editors. Biomedical Image Registration: Springer Berlin Heidelberg; 2010. p. 60-71.

278. Stevenson SB, Roorda A, editors. Correcting for miniature eye movements in high resolution scanning laser ophthalmoscopy2005.

279. Saalfeld S, Cardona A, Hartenstein V, Tomancák P. As-rigid-as-possible mosaicking and serial section registration of large ssTEM datasets. Bioinformatics. 2010;26(12):i57-63. doi: btq219 [pii] 10.1093/bioinformatics/btq219. PubMed PMID: 20529937; PubMed Central PMCID: PMCPMC2881403.

280. Lowe D. Distinctive Image Features from Scale-Invariant Keypoints. International Journal of Computer Vision. 2004;60(2):91-110. doi: 10.1023/B:VISI.0000029664.99615.94.

281. Li H, Lu J, Shi G, Zhang Y. Tracking features in retinal images of adaptive optics confocal scanning laser ophthalmoscope using KLT-SIFT algorithm. Biomed Opt Express. 2010;1(1):31-40. doi: 10.1364/BOE.1.000031. PubMed PMID: 21258443; PubMed Central PMCID: PMCPMC3005164.

282. Mujat M, Ferguson RD, Patel AH, Iftimia N, Lue N, Hammer DX. High resolution multimodal clinical ophthalmic imaging system. Opt Express. 2010;18(11):11607-21. PubMed PMID: 20589021; PubMed Central PMCID: PMCPMC2958093.

283. Rativa D, Vohnsen B. Analysis of individual cone-photoreceptor directionality using scanning laser ophthalmoscopy. Biomed Opt Express. 2011;2(6):1423-31.

doi: 10.1364/BOE.2.001423. PubMed PMID: 21698006; PubMed Central PMCID: PMCPMC3114211.

284. Pallikaris A, Williams DR, Hofer H. The reflectance of single cones in the living human eye. Invest Ophthalmol Vis Sci. 2003;44(10):4580-92. PubMed PMID: 14507907.

285. Jonnal RS, Besecker JR, Derby JC, Kocaoglu OP, Cense B, Gao W, Wang Q, Miller DT. Imaging outer segment renewal in living human cone photoreceptors. Opt Express. 2010;18(5):5257-70. PubMed PMID: 20389538; PubMed Central PMCID: PMCPMC3113600.

286. Byun J, Verardo MR, Sumengen B, Lewis GP, Manjunath BS, Fisher SK. Automated tool for the detection of cell nuclei in digital microscopic images: application to retinal images. Mol Vis. 2006;12:949-60. doi: v12/a107 [pii]. PubMed PMID: 16943767.

287. Curcio CA, Medeiros NE, Millican CL. Photoreceptor loss in age-related macular degeneration. Invest Ophthalmol Vis Sci. 1996;37(7):1236-49. PubMed PMID: 8641827.

288. Curcio CA. Photoreceptor topography in ageing and age-related maculopathy. Eye (Lond). 2001;15(Pt 3):376-83. doi: 10.1038/eye.2001.140. PubMed PMID: 11450761.

289. Lombardo M, Serrao S, Ducoli P, Lombardo G. Influence of sampling window size and orientation on parafoveal cone packing density. Biomed Opt Express. 2013;4(8):1318-31. doi: 10.1364/BOE.4.001318. PubMed PMID: 24009995; PubMed Central PMCID: PMCPMC3756574.

290. Chui TY, Song H, Burns SA. Adaptive-optics imaging of human cone photoreceptor distribution. J Opt Soc Am A Opt Image Sci Vis. 2008;25(12):3021-9. doi: 174847 [pii]. PubMed PMID: 19037393; PubMed Central PMCID: PMCPMC2738986.

291. Godara P, Siebe C, Rha J, Michaelides M, Carroll J. Assessing the photoreceptor mosaic over drusen using adaptive optics and SD-OCT. Ophthalmic Surg Lasers Imaging. 2010;41 Suppl:S104-8. doi: 10.3928/15428877-20101031-07. PubMed PMID: 21117594; PubMed Central PMCID: PMCPMC3124651.

292. Godara P, Wagner-Schuman M, Rha J, Connor TB, Stepien KE, Carroll J. Imaging the photoreceptor mosaic with adaptive optics: beyond counting cones. Adv Exp Med Biol. 2012;723:451-8. doi: 10.1007/978-1-4614-0631-0_57. PubMed PMID: 22183364; PubMed Central PMCID: PMCPMC3325514.

293. Chiu SJ, Lokhnygina Y, Dubis AM, Dubra A, Carroll J, Izatt JA, Farsiu S. Automatic cone photoreceptor segmentation using graph theory and dynamic programming. Biomed Opt Express. 2013;4(6):924-37. doi:

10.1364/BOE.4.000924. PubMed PMID: 23761854; PubMed Central PMCID: PMCPMC3675871.

294. Li KY, Roorda A. Automated identification of cone photoreceptors in adaptive optics retinal images. J Opt Soc Am A Opt Image Sci Vis. 2007;24(5):1358-63. PubMed PMID: 17429481.

295. Martin JA, Roorda A. Direct and noninvasive assessment of parafoveal capillary leukocyte velocity. Ophthalmology. 2005;112(12):2219-24. doi: 10.1016/j.ophtha.2005.06.033. PubMed PMID: 16257054.

296. Godara P, Dubis AM, Roorda A, Duncan JL, Carroll J. Adaptive optics retinal imaging: emerging clinical applications. Optom Vis Sci. 2010;87(12):930-41. doi: 10.1097/OPX.0b013e3181ff9a8b. PubMed PMID: 21057346; PubMed Central PMCID: PMCPMC3017557.

297. Access Economics 2010. The Global Economic Cost of Visual Impairment, report prepared for AMD Alliance International.

298. Rein DB, Zhang P, Wirth KE, Lee PP, Hoerger TJ, McCall N, Klein R, Tielsch JM, Vijan S, Saaddine J. The economic burden of major adult visual disorders in the United States. Arch Ophthalmol. 2006;124(12):1754-60. doi: 10.1001/archopht.124.12.1754. PubMed PMID: 17159036.

299. Rein DB, Wittenborn JS, Zhang X, Honeycutt AA, Lesesne SB, Saaddine J, Group VHC-ES. Forecasting age-related macular degeneration through the year 2050: the potential impact of new treatments. Arch Ophthalmol. 2009;127(4):533-40. doi: 127/4/533 [pii] 10.1001/archophthalmol.2009.58. PubMed PMID: 19365036.

300. Godara P, Siebe C, Rha J, Michaelides M, Carroll J. Assessing the photoreceptor mosaic over drusen using adaptive optics and SD-OCT. Ophthalmic Surg Lasers Imaging. 2010;41 Suppl:S104-8. doi: 10.3928/15428877-20101031-07. PubMed PMID: 21117594; PubMed Central PMCID: PMCPMC3124651.

301. Gocho K, Sarda V, Falah S, Sahel JA, Sennlaub F, Benchaboune M, Ullern M, Paques M. Adaptive optics imaging of geographic atrophy. Invest Ophthalmol Vis Sci. 2013;54(5):3673-80. doi: 10.1167/iovs.12-10672. PubMed PMID: 23620431.

302. Zayit-Soudry S, Duncan JL, Syed R, Menghini M, Roorda AJ. Cone structure imaged with adaptive optics scanning laser ophthalmoscopy in eyes with nonneovascular age-related macular degeneration. Invest Ophthalmol Vis Sci. 2013;54(12):7498-509. doi: 10.1167/iovs.13-12433. PubMed PMID: 24135755; PubMed Central PMCID: PMCPMC3832216.

303. Mrejen S, Sato T, Curcio CA, Spaide RF. Assessing the cone photoreceptor mosaic in eyes with pseudodrusen and soft drusen in vivo using adaptive optics

imaging. Ophthalmology. 2014;121(2):545-51. Epub 2013/11/05. doi: 10.1016/j.ophtha.2013.09.026. PubMed PMID: 24183341.

304. Spaide RF, Curcio CA. Anatomical correlates to the bands seen in the outer retina by optical coherence tomography: literature review and model. Retina. 2011;31(8):1609-19. doi: 10.1097/IAE.0b013e3182247535. PubMed PMID: 21844839; PubMed Central PMCID: PMCPMC3619110.

305. Panorgias A, Zawadzki RJ, Capps AG, Hunter AA, Morse LS, Werner JS. Multimodal assessment of microscopic morphology and retinal function in patients with geographic atrophy. Invest Ophthalmol Vis Sci. 2013;54(6):4372-84. doi: 10.1167/iovs.12-11525. PubMed PMID: 23696601; PubMed Central PMCID: PMCPMC3694790.

306. Stiles WS, Crawford BH. The Luminous Efficiency of Rays Entering the Eye Pupil at Different Points. Proceedings of the Royal Society of London Series B, Containing Papers of a Biological Character. 1933;112(778):428-50. doi: 10.2307/81711.

307. Ivers KM, Li C, Patel N, Sredar N, Luo X, Queener H, Harwerth RS, Porter J. Reproducibility of measuring lamina cribrosa pore geometry in human and nonhuman primates with in vivo adaptive optics imaging. Invest Ophthalmol Vis Sci. 2011;52(8):5473-80. doi: 10.1167/iovs.11-7347. PubMed PMID: 21546533; PubMed Central PMCID: PMCPMC3176071.

308. Boretsky A, Mirza S, Khan F, Motamedi M, van Kuijk FJ. High-resolution multimodal imaging of multiple evanescent white dot syndrome. Ophthalmic Surg Lasers Imaging Retina. 2013;44(3):296-300. doi: 10.3928/23258160-20130503-18. PubMed PMID: 23676237.

309. Carroll J, Neitz M, Hofer H, Neitz J, Williams DR. Functional photoreceptor loss revealed with adaptive optics: an alternate cause of color blindness. Proc Natl Acad Sci U S A. 2004;101(22):8461-6. doi: 10.1073/pnas.0401440101. PubMed PMID: 15148406; PubMed Central PMCID: PMCPMC420416.

310. Hofer H, Carroll J, Neitz J, Neitz M, Williams DR. Organization of the human trichromatic cone mosaic. J Neurosci. 2005;25(42):9669-79. doi: 10.1523/JNEUROSCI.2414-05.2005. PubMed PMID: 16237171.

311. Ach T, Best G, Rossberger S, Heintzmann R, Cremer C, Dithmar S. Autofluorescence imaging of human RPE cell granules using structured illumination microscopy. Br J Ophthalmol. 2012;96(8):1141-4. doi: 10.1136/bjophthalmol-2012-301547. PubMed PMID: 22760487.

312. Rossberger S, Ach T, Best G, Cremer C, Heintzmann R, Dithmar S. High-resolution imaging of autofluorescent particles within drusen using structured illumination microscopy. Br J Ophthalmol. 2013;97(4):518-23. doi: 10.1136/bjophthalmol-2012-302350. PubMed PMID: 23410731.

313. Talcott KE, Ratnam K, Sundquist SM, Lucero AS, Lujan BJ, Tao W, Porco TC, Roorda A, Duncan JL. Longitudinal study of cone photoreceptors during retinal degeneration and in response to ciliary neurotrophic factor treatment. Invest Ophthalmol Vis Sci. 2011;52(5):2219-26. doi: 10.1167/iovs.10-6479. PubMed PMID: 21087953; PubMed Central PMCID: PMCPMC3080173.

Vita

Adam Boretsky was born on July 17th, 1982, in Augusta, Georgia. He graduated with honors from Hardaway High School in Columbus, Georgia and went on to earn a Bachelor of Science degree in Biological Engineering from the University of Georgia in 2005. At UGA, Adam was involved in numerous engineering projects focused on the design of biomedical instrumentation. Upon graduation, he joined the Center for Biomedical Engineering at the University of Texas Medical Branch under the guidance of Dr. Massoud Motamedi. This experience working in an academic laboratory and with industry partners served to reinforce his desire to pursue an advanced degree. In 2008, Adam entered the Graduate School of Biomedical Sciences at UTMB and became the pilot student in the Human Pathophysiology and Translational Medicine program. Adam worked closely with his mentor, Dr. Motamedi, and co-mentor, Dr. Erik van Kuijk, to design and develop novel diagnostic methodology for retinal injury and disease. Adam plans to continue with his optical imaging and sensing training as a post-doctoral fellow at the U.S. Food and Drug Administration in the Center for Devices and Radiological Health investigating neuroprosthetic devices.

Education

The University of Texas Medical Branch, Galveston, TX
Doctor of Philosophy, Human Pathophysiology and Translational Medicine — July 2014

The University of Georgia, Athens, GA
Bachelor of Science in Biological Engineering — May 2005

Professional Certification

Lean & Design for Six Sigma (DFSS) Certification — 2007

Engineer in Training (E.I.T.) – License #022294 — 2005

Awards and Recognition

Invited speaker - Design of Medical Devices Conference, Minneapolis, MN	2014
Rose and Harry Walk Research Award for investigations into aging and age-related pathology	2013
Ann and John Hamilton Endowed Scholarship for academic excellence	2013
Travel Grant awarded by the National Eye Institute (NEI) to present at the Annual Association for Research in Vision and Ophthalmology (ARVO) Conference	2013
Invited speaker - The University of Houston College of Optometry and Vision Science	2012
Invited speaker - The Annual Vision Symposium at the University Of Minnesota	2012
Travel Grant to present at the Annual American Society for Laser Medicine and Surgery (ASLMS) Conference	2012
Principle Investigator - American Society for Laser Medicine and Surgery (ASLMS) Student Research Grant (ASLMS Grant I.D. S0811 - Boretsky)	2011/2012
Mason Guest Scholar Award in Bioengineering and Cellular Physiology	2011

Publications and Conference Proceedings

2014 ***Boretsky A,*** Gupta P, Tirgan N, Liu R, Godley BF, Zhang W, Tilton RG, Motamedi M. Nicotine Accelerates Diabetes-Induced Retinal Changes. *Curr Eye Res*. (Accepted April 2014)

2013 ***Boretsky A***, Mirza S, Khan F, Motamedi M, van Kuijk F. High Resolution Multimodal Imaging of Multiple Evanescent White Dot Syndrome (MEWDS). *Ophthalmic Surg Lasers Imaging Retina.* 2013; May-Jun; 44 (3):296-300.

2012 Chitchian S, Mayer M, ***Boretsky A***, van Kuijk F, Motamedi M. Retinal OCT Image Enhancement using Double-Density Dual-Tree Complex Wavelet Transform. *J. Biomed. Opt.* 17(11), 116009 (Nov 01, 2012).

2012 ***Boretsky A***, Khan F, Burnett G, Hammer DX, Ferguson RD, van Kuijk F, Motamedi M. *In vivo* Imaging of Photoreceptor Disruption Associated with Age-Related Macular Degeneration: A Pilot Study. *Lasers Surg Med.* 2012 Oct;44(8):603-10.

2012 Chitchian S, ***Boretsky A***, van Kuijk F, Motamedi M. An Edge Detection Approach for Mapping of the Human Cone Photoreceptor Mosaic using Adaptive Optics Scanning Laser Ophthalmoscope. Biomedical Optics, OSA Technical Digest (Optical Society of America, 2012), paper BSu3A.17.

2012 Tirgan N, Kulp G, Gupta P, ***Boretsky A***, Wiraszka T, Godley B, Tilton R, Motamedi M. Nicotine Exposure Exacerbates Development of Cataracts in a Type 1 Diabetic Rat Model. *Exp Diabetes Res.* (Epub Sep 20, 2012)

2012 Pocock G, ***Boretsky A***, Wang H, Golden D, Gupta P, Vargas G, Oliver J, Motamedi M. NF-kB activation as a biomarker of light injury using a transgenic mouse model. Proceedings of the SPIE, Vol. 8221 (2012)

2011 ***Boretsky A***, Motamedi M, Bell B, van Kuijk F. Quantitative Evaluation of Retinal Response to Laser Photocoagulation UsingDual-Wavelength Fundus Autofluorescence Imaging in a Small Animal Model. *Invest Ophthalmol Vis Sci.* 2011 Aug 9;52(9):6300-7.

2011 Pocock G, ***Boretsky A***, Gupta P, Oliver J, Motamedi M. Laser injury and in vivo multimodal imaging using a mouse model. Proceedings of the SPIE, Vol. 7897 (2011)

2009 Fox MA, Diven DG, Sra K, ***Boretsky A***, Poonawalla T, Readinger A, Motamedi M, McNichols RJ. Dermal scatter reduction in human skin: a method using controlled application of glycerol. *Lasers Surg Med*. 2009 Apr;41(4):251-5.

2007 Ballerstadt R, Kholodnykh A, Evans C, ***Boretsky A***, Motamedi M, Gowda A, McNichols R. Affinity-based turbidity sensor for glucose monitoring by optical coherence tomography: toward the development of an implantable sensor. *Anal Chem*. 2007 Sep 15;79(18):6965-74.

Conference Abstracts/Poster Presentations

2014 Jonathan Luisi, David Briley, **Adam Boretsky**, Gracie Vargas, and Massoud Motamedi. Automated layer segmentation in retinal OCT images. SPIE Translational Biophotonics 2014, 91551N-91551N-10

2013 Multimodal imaging of the retina in aging and age-related macular degeneration. **Adam Boretsky**, Erik van Kuijk, and Massoud Motamedi J Vis 2013 13(15): P30; doi:10.1167/13.15.65

2013 High resolution volumetric imaging in the murine retina. David Briley, **Adam Boretsky**, Nick Motamedi, and Massoud Motamedi J Vis 2013 13(15): P34; doi:10.1167/13.15.69

2013 Analysis of the Photoreceptor Mosaic in Patients with Each Stage of Dry Age-Related Macular Degeneration (AMD): Cone Density and Spacing as Image-Based Biomarkers. **Adam Boretsky**; Faraz Khan; Frederik J. van Kuijk; Massoud Motamedi. ARVO Poster 2013 #3441-C0162

2013 Molecular and Morphological Imaging of the Murine Retina Following Photothermal Injury and Hyperthermia Conditioning. David Gersztenkorn; **Adam Boretsky**; David Briley; Massoud Motamedi. ISIE Poster 2013 P44

2013 Increased Fundus Autofluorescence and Retinal Cell Infiltration in Middle-Aged Mice Fed with High Fat, Cholesterol-Rich Diet. Zhen-Yang Zhao; Yiqin Zuo; Pei Xu; Bo Yu; Massoud Motamedi; **Adam Boretsky**; Yan Chen; Jiyang Cai. ARVO Poster 2013 #161-C0166

2012 In vivo Imaging of Photoreceptor Loss Associated with Dry Age-Related Macular Degeneration Using Adaptive Optics Scanning Laser Ophthalmoscopy. **Adam Boretsky**, Faraz Khan, Garrett Burnett, Ryan Harris, Mark Stephens, Massoud Motamedi, Frederik van Kuijk. ARVO Poster 2012 #5666/A62

2012 Non-Invasive Monitoring of Changes in the Rat Retina Induced by Nicotine Toxicity and Diabetes Mellitus. Nima Tirgan, **Adam Boretsky**, Praveena Gupta, Bernard F. Godley, Ronald G. Tilton, Massoud Motamedi. ARVO Poster 2012 #5361/A386

2012 Complex Wavelet Denoising of Retinal OCT Imaging. Shahab Chitchian, Markus A. Mayer, **Adam Boretsky**, Frederik van Kuijk, Massoud Motamedi. ARVO Poster 2012 #3124/D1253

2012 Non-invasive in vivo imaging of photoreceptor cells at the single-cell level using an adaptive optics scanning laser ophthalmoscope (AO-SLO) compared with standard diagnostic methods in retinal disease: a case series. Cynthia I. Tung, **Adam Boretsky**, Gibran S Khurshid, Praveena Gupta, Massoud Motamedi. Asia Pacific Academy of Ophthalmology (APAO) Conference 2012

2011 Nicotine Exposure Exacerbates Development of Cataracts in a Type I Diabetic Rat Model. N. Tirgan, G.A. Kulp, P. Gupta, **A. Boretsky**, T.A. Wiraszka, B. Godley, R.G. Tilton, M. Motamedi ARVO Poster 2011 #794/D942

2011 Adaptive Optics SLO Imaging of Macular Photoreceptors: Variations in Automated Cone Density Measurements Based on Confocal Pinhole Diameter. **Adam Boretsky**, Faraz Khan, Frederik van Kuijk and Massoud Motamedi ARVO Poster 2011 #3196/A443

2011 Quantitative Evaluation of Laser Lesion Kinetics Using Dual Wavelength Fundus Autofluorescence Imaging. Massoud Motamedi, **Adam Boretsky**, Brent Bell, and Frederik van Kuij ARVO Poster 2011 #1723/A203

2010 Comparison of Subthreshold Laser Tissue Interaction Using Fundus Autofluorescence in Rats and Human. **Adam Boretsky**, Brent Bell, Massoud Motamedi and Frederik van Kuijk. ARVO Poster 2010 #302/D655

2009 Autofluorescence Imaging of the Retinal Pigment Epithelium to Monitor Benefits of Induced Hsp Upregulation in Response to Photothermal Damage. **Adam Boretsky**, Frederik van Kuijk, Brent Bell, Massoud Motamedi. 50th Annual National Student Research Forum (NSRF Conference). Physiology Poster Session 1 April 2009

2008 Short Term Fundus Autofluorescence Monitoring of Laser -Induced Injury in the Retina. Frederik van Kuijk, **Adam Boretsky**, Brent Bell, and Massoud Motamedi. ARVO Poster April 2008

Professional Society Memberships

The American Society for Laser Medicine and Surgery (ASLMS)
The Association for Research in Vision and Ophthalmology (ARVO)
The International Society for Optics and Photonics (SPIE)

Ad Hoc Reviewer

Investigative Ophthalmology and Visual Science
Journal of Ophthalmology
Ophthalmic Surgery, Lasers and Imaging: Retina